Universitat Autònoma de Barcelona

Graphene devices for cell bioelectronics

Jose Manuel de la Cruz Sánchez

Graphene devices for cell bioelectronics

Jose Manuel de la Cruz Sánchez

Facultad de Ciencias Físicas
Universidad Autónoma de Barcelona

Doctor in Physics
Ph.D.

Director: Prof. Jose Antonio Garrido Ariza
Director: Dra. Elena del Corro García
Tutor: Prof. Jordi Sort Viñas
Defense date: May 13th, 2022

Bellaterra, 2022

Así atravesamos la Mancha, triste y solitario país donde el sol está en su reino, y el hombre parece obra exclusiva del sol y del polvo. [...] la Mancha, si alguna belleza tiene, es la belleza de su conjunto, es su propia desnudéz y monotonía, que si no distraen ni sorprenden la imaginación, la dejan libre, dándole espacio y luz donde se precipite sin tropiezo alguno. La grandeza de D. Quijote no se comprende sino en la grandeza de la Mancha. En un país montuoso, fresco, verde, poblado de agradables sombras, con lindas casas, huertos floridos, luz templada y ambiente espeso, D. Quijote no hubiera podido existir, y habría muerto en flor, tras la primera salida, sin asombrar al mundo con las grandes hazañas de la segunda.

Don Quijote necesitaba aquel horizonte, aquel suelo sin caminos, y que, sin embargo, todo él es camino; aquella tierra sin direcciones, pues por ella se va á todas partes sin ir determinadamente á ninguna; tierra surcada por las veredas del acaso, de la aventura, y donde todo cuanto pase ha de parecer obra de la casualidad ó de los genios de la fábula; necesitaba de aquel sol que derrite los sesos y hace locos á los cuerdos, aquel campo sin fin, donde se levanta el polvo de imaginarias batallas, produciendo al transparentar de la luz, visiones de ejércitos, de gigantes, de torres, de castillos; necesitaba aquella escaséz de ciudades que hace más rara y extraordinaria la presencia de un hombre ó de un animal; necesitaba aquel silencio cuando hay calma y aquel desaforado rugir de los vientos cuando hay tempestad; [...] necesitaba, repito, aquella total ausencia de obras humanas que representen el positivismo, el sentido práctico, cortapisas de la imaginación, que la detendrían en su insensato vuelo; necesitaba, en fin, que el hombre no puesiera en aquellos campos más muestras de su industria y de su ciencia que los patriarcales molinos de viento, los cuales no necesitaban sino hablar, para asemejarse á colosos inquietos y furibundos que desde lejos llaman y espantan al viajero con sus gestos amenazadores. Tal es la Mancha.

- Benito Pérez Galdós, *Bailén*

Acknowledgements

No sé muy bien como empezar esto, la verdad es que nunca he sabido como comenzar las historias. Pero por lo primero por lo que estoy agradecido es por poder escribir estos agradecimientos en castellano después de más de 200 páginas expresándome en inglés.

Si empezamos por el principio, tendría que agradecer a Gloria por ser la primera persona en empujarme hacia la cienca, a Susana Fernández por ser la primera poner patas arriba mi realidad hablándome de masas negativas y antimateria, a Vicente Camacho por ser la primera persona que dió por sentado que la física era lo mío y a mis "amigos los másters" por descubrirme el mítico futuro que esconden las estrellas, tener siempre el hacha afilada y el vaso lleno.

Avanzando un par de años, también debería agradecer a todo el grupo de la facultad por hacerme persona en Madrid, en especial a Rodrigo y a Víctor por aguantarme en Múnich. Una vez en Barcelona, tendría que agradecer a Antón, Xavi, Edu y todo el GAB el apoyo y la ayuda durante estos 6 años. También tendría que agradecer a Steven y Clement todos los consejos y la guía que me han dado; a Andrea demostrarme que aunque me empeñe en ser absolutamente insoportable siempre habrá gente que lo sea más que yo; a Damiá por enseñarme el maldito patch clamp en el Biolab del ZNN un viernes a las 11 de la noche; a Pablo por demostrarme empíricamente que el comunismo no tiene cabida en una sociedad civilizada; a Marta por descubrirme la ratafía y a Pilar por enseñarme que los mejores references son de platino y organizar el mejor viaje de la tesis.

Un párrafo aparte se merecen Jose, por intentar que esta tesis llegase al mejor puerto posible a pesar de sus obvias deficiencias como director y por demostrarme que quien a buen árbol se arrima, buena sombra le cobija; Elena, por enseñarme la diferencia entre escaldar un huevo y escalfar un tomate y el ciclismo, por hacer que la mayor parte de esta tesis tome forma mientras rodaba por las carreteras infinitas de La Mancha o escalaba el Estenalles.

Para el final me dejo a las personas que por estar siempre ahí a veces se dan por sentado, en especial a mis padres y hermanos. Soy un auténtico privilegiado

por haber tenido unos padres y unos abuelos que no sólo me han dicho, sino que me han demostrado día a día que la única forma de conseguir cualquier cosa que merezca la pena es el trabajo, el esfuerzo y la constancia.

Y a Laura, qué menos que agradecerte la complicidad durante todos estos años, además de la infinidad cosas que sólo tú y yo sabemos.

Parafraseando a John Donne, no man is an island entire of itself; every man is a piece of the continent, a part of the main. Tendría que echaos a todos la culpa del naufragio que es esta tesis. A todos vosotros, no sé si decíos gracias o lo siento.

Abstract

Advancements in neuroscience are made possible by the progressive development of new tools and techniques that offer researchers the capabilities to image and record more and more aspects of the nervous system. Among them, microelectrode arrays allow us to directly measure and study the electrical activity produced by the brain and other organs of the nervous system with great spatial and temporal resolution. Furthermore, electrodes allow us to bidirectional interface with neural tissue, delivering electrical stimulation that can be used to further study the brain or even to restore lost capabilities.

The need for stable and biocompatible materials, yet able to acquire high signal-to-noise recordings and deliver enough current to successfully stimulate neural tissue has driven researchers to explore new materials to fabricate electrodes aimed to interface with the nervous system. Within this framework, we have explored the capabilities of different graphene-based materials to bidirectionally interact with nervous tissue.

In this thesis, we have developed low noise rigid single layer graphene (SLG) microelectrode arrays (MEA) and have used them to record electrical activity in primary cortical cultures. We have also developed transparent and flexible SLG probes, containing one macro-electrode, and used them to record electroretinograms (ERG), benchmarking them against the current state of the art for animal recordings using a commercially available clinical setup. Furthermore, we have pushed the capabilities of commercially available electrodes by developing transparent and flexible MEA probes made of SLG, that allow us to obtain spatial information of the corneal potential. In this work, we also present the fabrication of novel reduced graphene oxide (rGO) electrodes; this technology has allowed us to develop rGO MEA with high charge injection capabilities and low electrical noise values. We have demonstrated that these MEA are able sustain healthy hippocampal primary cultures and to bidirectionally interface them, performing simultaneous recording and stimulation. Finally, and to exploit the versatility offered by our graphene-based MEA, we have explored three different techniques

to guide and control the growth of neurons plated on top of our SLG and rGO devices, aiming to provide new tools to study bottom-up neuroscience.

Overall, the results presented in this thesis prove that graphene-based electrode technology, with its stability, biocompatibility and extraordinary electrical performance, is an extremely valuable tool to perform in vitro and in vivo neuroscience studies.

Abstract

Los avances en neurociencia son posibles gracias al desarrollo progresivo de nuevas herramientas y técnicas que ofrecen a los investigadores la capacidad de visualizar y registrar cada vez más aspectos del sistema nervioso. De entre todas estas herramientas, los electrodos y las matrices de microelectrodos nos permite medir y estudiar directamente la actividad eléctrica producida por el cerebro y los demás órganos del sistema nervioso, con una gran resolución espacial y temporal. Además, los electrodos nos permiten establecer una comunica ción bidireccional con el tejido neural, aplicando pulsos de estimulación eléctrica que pueden ser utilizados para estudiar explorar distintos aspectos del cerebro o incluso para restaurar las capacidades neurológicas perdidas a causa de enfermedades o accidentes.

La necesidad de materiales estables y biocompatibles, pero a la vez capaces de registrar actividad eléctrica con bajo ruido e inyectar suficiente corriente como para estimular el tejido neural, ha llevado a los investigadores a explorar nuevos materiales para fabricar electrodos destinados a interactuar con el sistema nervioso. Dentro de este marco, hemos explorado las capacidades de diferentes materiales basados en el carbono para interactuar bidireccionalmente con el tejido nervioso.

En esta tesis, hemos desarrollado matrices de multielectrodos de grafeno monocapa con bajo ruido y las hemos utilizado para medir actividad eléctrica en cultivos corticales primarios. También hemos desarrollado dispositivos de grafeno monocapa transparentes y flexibles, con un sólo macroelectrodo, y los hemos usado para medir electrorretinogramas, comparándolos con el estado actual de la técnica para uso animal, utilizando un equipo de medida aprobado para uso clínico y comercialmente disponible. Además, aprovechando la transparencia del grafeno monocapa, hemos desarrollado matrices de microelectrodos transparentes y, que nos permiten obtener información espacial del potencial corneal. En esta tesis, también presentamos la fabricación de nuevos electrodos de óxido de grafeno reducido, que nos han permitido desarrollar matrices de microelectrodos con altas capacidades de inyección de carga y bajos valores de ruido eléctrico. Hemos

demostrado que estas matrices de microelectrodos son capaces de permitir el crecimiento y desarrollo de cultivos primarios hipocampales saludables y de comunicarse de forma bidireccional con ellos, realizando medidas y aplicando estímulos de forma simultánea. Finalmente, y para explotar la versatilidad de nuestras matrices de microelectrodos basadas en grafeno, hemos explorado tres técnicas diferentes para guiar y controlar el crecimiento de neuronas cultivadas sobre nuestros dispositivos, con el objetivo de desarrollar nuevas herramientas diseñadas para estudiar diversos problemas neurocientíficos empleando la bottom-up neuroscience.

En general, los resultados presentados en esta tesis demuestran que los electrodos basados en el grafeno, con su estabilidad, biocompatibilidad y extraordinarias capacidades eléctricas, son herramientas extremadamente valiosas para realizar estudios de neurociencia *in vitro* e *in vivo*.

Table of Contents

List of Figures

List of Tables

1

Graphene-based electrodes for bioelectronics

I have approximate knowledge of many things

Demon Cat
Adventure Time

In this chapter we will discuss the motivation of this thesis, as well as provide basic concepts related to neuroscience, graphene and its interaction with liquid electrolytes that are necessary to interpret the experimental results discussed in the following chapters. This chapter concludes with a brief description of the scope of this PhD thesis.

1.1 Motivation of this work

Everything what we see, hear or feel is conveyed from our senses to our brain through electrical impulses. Our identity, our memories and our whole world are contained within the approximately 1300 grams of organ that is our brain. Therefore it is no surprise that one of humanity's long lasting aspirations has been to unravel the mechanisms that make our brains work.

In a purely practical sense, understanding how our brain and nervous system work is one of the cornerstones to improve our quality of life. Studies show that in

2010 an estimated 180 million people were affected by brain diseases in Europe, which amounts to one third of the total population [1], positioning brain diseases as the major health problem in developed countries. Furthermore, and in order to raise awareness about this issue, several studies have estimated the total cost of brain disorders, in Europe in 2010 only, in more than 800 billion euros [2, 3]. In addition, the huge complexity of the human brain makes brain disorders more difficult to analyse, diagnose and treat than the rest of diseases, making neuroscience research fundamental to address this issue [4]. This perspective has pushed for the creation of big collaborative and multidisciplinary research projects such as the Human Brain project in Europe [5, 6], the BRAIN initiative [7, 8, 9] and the Allen Brain Atlas [10, 11] in the USA. With these facts in mind, it is obvious that addressing the issue of brain diseases is not only an unquestionable emergency but a fascinating challenge for our society.

Now that we have highlighted the importance to study and understand the brain the next question we need to answer is how to do it.

The oldest methods rely on studying behavioural changes of patients that have sustained an injury and then performing a *post mortem* examination of the brain to understand how it was damaged, linking the behavioural change to an specific brain area. A famous example of this method is the case of Phineas Cage, a railway worker who, in 1848, had a work accident that caused an iron rod to perforate his skull, destroying his frontal lobe. Cage survived the accident and made a complete physical recovery, but his behaviour was completely altered by the brain injury [18], he became an unpredictable and violent person. Another interesting case is the "Tan" patient from Paul Broca, which he tended to in 1861. This patient had lost the ability to speak voluntarily, what today is called aphasia, being only able to say "Tan", but having completely normal behaviour otherwise. In a *post mortem* examination after the patient's death, Broca found that he had sustained damage in the left frontal lobe and hypothesised that this region was related to speech production [19]. Today, that region in the frontal lobe is known as Broca´s area.

Although studying the behavioural changes after an injury is an approach that suffers from many and severe setbacks, like the complete lack of control over the injury or the need to wait for a *post mortem* examination, it yielded some interesting results. The two examples above illustrate how neuroscientists in the nineteenth century came up with the idea of cerebral localization, meaning that specific parts of the brain can control specific aspects of behaviour, thoughts or even personality. Even today, studying behavioural changes is an approach used, to some extent, to explore complex brain problems like anxiety [20] and depression [21] in the form of behavioural test with animal models.

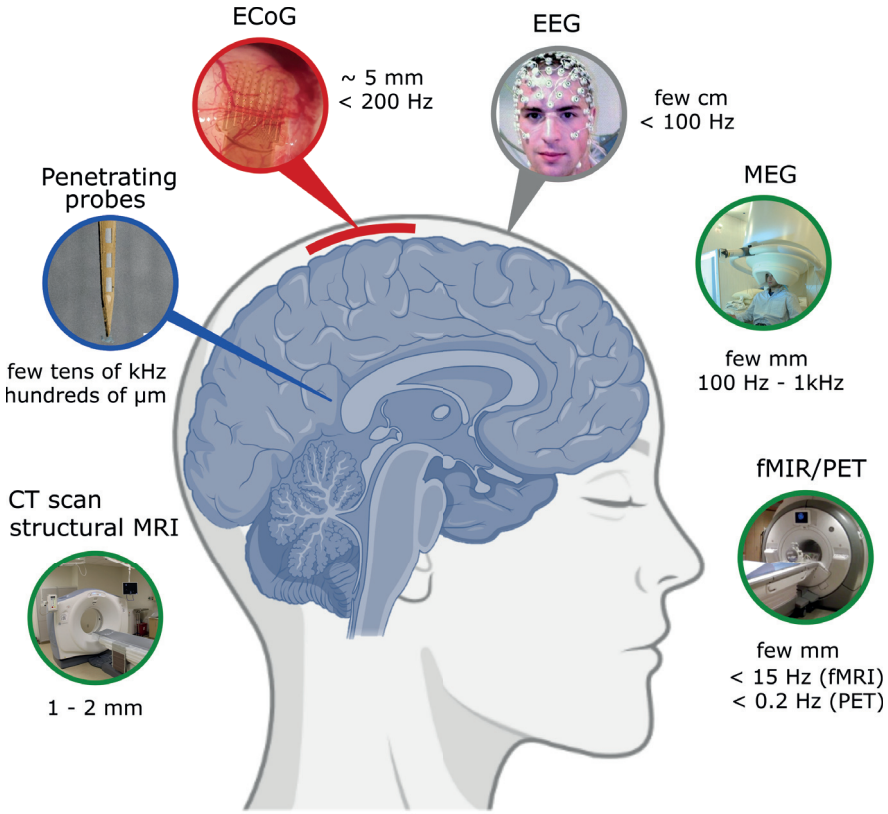

Figure 1.1: Techniques to study neuroscience - Schematic representation of the different techniques used to study the brain, the body regions they need to have access to and their spatiotemporal resolution. Source of spatiotemporal resolution: MRI and CT [12], Penetrating, ECoG, EEG [13], fMRI [14], PET [15, 16] and MEG [17].

In contrast to the behavioural test, a more modern approach is to study brain structure and function using neuroimaging tools that allow us to directly visualize either the structure or the functionality of the brain. To visualize the structure we can use magnetic resonance imaging (MRI) [22], which can distinguish grey matter from white matter due to their differences in fat content, or computerized tomography (CT) scans, which are computer reconstructed images from X-rays scans acquired at different angles. The tools to image brain function, on the other hand, are based on measuring changes in the blood flow, signaling active zones of the brain during a particular task. Such tools are functional MRI [23] and functional ultrasound imaging (fUS) [24]. Although it does not monitor blood flow, positron emission tomography (PET) is another functional neuroimaging technique worth mentioning. In PET scans a radioactive-labeled molecule is introduced in the body and the emitted gamma rays are detected making possible to trace back the position of the active brain area in a particular moment [25]. PET scans are normally coupled with CT scans, allowing for simultaneous structural and functional imaging. The main advantage of these tools is that they are not invasive and can cover relatively large areas of the brain at once. On the down side, their spatiotemporal resolution is quite poor compared with other techniques that will be discussed next.

Finally, to directly study the brain electrophysiology instead of the changes that it produces in the blood or the metabolism, we have a variety of tools based on electrical activity measurements. These techniques can be divided into non-invasive and invasive.

The non-invasive techniques do not require to introduce the recording electrodes inside the body and can be performed without any kind of surgery. One example of this is electroencephalography (EEG). EEG measures the brain electrical activity using electrodes typically placed on the scalp. EEG offers good temporal resolution but poor spatial resolution and the signal gets attenuated when traveling through the skull [26]. Improving on the spatial resolution provided by the EEG, we have magnetoencephalography (MEG) [27]. MEG works by measuring the magnetic field produced by the ionic currents in the brain; such signals do not suffer attenuation when crossing the bone. This technique, however, requires a bulky and expensive setup, when compared with EEG, and it needs to be in a specially isolated room, which severely limits its use.

For the invasive techniques, like electrocorticography (ECoG) [26] or brain penetrating electrodes [28, 29], the electrodes are directly in contact with the brain tissue. In the case of ECoG, the electrodes are placed on the surface of the cerebral cortex, meanwhile for the brain penetrating probes they are inserted deep in the brain. A common factor to all invasive electrophysiology techniques is

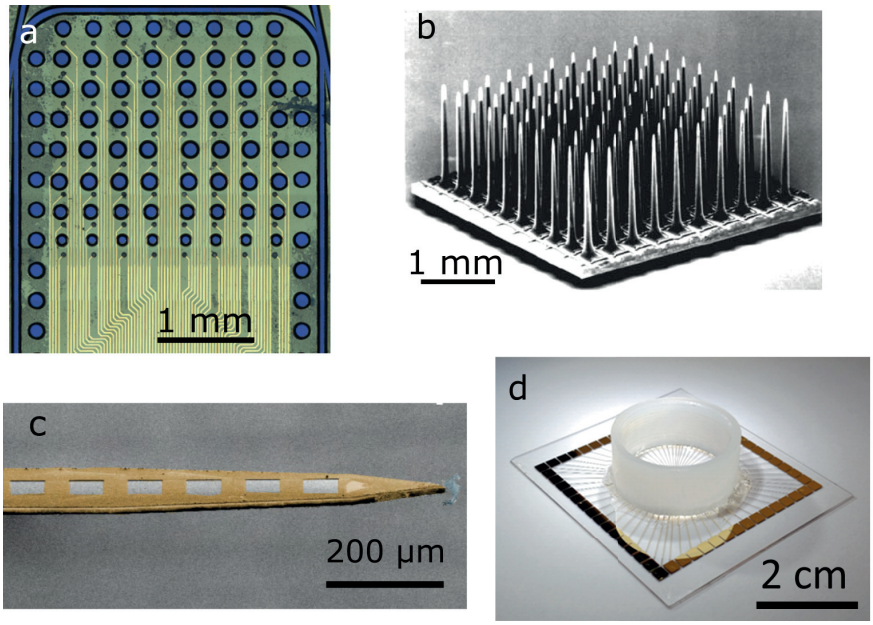

Figure 1.2: Different types of MEA - a) Flexible reduced graphene oxide ECoG array [13]. b) Utah array. c) graphene Deep Neural Probe (gDNP) [32]. d) Rigid single layer graphene MEA.

that they provide better spatiotemporal resolution compared to their non-invasive alternatives, but at the cost of higher invasiveness [30]. Other problems with these types of techniques are that they are laborious, requiring to insert the electrodes in a surgical procedure, they pose significant risk for the patient, having even the potential to be stressful for the patient, either human or animal, raising all short of ethical dilemmas [31]. To tackle these issues an alternative strategy is to use brain slices or cell cultures to investigate the response of the tissue to certain stimulus; these approaches are formally referred to as *ex vivo* and *in vitro*, although they might not always predict the exact *in vivo* response, they offer a huge degree of control over the experimental conditions, less laborious experimentation and do not pose that many ethical issues.

One of the most used techniques to study *in vitro* neuroscience is to combine dissociated neural cultures with multi-electrode arrays (MEA) recordings. MEA neural recordings from dissociated neural cultures have been an invaluable neuroscience tool for decades, since the pioneer work of Pine in 1980 [33]. Since then, the applications of this technology have diversified, making valuable contributions to different fields such as pharmacological testing, diagnostics and the investigation of neuronal growth and development [34, 35, 36]. The use of dissociated neural cultures on MEA has been of special relevance to study the

bursting activity and synchronization of neural networks, where the repetition of certain burst parameters has been proposed as the basis for memory traces [37, 38]. Down to the single neuron level, high density MEA have also been used to study axonal tracking, axonal conduction and propagation of action potentials in neurons [39]. Additionally, when the neurons are plated in sufficiently low density, techniques such as optical and fluorescence microscopy can be employed together with MEA recordings, providing detailed maps of functional connectivity with single cell resolution [40].

The great promise that MEA technology holds for *in vitro* neuroscience studies has pushed the development of new materials and techniques to improve the stability, biocompatibility and miniaturization of MEA devices [41, 42], leading to the commercial availability of many MEA for different applications [43, 44, 45, 46]. Within the field of bioelectronics, graphene is a material that has attracted significant attention lately. Thanks to its high interfacial capacitance, its chemical stability at physiological conditions, its wide electrochemical potential window and transparency, graphene has extensively been used for the detection of relevant biomolecules as well as electrical cell signals [47, 48].

Thus, combining graphene with MEA technology provides a promising approach to study *in vitro* neuroscience. The stability, electrical performance and transparency of graphene combined with the high degree of control over the experimental conditions of MEA neural cultures offer us a unique opportunity to explore the electrical responses produced by neurons, without having to deal with all the setbacks that *in vivo* neuroscience poses. This approach can complement all the techniques we have described in this section, moving us one step closer to achieving a deep and meaningful understanding of the brain, one of the most complex and fascinating challenges that humanity has ever faced.

1.2 Graphene

In this section we will introduce graphene, the material on which all the bioelectronic devices used in this thesis are based on, and discuss its atomic structure, band structure and most notorious properties.

Graphene is a two-dimensional crystal formed by carbon atoms distributed in a honeycomb lattice, such as the one shown in Figure 1.3a. It was first described by Wallace in 1947 in his seminal work [49], where he developed the band theory for graphite by neglecting the interaction between the different layers of graphite. It was not until half a century later that Novoselov and Geim managed to isolate and study experimentally the electronic properties of one of those layers [50], a work that was awarded with the Nobel prize in Physics in 2010 [51].

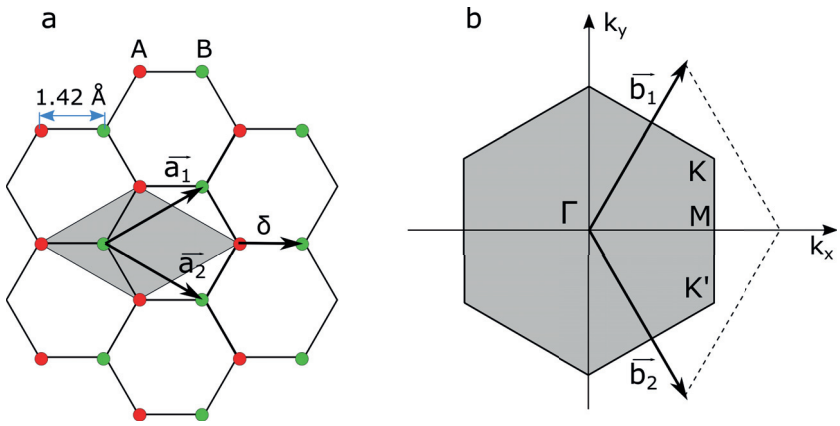

Figure 1.3: Graphene Lattice - a) Real space graphene lattice, showing the lattice constant, the two Bravais lattices in red and green and the unit cell in grey. b) Reciprocal space graphene lattice, showing the Brillouin zone, the Γ, K, M and K' points and the reciprocal unit vectors, $\vec{b_1}$ and $\vec{b_2}$.

The structure of graphene structure is what confers it its remarkable mechanical, optical and electrical properties; it is a monolayer of carbon atoms, disposed in a hexagonal lattice, held together by three sp^2-hybridized σ bonds from each carbon. The strength of this covalent carbon-carbon bond makes pristine graphene extremely stable both mechanically [52] and chemically [53]. Additionally, and due to being a monolayer with only one atom thickness, graphene has outstanding transparency to visible light, reaching almost 98 % transmission [54]. However, these properties are severely compromised when defects are introduced in the lattice. It has been proven experimentally that the creation of sp^3 vacancies by oxygen plasma treatment decrease the breaking strength and the Young modulus of graphene [55, 56]. In the same way, defects on the graphene lattice decrease its chemical stability [57].

The graphene lattice can be decomposed in two identical Bravais lattices A and B (see Figure 1.3a) displaced by one lattice constant $\delta = a(1, 0)$, with $a = 1.42$ Å. Each sublattice can be describe by the two vectors:

$$\vec{a_1} = \frac{a}{2}(3, \sqrt{3}) \qquad \vec{a_2} = \frac{a}{2}(3, -\sqrt{3}) \tag{1.1}$$

that form graphene´s unit cell.

Taking the Fourier transform of the Bravais lattice yields the reciprocal lattice, whose primitive cell (the Brillouin zone) is described by the reciprocal unit vectors:

$$\vec{b_1} = \frac{2\pi}{3a}(1, \sqrt{3}) \qquad \vec{b_2} = \frac{2\pi}{3a}(1, -\sqrt{3}) \tag{1.2}$$

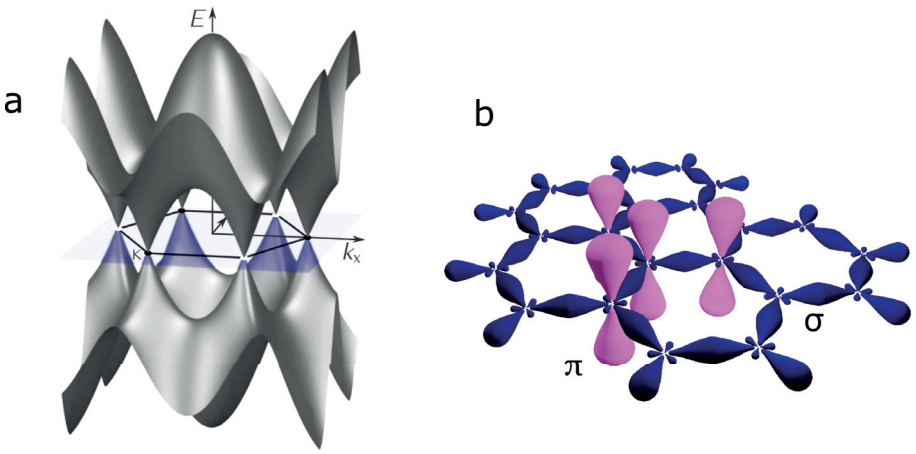

Figure 1.4: Graphene band structure and bonds - a) Graphene band structure, showing the valence and conduction bands meeting at the corners of the Brillouin zone, the so-called Dirac points. b) Graphene structure showing the σ bonds, responsible for its mechanical and chemical stability, and the π orbitals, responsible for its band structure. Adapted from [58] and [59].

Graphene´s Brillouin zone is also a hexagonal lattice, and at the corners of each primitive cell we can find the K and K´points, shown in Figure 1.3b and 1.4a. These points are of special interest for the description of the band structure of graphene. The π orbitals perpendicular to the graphene lattice plane are responsible for graphene´s band structure [60] (see Figure 1.4b). If we employ the next-neighbour tight-binding approach to calculate the graphene band structure, we find out that the valence and conduction bands touch at the K and K´points, as shown in Figure 1.4a, implying that graphene behaves as a zero-band gap semiconductor. At the K and K´points the dispersion relation can be approximated to first order as:

$$E_{\pm}(\vec{q}) \approx \pm v_F \mid \vec{q} \mid \tag{1.3}$$

with the plus and minus sign accounting for the conduction and valence bands, respectively, v_F the Fermi velocity, which for the case of graphene is a constant equal to 10^6 m/s, and $\vec{q}$ the momentum vector relative to the corner of the Brillouin zone, i.e. $\vec{q} = \vec{k} - \vec{K}$. For a rigorous derivation of Equation 1.3 see [60].

Interestingly, in Equation 1.3 there is no contribution from the mass of the charge carrier particle, pointing out to a vanishing effective mass. The quasiaparticles that fulfill this energy momentum relationship are called massless Dirac fermions, since they are best described by the Dirac equation; this equation

models the behaviour of quantum particles moving close to the speed of light [61]. For the same reason, the K and K´points are called Dirac points. In this regard, graphene provides a new way to experimentally test quantum electrodynamics (QED) phenomena by studying the properties of these massless Dirac fermions [62].

Another consequence of the graphene band structure is the low density of states (DOS) near the Dirac points, that is given by [60]:

$$\rho(E) = \frac{2A_c \mid E \mid}{\pi \quad v_F^2} \tag{1.4}$$

with A_c the area of the unit cell. The low DOS close to the Dirac points means that there is a notable variation in the Fermi level when changing the graphene charge, which in turn plays a role in the interfacial capacitance of graphene. These result will be further addressed in section 1.3.2.

1.3 Electrode-Electrolyte Interface

Throughout this work electrodes are employed to interface with the nervous system in two distinctive ways: recording neural signals and stimulating neural activity. This section deals with the properties and behaviour of the electrode/electrolyte system, explaining the theory behind the charge injection processes and discussing how different charge injection processes affect both recording and stimulating electrodes. This section also provides an introduction to impedance spectroscopy as a device characterization tool, as well as some notions on the equivalent circuit modeling. The section concludes with a discussion on the noise processes at the electrode/electrolyte interface and their relation to the impedance.

1.3.1 Faradaic vs non-faradaic processes

When an electrode is submerged into an electrolyte and a potential difference is applied between the electrode surface and the electrolyte bulk, current flows through the electrode-electrolyte interface. These charge injection processes are divided in two categories: faradaic and non-faradaic processes [63].

1.3.1.1 Faradaic Processes

When electrons are supplied to or taken from the electrolyte via reduction-oxidation (redox) reactions, the charge-injection process is called faradaic. If the Fermi energy (E_F) of the electrons in the electrode matches the energy of one of the vacant molecular orbitals of a given chemical species in the electrolyte,

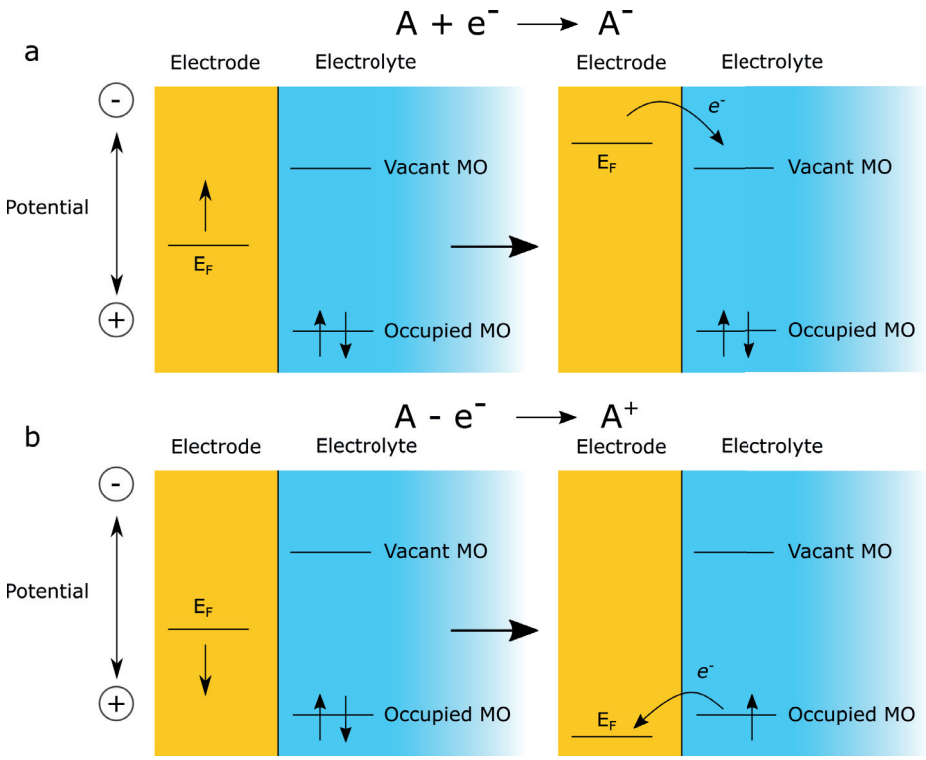

Figure 1.5: Scheme of a red-ox process - Schematic representation of a) reduction and b) oxidation process. The highest occupied and the lowest vacant molecular orbitals (MO) as well as the Fermi level (E_F) of the electrode are shown. Figure based on [63].

said electron can transfer across the electrode/electrolyte interface reducing that particular species [63, 64]. The opposite, when an electron transfers from one of the occupied molecular orbitals of a species in the electrolyte to the electrode produces an oxidation reaction. An schematic representation of the faradaic charge injection process is given in Figure 1.5.

Redox reactions can be classified in two categories: reversible and irreversible, depending of the relative rates of mass transfer and the reaction kinetics. When the kinetics of the reaction are relatively slow compared with the mass transfer of the produced chemical species, the species diffuse away onto the electrolyte bulk and cannot be recovered upon potential reversal. The reaction is then irreversible. On the contrary, when the mass transfer is relatively slow compared with the the kinetics of the reaction, the produced species accumulate at the electrode/electrolyte interface and the reaction is reversible.

In recording electrodes, faradaic processes are not a major concern [65]. Since the extracellular potential fluctuations created by the neurons range from the

few tens or hundreds of μV, in individual action potentials [47], to the few tens of mV in whole network activity such as cortical spreading depression [66], the deviation from the equilibrium voltage (U_{eq}) is a few orders of magnitude below that the one needed to induce faradaic reactions.

For stimulating electrodes, on the other hand, the faradaic processes gain more importance, since in this case the electrodes potential moves far away from the equilibrium potential (U_{eq}) of the system and, potentially, into the donor and acceptor bands of the electrolyte, as shown in 1.5. Ideally, if any Faradaic reaction take place at the electrode/electrolyte interface, they should be reversible reactions. The main reason for this is that since the nervous system is a delicate environment, where many different types of cells function together to keep the homeostatic equilibrium [67], the build up of reduced or oxidised species can distort this equilibrium, triggering anti-inflammatory responses [65]. Another important reason is that these redox species contribute to electrode deterioration, shortening its operational lifespan. One way to achieve reversible reactions is by carefully engineering the waveform of the pulses used to deliver the tissue stimulation, as we will discuss later in section 1.4.2.

1.3.1.2 Non-Faradaic Processes

When in the current flow there are no electrochemical reactions present, the charge injection process is called non-faradaic or capacitive. The electrodes that fulfill this condition are called *ideal polarizable electrodes* (IPE); while no real electrode behaves as an IPE, there are electrode-electrolyte systems than can approach this ideal IPE behaviour within a certain potential range [63].

In an IPE all the charge transfer is produced by the movement of ions in solution that charge the interfacial capacitance. The simplest way to explain this capacitance is with a model in which the ions in the solution migrate to the interface of the electrode in order to neutralize the charge induced at the electrode surface when a potential is applied. This approach was first proposed by Helmholtz [68] and it yields a constant capacitance (C_H) similar to a parallel plate capacitor:

$$\sigma = \frac{\epsilon\epsilon_0}{d}V \qquad\qquad C_H = \frac{\delta\sigma}{\delta V} = \frac{\epsilon\epsilon_0}{d} \tag{1.5}$$

where σ is the charge stored, ϵ_0 is the dielectric constant of the vacuum, ϵ is the dielectric constant of the electrolyte, V is the applied voltage between the electrode and the bulk of the solution and d the distance between the charges in the solution and the charges in the electrode.

The problem with the Helmholtz model is that the experimental data shows a capacitance that is voltage dependent [63]. To solve this problem, Gouy and Chapman proposed a model in which they took into account the thermal motion of ions. In this model, the ion concentration at a certain distance x from the electrode´s surface is given by a Boltzmann distribution:

$$n_i(x) = n_i^o e^{-z_i e\phi(x)\beta} \tag{1.6}$$

with n_i the number of ion of species i, n_i^o the number of ion of speciesin the bulk, z_i the valence number of ion i, e the charge of the electron, $\beta = 1/k_B T$ and ϕ the electrostatic potential depicted in Figure 1.6b. ϕ is the potential at every point of the electrolyte, it is dependent on the distance from the surface of the electrode and it should not be confused with the applied voltage V from Equation 1.5.

Using Equation 1.6 we can calculate the charge per volume at a distance x from the surface as:

$$\rho(x) = \sum_i n_i e z_i = \sum_i n_i^o e z_i e^{-z_i e\phi(x)\beta} \tag{1.7}$$

Combining Equation 1.7 with the Poisson equation

$$\rho(x) = -\epsilon\epsilon_0 \frac{\delta^2\phi}{\delta x^2} \tag{1.8}$$

allow us to find a relationship between the potential and the charge distribution. If we substitute Equation 1.7 in Equation 1.8, integrate and use Gauss law to calculate the superficial charge we can arrive to the expression:

$$\sigma^E = -\sigma^S = \sqrt{\frac{8\epsilon\epsilon_0 n^o}{\beta}} \sinh\left(\frac{ze\beta\phi_0}{2}\right) \tag{1.9}$$

with σ^E and σ^S the specific superficial charge in the electrode and in the solution respectively.

Differentiating the charge density in Equation 1.9 with respect to the potential yields the Gouy-Chapman capacitance:

$$C_D = \frac{\delta\sigma^M}{\delta\phi_0} = \sqrt{2z^2e^2\epsilon\epsilon_0 n^o\beta}\cosh\left(\frac{ze\phi_0\beta}{2}\right) \tag{1.10}$$

The deduction of this expression can be followed in detail in [63].

The Gouy-Chapman capacitance from Equation 1.10 can successfully model the capacitance dependence on the potential but it fails in two aspects. First, the experimental values of the capacitance are usually much lower than the predicted

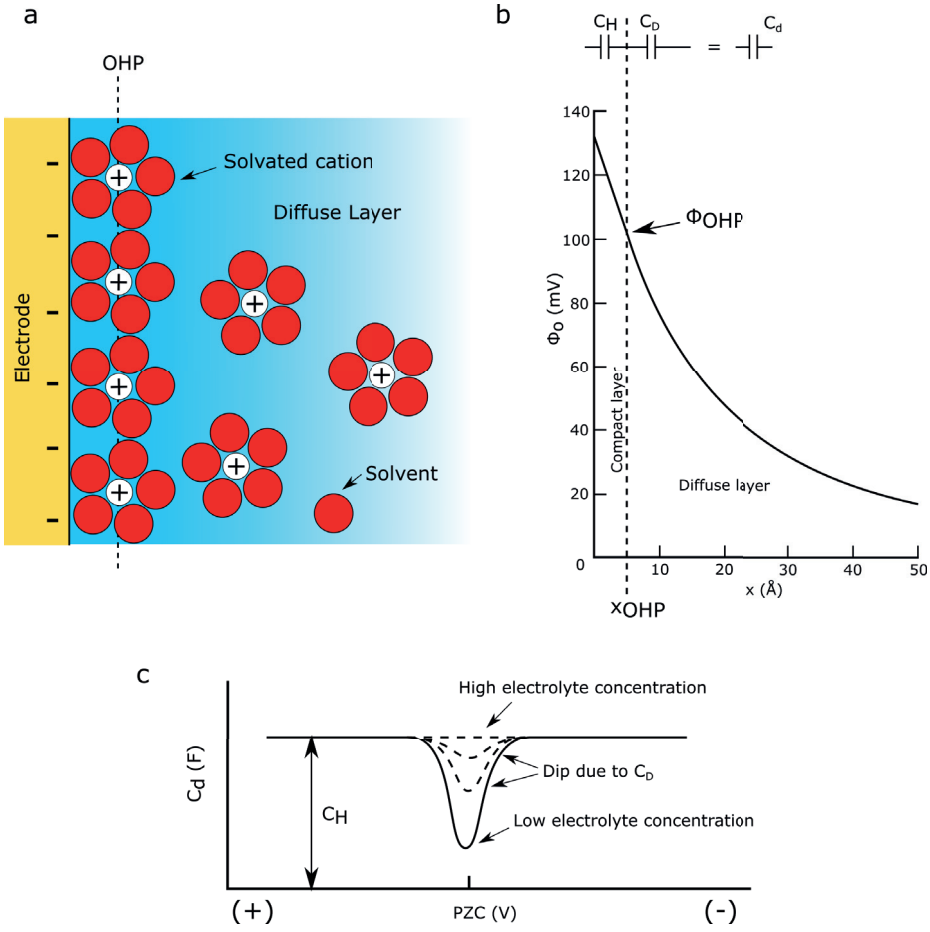

Figure 1.6: Model of the double layer capacitance - a) Illustration of the ionic distribution in the double layer model. The outer Helmholtz plane (OHP) is defined by the plane of closest approach of ions to the electrode´s surface. From there towards the electrolyte the ion concentration follows a Poisson-Boltzmann distribution b) Electrostatic potential profile of the double layer across the electrolyte. The potential value is calculated for a 10 mM 1:1 electrolyte at 25 ºC. x_{OHP} and ϕ_{OHP} mark the position of the OHP and the potential at that point respectively. c) Schematic representation of the double layer capacitance for different electrolyte concentration as a function of applied potential. PZC marks the Point of Zero Charge, the potential at which the net charge on the electrode' surface is zero. Figure based on [63].

ones. Secondly, the Gouy-Chapman theory predicts that the capacitance will monotonically increase with both increasing and decreasing potentials, something that contradicts the empirical data.

The main flaw in the Gouy-Chapman theory is that the ions are considered as point charges that can approach to the electrode´s surface arbitrarily close, reaching even zero separation distance at high polarization. However, in reality, the ionic radius cannot be arbitrarily small and, furthermore, the ions are surrounded by a layer of the solvent ions. This led Stern to propose the existence of a plane of closest approach, the so-called *Outer Helmholtz Plane (OHP)*, that is defined by the location of the centers of the closest solvated ions. From the OHP outward, the ions in the solution behave accordingly to the Gouy-Chapman theory, creating the so-called diffuse layer. When the concentration of ions or the applied voltage are high, the charges in the solution compress against the OHP and the situation closely resembles the Helmholtz model. On the contrary, when the ionic concentration or the applied voltage are low, the thickness of the diffuse layer extends into the electrolyte and the behaviour of the capacitance is described by the Gouy-Chapman theory. Therefore, the Stern modification for the Gouy-Chapman model can be written as:

$$\frac{1}{C_{GCS}} = \frac{1}{C_H} + \frac{1}{C_D} = \frac{x_{OHP}}{\epsilon\epsilon_0} + \frac{1}{\sqrt{2z^2e^2\epsilon\epsilon_0 n^o\beta}\cosh\left(\frac{ze\phi_0\beta}{2}\right)} \tag{1.11}$$

with x_{OHP} and ϕ_{OHP} the distance of the OHP from the electrode and the value of the ϕ potential at that point, as shown in Figure 1.6b. The model given by Equation 1.11 is known as the Gouy-Chapman-Stern model and its dependence with the applied voltage and the electrolyte concentration is illustrated in Figure 1.6c.

Once we have dealt with the theory behind the capacitive charge transfer, we can analyse its application in the study of charge delivery. We can calculate the amount of charge injected by an IPE as that of a pure capacitor:

$$Q = C_{dl}\Delta V \tag{1.12}$$

In Equation 1.12, C_{dl} stands for the capacitance of the double layer and accounts for the total interfacial capacitance of the electrode. Another way to express that capacitance is:

$$C_{dl} = c_i ESA \tag{1.13}$$

where c_i is the interfacial capacitance per unit area and ESA is the Electroactive Surface Area. The ESA should not be confused with the Geometric Surface Area (GSA), meanwhile the GSA is the physical dimension of the electrode and it is used to define current and charge densities, the ESA determines the total amount of surface that is able to inject current. In the case of porous materials, for example, the ESA is bigger than the GSA.

Combining Equations 1.12 and 1.13 we can readily see that in order to inject high amounts of charge Q with non-faradaic processes we need electrodes that behave as IPEs over a large range of potential ΔV; they also need to have high specific interfacial capacitance c_i and large ESA.

1.3.2 Graphene Quantum Capacitance

The case of SLG electrodes in solution is particularly interesting, since the double layer capacitance model described by Equation 1.11 cannot explain on its own the empirical data [69]. The discrepancy between the experimental data and the theory arises from the graphene quantum capacitance. This capacitance has its origin in the low density of states that graphene has around the Dirac point, making the amount of energy needed to add an extra electron to the graphene sheet non-negligible (see Section 1.2). The quantum capacitance is proportional to the number of states and takes the form [70]:

$$C_Q = \frac{2e^2}{\hbar v_F \sqrt{\pi}} \left(|n_G| + |n^*|\right)^{1/2} \tag{1.14}$$

where n_G stands for the voltage induced carrier concentration and takes the form:

$$n_G = \left(\frac{eV}{\hbar v_F \sqrt{\pi}}\right)^{1/2} \tag{1.15}$$

with n^* the effective charged impurity concentration. Moreover, and due to the hydrophobic nature of graphene, there is an angstrom-scale gap between the electrode and the electrolyte. This acts as an additional parallel plate capacitor that, together with the double layer capacitance, dominates over the quantum capacitance for voltages larger than a few hundred of millivolts. More detailed information on this phenomena can be found on [70] and [69].

1.3.3 Electrochemical Impedance of electrode-electrolyte interfaces

Electrochemical impedance spectroscopy (EIS) is a technique to measure the impedance of a system in which a working electrode is held to a fixed voltage or current while a small amplitude sinusoidal perturbation, either in voltage or current, is applied. When the fixed magnitude is the voltage, the technique is called potentiostatic electrochemical impedance spectroscopy (PEIS). Normally, a sinusoidal wave between 10 to 50 mV root mean square (RMS) is applied, sweeping a predefined range of frequencies, and the impedance between a working and a counter electrode is measured. This technique is specially relevant in the characterization of recording electrodes for neural applications, since the small potential oscillations applied are in the same range that the typical neural activity [65].

Usually EIS is performed using a 3 electrode set up, on which, in addition to the working and the counter electrodes, a reference electrode is included. The reference electrode has a high impedance when compared to the counter electrode, so that all the current injection happens at the counter electrode. In this way we can have a stable reference electrode which yields accurate voltage measurements [63].

Since the EIS techniques reduces our electrode-electrolyte system to a impedance subjected to small sinusoidal oscillation, we should be able to represent its response by an equivalent circuit. Then, the identification of the model´s components of the equivalent circuit with the elements of the real system allows us to gain knowledge about the properties of our electrode/electrolyte system. A model commonly used to fit such circuits is the Randles model [63], depicted in Figure 1.7. It consist of a resistance R_Ω generally representing the resistances of the track and the electrolyte and a capacitance C_{dl} and a resistance R_f in parallel, representing the charging of the double layer and the faradaic charge transfer, respectively. Additionally, a Warburg element Z_W can be added in series with R_f to account for the finite mass transfer of the redox species to the electrolyte bulk.

Even though until now we have always referred to the electrodes used in this thesis as close to IPEs, surface inhomogeneities and the grain boundaries of the electrode material, among others, deviate the behaviour of a real electrode from that of an IPE [71]. To model those deviations from the ideal behaviour, we can

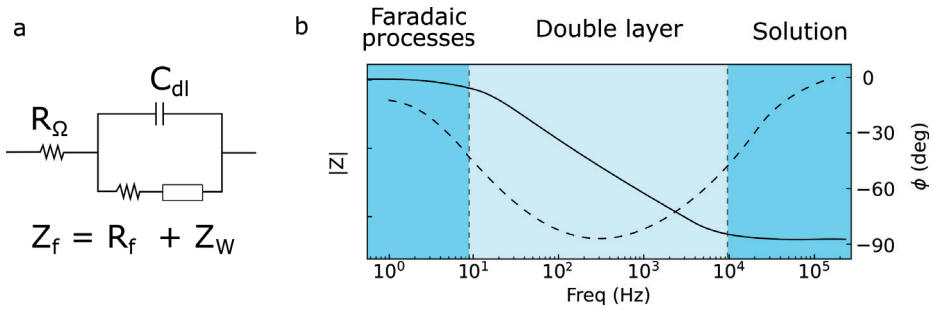

Figure 1.7: Randles equivalent circuit used to model the frequency response of the electrode/electrolyte interface - a) Schematic of a Randles circuit including a Warburg element to model the mass transfer of redox species into the electrolyte bulk. b) Bode plot of a typical Randles circuit. Figure based on [63].

substitute the double layer capacitance C_{dl} in the Randles model of Figure 1.7a by a constant phase element (CPE):

$$Z_{CPE} = \frac{1}{w^\alpha Q} e^{-i\alpha\pi/2} \tag{1.16}$$

where w is the angular frequency, i is the imaginary unit and α is an ideality coefficient [71]. When the CPE behaves as a perfect capacitor, n accounts to 1 and then Q is equal to the capacitance. In the opposite case, when the CPE models a perfect resistance, α equals to zero and Q becomes $1/R$.

1.3.4 Noise processes in electrode-electrolyte interfaces

When using electrodes to record neural activity, noise is the main limitation; signals with amplitude smaller than the noise baseline cannot be measured. There are many factors that can affect the noise baseline of a recording setup, including environmental noise, the noise of the recording electronics or the noise created by the recording electrode/electrolyte/reference electrode cell. In order to reduce the noise of a recording experiment the environmental noise is normally shielded using a Farady cage, when possible, and the recording electronics are carefully chosen so their baseline noise levels are well below that of the used recording electrodes. That leaves the recording electrode/electrolyte/reference electrode cell as the main noise source of the system.

Accordingly to the fluctuation-dissipation theorem [72], the noise properties of a system in thermodynamic equilibrium can be fully characterized by its dissipation processes. Since capacitors do not dissipate energy, the noise characteristics of the electrode/electrolyte/electrode system can be fully understood by assigning

a current noise source to each resistor in the system under study (Figure 1.8). For each element, the voltage noise will have the form:

$$V_n^2 = 4k_B T \int_{f_1}^{f_2} Re(Z) df \tag{1.17}$$

in agreement with the Johnson-Nyquist theory for thermal noise [73]. In Equation 1.17, V_n is the RMS voltage noise, f_1 and f_2 delimit the frequency band under study and $Re(Z)$ is the real part of the impedance, to which the noise source is associated.

According to Equation 1.17, the noise of the reference electrode can be minimized using electrodes with a small $Re(Z)$, something that it is normally achieved using large reference electrodes. However, the same approach cannot be taken with the recording electrode when using micro electrodes.

If the working electrode behaves as an IPE, accordingly to Equation 1.17 their voltage noise contribution will be zero and all the noise will arrise from the track and electrolyte resistances. However, as discussed previously, the surface inhomogeneities and the grain boundaries of the electrode material deviate the ideal behaviour from that of an IPE and make a CPE circuit element more suitable to describe the behaviour of such electrodes. Figure 1.8 shows where the energy dissipation occurs and where the noise arises in a capacitive, non-ideal electrode.

According to Figure 1.8, dissipation occurs along the electrode due to the electrode resistance, across the electrode/electrolyte interface through the leakage current produced by defects on the electrode surface and on the electrode insulation and across the CPE of the double layer capacitance. The elements in Figure 1.8 are modeled as noiseless elements and their associated voltage noises are represented separately. At low frequencies, the voltage noise $V_E + V_L$ dominates over the CPE noise, while at high frequencies the V_E is the one that dominates. In the frequency range dominated by the double layer, approximately form 10 Hz to 10 kHz, V_{DL} is the most important term for the noise. If we take the real part of equation 1.16 and plug it into 1.17, we obtain the V_{DL} noise as:

$$V_{DL}^2 = 4k_B T \int_{f_1}^{f_2} \frac{cos(\alpha\pi/2)}{(2\pi f)^\alpha Q} df \tag{1.18}$$

From equation 1.18 and Figure 1.8 we can see that to reduce the voltage noise in the frequency range dominated by the CPE, we have to maximize the Q factor, that for the case of almost completely capacitive electrodes, stands for the electrode's capacitance.

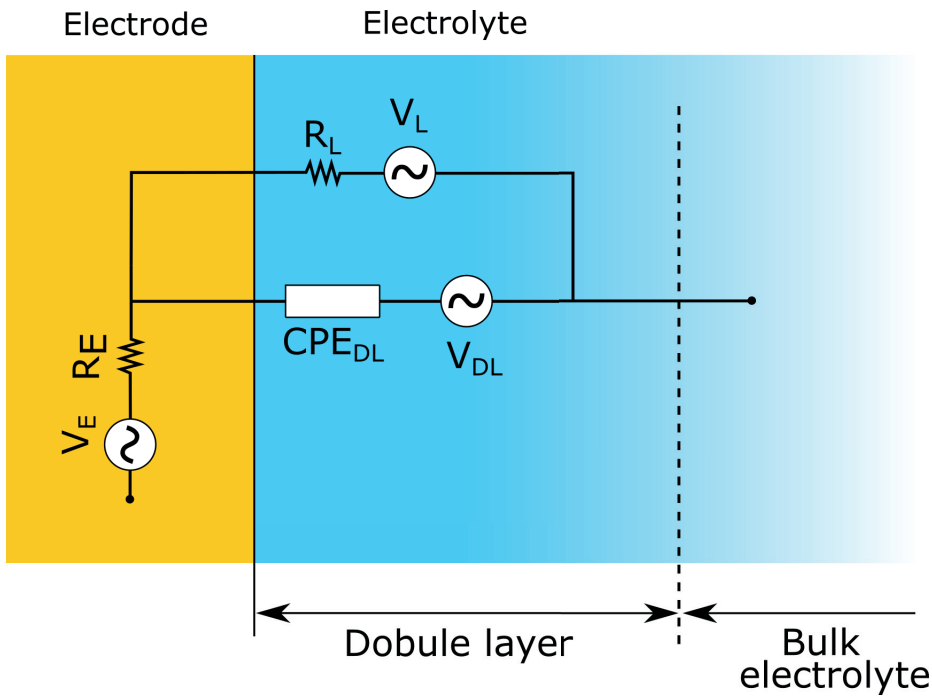

Figure 1.8: Noise sources of a non-ideal electrode - Half-cell noise circuit of a non-ideal electrode. Besides the double layer CPE (CPE_{DL}), we have taken into account the internal resistance of the electrode (R_E) and the leakage resistance (R_L) that can happen due to surface defects or passivation imperfections. All the elements in this circuit are modeled as noiseless elements and their voltage noise is represented explicitly. Figure based on [74].

1.4 Bioelectricity

Neurons are the fundamental component of the nervous system. They have the role of generating and propagating the electrical activity that controls, regulates and communicates different parts of the body. Neurons are composed of three main parts: dendrites, that are branches of the neuron designed to receive information from a variety of sources; the soma, which contains the nucleus and other fundamental organelle; and the axon, the main cell projection in charge of transmitting electrical information to other cells. Neurons communicate with other cells via the release of chemical compounds called neurotransmitters or by allowing ions to flow from one neuron to another via gap junction channels, forming chemical and electrical synapses, respectively. Chemical synapses are the most abundant type of synapse in higher vertebrates. The three main neuron parts, as well as a scheme of a chemical synapse, are shown in Figure 1.9.

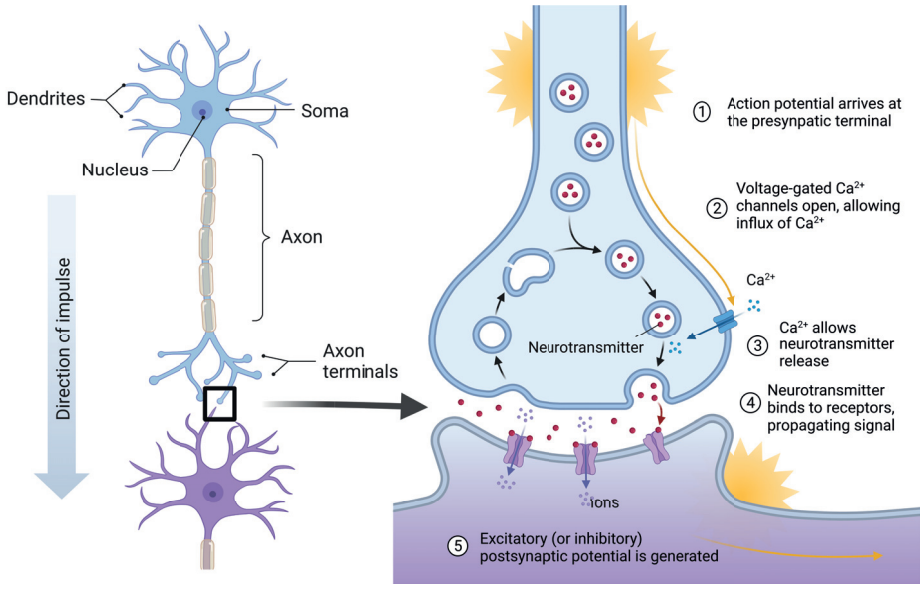

Figure 1.9: Neuron structure and synapse - Main components of a neuron and detail of synaptic transmission, showing the arrival of the action potential, the fuse of vesicles and neurotransmitter release and the generation and propagation of the postsynaptic activity. Figure created with BioRender.

The generation and propagation of electrical signals in neurons, and other electrogenic cells, is governed by the potential difference across the lipidic cellular membrane. This transmembrane potential (V_{mem}) is created by the difference on ionic concentration inside and outside the cell, a difference that is maintained by ionic channels and the sodium-potassium pump. Ionic channels are transmembrane proteins that are only permeable to specific ionic species; they can be passive or active (mechanically, chemically or voltage gated). The sodium-potassium pump is an active enzyme that consumes energy, in the form of ATP molecules, to pump positive charges out of the cell body. In the absence of external inputs, all these proteins work together to maintain a equilibrium resting potential that in most neurons lies around -70 mV.

Upon small perturbations, the ionic channels and the sodium-potassium pump are able to restore this equilibrium potential. However, if a strong enough perturbation is presented and the transmembrane potential crosses a certain voltage threshold, a series of voltage gated ion channels are activated. These ion channels work together to produce a fast, transient variation of the transmembrane potential, called an action potential. Action potentials typically have duration of a few milliseconds, amplitudes in the order of a hundred millivolts and are able to propagate along the axons of neurons. When the action potential reaches a

presynaptic terminal, Ca^{2+} voltage gated ion channels are activated, allowing vesicles containing neurotransmitters to be fused with the cellular membrane and releasing its content into the synaptic cleft. At the other side of the synaptic cleft, in the postsynaptic area of a neighboring neuron, proteins called neuroreceptors bind to the specific neurotransmitters released by the presynaptic neuron. These neuroreceptors then act on specific ion channels, creating excitatory (EPSP) or inhibitory (IPSP) postsynaptic potentials or modulating the electrical activity in a long lasting manner. A schematic representation of synaptic transmission is provided in Figure 1.9.

For a detailed description of ion channels and action potential creation and propagation see [67]. For a detail description of synaptic transmission, see [75].

1.4.1 Recording biological potentials

Above, we have explained how electrical signaling is generated and how it propagates from neuron to neuron. These phenomena are controlled by the potential difference between the inside and the outside of the cell, the transmembrane potential. The problem is that when measuring bioelectrical signals, one normally does not have access to the interior of the cellular membrane. Only with some special techniques, such as patch clamp, is that possible. However, this technique normally destroys the cell and suffers from a really low throughput. Since it is necessary to perforate the membrane and insert individual electrodes inside each cell, it is limited to record from a few hundred of neurons simultaneously, in the best of cases [76]. Another approach to extract information from the electrical signals propagated from neurons is to record the extracellular potential that the neurons generate.

The extracellular potentials is comprised of the individual contributions of the currents (I_i) flowing from each of the individual ion channels (i), and it has the form:

$$V_E(\vec{r}, t) = \frac{1}{4\pi\sigma} \sum_i \frac{I_i(t)}{\vec{r} - \vec{r_i}} \tag{1.19}$$

with σ the conductivity of the extracellular media and $\vec{r}$ the distance. Since V_E depends on the distance from the current source ($\vec{r} - \vec{r_i}$), the amplitude of the extracellular potential diminishes amplitude quickly when we get far away from the neuron. For illustrative purposes, Figure 1.10a shows a model of a pyramidal cell of layer 5b in the mammalian neocortex, taken from [77]. The transmembrane (V_{mem}) and extracellular (V_E) potentials for this neuron model have been simulated and represented using the NEURON software [78] together with Python 3.6 [79] and the LFPy module [80]. We can readily see how the

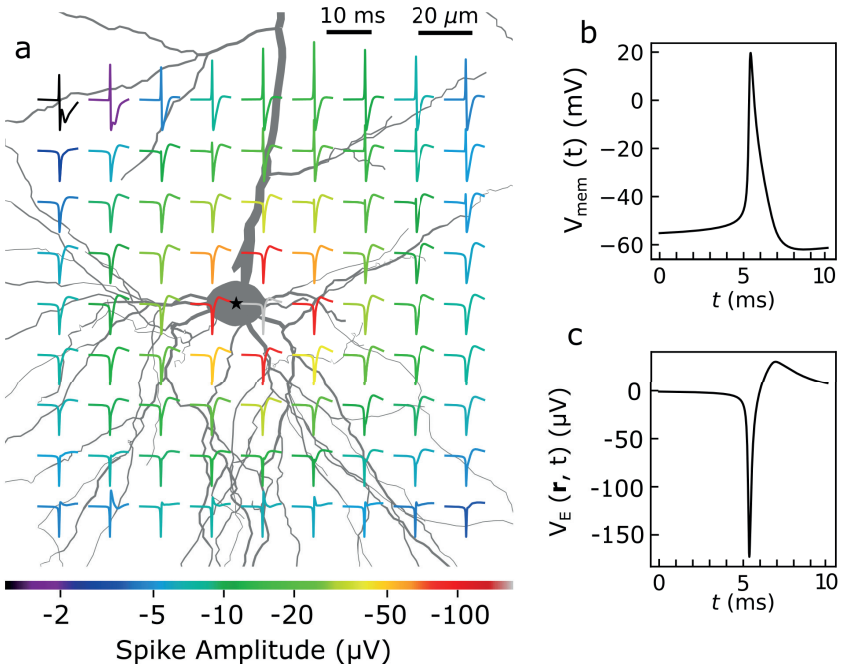

Figure 1.10: Comparison between the transmembrane and the extracellular potential - a) Simulation of how the extracellular potential created by a pyramidal neuron changes its shape and amplitude when moving away from the soma of the neuron, where the transmembrane potential is located [77]. b) Simulated transmembrane potential of the same neuron at the soma, marked by the black star. c) Simulated extracellular potential of the neuron at the soma, marked by the black star. Simulated using the NEURON software [78] and the LFPy Python module [80].

amplitude of the extracellular spike decreases by two orders of magnitude when we move just 100 μm away from the neuron soma. Figure 1.10b and c show that the simulated extracellular potential is 3 orders of magnitude lower than the transmembrane potential at the neuron soma, which is marked by a black star.

From Figure 1.10, it is clear that in order to detect action potentials the recording electrode should be as close as possible to the neuron. Additionally, it has been shown that small electrodes, in the order of 10 x 10 μm^2, record higher amplitude signals with better frequency resolution than bigger electrodes [81]. The reason for that is that bigger electrodes are subjected to spatial averaging, integrating regions far apart from the neuron, where the extracellular potential remains unaffected by the neuron action potentials, blurring local events and diminishing the peak-to-peak amplitude of the recorded signal. For these reasons, MEA with electrode sizes similar to that of neurons are required to properly capture the extracellular potential produced by electrogenic cells [82]. Another advanteguous application of MEA techonology is the recording of local field

potentials (LFP), which are the low frequency part (< 500 Hz) of the extracellular potential, produced by the synchronous activity of many individual cells. These LFPs propagate across wide areas of the brain and other parts of the central nervous systems [83, 84]. Thus having arrays of microelectrodes allow us to study how LFP signals evolve when they propagate through the brain and to extract information of how they relate to certain brain disorders [28, 66]. To sum up, MEA allow for high throughput, high amplitude extracellular potential recordings, with spatial resolution in the micrometer range [85, 86] and with sampling rates in the range of tens of kHz [46].

1.4.2 Stimulating biological potentials

Electrical stimulation of neural tissue is achieved depolarizing the membrane of neurons by applying a flow of ionic current between at least two electrodes, one of which should ideally be in close proximity to the targeted tissue [65]. Stimulating electrodes can be divided in two different families attending to their size. Macroelectrodes are able to inject high amounts of charge with low-charge density threshold and have GSA larger than 10^5 μm^2. On the other hand, microelectrodes have lower charge injection capabilities but with high-charge density threshold and areas smaller than 10^4 μm^2. Microelectrodes have two obvious advantages over macroelectrodes: their high-charge density allow for lower stimulation thresholds [87, 88] (i.e. less charge is needed to induce a neural response, since it is more concentrated); they can stimulate a smaller volume of tissue, which allows for higher spatial resolution and stimulus control.

Another important aspect to consider when stimulating neural tissue is the design of the stimulation pulse. The first choice when engineering a pulse is which magnitude to control, the current or the voltage. Normally, researchers have favored the used of current pulses, since the elicited neural responses can be modeled more easily than voltage pulses [89]. Nevertheless, voltage pulses have their advantages: the hardware used in the pulse generation is simpler [90] and, more importantly, when a voltage pulse is applied avoiding Faradaic reactions is just a matter of staying inside the electrode potential window. On the other hand, the only way to avoid Faradaic processes when using current pulses is to continuously monitor the impedance of the stimulating electrodes and adjusting the injected current accordingly.

The second important choice when designing stimulating pulses is the shape of the pulse itself, i.e. number, amplitude, duration and polarization of the pulse phases. Concerning the polarity of the pulse phases, the threshold to generate an electrical response in a neuron is lower for cathodic than for anodic pulses [64].

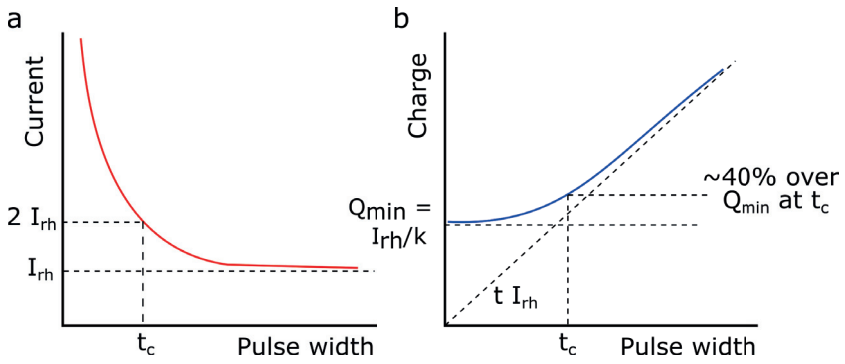

Figure 1.11: Strength-duration and charge-duration curves - a) Current threshold to elicit an electrical response in a tissue as a function of the pulse phase width. b) Charge threshold needed to elicit and electrical response per pulse phase as a function of function of the phase width. Adapted from [91]

This can be explained from the fact that at resting potential there is more positive charge inside the neuron than outside. That is, injecting addition positive charge into the neuron with an anodic pulse will further hyperpolarize it. In areas further apart from the electrode, the positive current will flow out of the cell, leading to a membrane depolarization in that area. If the anodic pulse is strong enough, that current flow might eventually elicit an action potential. If we revert this reasoning, when delivering a cathodic pulse the negative current flowing from the electrode directly depolarizes the area of the membrane closest to the electrode, eliciting an action potential. With regard to the number of phases, charged-balanced pulses with two phases of opposed sign and equal charge are common practice [65], ensuring that a net zero charge is injected into the tissue. The reason to use this strategy is that, upon repetitive stimulation, voltage can build up at the electrode/electrolyte interface. This voltage might push the electrode outside of its potential window, producing Faradaic reactions and damaging the electrode and the neural tissue (see section 1.3.1.1).

Finally, the amplitude-duration relationship of the stimulating pulse can be derived from the strenght-duration curves [92]. These curves are plots of the minimum current needed to stimulate a particular tissue with a pulse of certain duration. They take the form [92]:

$$I_{th} = \frac{I_{rh}}{1 - exp(-W/\tau_m)} \tag{1.20}$$

Equation 1.20 is know as the Weiss-Lapicque equation and relates the delivered current threshold I_{th} necessary to create an electrical response in a tissue with the width of the pulse (W); τ_m is a membrane time constant, that varies depending on the type of neural tissue or culture we want to stimulate [93, 94, 95]; and

I_{rh} is the rheobase current. The rheobase current is the minimum current that can elicit an electric response. Longer pulses with lower current amplitude give time to the charge inside the neuron to redistribute [96, 92]. Furthermore, if the pulse is long enough the inactivation of the sodium ion channels eventually overcomes the current being injected from the electrode [97]. The pulse width corresponding to twice the rheobase current is called chronaxie (t_c), and it gives a good estimation of the practical pulse width and current to elicit an electrical response. In addition, when comparing different tissues or tissue conditions, the chronaxie provides a way to compare their excitability. Figure 1.11a shows the representation of a strength-duration curve, including all the parameters discussed above.

Figure 1.11b shows the charge-duration curve, which plots the threshold charge (Q_{th}) versus the pulse width. This figure shows that short pulses stimulate more efficiently, i.e., they need less charge to produce an electrical response. However, short pulse widths are limited by the stimulator electronics and the ability of the electrodes to deliver high currents [65] in short time. Additionally, for the charge-duration curve, the minimum charge Q_{min} is defined as the rheobase current divided by an empirical factor k. This factor, which takes values between 2.0 and 1.5, depends on the injected charge per phase and the area of the stimulating electrode and it is used to account for the maximum safe level of stimulation for each tissue [98]. In a practical case, Q_{th} is close to Q_{min} when pulses of tens of microseconds are used.

1.4.3 Cell-electrode coupling: the point-contact model

In order to use MEA to record the extracellular potential produced by electrogenic cell and to stimulate electrical responses, it is necessary to understand how the cell/electrode electrical coupling works. To do so, we use a modification of the point contact model [99], depicted in Figure 1.12a. This model is based on the assumption that there are two different parts of the cell membrane: the free membrane (FM) and the junction membrane (JM). The free membrane is the area that is not attached to the electrode and is defined by A_M - A_J, where A_M is the total area of the cell membrane and A_J is the area of the junction membrane, i.e. the membrane that is in contact with the electrode. Between the junction membrane and the electrode there is a small cleft of a few tens of nanometers, that we will model using a mean extracellular potential V_J and a conductivity per unit area g_J. Additionally, we distinguish another two potentials: the intracellular potential (V_M) and the electrode potential (V_E). The electrode is described by its capacitance per unit area (C_E). The free and the junction

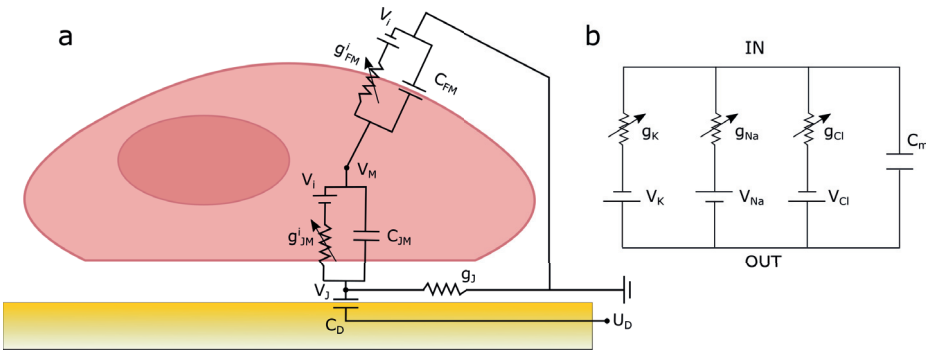

Figure 1.12: Scheme of the point contact model - a) Representation of the coupling between a cell and an electrode. b) An scheme of the membrane according to the Hodgkin-Huxley model. The ion channels are substituted by variable resistances under a Nerst potential and the membrane is represented as a capacitor

membrane are both modeled by a membrane equivalent circuit according to the Hodking-Huxley model [97], as shown in Figure 1.12b, where the ion channels are represented by variable resistances driven by the Nernst potential of each ion and the cell membrane represented by a capacitor. For the two different parts of the cell membrane used in the point contact model, the ionic conductance is represented by g^i_{FM} and g^i_{JM}, the Nernst voltage V_i of each ion i and the membrane capacitance C_{FM} and C_{JM} for the free membrane and the junction membrane, respectively.

If we apply the first Kirchhoff's law ($\sum_n I_n = 0$) to the two nodes in Figure 1.12a and replace the term corresponding to the current flowing through the junction membrane, we obtain the equation that describes the coupled dynamics of the intracellular potential V_M and the electrode potential V_E:

$$(A_M - A_J)\left[C_{FM}\frac{dV_M}{dt} + \sum_i g^i_{FM}(V_M - V_i)\right] = g_J V_J + A_J C_E\left(\frac{dV_E}{dt} - \frac{dV_J}{dt}\right) \tag{1.21}$$

From Equation 1.21 we can extract two straight conclusions. The first one is that the lower the junction conductivity g_J, the better the coupling between the cell and the electrode, since less current will be lost through the cleft. The second one is that the bigger the area of the junction membrane A_J, the better the coupling between the cell and the electrode, since there is less current lost through the free membrane. For both cases, better coupling translates into a larger V_E signal.

1.5 Scope of this thesis

In this chapter, we have described the structure and properties of graphene, the core material around which this thesis revolves. Then, we have given some notions about the electrode-electrolyte interface and the fundamental processes that take place when electrodes are used to inject charge in a solution and to record voltage signals from it. Finally, we have briefly presented the most important component of the nervous system, the neuron, and discuss how they generate and propagate electrical signals. Once we have introduced the basic concepts needed to follow the methodology and interpret the experimental results presented in following chapters, we can present the scope of this thesis.

The main objective of this doctoral thesis is to explore the capabilities of single layer graphene and graphene oxide to fabricate devices able to interact with the nervous system, recording electrical activity and delivering electrical stimulation, with the aim to study neurological systems. To this regard, we have developed electrodes and microelectrode arrays fabricated with graphene-based materials as new tools to explore different components of the nervous system, and used them to gain insight on how specific neural systems work.

Chapter 2 is devoted to single layer graphene. There, we explore how SLG is synthesized, transferred to different substrates and incorporated in the fabrication of MEA in both rigid and flexible substrates. Then we characterize the electrical performance of those MEAs and use them to explore different components of the nervous system. The rigid MEAs are used to culture *in vitro* neurons and record their electrical activity. The flexible MEAs are used to perform electroretinogram recordings, benchmarking the performance of our flexible graphene electrodes and MEAs against the current state of the art and discussing potential advantages of our technology and how those advatages might benefit the field of electroretinography.

In Chapter 3 we present the fabrication of reduced graphene oxide MEAs, taking advantage of its high porosity, low interfacial impedance and high charge injection capabilities to stimulate neural activity. The electrical performance of the fabricated MEAs is discussed in chapter 3. Further, we study their use for *in vitro* neural network cultures. Since these MEAs are fabricated on thin pyrex substrates, it is possible to perform simultaneous oil immersion microscopy and electrical recording and stimulation, a characteristic that is exploited in order to study how neural networks respond to different types of electrical stimulation.

In Chapter 4 we explore different techniques for neuronal guidance. These techniques aim to control the geometry and connectivity of *in vitro* neural networks, in order to create controlled and reproducible neural circuits that can

be thoroughly studied to gain understanding on how neural circuits function in the nervous system. To that regard, we try 3 different approaches: we exploit the different wettability properties of the materials used to passivate MEA, we stamp cell adhesive proteins in culture substrates using microcontact printing and we physically constrain the growth of networks using PDMS microstructures.

Finally, in Chapter 5 we sum up the conclusions extracted from all our experimental work and discuss potential applications of graphene-based MEA in neuroscience.

2

Single Layer Graphene Electrodes: Fabrication, Characterization and Applications

Servía en la venta una moza asturiana [...]
del un ojo tuerta y del otro no muy sana

El ingenioso hidalgo Don Quijote de la Mancha
Miguel de Cervantes

The SLG devices used in this thesis can be divided in two categories: rigid MEAs for *in vitro* applications and flexible probes, containing one or multiple electrodes, aimed at *in vivo* experiments. Despite having two very different target applications, both types of devices share almost the totality of the fabrication and characterization processes. This chapter provides an overview of the work done with both types of devices. First, the synthesis of the graphene is described, as well as the transfer and fabrication processes employed to build the devices used in this section. Next, we describe the characterization of the rigid MEAs and introduce their role as tools for *in vitro* neuroscience. Finally, we present the

characterization of our flexible graphene probes and discuss their use to record *in vivo* retinal activity.

2.1 Device fabrication

The complete fabrication of the SLG devices developed in this thesis is explained in this section. Starting from the synthesis of graphene based on the catalytic decomposition of methane, to the transfer of graphene to the target substrate and the photolitography steps employed to fabricate the complete device.

2.1.1 Graphene synthesis by chemical vapor deposition

Since single layer graphene was first isolated in 2004 by Novoselov and Geim [50] the scientific community has developed many methods to grow graphene. There are two differentiated strategies to prepare graphene: the top-down and the bottom-up approach [100].

The top-down approach involves breaking down the individual layers of graphite, overcoming the Van der Waals forces that keep graphite together. Normally these methods suffer from low yield and the short supply of graphite with a high enough level of graphitisation and regular morphology. To date, the top-down method that yields the highest quality, not only of graphene but of many other 2D materials, is the mechanical exfoliation [101]. This method consist of placing an adhesive tape on top of a highly oriented piece of graphite and stripping it off. After that the tape is placed on the target substrate and peeled off, leaving the graphene flakes on the substrate. Despite the high quality of the flakes, their reduced dimensions, in the order of tens of microns, limit the use of this method in wafer scale applications. Other examples of top-down approaches are electrochemical exfoliation [102, 103], solvent-based exfoliation [104, 105], arc discharges [106, 107], or unzipping of carbon nanotubes [108, 109].

With the bottom-up approach the goal is to synthesise graphene from molecules and compounds that contain carbon atoms. The bottom-up approach is the only synthesis method that allows to fabricate centimeter scale graphene sheets that, in some cases, can be directly grown on top of the target substrate. The large scale graphene layers are created when different crystals, that nucleate at different positions in the substrate, merge. Therefore, it is of utmost importance to tune the growth parameters correctly and to prepare the substrate in order to achieve the maximum graphene quality possible. The graphene community has managed to optimize this method, with several groups reporting centimeter scale crystals grown using the bottom-up approach.

The main two methods to obtain graphene using the bottom-up approach are epitaxial growth on silicon carbide (SiC) and chemical vapor deposition (CVD). The epitaxial growth consists on the formation of a graphene layer after the sublimation Si atoms on the surface of the SiC substrate at high temperatures (1000 ºC) [110], which leaves an excess of carbon atoms that graphitisize [111]. The advantages of this method is that the graphene film is directly grown on a SiC wafer that is readily compatible with most of the micro and nano fabrication processes used to manufacture micro and nano electronics. The main downsides are the relatively high cost of the SiC, the lower carrier mobility of the graphene produced by this method in comparison with CVD grown graphene [112, 113, 114] and the difficulty of transferring the graphene to other substrates.

The CVD growth method is based on the decomposition of a carbon source, normally CH_4, on the surface of a metal, usually Cu or Ni, which acts as catalyst. The high carbon solubility in Ni makes it the material of choice when growing Few Layers Graphene (FLG) or CVD graphite [115]. On the other hand, when Single Layer Graphene (SLG) is the desired material, the low carbon solubility in Cu makes it the ideal candidate to be used as a catalyst. The advantages of this growth method are that it is easily scalable, with graphene films up to 75 cm being fabricated and transferred by roll-to-roll methods [116], the relative low cost of the metals used as catalysts and the decent mobility, up to 16 000 cm^2/Vs [117]. As disadvantages we could mention the need of high temperatures and vacuum for the growth, as well as the need to transfer the graphene to other substrates since the conductivity of the metal film would prevent its use in most electronic applications. However, there are relatively easy transfer methods that with the appropriated optimization allow graphene technology to be compatible with most electronic applications [118].

Due to the aforementioned reasons, the method chosen for the graphene fabrication in this thesis is the CVD growth on copper substrates using CH_4 as a precursor.

2.1.2 CVD graphene growth on Cu films

The growth of graphene using a Cu catalyst was first developed by the group of Luigi Colombo and Rodney Ruoff at the University of Texas [112]. It was achieved by placing a Cu foil (25 μm thick) inside an oven at 1000 ºC under a controlled mixture of CH_4 and H_2. Since that seminal work, many efforts have been devoted to improve the quality of the CVD graphene, increasing its mobility, decreasing the number of defects and developing more cost-effective strategies for this process.

2.1.2.1 Preparation of the Cu substrate

One of the key areas to improve the quality of CVD graphene is the copper film preparation. Since the polycrystaline nature of CVD graphene has been identified as one of the most important factors reducing mobility [119] (transport inside the same grain can reach mobilities up to 2700 cm^2/Vs), a considerable effort has been devoted to reduce grain boundaries. The formation of grain boundaries in graphene is caused by the orientation mismatch of the neighbour graphene nuclei at the start of the growth [120]. With this in mind, lowering the nucleation density will result in a graphene sheet with bigger grains and, thus, reduce the number of grain boundaries. It is at this step that the proper preparation of the Cu substrate comes into play. Techniques such as electrochemical polishing[121], thermal annealing [122] or hydrogen annealing [123] have proved to be useful reducing the number of nucleation sites on the copper substrate and thus reducing the grain boundaries in the graphene sheet.

Based on these results, we prepare our Cu substrates for the growth process by electropolishing commercial Cu foils in order the reduce to copper roughness and, consequently, the nucleation density using a variation of the method described in [121]. Shortly, we cut two pieces of 14 x 6 cm of a commercially available 25 μm copper foil and mount them on a custom made teflon holder. After that, we introduce the teflon holder with the Cu foils into a beaker, fill it with the electrochemical solution described in Table A.1 and connect the Cu foils to the two terminals of a DC power supply. Then a voltage of 7 V is applied between the two Cu foils for 5 minutes, resulting in an approximate current density of 90 mA/cm^2 which etches away the grooves and impurities on the foil acting as the anode. After that the film is rinsed with distilled water, isopropanol and ethanol, dried with nitrogen and the borders of the Cu foil covered by the teflon cell are cut away, leaving a growth area of 4 x 8 cm. Figure 2.1 a and b shows the copper foil mounted on the cell and during the electropolishing procedure, respectively.

Once the copper foil has been electropolished, we mount it in a quartz holder and introduce it on the quartz tube of a three zones hot wall reactor to proceed with the growth. The quartz tube is connected to a vacuum pump on one extreme and to the inlets of the gasses that are required for the growth on the other. The type and flux of gasses injected into the tube are controlled and monitored continuously by mass flow controllers. During the first phase of the growth we heat up the oven to 1050 ºC and perform an annealing of the Cu foil in Ar (400 sccm) at a pressure of 100 mbar. In this step, with temperatures close to copper melting point, the surface reconstructs, offering a more suitable platform for graphene growth. In former processes, a flow of hydrogen was added in order to

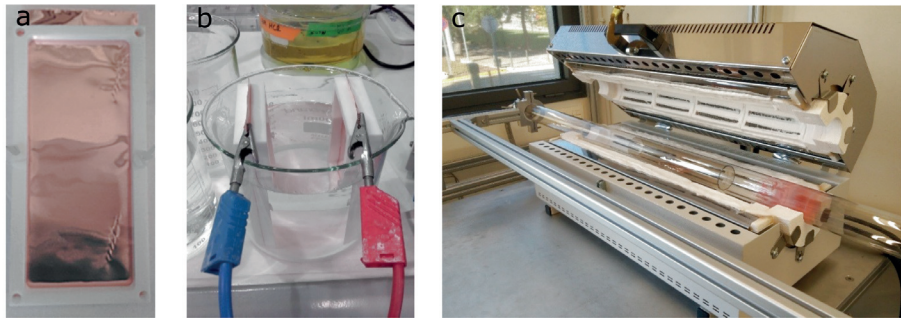

Figure 2.1: Electropolishing and hot wall reactor setups - a) Copper foil piece of 14 x 6 cm mounted on the teflon holder used for the electropolishing. b) Two pieces of copper foil, acting as anode and cathode, on the beaker filled with electropolishing solution and connected to the DC power supply. c) Picture of the hot wall reactor used for the graphene growth during this thesis.

remove Cu oxide, but some studies [124, 125] have shown that Cu oxide acts as a barrier passivating the nucleation sites, which can reduce the nucleation density and can produce graphene crystals of centimeter scale [124].

2.1.2.2 Graphene CVD growth

The graphene growth on Cu substrates is produced by the adsorption of the carbon supplied by the decomposition of a carbon based precursor. Due to copper's low carbon solubility, most of the carbon is absorbed at the surface, with a small percentage making it into the bulk. The chemisorption and desorption processes compete with one another, raising the carbon concentration on the surface of the copper until the supersaturation limit is locally reached, leading to the formation of a nucleation site at that particular location. The chemisorbed carbon diffuses through the surface of the copper foil attaching and detaching to the initial nucleation sites and making the graphene crystals grow. Then, one of two processes can happen depending on the chemisorbed carbon concentration at equilibrium (C_eq): either carbon depletes before nuclei coalescence, yielding an incomplete growth, or the nuclei coalesce and form a continuous film [126, 127]. If complete coverage is achieved, the catalytic decomposition of methane stops finishing the growth and making this process a self-limiting process. The whole process is illustrated in Figure 2.2.

Following the 40 minutes annealing process to prepare the Cu substrate, we proceed to the next phase in our process, the growth phase. In this phase, the pressure is reduced, the Ar flow is increased to 1000 sccm and H_2 and CH_4 are introduced at around 20 and 0.5 sccm, respectively. The duration of the growth phase is around 5 minutes. During this phase, CH_4 is adsorbed and catalytically

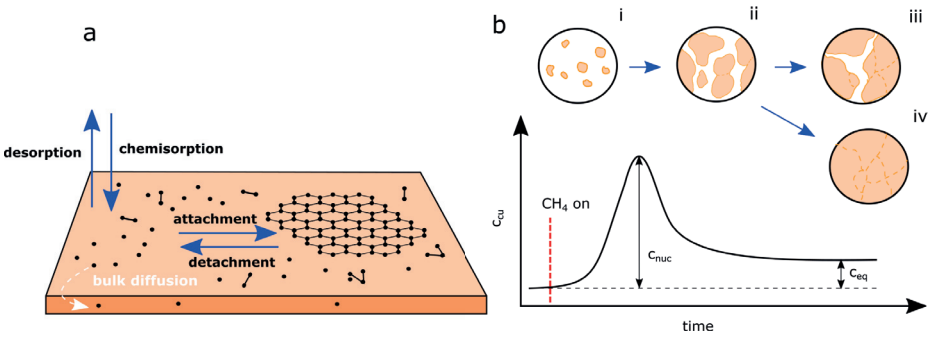

Figure 2.2: CVD graphene growth on Cu substrate - a) Schematic representation of the different processes that take place at the copper foil during graphene growth. b) Evolution of the nucleation and growth of the graphene grains. i) Graphene nucleation sites are formed where the C concentration exceeds the supersaturation limit. ii) Graphene crystals grow via the attachment of other absorbed C atoms. iii) Growth stopped by the depletion of absorbed C atoms. iv) Growth stopped when the crystals merge together and stop the absorption of carbon. Figure based on [128].

decomposed in carbon atoms and hydrocarbon molecules (C and CH_x with x from 0 to 3) on the surface of the Cu. The role of the hydrogen mixed with the methane is to aid on the chemisorption of the methane by the copper substrate [129].

Once the growth phase is over, CH_4 and H_2 flows are shut down and the Ar flow is reduced to 400 sccm. The quartz tube is taken out of the oven and is left to cool down for 30 minutes, before purging the system, breaking the vacuum and taking the copper foil out of the tube. In order to improve the reproducibility of the graphene transfer and to ensure the quality of the graphene film, the samples are produced upon demand and stored on a vacuum desiccator until they are used.

Figure 2.3 shows a schematic representation of the different phases of the growth as well as the pressure, temperatures and gases used for each step.

It is worth mentioning that the graphene growth process is extremely sensitive to variations in the copper foil source and preparation, the growth conditions and even the different contaminants adsorbed on the reactor´s quartz tube [130]. It is because of these reasons that the proper characterization of the material is extremely important in order to ensure experimental reproducibility and that the material quality meets the standards required for device fabrication. The methods employed to characterize the graphene films and ensure a high quality are discussed in Appendix A.

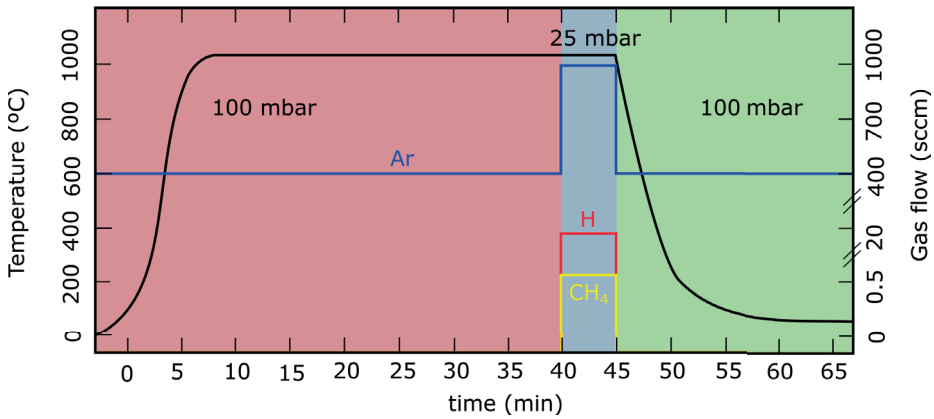

Figure 2.3: Temperature, pressure and gas flow during CVD growth of graphene - The red shaded part marks the heat up and annealing phase, the blue shaded part marks the growth phase and the green shaded part marks the cool down phase.

2.1.3 Transfer

As explained in section 2.1.2, the graphene used in this thesis is grown on top of Cu. However, for most electronic applications, graphene needs to be transferred to a semiconducting or isolating substrate, making necessary a transfer process. Due to the nature of this transfer process, the graphene sheet is manipulated and covered with different carrier polymers, so special care must be paid in order to reduce contamination and to obtain the highest graphene quality possible. For the fabrication of the devices used in this thesis two different transfer methods were tested: wet transfer [131] and dry transfer [132].

The wet transfer of CVD grown graphene consist on etching away the sacrificial copper substrate using acids of metallic salts to release the graphene layer.

For this process, the graphene is protected and supported by a spin coated layer of PMMA A4[1]. After that, the Cu is placed on a hotplate at 40 ºC during 15 minutes to evaporate the solvent and dry the PMMA. In order to remove the graphene that grow on the back of the Cu, the foil is placed on a wafer facing down and introduced into an ICP-RIE; [2] a short etching step (40 W HF, 40 sccm Ar and 40 sccm O_2 during 6 minutes) is performed while keeping the chuck temperature at 20 ºC to avoid hardening the PMMA. After the backside graphene has been removed, the copper is placed floating on a solution of 0.5 M $FeCl_3$ and 2 M HCl (1:2), with the PMMA and the graphene facing up, during 5 hours. After this time the Cu foil is completely etched away by the $FeCl_3$/HCl solution,

[1] MicroChemicals GmbH
[2] PlasmaPro 100 Cobra, Oxford Instruments

leaving the graphene floating on top and protected by the PMMA. To clean the graphene layer, the material is transferred to a beaker containing DI water and left floating for one hour. The cleaning process is repeated at least three times. After that, the target substrate is plasma cleaned and the graphene layer is fished in the desired location and left to dry for 15 minutes at 40°C. Once the water has completely evaporated and the graphene layer is fixed to the substrate, an annealing is performed doing a temperature ramp to 180°C of 30 minutes duration in vacuum conditions. When the substrate has cooled down to room temperature, the supporting PMMA layer is removed by flushing with acetone and then with a 30 minutes acetone bath and a 30 minutes isopropanol bath. The sample is finally blown dry with nitrogen. The whole process is depicted in Figure 2.4.

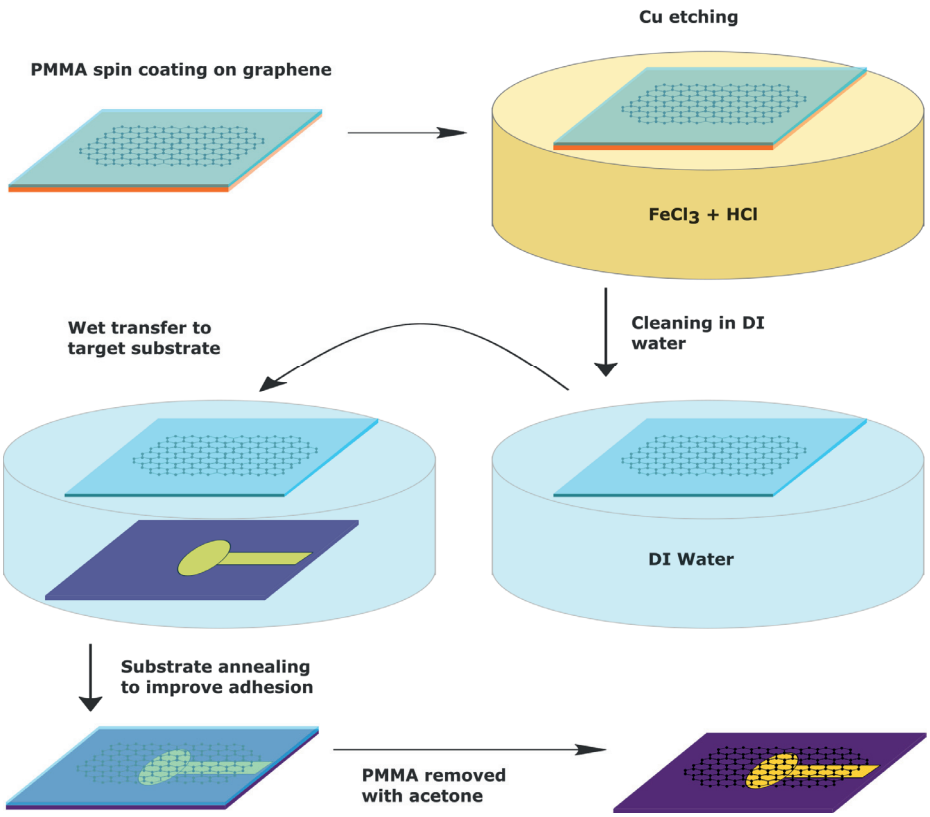

Figure 2.4: Graphene Wet Transfer - Schematic representations of the steps involved in the graphene wet transfer process used in this thesis.

One of the major challenges of the wet transfer is the removal of the backside graphene. Later during this thesis, we identified the graphite holder used to hold the copper foil in place during the growth process as the main source of the

backside graphene. Switching to a quartz holder greatly reduced the amount of backside graphene; nevertheless, it was still necessary to remove the backside graphene while maintaining intact the quality of the single layer graphene of the front side. For that we tried different methods.

The first method we tried was to partially etch the copper and flush with high pressure water. The partial etching exposed part of the backside graphene and the stream of high pressure water completely removed the remaining backside graphene. The problem of this method is that the water pressure can wrinkle the Cu foil with the single layer graphene on top, creating areas of strain and reducing graphene´s mobility.

The second method we tried was to remove the backside graphene with a solution of nitric acid. Prior to the Cu etching step, the Cu foil was placed floating on top of a 10% HNO_3 with the backside graphene facing down. The nitric acid completely etches the backside graphene and then the wet transfer procedure is continued as previously explained. The main problem of this method is that once the backside graphene is removed, the HNO_3 etches the Cu quickly. Since the amount of backside graphene can vary from growth to growth, it is not possible to know exactly how long will take for the HNO_3 to completely remove the backside graphene and start dissolving the copper. Additionally, the exothermic nature of this process creates bubbles that can spill HNO_3 on top of the sample. This nitric acid quickly etches away the PMMA supporting layer and the graphene, creating defects in the sample.

The third method we tried was to tape the copper to a wafer, leaving the backside part exposed. Then the backside was etched using a plasma cleaner[3] at 200 W, 50 sccm O_2 during 1 minute. Concerns regarding the stability of the plasma produced by our machine lead us to use an ICP-RIE machine instead, in order to prevent overheating of the PMMA and to have a higher degree of control over the process parameters.

An important point to optimize in this method is the duration of the DIW cleaning baths. We had to carefully monitor the cleaning of Fe and Cu traces on the graphene sample after the etching, in order to ensure that all residues were removed. This was done by measuring samples with increasingly DIW cleaning times on an EELS detector on a Transmission Electron Microscope (TEM) [4] until no more iron or copper residues could be detected.

The advantages of the wet transfer method are that it is a reliable process that reduces to the minimum the graphene manipulation and that has the possibility to be completely automatized[133], removing any reproducibility issues caused

[3]PVA Tepla PS 210
[4]FEI Tecnai G2 F20 HR(S)TEM

by the human factor. These advantages made us choose the wet transfer over the dry transfer, which is discussed in detail in Appendix B, as the standard procedure for the fabrication of the devices used in this thesis.

2.1.4 Wafer scale fabrication of SLG devices

During the course of this work two main strategies have been developed to fabricate graphene MEAs. The first one focuses on building the graphene MEA on rigid substrates for *in vitro* applications. In the second one, the devices are built on a flexible substrate in order to achieve the necessary needed for *in vivo* applications. Despite their different target applications, both strategies share common fabrication procedures and the basic workflow followed to build the devices is as follows: patterning of the metal leads, growth and transfer of the graphene, definition of the electrode and passivation of the device.

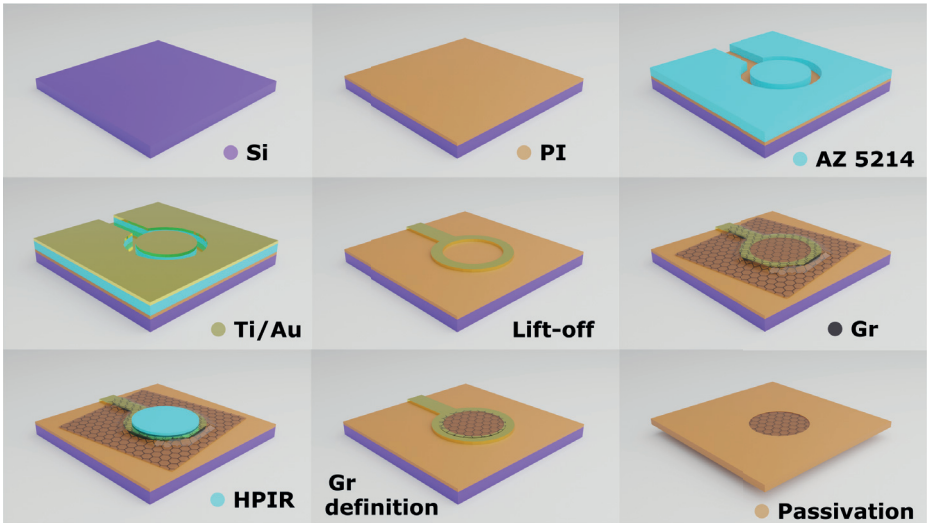

Figure 2.5: SLG device fabrication - Schematic of the steps followed to fabricate SLG flexible devices. For the fabrication of rigid devices the same steps are followed with the exemption of the PI spin coating and the final release from the sacrificial Si wafer.

In order to fabricate the SLG devices used in this thesis, the graphene layer has to be transferred to a suitable substrate: borosilicate for the rigid MEA and polyimide for the flexible ones. Furthermore, it has to be cut to shape, contacted with metals to interface with the recording electronics and, then, the whole device but the electrode's active area has to be passivated to avoid shortcuts through the electrolyte. Because the size of the electrodes is in the order of tens of microns, all this process is done by means of photolitography.

All the individual steps are depicted in figure 2.5 and detailed next. The detailed fabrication parameters used in each step can be found in Appendix C.1.

1. **Flexible substrate deposition.** For the fabrication of flexible devices, a layer of non-photodefineable polyimide is spin coated on top of a sacrificial Si wafer. Prior to the spin coating, the wafers are dehydrated on an oven at 200ºC during 30 minutes and plasma cleaned at 500 W during 5 minutes with 600 sccm O_2. After that, a layer of polyimide PI 2611[5] is spin coated to obtain a layer of 7.5 μm thickness. Then, the PI is softbaked in ambient conditions and hardbaked nitrogen.

2. **Track metalization.** In order to define the metal tracks used to contact the electrode´s graphene active area, a standard photolitography process is performed. For this process, a negative AZ[6] resist is patterned, a layer of Ti/Au (20/200 nm) is evaporated using an electron beam evaporator [7] followed by an acetone lift-off.

3. **Graphene Transfer.** After the tracks are defined, the graphene is transferred to the wafer using the wet transfer process described in 2.1.3.

4. **Graphene definition.** To define the graphene, a photolitography process using a positive resist[8] is performed in order to protect the electrode´s active area. After this, the unprotected graphene is etched away using an ICP-RIE[9] step (15 W HF, 150 W ICP, 50 sccm Ar and 60 sccm O_2, 1 minute)

5. **PI structure.** For the flexible devices the polyimide substrate needs to be cut to shape. This is done by protecting all the device but the cutting lines with a resist[10]. Then the unprotected polyimide is etched away with ICP-RIE (250 W HF, 500 W ICP, 10 sccm CF_4 and 40 sccm O_2, 12 minutes)

6. **Passivation.** Two different processes are used to passivate the metal tracks and avoid that the electrolyte shortcuts the electrodes. The first process uses a photodefineable, permanent PI resist[11] that is generally used to passivate flexible devices; the Young modulus and the water intake of this photodefineable PI is close to that of the PI 2611 used for the substrate. The second passivation process uses a permanent SU8 resist[12]; this resist is

[5] HD Microsystems
[6] AZ 5214 E, Merck Performance Materials GmbH
[7] ATC-8E Orion, AJA International
[8] HPIR 6512, FujiFilm
[9] PlasmaPro 100 Cobra
[10] AZ 9260, Merck Performance Materials GmbH
[11] HD8820, HD Microsystems
[12] SU8 2005, MicroChemicals GmbH

normally used to passivate rigid devices in which a specific surface chemistry is needed.

A significant amount of work was also devoted to improve the fabrication protocols in order to obtain high quality devices. Monitoring the level of photolitographic residues during the fabrication using Raman spectroscopy has led the team to develop techniques to protect the graphene during the fabrication using evaporated copper. Alternative passivation strategies were also investigated. On the one hand, the use of Al_2O_3 yielded interesting results in terms of cell attachment, which will be discussed further in Chapter 4. On the other hand, the use of the photodefineable PI, instead of the until then standard SU8 resist, significantly reduced the amount of time and work needed to passivate the devices.

2.2 Neural Cultures on SLG MEA

This section summarizes the studies performed with rigid SLG MEA. Here we discuss the MEA design and its characterization in terms of impedance spectroscopy and noise power. Furthermore, we test the devices by culturing primary cortical neurons and recording their spontaneous electrical activity.

Since SLG and graphene-based materials unite many of requisites for a good active MEA material, already discussed in Chapter 1, the use of these materials has attracted a great deal of attention from the neurotechnology field in the last years [134]. Particularly, SLG has been proved to be a well suited material for neuronal cultures [135], been able to sustain neural growth even without coating with protein layers [136]. In addition, SLG and graphene-based materials do not show toxicity on cell lines [137] and dissociated cultures [138]. With all these characteristics in mind and the electrical performance we already discussed in chapter 1, we set out to fabricate, characterize and test a rigid SLG MEA to be used in *in vitro* neuroscience studies.

2.2.1 MEA design and characterization

The rigid single layer graphene MEAs used during this thesis contain 60 electrodes of 3 different sizes, with diameters of 25, 50 and 100 μm. In order to avoid leakage currents from the metal acting as tracks, we use a ring contact instead of a complete back contact. The ring design ensures that, even if there is an opening in the graphene, the electrolyte will contact the isolating borosilicate substrate instead of the metal. The metallic ring perimeter overlaps 3 microns with the perimeter of the graphene electrode and the passivation layer overlaps 6 microns with the graphene sheet, as shown in Figure 2.6a. This ensures that, even with

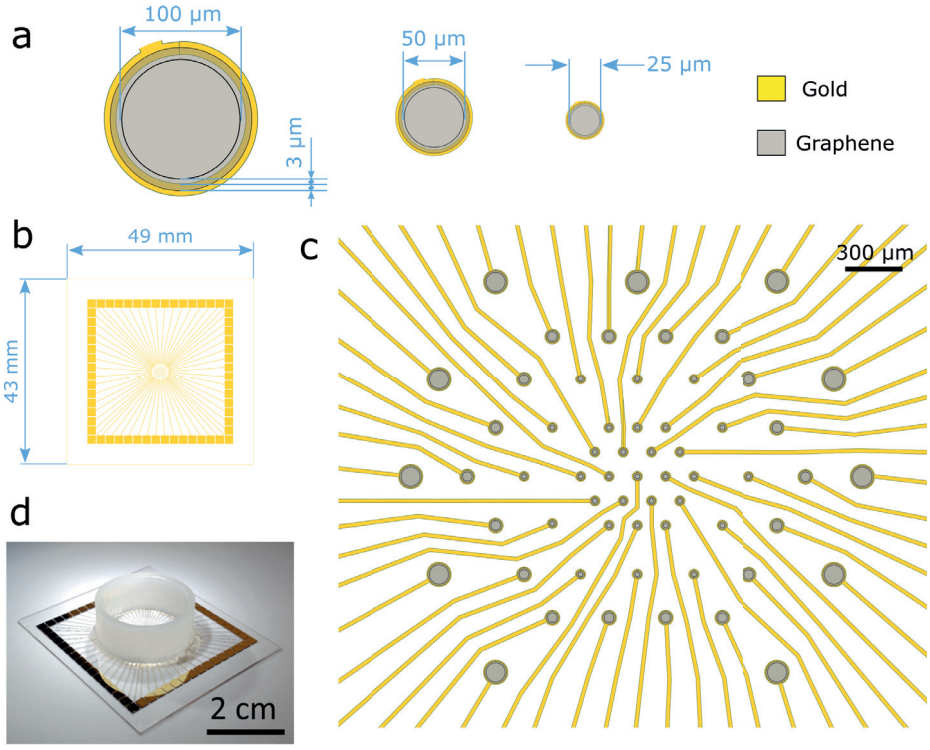

Figure 2.6: Rigid SLG MEA Design - Design specifications of the rigid SLG MEA used in this thesis. The MEA contains 25, 50 and 100 μm diameter electrodes distributed in a hexagonal pattern. In the first and the second hexagon starting from the centre, the electrodes have a pitch of 150 μm and a pitch of 300 μm for the rest. The whole MEA dimensions are 43 x 49 mm. A 24.5 mm diameter methacrylate ring is glued to the surface of the MEA to act as culture well.

small errors in the alignment of the masks, the electrolyte will not make contact with the metallic tracks. The whole MEA has a dimension of 43 x 49 mm (Figure 2.6b), the 60 electrodes cover an active area of 1.2 x 1.2 mm and the layout of the connecting pads matches that of the standard MultiChannel System 60 electrode MEA layout, in order to ensure compatibility with commercial MEA recording systems. The electrodes in the MEA are disposed in a hexagonal pattern, such as that commonly used for retinal recordings [139], arranged in 5 concentric hexagons with one single electrode in the centre, as shown in Figure 2.6c. The separation between the two inner hexagons is 150 μm and 300 μm between the rest. The fabrication of these devices is done in a 4-inch wafer, following the steps described in section 2.1.4. At the end of the process the wafer is diced to obtain the individual MEA. In order to create a well suitable for cell culture, we placed a methacrylate ring of 24.5 mm inner diameter and 10 mm height on the MEA and secured into place using a biocompatible resist[13].

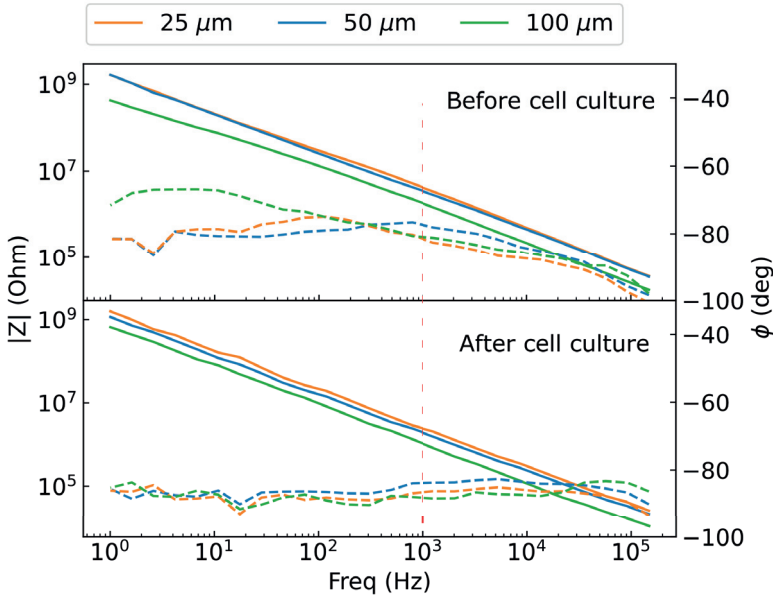

Figure 2.7: Rigid SLG MEA Characterization - EIS Bode plot of the 3 electrode sizes used for the recordings with rigid MEA. The solid lines stand for the module of the impedance (|Z|), the dashed lines the phase (ϕ) and the red dashed line marks the 1 kHz frequency. The top graph shows the EIS before the cell cultures while the bottom graph shows the EIS after the cultures.

To assess the capabilities of the rigid SLG MEA we performed 3 different test: EIS (Figure 2.7), recording of artificial signals (Figure 2.8 a - c) and a baseline noise characterization (Figure 2.8d).

[13] 302 - 3M, Epo-Tek

For the EIS characterization the MEA was connected to a multiplexed[14] potentiostat[15] using an Ag/AgCl reference electrode[16] and a platinum sheet as a counter electrode. The methacrylate well was filled with PBS[17] (10 mM PBS, 137 mM NaCl and 3 mM KCl at pH 7.4) and a small sinusoidal signal (20 mV) was applied with frequencies ranging from 1 to 10^5 Hz. The data from figure 2.7 shows the impedance spectrometry of 3 electrodes with different sizes before and after being used in a cortical neuron culture. All electrodes show the same behaviour: the modulus of the impedance is inversely proportional to the frequency and the phase stays close the -90 º over the studied frequency range. Accordingly to the theory explained in section 1.3, the electrodes behave like an IPE with a ideality index close to 1 (Equation 1.16), and therefore, their impedance can be described by the impedance of an ideal capacitor (Equation 2.1).

$$Z_c = \frac{1}{iwC} \tag{2.1}$$

Comparing the impedance spectroscopy of the electrodes before and after the cell culture (Figure 2.7) we can appreciate that the phase becomes flatter and goes closer to -90 º, that indicates a more capacitive behaviour. A possible explanation for this phenomenon is that the 70 % ethanol solution used to sterilize the MEA before seeding the neurons can clean the residues left after the fabrication [140]. A more homogeneous interface will result then in a more capacitive behaviour [71].

In order to assess the rigid SLG MEA for *in vitro* measurements, we first tested their capability to record artificially generated signals. To do so, we connected the rigid SLG MEA to an electrophysiology recording system[18] using an Ag/AgCl reference electrode with the signal generator[19] connected in series. The MEA, preamplifier and signal generator were placed inside a grounded faraday cage. We recorded simulated high frequency (hippocampal neuron spikes) and low frequency (electroretinograms) signals using a 60 electrode rigid SLG MEA. Figure 2.8a shows the hippocampal neuron spikes recorded by three different sizes of electrodes, while Figure 2.8b shows a close up of the same signal. Both figures show a stable signal and low noise, allowing to perfectly recognise all the features of the simulated hippocampal neural spikes. Figure 2.8c shows a low frequency electroretinogram signal, bandpass filtered between 0.5 and 300 Hz, recorded by 3 different electrode sizes. The recording capabilities of the rigid

[14] MP-MEA Multiplexer, Bio-Logic SAS
[15] SP-200, Bio-Logic SAS
[16] FlexRef, WPI
[17] PBS tablets, Sigma-Aldrich
[18] OpenEphys Adquisition Board with Intan RHD2132 amplifier boad
[19] ME-W-SG, Multichannel Systems GmbH

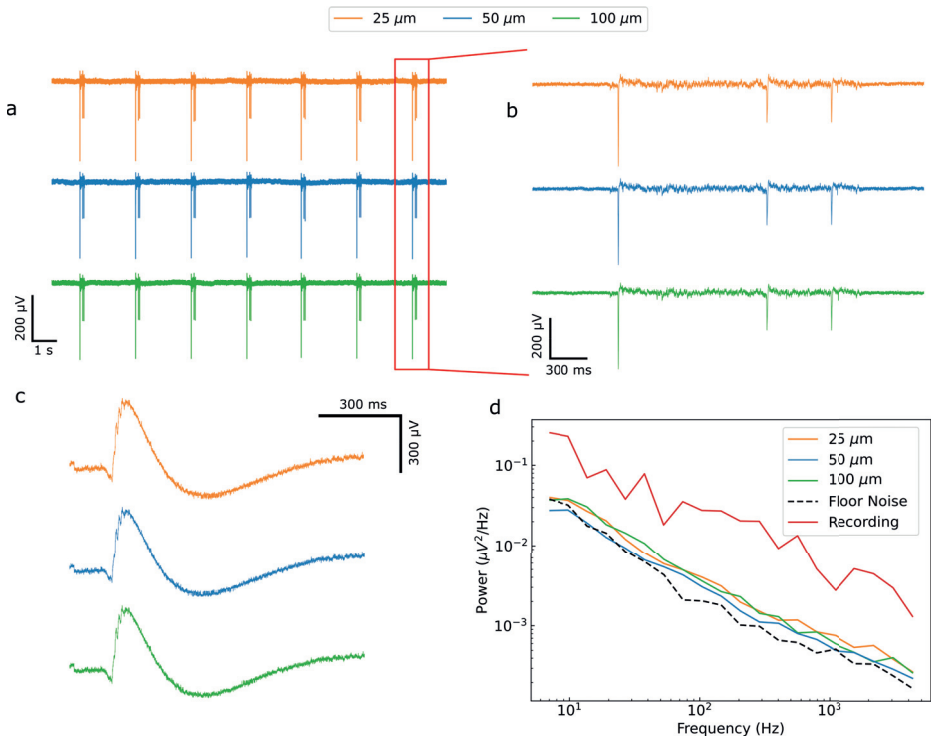

Figure 2.8: Rigid SLG MEA performance assessment - Characterization of the rigid SLG electrodes performance. a) - c) voltage signals generated by the MCS MEA Signal Generator for the 3 electrode sizes used for the SLG rigid MEA. a) Hippocampal neuron spikes. b) Close up of the hippocampal neuron spikes. Both signals were bandpass filtered between 200 and 5 kHz. c) Electroretinogram, signal bandpass filtered between 0.5 and 300 Hz with an additional notch filter at 50 Hz. d) PSD of the noise baseline of the 3 different electrode sizes; for reference the PSD of the background noise of the recording setup with the amplifier channels connected to ground and the PSD of a typical *in vitro* recording are also shown.

SLG MEA also allow to perfectly capture relevant the signal features of the low frequency range.

To assess the intrinsic electrode noise, we removed the signal generator from the set up and obtained the PSD of the system by recording a 1 minute voltage trace and calculating its Fast Fourier Transform (FFT) between 5 and 5 kHz with a custom Python 3.6 code. This calculation gives the power noise of the electrodes at each frequency and its represented in Figure 2.8d for electrodes of the three different sizes present in the rigid SLG MEA. For reference, we present the background noise PSD of the recording setup, with all the amplifier channels connected to ground, that show a power slightly lower than that of the electrode´s PSD. We also present the PSD of one of the *in vitro* recordings from Figure 2.10, showing that the PSD´s power is more than one order of magnitude

higher than the PSD of the recording electrodes. To obtain the V_{RMS} noise of the electrodes, we can integrate the PSD over the frequency range of interest, i.e. 5 to 5 kHz for these electrodes. The V_{RMS} noise of the three different sizes of electrodes yields a value of 2 μV, proving again the good performance of this electrodes.

An interesting observation we can point out is that for these electrodes, the V_{RMS} noise is very low although the impedance relatively high, in the range of 1 to 4 MOmhs at 1 kHz (Figure 2.7). Lowering the electrode impedance has been the most standard approach in order to reduce electrode V_{RMS}, but, as already discussed in section 1.3.4, the Johnson-Nyquist theory for thermal noise [73] states that only the real part of the impedance contributes to the V_{RMS} noise. With that in mind, and since our electrodes behave almost as ideal capacitors, the modulus of the impedance alone is not a good predictor of the noise level and it is necessary to take into account external factors, such as the ratio of the electrode impedance to the amplifier input impedance and the noise of the electronics. This observation has also been pointed out in different experimental [141, 142] and theoretical [143] studies that have demonstrated that the impedance module alone is not significant to determine electrode noise.

2.2.2 *In vitro* recordings using the rigid SLG MEA

Once we were confident of the performance of our rigid SLG MEA, we went ahead to test them in *in vitro* recordings. To do so, we sterilized the electrodes by immersing them in 70 % ethanol during one hour. After that, we removed the ethanol and rinse the electrodes thoroughly with sterile PBS[20] and coated the surface of the MEA with Poly-D-Lysine[21] for 2 hours before rinsing the MEA again with PBS. The neurons were obtained from the cortex of 17 days old rat embrios that were disaggregated accordingly to the procedure detailed in Appendix D.1 and plated with a density of $2{,}5 \cdot 10^4$ cells/cm^2. The neurons were cultivated for at least 14 days before they were used for the recordings. Figure 2.9 shows pictures of the cortical neurons on top of the surface of the rigid SLG MEA at different growth stages.

For the *in vitro* recordings, the MEA was connected to the recording setup using an sterilized Ag/AgCl pellet electrode as a reference and placed inside a faraday cage. The recordings were acquired using the OpenEphys GUI v 0.5.4 and processed using Python 3.6 with the Neo [144] and PhyREC modules. Figure 2.10 shows a representative recording of a culture of cortical neurons at DIV 15 acquired with a rigid SLG MEA. We can observe spontaneous synchronized activity over

[20] PBS, pH 7.4 (1X), Gibco
[21] P6407, Sigma-Aldrich

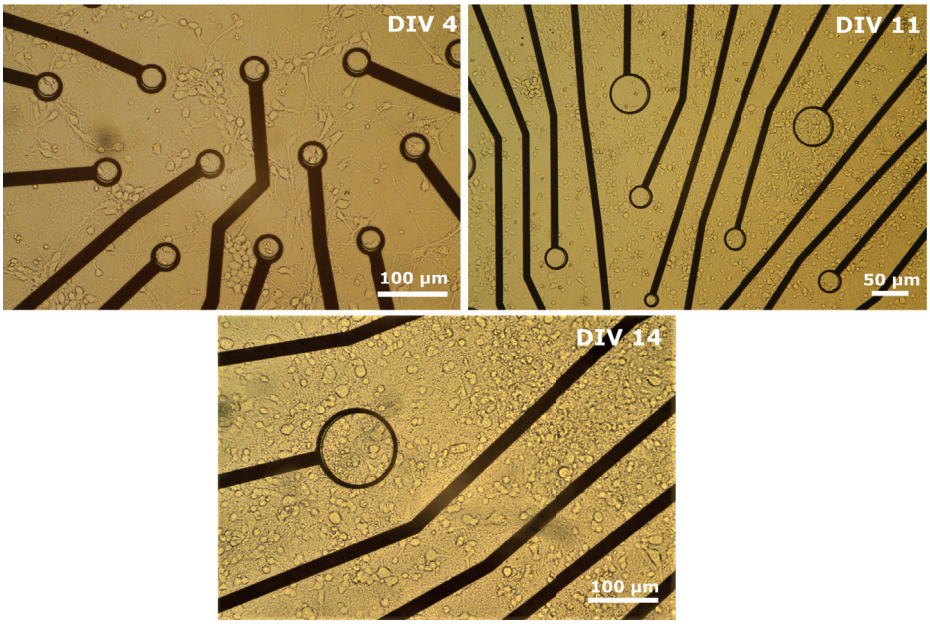

Figure 2.9: Cortical Neuron Culture - Culture of cortical neurons plated on top of the SLG rigid MEA at 3 different development times; 4, 11 and 14 days.

different channels, sign of a mature culture that has formed synapses across the network [145]. We can also observe channels that show a non-synchronous spiking pattern, like the second channel from the top, and channels with different spike amplitude, due to the different distances of the electrodes to the spiking neurons.

In order to explore in more detail the electrophysiological signals recorded with the rigid SLG MEA, we set out to analyse the shape of the recorded spikes using a custom spike sorting algorithm developed with Python 3.6 and the Sklearn [146] library. The algorithm bandpass filters the data and detects the spikes by identifying negative peaks that are larger than 3.5 times the V_{RMS} [147] of the culture in a time window during which no spikes occurred. Then it stores a recording segment of 3 milliseconds around the detection point, 1 ms before and 2 ms after the threshold crossing, as well as some metadata such as the time point of the event and the channel on which it was recorded. Figure 2.11a shows the superposed segments detected in the recordings shown in Figure 2.10. Then, the algorithm extracts two features of the stored segments: the amplitude of the spike (defined as the difference between the maximum and the minimum voltage) and the spike duration (defined as the time difference between the maximum and the minimum of the signal). The algorithm plots this 2 features and uses a k-means clustering method to identify groups in the data and color code them accordingly. Figure 2.11b shows the clusters detected by the algorithm from the

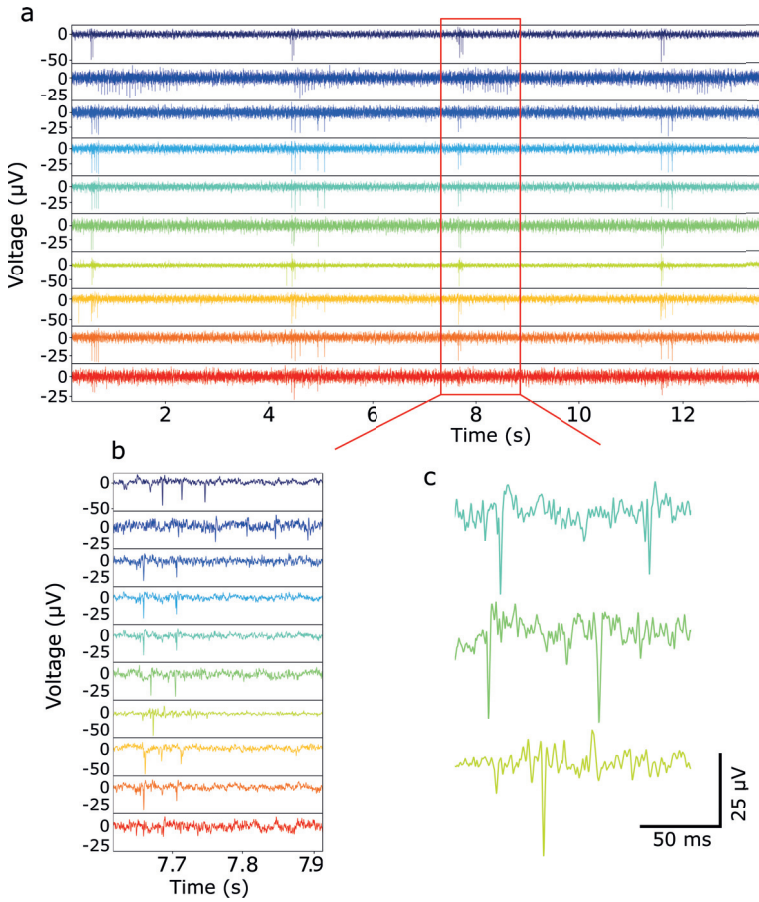

Figure 2.10: In Vitro recordings of neural cultures with the rigid SLG MEA - a) Recording of neural cultures such as those shown in Figure 2.9 at DIV 15 showing spiking activity. b) Zoom of one of the spikes trains, showing synchronized activity across the electrodes. c) Close up of the spikes present in 3 selected channels.

spikes in Figure 2.11a. From this figure we can readily see that the feature that separates the two clusters is the sign of the duration. The spikes in the orange cluster have a positive duration, meaning that the spike maximum precedes the minimum. On the other hand, the spikes of the blue cluster have a negative duration, i.e. the minimum of the signal occurs before the maximum. Figures 2.11c-d show the averages of the two distinctive spike groups obtained with the described algorithm applied to the recordings from Figure 2.10. Looking into the metadata of the spikes classified in the blue cluster reveals that the vast majority of them were recorded with the only channel that shows non-synchronous activity in Figure 2.10. This suggests that the different spike shapes have a biological

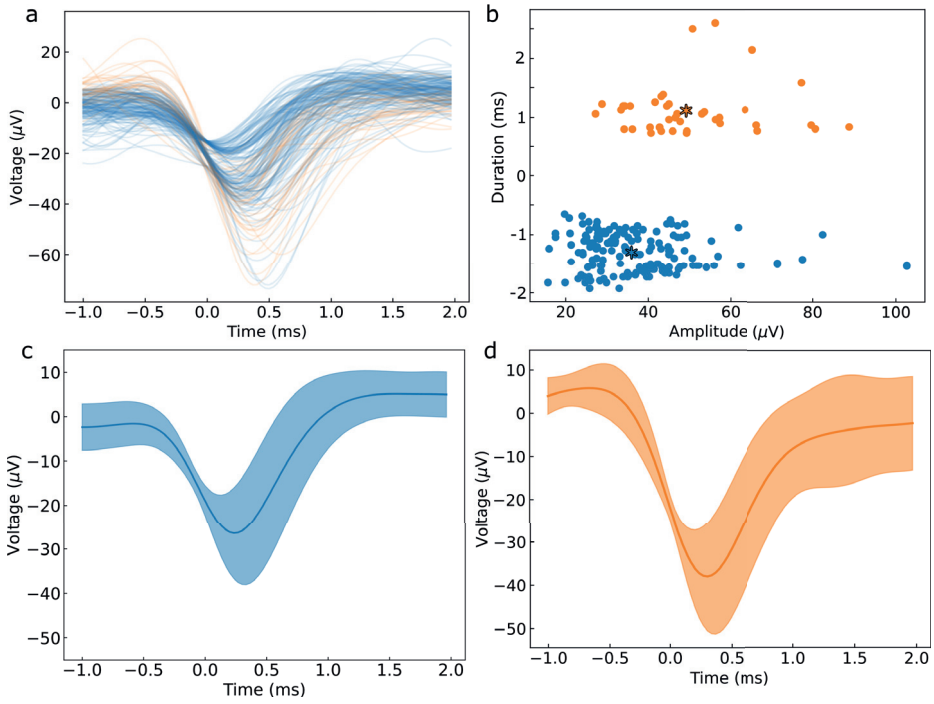

Figure 2.11: Analysis of the spikes recorded with the rigid SLG MEA - a) Spikes detected in the recordings shown in Figure 2.10; colored accordingly to the clusters found by the K-Means clustering algorithm shown in b). The center of each cluster is marked by an asterisk. c) and d) Averages of the 2 distinctive spike shapes found with the clustering algorithm. The solid line represents the averaged signal and the shaded region represents the standard deviation.

origin; the blue and orange cluster are composed of non-simultaneous spikes produced by two different active areas in the culture.

2.3 ERG recordings with flexible SLG electrodes

This section summarizes the fabrication and characterization of flexible SLG devices as well as their use to record electroretinograms (ERG). We benchmark our flexible and transparent electrodes against the current state of the art for rodent ERG, using an animal model that expresses a P23H mutation and induces a degenerative loss of photoreceptors. Additionally, we discuss the use of SLG MEA to perform multi-site ERG recordings and its possible applications to obtain topographical information of the ERG across the cornea. The results shown in this section have been published in [148] and were carried out at the Vision Institute in Paris in collaboration with the group of Prof. Serge Picaud.

2.3.1 Introduction to Electroretinography

Electroretinography is a technique that measures the changes that occur in the transretinal potential when a light stimulus is presented to the eye.

In order to fully understand ERG, we summarize here basic notions about the retina composition and its functioning. Despite his location inside of the eye, the retina is a part of the Central Nervous System (CNS) and as such it is composed of different types of neurons whose principal task is to transduce visible electromagnetic radiation into action potentials and send them to the brain through the optic nerve. There are 5 different types of neurons on the retina: photoreceptors, bipolar cells, ganglion cells, amacrine cells and horizontal cells. The principal information gateway from the photoreceptor to the brain is the photoreceptor to bipolar cell to ganglion cell chain. There are two types of photoreceptors, rodes and cones, and their main function is to transduce photons to intracelullar potential. Several photoreceptors are connected to each bipolar cells forming what is called a receptive field. Bipolar cells are sensitive to a particular receptive field and increase their intracellular potential when, in their receptive fields, bright spots appear (ON-bipolar cells) or vice-versa (OFF-bipolar cells). These bipolar cells, in turn, connect to ganglion cells. Ganglion cells encode the gradual intracellular potential changes from bipolar cells into spiking rates that are sent to the brain through their axons. The axons of the ganglion cells form the optic nerve. Horizontal and amacrine cells are responsible, among others, for lateral inhibition modulating the responses of ganglion and bipolar cells, allowing them to adapt, for example, to changes in the luminosity level of the environment. An schematic view of the components of the retina and their location is shown in Figure 2.12, a detailed explanation of the retinal function and light transduction mechanism can be found in [67].

ERG is broadly used as a diagnostic test by clinicians to assess the functionality of different neurons of the retina [149]. It is a technique that involves placing an electrode on the cornea, flashing the eye with a controlled light stimulus, and recording the transretinal potential from the surface of the cornea. The schematic of a typical ERG set up is depicted in Figure 2.13. Since ERG signals result from the synchronized multi-unit activity of retinal neurons responding to a defined light stimulation they are made of different components, each of them related to different cell types.

The principal components of an electroretinogram are the a-wave, the b-wave and the oscillatory potentials (OPS), as shown in Figure 2.13. The a-wave is the first depolarization that occurs inmediately after the light stimulus. It is not always present on a healthy ERG; since it is not generated when the retina is

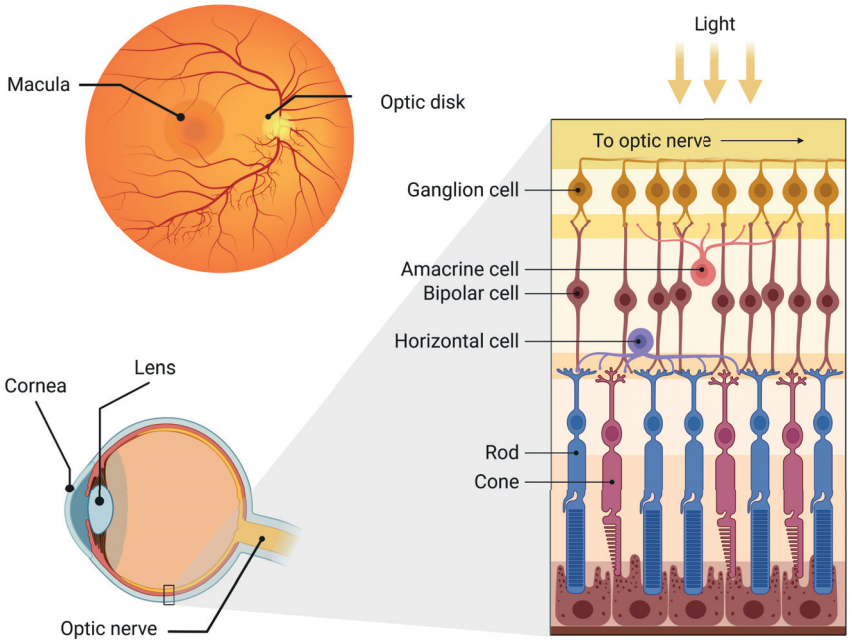

Figure 2.12: Retina structure - Components of the retina and detail of its layers and the cells that compose them. The macula is the area of the retina with highest concentration of cones and where the vision is more acute. The optic disk is where the axons of the ganglion cells leave the retina, forming the optic nerve. Created with BioRender.

not dark adapted, in the so-called photopic conditions. It is produced by the hyperpolarization of the photoreceptors from the outer layers of the retina as a response to the light stimulus [150, 151]. The b-wave is the main feature of the ERG: it is the positive wave that follows the a-wave and is produced by the depolarization of the ON bipolar cells. The fast oscillations between 100 and 150 Hz present in the rising phase of the b-wave are the OPS. The waves have an amplitude of a few tens of µV and result from the fast depolarization and hyperpolarization of the amacrine cells [152, 153]. Since each of the ERG components is linked to different retinal cells, it is possible to identify retinal diseases analysing an ERG signal [154].

The amplitude and latency of the a-wave is defined by the local minimum of the ERG response inmediately after the stimulation. The amplitude of the b-wave is defined by the maximum amplitude of the ERG plus the amplitude of the a- wave. The latency of the b- wave is defined by the time point at which the maximum ERG amplitude is achieved, taking the stimulus as time zero. For an animal with normal sight and completely dark adapted, i.e. under scotopic

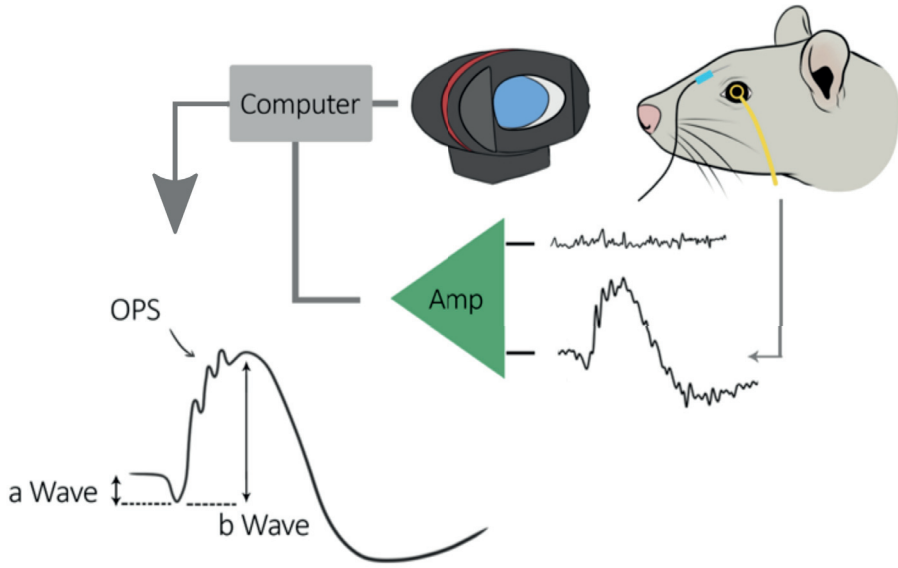

Figure 2.13: ERG recording setup - Schematic representation of the ERG recording setup used for our experiments. A Ganzfeld stimulator illuminates the eye of the rodent and the signal from the retina is recorded with a graphene electrode. The recorded signal is subtracted from that of a reference electrode placed on the forehead and amplified with an operational amplifier.

conditions, the usual a-wave parameters are in the range of a few hundreds of µV amplitude and few tens of millisecond delay after the light stimulus. A delay in latency or a decrease of the a-wave amplitude might indicate photoreceptor loss or a phototransduction dysfunction [155, 156]. The latency and amplitude values of the b-wave are in the range of 100 milliseconds and 1-2 mV, respectively, depending on the stimulus intensity, the light adaptation of the animal and the type of electrode used to record the ERG.

The ERG recording electrodes commercially available can be divided in two main categories: conjunctival and corneal electrodes [157]. A conjunctival electrode is made by bending a metal conductor, either a wire or a foil, in order to shape it appropiatedly to make contact with the bulbar conjunctiva. Figure 2.14b-d show the so called HK hook and the DTM ERG electrodes which are the most widely used conjuctival electrodes. Corneal electrodes, on the other hand, are normally fabricated by attaching metallic conductors to a contact lens, or similar, in order to place them over the surface of the cornea. Figure 2.14a-c show two of the most common corneal electrodes, the Burial-Allen and the JET ERG recording electrodes, respectively. Despite interfering with the central vision,

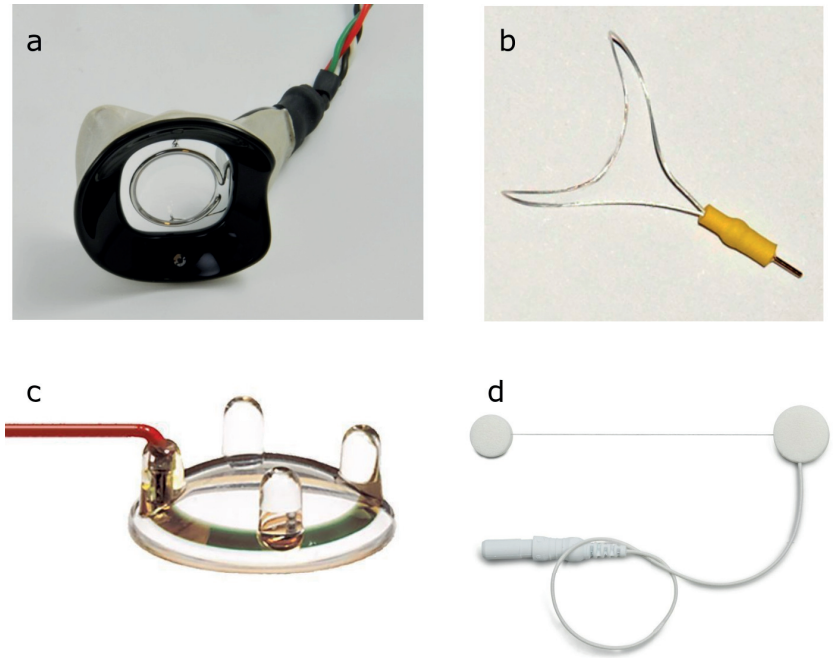

Figure 2.14: Current state of the art for ERG recording electrodes - a) and c) are corneal electrodes (Burian-Allen and JET, respectively). b) and d) conjunctival electrodes (HK hook and DTM, respectively).

their high signal amplitude make corneal electrodes the clinical standards [158, 159, 160].

Both types of commercial electrodes present two important drawbacks: they are uncomfortable, since they are made of rigid materials, and they prevent from recording multi-site activity, since the opacity of the metallic conductors partially blocks the light stimulus. Fully transparent MEA will allow for multi-site ERG recordings without blocking the light stimulus used to stimulate the retina, providing local information of the cornea's electrical potential which could be used to monitor local retinal pathologies [161, 162]. Graphene electrodes, because of their flexibility and transparency can offer novel solutions for ERG measurements. Recently, graphene has been successfully used to fabricate electrodes for electroretinogram recordings [157].

2.3.2 Device design and characterization

Five different types of ERG electrodes have been used in this study. The first one is a commercial corneal gold electrode made by bending a gold wire to create a toroidal electrode with an outer diameter of 3 mm and an inner diameter of 1.5 mm. This electrode is shown in Figure 2.15a.

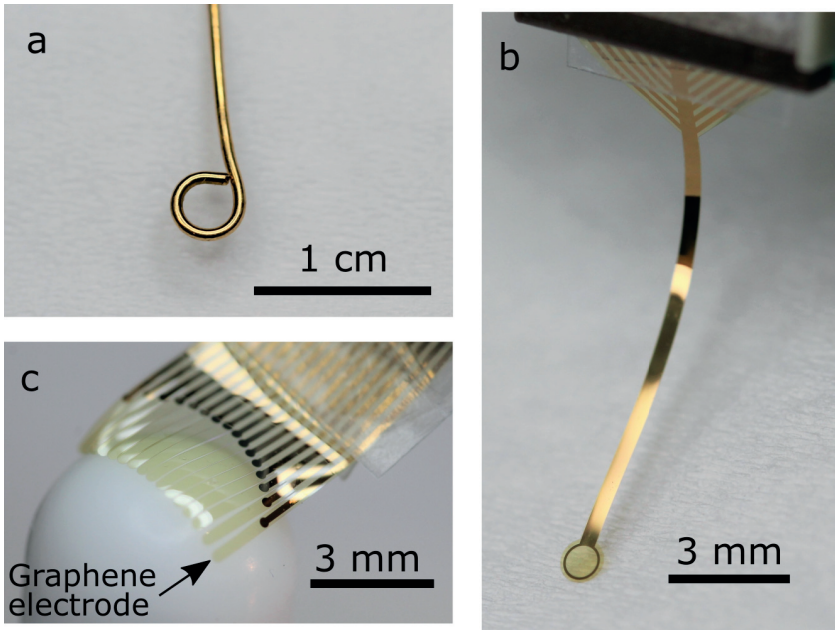

Figure 2.15: ERG electrodes used in this work - a) Image of a gold electrode, which is current state of the art for ERG recording in rodents. b) Flexible probe containing a graphene macroelectrode, of 1 mm diameter. c) Image of a linear MEA probe showing how the finger-like design allows the individual electrodes to conform to a spherical shape.

The other four probes used in this study are flexible and transparent SLG electrodes. Their detailed specifications are given in Figure 2.16.

The first generation of flexible probes has two designs. The first design is a probe containing one single macroelectrode of 1 mm diameter that covers the entire head of the probe (Figure 2.16a, macroE probe). The second design consist of an MEA of 4x4 array of 100 μm diameter electrodes with 300 μm center-to-center spacing (Figure 2.16b, μE16 probe). A picture of a macroE probe is shown in Figure 2.15b. Both probe designs share the same external dimensions: a total length of 24 mm and a circular probe head with 1.5 mm of diameter. These two designs were used on a first round of experiments; the macroE was systematically benchmarked against the commercial gold electrode and the μE16 probe was used to try to detect topological differences in the ERG signal across the surface of the cornea.

However, after the first round of experiments the limitations of the μE16 probe became obvious. The array covered an area of 0.7 x 0.7 mm^2, which it is only a fraction of the total area of an adult Sprague Dawley rat cornea, (approximately 3.5 mm radius) [163]. This meant that the majority of the corneal surface was left unmonitored and that information about the topographical corneal potentials

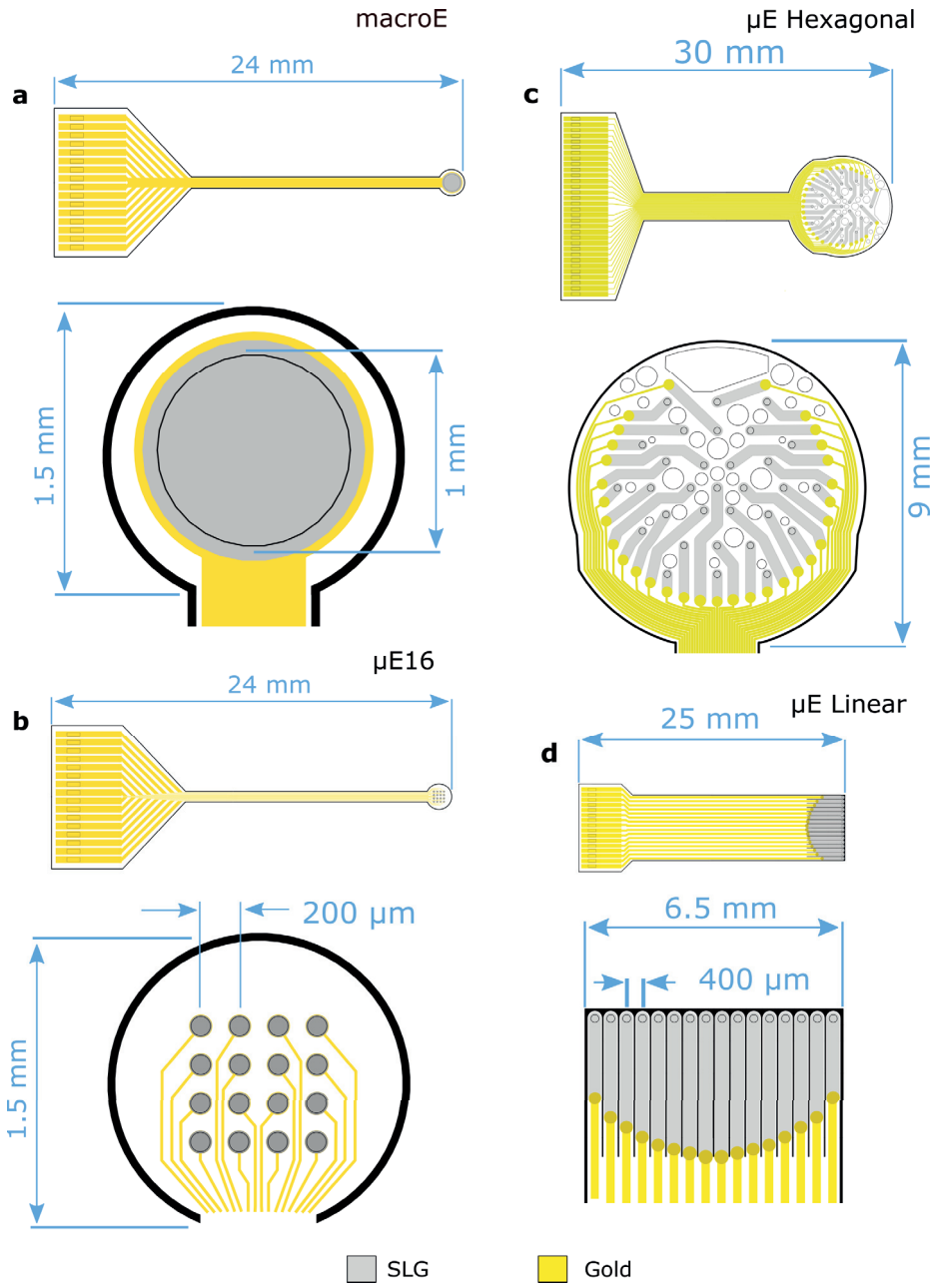

Figure 2.16: ERG probe design - Design specifications of the SLG probes used in this study. a) First generation probe containing only one macroelectrode of 1 mm diameter (macroE). b) First generation probe containing an array of 16 x 16 electrodes of 100 μm diameter (μE16). c) Second generation probe with 31 electrodes of 200 μm diameter distributed in an hexagonal pattern (μE Hexagonal). d) Second generation probe containing a linear array of 16 electrodes with 200 μm diameter (μE_Linear).

might be incomplete. Additionally, the rectilinear distribution of the electrodes of the MEA was not optimal to monitor a hemispherical surface and the metal tracks could block part of the light stimulus. Building upon the experience acquired from the first round of experiments, we designed a second generation of probes to overcome those limitations.

For the second generation we designed probes with a bigger head, in order to completely cover the corneal surface. The additional space in the probe head allowed us to include more electrodes (thus gaining resolution) and bigger electrodes (to increase the SNR). Moreover, we replaced the gold tracks from the μE16 probe with graphene tracks to avoid casting shadows on the retina. Since graphene´ sheet resistance is orders of magnitude bigger than that of gold, the tracks were made wider, optimizing the width-to-length ratio in order to keep the track resistance to a minimum. Finally, the PI substrate was structured to facilitate the adhesion of the probe to the cornea.

The second generation of probes included two different designs. The first design is a probe containing 31 electrodes of 200 μm diameter distributed in an hexagonal pattern covering an active area of 6.5 mm diameter, as shown in Figure 2.16c (μE Hexagonal probe). This hexagonal pattern has the center electrodes closer together, allowing for more resolution at the center of the cornea, such as those commonly used to stimulate and record electrical activity in the retina [139]. Finally, openings in the head of the probe were added to allow the tears to flow through and improve the adhesion between the μE Hexagonal probe and the cornea. The second design consist of a linear array with 16 electrodes of 200 μm diameter, as shown in Figure 2.16d (μE_Linear). This probe was design to record signals across the diameter of the cornea. The PI substrate in the linear probe was structured in a finger-like design, allowing each individual electrode to move independently from the others. This substrate design confers the probe the capability to conform to spherical shapes, as shown in Figure 2.15c.

All the flexible ERG probes used in this study were fabricated following the procedure described in 2.1.4. Shortly, polyimide was spin coated to act as substrate on top of which titanium and gold tracks were evaporated. Then the CVD grown graphene was transferred and patterned by reactive ion etching. Finally, the active area of the electrode was defined by passivating non-active areas of the device using a second layer of photo-definable polyimide. An overview of the layers of a finished ERG probe is given in Figure 2.17. The probes were then placed in a zero-insertion force connector to interface with the recording and characterization set ups, in order to asses the functionality of the devices by means of EIS and by characterizing their noise performance.

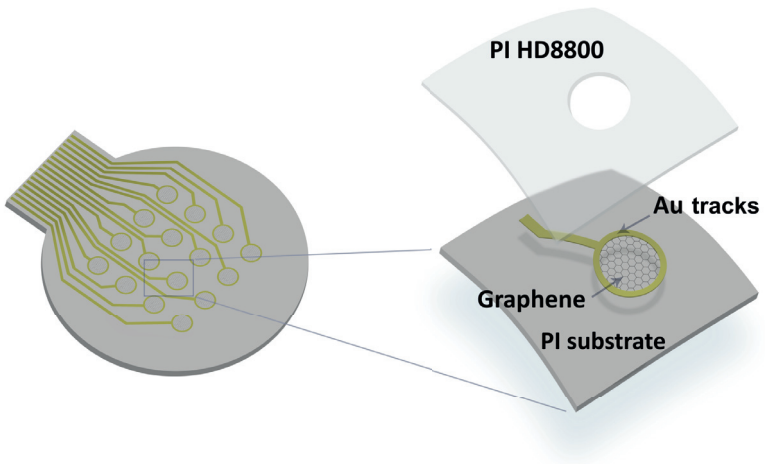

Figure 2.17: Layers of the ERG probes - Schematic view of the layers of the ERG probes fabricated in this thesis. A layer of PI is used as substrate, the gold tracks and the SLG active area are defined by photolithography and a layer of photodefineable PI (HD 8820) is used to passivate the device.

Figure 2.18a shows the EIS Bode plot of the electrodes used in this study. To obtain the impedance spectra, we used the same setup than for the rigid SLG MEA EIS characterization. Shortly, the electrodes were submerged in a bath of PBS at physiological conditions and placed inside a faraday cage in order to shield the signal from ambient noise. A three electrode setup was used, with a platinum sheet as a counter electrode and a Ag/AgCl as a reference electrode, connected to a potentiostat. All the electrodes used in this experiments show the same behaviour in the studied frequency range (0.5 to 300 Hz): the magnitude of the impedance is inversely proportional to the frequency and the phase stays close to -90 degrees. The phase behaviour show in Figure 2.18a indicates that these electrodes behave as IPEs with an ideality index close the 1 (Equation 1.16), making possible to describe their Bode spectrum by Equation 2.1, which describes the capacitance of an ideal capacitor.

Paying attention now to the magnitude of the impedance, we can see that the impedance of the commercial gold electrode is three orders of magnitude lower than the impedance of the graphene macroE. Meanwhile, the impedance difference between the macroE and the graphene μE is one order of magnitude. This differences can be readily explained by taking into account that the total capacitance is a function of the ESA, as shown in Equation 1.13. Because for the graphene electrodes used in this study the GSA and the ESA coincide, the difference in capacitance is proportional to the difference in the electrodes GSA. The area of the graphene μE is 0.03 mm^2 and the area of the macroE is 0.785

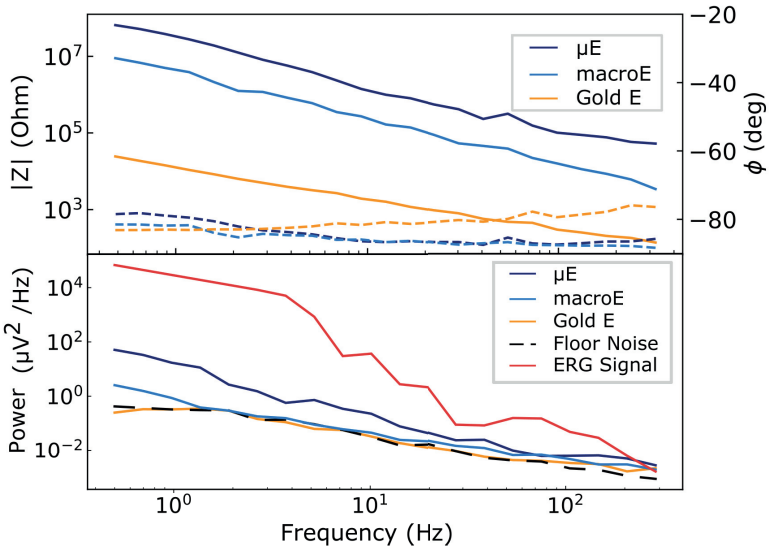

Figure 2.18: ERG Electrode characterization - Electrical characterization of a 200 μm diameter graphene microelectrode (μE), graphene macroelectrode (macroE) and gold electrode (gold E). Top) EIS Bode plot of the electrodes used in this study. Solid lines denote the module |Z| of the impedance and dashed lines the phase. Bottom) PSD of a noise baseline measured with the same electrodes shown in the top part; for reference the PSD of the background noise of the recording setup with the amplifier channels connected to ground and the PSD of a typical ERG signal are also shown.

mm^2, roughly matches the impedance difference. In the case of the gold ring electrode, its area is more difficult to calculate since it is just a naked wire without passivation (Figure 2.15a), and the total area of the electrode depends to which extend the characterization media covers the electrode. However, in order to avoid this issue, only the loop of the electrode is submerged in media during the characterizations, leaving us an area of 45 mm^2; this again, roughly matches the impedance difference to the graphene electrodes.

In order to asses the electrode intrinsic noise, we investigated the PSD of the different electrodes used in this study following the same procedure than the one used for the rigid SLG MEA (section 2.3.4). Briefly, the probes were connected to the recording electronics, the head of the probes were submerged in a bath of PBS, connected to a Ag/AgCl reference electrode and placed inside a faraday cage. Then, we obtained the PSD of the system by recording during 1 minute and calculating its FFT between 0.5 and 300 Hz with a custom Python code. This calculation yielded the noise power of the electrode at each frequency, as represented in Figure 2.18b. To obtain the PSD of the setup's floor noise, the probe was removed from the setup we just described, all the channels were

connected to ground and a 1 minute signal was measured to calculate the FFT. The setup´s floor noise is shown in Figure 2.18b. Finally, to obtain the PSD of an ERG signal (see Figure 2.18), we calculated the FFT of one of the signals acquired during a recording session, whose setup and experimental conditions will be detailed in section 2.3.3.

In the PSD of Figure 2.18 we can see that at low frequencies, the difference between the graphene macroE and the graphene μE is one order of magnitude and decreases with increasing frequency. Figure 2.18b shows that the noise spectral density of the commercial gold electrode, the graphene macroE and the setup´s floor noise remain the same over the whole frequency range, except at frequencies below 1 Hz, where the graphene macroE power slightly increases with respect to the other two. Figure 2.18b also shows that the PSD of a typical ERG recording is several orders of magnitude higher than that of any of the electrodes, demonstrating the the PSD noise level of the electrodes used for this study do not limit the quality of the recorded ERG signals.

Now we can use the Jonhson-Nyquist noise theory explained in section 1.3.4 to understand the differences in the power signals shown in Figure 2.18. From Equation 1.17, one could expect that the impedance difference between the three studied ERG electrodes (Figure 2.18, Top) would translate into a power difference. However, as the PSD shown in Figure 2.18 reveals this is not the case for all 3 electrodes. It is true that the impedance difference between the graphene μE and the graphene macroE translates into a power difference; however, there is no difference between the gold electrode and the graphene macroE, despite their impedance being more than two orders of magnitude apart. If we use Equation 1.17 to calculate the RMS voltage noise we get 4.9, 1.8 and 1.4 μV for the graphene μE, the graphene macroE and the commercial gold electrode, respectively. We have to be aware that Equation 1.17 relates the RMS voltage noise with the real part of the impedance, while Figure 2.18 displays the module. However, since all 3 electrodes have the same impedance phase, the real part of the impedance represents roughly the same proportion of the impedance module for all of them.

We attribute this inconsistency between what we expect from the Johnson-Nyquist theory and what we measure in our noise baselines to the contribution of the floor noise of the recording electronic setup. Since the noise and the impedance of our electrodes are low enough, the floor noise of the recording setup becomes the limiting factor. So, in our case, the higher impedance of the macroE probe does not translate into a noise increment and does not hamper the quality of the ERG signal; at the same time, the macroE probe offers important advantages in terms of flexibility and transparency.

2.3.3 ERG recordings

We benchmarked the capabilities of the graphene macroE to record ERGs against the commercial gold electrode by following the photoreceptor degeneration in a retinitis pigmentosa animal model. Retinitis pigmentosa is a degenerative disease that causes the loss of photoreceptor cells in the retina producing night blindness and a progressive loss of the visual field. Affecting 1 in 4000 people, retinitis pigmentosa has its onset in childhood, it is generally inherited from the progenitors and involves mutation in at least one of more than 50 identified genes [164].

As an animal model, we chose the heterozygous P23H rat model. It is one of the most common retinitis pigmentosa models and it was developed by introducing a mutated rhodopsin gene on a Sprague Dawley wild-type rat [165, 166, 167]. The P23H genotype has been fully characterized [168] and heterozygous animals show a significantly slower photoreceptor degeneration than the homozygous type.

For this study, we took full field ERG (ffERG) under scotopic and photopic conditions in order the study the function of rod and cone photoreceptors respectively [169]. We choose animals 1, 2, 3, 5 and 7 months old in order to study the progressive photoreceptor degeneration. These animals were generated by cross breeding homozygous transgenic P23H rats[22] with wild-type Sprague Dawley rat[23]. The animals were housed in a controlled environment and kept in the dark for at least 8 hours before the ERG recordings. When handling was necessary it was done under red light conditions to maintain the dark adaptation. For the experiments the animals were anesthetized using a mix of ketamine and medetomidine. A detailed description of the housing conditions and the anesthetic protocol can be found in Appendix E.1.

After the anaesthesia the animal was placed in a faraday cage and the ground and reference electrodes were inserted in the back and the forehead, respectively [162]. The commercial gold electrode was placed covering the left cornea of the animals, the graphene macroE was placed on the right cornea and both electrodes were covered with ocular gel[24]. For the light stimulation we used a Ganzfeld stimulus generator[25], to comply with the ISCEV guidelines on ffERG recordings [170]. The data was acquired using the Espion software and processed with a custom Python 3.6 code with the Neo [144] and PhyREC libraries. We maintained eye hydration during the ERG recording by using ocular gel.

[22] Matthew LaVail Laboratory, USCF School of Medicine
[23] Janvier Labs, France
[24] Dechra Pharmaceuticals
[25] ColorDome Binocular Flash Stimulator, Diagnosys

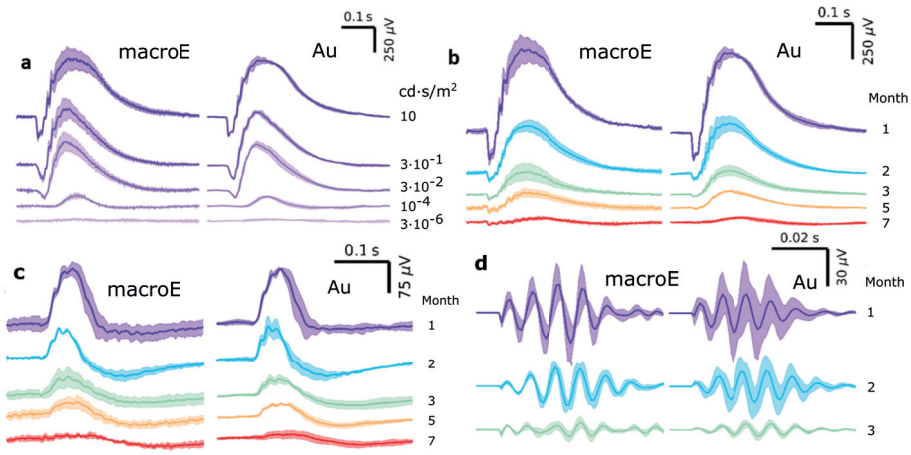

Figure 2.19: ERG recording comparison between the graphene macroE and a commercial gold electrode - Comparison of the ERG recordings between the graphene macroE and a commercial gold electrode on P23H degenerating rats under scotopic and photopic conditions. The results are the averages over 4 different animals, represented by the solid line. The shaded area represents the standard deviation of each measurement. a) ERG recorded under different stimulation intensities (ranging from 10 to $3 \cdot 10^{-6}$ cd $\cdot$ s/m²) in 27 days old rats under scotopic conditions. b) ERG recorded in animals of different ages using a stimulation of 10 cd $\cdot$ s/m² under scotopic conditions. c) ERG recorded in animals of different ages with a stimulation of 10 cd $\cdot$ s/m² under photopic conditions. d) Oscillatory Potentials (OPS) under scotopic conditions for animals 1, 2 and 3 months old.

For the scotopic recordings we used white light with an intensity of $3 \cdot 10^{-6}$, $3 \cdot 10^{-5}$, 10^{-4}, 0.03, 0.3, 3, and 10 cd $\cdot$ s/ m^2. We perform 5 flashes of each intensity with a duration of 4 ms and a rest period of 20 seconds between flashes to maintain the dark adaptation. For the photopic conditions we had to adapt the animals to light, which was done by a 5 minute exposure to a 20 cd $\cdot$ s/ m^2 white light intensity. After the light adaptation, we delivered 10 flashes with a light intensity of 10 cd $\cdot$ s/ m^2, a duration of 4 seconds and a 30 second rest period between flashes. All this protocol followed the ISCEV guidelines and it was performed using a commercial ERG system approved for clinical use[26]. The results obtained during these measurements are presented in Figure 2.19. The solid lines represent the average value obtained over 4 different animals and the shaded region denotes the standard deviation of the data set.

Figure 2.19a shows the ERG recorded on the youngest animals, 1 month of age, under scotopic conditions and different stimulation intensities and for both the graphene macroE (left) and the gold electrode (right). Since these animals

[26] E3 Desktop, Diagnosys

are too young to show evident signs of photoreceptor loss, their ERGs are quite similar to those of healthy animals (the ERG of a healthy animal is shown, for example, in Figure 2.21b. The amplitude of the a-wave and the b-wave decreases with decreasing stimulation intensity. For an intensity of 10^{-4} cd $\cdot$ s/ m^2 the a-wave completely disappears and for intensities of $3 \cdot 10^{-6}$ cd $\cdot$ s/ m^2 we got a completely flat response. The signal-to-noise ratio (SNR) reaches a value of 45 for both the gold and the graphene macroelectrode for the highest stimulation intensity.

Figure 2.19b shows the degeneration of the photoreceptors at increasing animal age measured with the graphene macroE (left) and the gold electrode (right). The light stimulation intensity is fixed at 10 cd $\cdot$ s/ m^2. For the 1 month old animals the signal is quite similar to that of a healthy animal, as already discussed, however, at 2 months of age we can already appreciate a significant amplitude reduction of both the a- and the b- waves. The degeneration progresses with time, leading to a complete disappearance of the a-wave at 5 months of age and an almost flat response for 7 months old animals. If we quantify the degeneration, comparing it to the youngest animals, we see that at 2 months of age both gold and graphene electrodes reveal a reduction in the a-wave of 75 % (from -165 to -35 µV in average). For the b-wave, the degeneration is slightly smaller, both electrodes reveal the same amplitude reduction: 55 % (from 800 to 360 µV). We can also note that the b-wave latency of the oldest animal (7 months) suffers a delay of 40 ms in average compared to that of the youngest animal (1 month). Again, the same b-wave latency delay is detected with both electrodes.

We can also compare the performance of the two electrodes under photopic conditions. Figure 2.19c shows the ERG recordings of increasingly old animals at said conditions. It can be observed that, due to light adaptation and the low cone population in the rat retina, the a-wave is missing even in the youngest animals (1 month). Regarding the b-wave, it shows an amplitude decrease associated with the photorecptor loss: 40 % decrease in average at month 2 and an almost flat response at 7 months of age. Again, both electrodes show the same behaviour.

By bandpass filtering the ERG signal from the three youngest animals (1, 2 and 3 months) in Figure 2.19b between 100 and 150 Hz, we can visualize the OPS. (see Figure 2.19d). These OPS also reveal the retinal degeneration. Taking the third maximun of the OPS as a reference, from month 1 to month 2 we can observe a 10 millisecond increment in latency and a mild reduction in signal amplitude, from 38 to 28 μV. If we compare month 2 to month 3, the degeneration progresses; despite the latency remaining mostly constant, there

is an important decrease in the signal amplitude, making the OPS completely disappear from 5 months on.

An important difference of the OPS in Figure 2.19d from the rest of the data presented in the same figure is that, for the youngest animal, there appears to be an amplitude difference between the gold electrode and the graphene macroE, with 31 and 45 µV peak to peak signal amplitude, respectively. However, if we run a significance test, we find out there is no actual statistical difference between both measurement populations. This is due to the large standard deviation on the the OPS recorded with the commercial gold electrode, caused by one of the signals being particularly low. Quantitatively, the t-test gives a p = 0.55, the analysis was performed with a custom Python 3.6 code using the stats.ttest_ind() function from the Scipy library.

Figure 2.19 indicates that the standard deviation of the ERG measured with the graphene macroE is always bigger than that of the commercial gold electrode, with the exception of the OPS we discussed before. This fact is particularly evident on the scotopic b-wave shown in Figure 2.19a and b. Since there is no apparent difference in the noise power from these two electrodes, as already shown in Figure 2.18b, a possible explanation for this could be the difference in size between these electrodes. The gold electrode is considerably bigger than the graphene macroE (3 mm vs 1 mm) and, consequently, it is easier to be placed in the same place across different animals. Differences in electrode positioning might results in ERG measurements with bigger uncertainty, as we will discuss further in section 2.3.4.

Figure 2.20 and Table 2.1 summarize the effect of the photoreceptor degeneration, shown by the amplitude of the a-wave and the b-wave in scotopic conditions and the photopic b-wave. As discussed before, all waves show a progressive degeneration with age. The b-waves recorded at 1 month of age show an amplitude of around 800 μV for scotopic conditions and around 140 μV for photopic conditions and they decay progressively until month 7, where they reach values of 50 μV for scotopic and 10 μV for photopic conditions. The amplitude reduction of the scotopic a-wave is even quicker, it starts with an amplitude of around 160 μV at 1 month of age and completely disappears at month 3.

$$Amp(t) = Amp_{max} e^{-\frac{t}{\tau}} + Amp_{min} \tag{2.2}$$

If we fit the data from Table 2.1 to an exponential decay function (Equation 2.2), we can obtain the decay rates (τ) for the scotopic a-wave and b-wave and the photopic b-wave for the macroE and the Au electrode, as represented by the solid lines in Figure 2.20. The τ values yielded by the fit for scotopic a-wave are

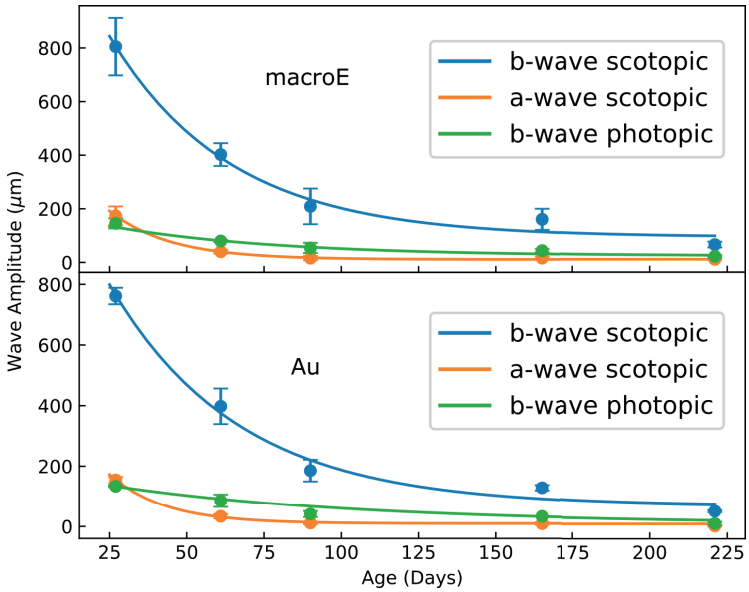

Figure 2.20: Summary of experiments on photoreceptor degeneration - Maximum amplitude of the scotopic a-wave and b-wave and photopic b-wave recorded with the graphene macroE (top) and a commercial Au electrode (bottom) with a stimulation intensity of 10 cd · s/m². The circles represent an average for all animals and the error bars the standard deviation. The solid lines are the fitting of Equation 2.2 to each data set. For convenience, the absolute value of the a-wave is presented.

n = 20		1 month		2 months		3 months		5 months		7 months	
		Amp	Lat	Amp	Lat	Amp	Lat	Amp	Lat	Amp	Lat
a-wave	macroE	-170	10	-40	11	-16	11	-31	11	-21	11
	Au	-150	10	-34	9	-12	11	-7	16	-3	20
b-wave	macroE	810	110	360	100	190	110	150	110	55	160
	Au	760	110	370	100	170	110	120	100	37	140
b-wave Photopic	macroE	150	65	70	51	44	60	32	65	12	75
	Au	130	62	80	50	37	60	30	64	9.2	65

Table 2.1: Summary of ERG parameters recorded for the retinal degeneration - Sum up of the amplitude and the latency of the scotopic a-wave and b- wave and the photopic b-wave with a stimulation intensity of 10 cd · s/m². The amplitude has units of μV and the latency of ms.

p value (n = 20)	1 month	2 months	3 months	5 months	7 months
a-wave	0.570	0.034	0.335	0.005	0.023
b-wave	0.765	0.972	0.460	0.480	0.085
b-wave Photopic	0.673	0.467	0.251	0.675	0.077

Table 2.2: Statistical significance of the retinitis pigmentosa study - Results of the statistical significance study comparing the amplitude of the scotopic a-wave and b-wave and the photopic b-wave for all ages with a stimulation intensity of 10 $\mathrm{cd} \cdot \mathrm{s/m^2}$.

$17.7 \pm 2.5\ day^{-1}$ and $19.6 \pm 2.4\ day^{-1}$ for the gold electrode and the macroE probe respectively, meanwhile for the scotopic b-wave are $41.7 \pm 7.7\ day^{-1}$ and $\pm\ 7\ day^{-1}$ respectively. Under photopic conditions the τ values are somewhat different at first sight, $81 \pm 55\ day^{-1}$ for the gold electrode and $54.3 \pm 28\ day^{-1}$ for the macroE probe. However, since the standard error of both constant is large enough, both values are still in good agreement.

Table 2.2 shows the results of the significance analysis performed for animals of 1, 2, 3, 5 and 7 months old under scotopic and photopic conditions and a stimulation intensity of 10 $m^2/\mathrm{cd} \cdot \mathrm{s}$. The analysis was performed with GraphPad Prism using a paired student t-test. We find that there are no statistical differences between the amplitude of the b-wave under scotopic or photopic conditions when they are recorded with the commercial gold electrode or the graphene macroE ($p < 0.025$). However, there are statistical differences between the scotopic a-wave when recorded with the two electrodes under study. The data from Table 2.2 indicates that for months 5 ($p = 0.005$) and 7 ($p = 0.023$), the differences between the scotopic a-wave recorded with the commercial gold electrode and the graphene macroE are statistically significant ($p < 0.025$). These statistically different values are due to the fact that the a-wave disappears for P23H rats older than 5 months.[168]. Then, in our measurements, the ERG recorded at those ages are mainly stochastic electrical noise of the recording system that has no correlation across trials.

Altogether, the results we present here confirm the suitability of SLG electrodes to record electroretinograms. While the graphene macroE is transparent, flexible and smaller than the commercial gold electrode, it allows for faithful ERG recordings that accurately reflect the photoreceptor degeneration on a retinitis pigmentosa P23H rat model, exhibiting comparable SNR to the commercial gold electrode.

2.3.4 MEA Recordings

As stated before, one of the main advantages of using graphene as an active material for the fabrication of ERG electrodes is its transparency, which allow the fabrication of ERG recording MEAs. These MEAs are able to perform multisite recordings of the whole corneal surface without blocking the delivered light stimulus. It has been already suggest that the signals from multiple-site ERG recordings have the potential to provide information about local retinal deficiencies [162].

The current state of the art to obtain local information about the electrical activity of the retina is multifocal ERG (mf-ERG). It is used in patients that have poor vision but a normal appearing retina and that have extinguished the diagnosis capabilities of Ganzfeld ERGs. mfERG is able, among others, to discriminate between optic-nerve and retinal damage [171]. mfERG is performed by showing variable patterns in a screen with a duration of 10 ms and recording the whole retinal response with a single macroscopic electrode, such as those discussed in section 2.3.1. Then, a software reconstructs the response of the different retinal segments so it can be compared to a normal population in order to spot retinal deficiencies. For the particular case of retinitis pigmentosa, even when Ganzfeld ERG may be nonrecordable in the late stages of degeneration, researchers have been able to obtain mfERG responses [171].

Because mfERG is a relatively long test, takes almost half an hour to complete for both eyes, the procedure requires the patient to remain still for the whole duration of the measurement. This makes mfERG difficult to perform in young children or patients with involuntary tremors, such as Parkinsons´. By using MEA ERG, topographical information of the retina can be extracted with only one stimulation flash [162, 161]. This could potentially allow physicians to get information from different retinal regions in shorter recording session, increasing the patient comfort.

To demonstrate the capabilities of graphene-based MEA ERG devices, we fabricated transparent MEA ERG probes with two different designs. A detailed description of these devices have been provided in section 2.3.2 and in Figure 2.16b, c and d. Figure 2.21 shows different ERG recordings acquired with MEAs, using the same recording electronics we used for the noise characterization of the devices. The recording were acquaired with the OpenEphys GUI software and processed with a custom Python 3.6 code using the Neo [144] and PhyREC libraries. These ERG were recorded on healthy animals, under a stimulation intensity of 10 $\mathrm{cd \cdot s/m^2}$ and averaged over 20 flashes. In this way, the SNR of Figure 2.21 can be directly compared with that from the youngest animals

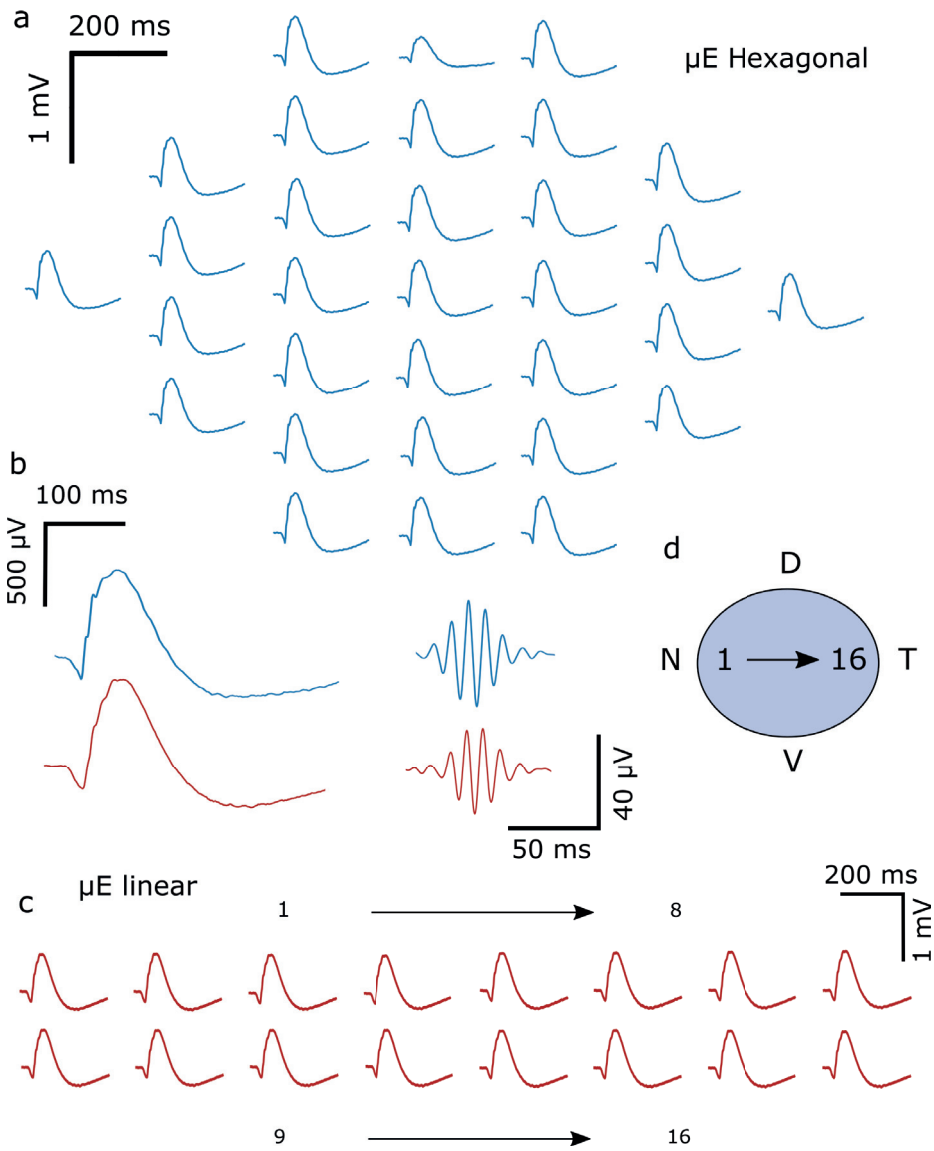

Figure 2.21: ERG Recordings with transparent graphene MEA probes - a) Mapping of the corneal potential performed with the μE Hexagonal MEA. The distribution of the signals in the figure corresponds with the position of the electrodes on top of the cornea. b) Close-up of representative ERG signals measured with the μE Hexagonal probe (blue) and the μE_Linear probe (red). Also shown OPS signals acquired applying an additional bandpass filter between 100 and 150 Hz. c) Mapping of the corneal potential performed with the μE_Linear MEA; the schematic in d) indicates the position of the electrodes on the cornea. Electrodes number 1 and 16 are in the nasal and temporal position respectively. Data shown is an average of 20 flashed at 10 cds/m^2 stimulation intensity under scotopic conditions and filtered between 0.5 and 300 Hz.

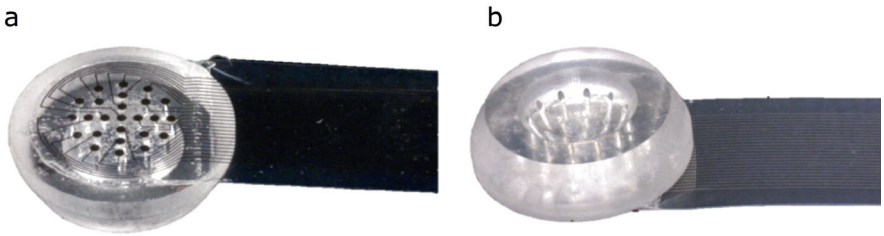

Figure 2.22: PDMS-well ERG MEA - Contact Lens Electrode Array (CLEAr Lens) used for MEA ERG recordings. a) Distal and b) corneal side of lens. Source: [161]

shown in Figure 2.19. Figure 2.21a shows a mapping of the corneal potential recorded with the μE Hexagonal MEA. The position of the signals in the figure corresponds with the location of the electrodes on the corneal surface. Figure 2.21c, on the other hand, shows the ERG recordings obtained with the linear μE linear array, positioned on the cornea following the nasal-temporal direction, as schematically depicted in the inset of Figure 2.21d. Figure 2.21b is a close up of 2 ERGs recorded by the μE Hexagonal probe (in red) and the μE linear probe (in blue). Band-pass filtering the signals between 100 and 150 Hz allow us to see the OPS, proving that all ERG features can be perfectly captured using our transparent graphene MEAs.

MEA ERG recordings have been previously used to characterize spatial differences on the corneal potential [161] or to locate induced injuries on the retina [162]. In these studies, the size and density of the electrodes was limited by the opacity of the electrodes material. This opacity meant that the electrodes cast shadows on the retina that, in some cases, blocked up to 35% of the stimulation flash [161]. Another problem of the electrodes used in these previous studies is the electrode placement. In other to minimize the diffraction pattern caused by the electrodes, the researchers had to use an intricate PDMS well system to place the electrodes further away, such as that shown in Figure 2.22.

To overcome these limitations, we set out to use our transparent MEA ERG to detect retinal lesions. For that purpose, we induced lesions on the temporal-ventral retinal quadrant of 10 Long Evans rats using a laser pulse with 500 mW power and 100 ms duration. Prior to the procedure, the animals were anesthetized following the same protocol described for the ERG recordings (60 mg/kg ketamine and 0.4 mg/kg Domitor). After the procedure, the animals were allowed to recover for at least 7 days and then we measured the ERG following the procedure discussed previously for MEA ERG recordings. In a first set of experiments, we used the

first generation 16-electrode MEA to measure the ERG of the animals before and after the injury. However, and possibly due to the small size of the probe compared to the size of the animal´s eye, we were only able to see a generalized amplitude reduction in all the electrodes. That problem led us to repeat the lesion experiment using the second generation of ERG MEA.

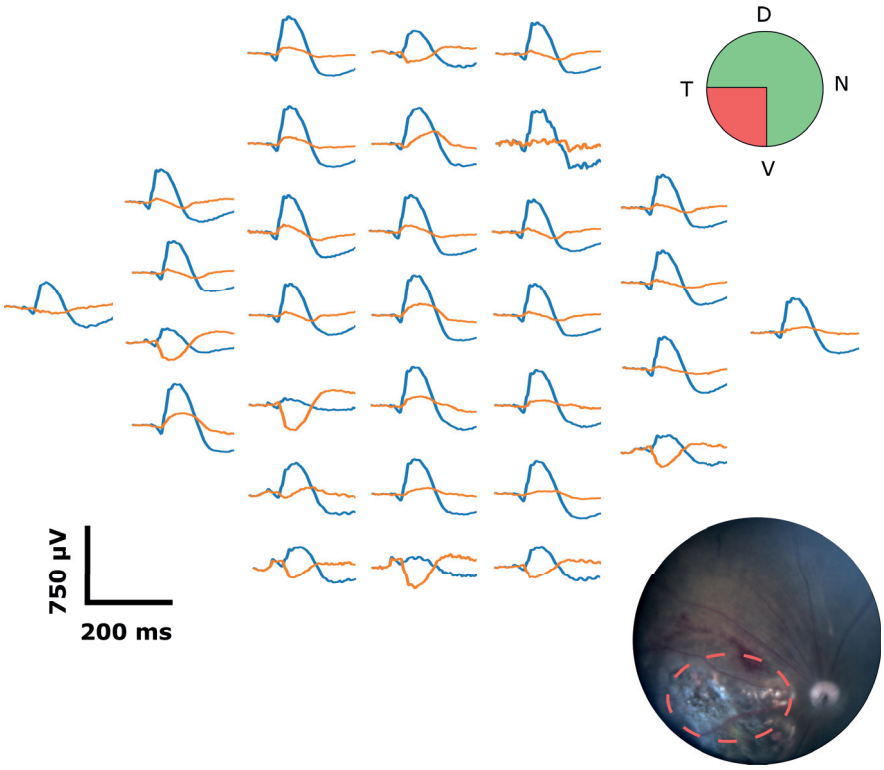

Figure 2.23: Injury study with MEA ERG - MEA ERG of a rat with an induced retinal lesion taken with the 31-electrode MEA. The blue trace represents the ERG signal measured by each electrode. The orange signal represents the subtraction of the ERG signal measured by each electrodes from the average signal of all electrodes. A picture of the retina with the induced lesion in the temporal-ventral quadrant is also shown, with the injured region marked in red. Data shown is an average of 20 flashed at 10 cds/m^2 stimulation intensity under scotopic conditions and filtered between 0.5 and 300 Hz.

The data obtained from these experiments is presented in Figure 2.23. The blue traces shows the ERG recordings obtained with the μE Hexagonal probe from an animal with a retinal lesion, measured under scotopic conditions, averaged from 20 flashes of 10 c $\cdot$ ds/m^2 intensity and band-pass filtered between 0.5 and 300 Hz. In order to highlight the differences across electrodes, we have subtracted the ERG signal recorded with each electrode from the averaged signal of all electrodes, plotted in orange and referred to as "subtracted signal". This means

that a flat subtracted signal shows that the recording of that particular electrode is similar to the average ERG signal. A large subtracted signal shows that that electrode records a signal that is quite different from the average. If the subtracted signal has a positive b-wave, it means that the signal recorded by that particular electrode is larger than the average, and the opposite if the b-wave is negative. With this criteria in mind, we can see that the majority of the high amplitude, inverted subtracted signals, that account for lower than average ERG recordings, accumulate in the lower left part of the plot, which corresponds with the lesion location on the temporal-ventral quadrant of the retina.

In the results presented in Figure 2.23 we are able to match the position of the injury with the area that has the lowest ERG amplitudes, but that is not always the case. For many animals, the variability in the injury position, shape and size (with up to a 65 % variation in area), together with the intrinsic variability of the ERG signals, the lack of a well developed method to position the probe in a reproducible way and the small nature of the ERG signals (reported to be around 3% by some simulation works [172]) made impossible to consistently infer the position of the injury from the ERG data.

2.4 Conclusions

In this chapter we have shown the capabilities of our rigid SLG MEA to record *in vitro* electrophysiological signals. We have characterized the devices in terms of Impedance Spectroscopy and V_{RMS} noise power, showing that the electrodes have an almost purely capacitive behaviour and how that behaviour translates into a low V_{RMS} noise. From there, we have proven that the electrodes are suitable to detect electrophysiological signals simulated by a signal generator connected in series to the reference electrode. Additionally, we have demonstrated that our rigid SLG MEA is compatible with cortical neuron cultures, allowing for the development of a healthy network and for the recording of spontaneous synchronized activity and the identification of different spikes shaped that are link to different active areas. Furthermore, the low noise of the recorded activity allows us to use a relatively primitive feature extraction method, such as the duration and amplitude method, that only yield good results in recordings with high SNR [173]. The studies shown in section 2.2 also served to assess whether the rigid SLG MEA are a viable platform for neural guidance experiments, that will be discussed in detail on Chapter 4.

In order to expand the capabilities of electroretinography, the next generation of ERG recording electrodes should fulfil precise requisites. Due to the sensitive nature of the cornea, ERG recording electrodes have to be chemically inert

in contact with biological tissue and flexible enough so they can conform to the hemispherical eye surface, ensuring a good electrical coupling, without mechanically damaging it. Also, the ERG recording electrodes have to be sensitive enough to detect the changes in potential produced by the retina, sometimes in the range of tens of microvolts. Furthermore, the ERG electrodes should ideally be transparent, in order to provide maximum flexibility in the device design, allowing for the fabrication of MEA. Given this particular set of requirements, graphene is very attractive for the fabrication of ERG recording electrodes.

In the study shown in section 2.3, we have benchmarked the performance of our soft and transparent graphene electrodes against the current state of the art electrodes for ERG recording in animals. To do so, we have used a commercially available clinical setup to follow up the photoreceptor degeneration in a P23H animal model. We have observed drastic vision loss after 2 months of age, denoted by an amplitude reduction of all the characteristic features of the ERG using both the commercial gold electrode and our graphene macro electrode. We have also confirmed that the signals recorded by both electrodes are not statistically different, proving that our flexible and transparent graphene electrodes are perfectly suited to diagnose a photoreceptor degeneration.

In addition, we have exploited the transparency of graphene to fabricate MEA. This transparent probes allow us to perform multisite ERG recordings and have the potential to extract topographical information of the corneal potential, they are also able to capture with fidelity the characteristic features of an ERG signal, such as the a- and b- waves and the OPS. In this section we have also used our MEA ERG to detect induced retinal lesions, although an amalgam of factors, including the lack of a well develop method to position the MEAs, the variability in injury size and position and the intrinsic variability of the ERG signals, have prevented us from obtaining conclusive results. More work needs to be devoted in order to make the most of this new tool. In particular, the use of novel MEA encapsulation materials with viscoelastic properties [174] could help to achieve more accurate device positioning and accurate simulations [172] could assist in the location of retinal injuries using the electrical information provided by the MEAs.

Altogether, our results indicate that graphene is an excellent candidate for the fabrication of ERG recording electrodes. Its sensing capabilities, together with its chemical stability, flexibility and transparency, provide new possibilities to explore aspects of electroretinography that have remained unexploited until now.

3

Reduced Graphene Oxide MEA

"I miss my dark science budget"
"What the hell is dark science?"
"It´s basically science ... but darker"

Dr. Krieger and Ray Archer

This chapter provides an overview of the work done with reduced graphene oxide (rGO) electrodes. First, we introduce the fabrication of the material and its integration into microfabricated MEAs. Then, we discuss the characterization of the fabricated electrodes in terms of interfacial impedance, voltage noise and charge injection. Finally, in order to explore the capabilities of the rGO MEA, we use them to bidirectionally interface hippocampal neuron cultures.

3.1 Device fabrication

This section describes the fabrication of the rGO MEAs, including the preparation of the rGO films, their transfer to target substrates and the microfabrication processes involved in the production of the finished device.

3.1.1 rGO film preparation

GO is generally obtained by chemical oxidation of naturally occurring flake graphite [175]. Before the oxidation process, the flake graphite is purified in order to remove contamination by other elements [176]. The abundance of defects in the graphite π-structure serve as reaction points for the oxidation [177, 178] process, yielding a dispersion of hydrophilic GO flakes in the solvent used for the oxidation. The size of the obtained flakes ranges from the tens of nanometers to the tens of microns; GO flakes can be easily dispersed in water [179], which have led to GO/water solutions being commercially available from many sources and at an affordable price [180, 181]. In order to use the GO dispersion in certain applications it is necessary to remove the water. Two of the most common methods to do so are evaporation via spray drying [182, 183] and filtration [184, 185]. Spray drying consist in spraying the GO solution in a high temperature environment so that only the solute remains. Filtration, on the other hand, works by forcing the GO solution, normally with vacuum, through a membrane whose pores are smaller than the GO flakes so they are captured by the membrane. We choose filtration because of this method facilitates a stacking of flakes almost parallel to each other and allows to control the thickness of the GO layer by changing the volume of solution that is filtrated; finally, it can be scaled for industrial production [186, 187].

For our fabrication we used a commercially available 10 g/L GO solution in water[1], which we diluted in DI water to 0.5 g/L to facilitate its manipulation. The flakes present in this solution are 500 nm wide (average x-y lateral dimension) and 1-1.2 nm thick (average z-dimension)[188]. We choose these flakes for their small size, since it maximizes the amount of edges per unit area; it has been reported that the density of states is higher in the edges [189, 190], which in turn is expected to facilitate the adsorption of ions and thus to increase the double layer capacitance of the fabricated film [191]. To filter the GO solution we used two different types of membranes, depending on the type of transfer procedure. Nitrocellulose membranes[2] with a pore size of 20 nm were used in processes that required dry transfer. On the other hand, alumina membranes[3] with a pore size of 25 nm were used for wet transfer processes. Both membranes yielded circular GO films of 35 mm diameter. For the filtration, the membranes were placed in a kitasato (Figure 3.1b) connected to a filtration pump, we poured 40 mL of 0.5 g/L GO solution and run the filtration pump for a minimum of 5 hours. After the solution was completely filtered, the membranes were dried in a hotplate at 40

[1] N002-PS-1.0 Aqueous Nano Graphene Oxide Platelets, Angstron Materials
[2] Anodisc 47, Whatman
[3] VSWP04700, MF-Millipore

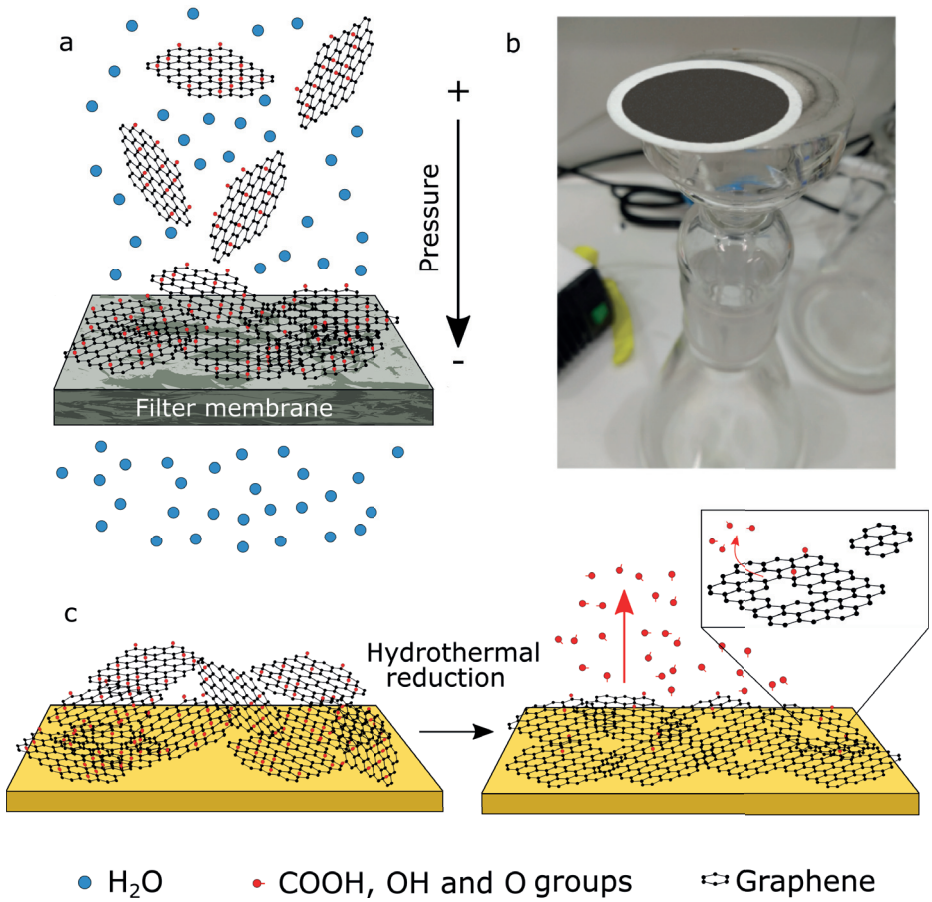

Figure 3.1: rGO fabrication - a) The solution containing GO flakes is filtered using a filter membrane and a kitasato, shown in b). c) The stack of filtered GO flakes is transferred to the target substrate and hydrothermally reduced, eliminating oxygen groups and opening nanometer sized pores on the flakes.

ºC for 5 minutes. Figure 3.1a shows a schematic representation of the filtration process.

The GO flakes contain high quantities of oxygen functional groups, like hydroxyl and epoxide in the basal plane and carbonyl and carboxyl groups on the edges [192]. These groups make GO a versatile material for many applications, since multiple functionalizations can be made using these groups as anchor sites. However, the presence of these oxygen groups yields the GO electrically isolating, that is why in order to use it for electronic applications it is necessary to eliminate them with a reduction process.

Although almost intact graphene has been obtained from carefully reducing low defect GO [193], the restoration of the graphene lattice is normally not

achieved [187]. During the reduction process, the color of the material changes from brown to black and holes can appear in the GO flakes [194] that, depending on the application, can be useful.

A variety of methods are used to reduce graphene oxide. Chemical reduction uses chemical compounds, like hydrazine, that react with the oxygen functional groups present in the GO [195, 196, 197, 198]. In electrochemical reduction, electrons are supplied to a solution containing GO, breaking the oxygen covalent bonds and releasing it into the solution [199, 200, 201]. The elctrochemical reduction method is particularly interesting because, unlike chemical reduction, it does not involve the use of harmful chemicals. In addition, since the reduction of the GO mainly takes places in the surface of the electrodes used for the electrochemical reaction, it is attractive in the case of battery and supercapacitor applications. Another type of reduction is the hydrothermal reduction which exploits the fact that subcritical water can react with the oxygen groups present in the graphene oxide, releasing many of them [202, 203, 204, 205]. During this hydrothermal reduction process applied to our GO films, the distance between the GO layers decreases and nanometer size pores are created in the flakes [206, 13]. Hydrothermal reduction is environmentally friendly, simple and cost effective; in addition, this reduction method can open pores more efficiently, which is particularly interesting for the fabrication of neural electrodes, since it achieves high capacitance and low impedance. Those reasons lead us to use hydrothermally reduced GO for the fabrication of our electrodes.

After the hydrothermal reduction process, we achieved a 1.6 μm thick film, composed of horizontally stacked flakes of graphene oxide with a interplanar distance of 4 Åand nanometer sized pores that connect the different planes [13]. The RMS roughness of the material is 55 nm over a 5 x 5 μm^2 area, approximately the area of a neuron. Furthermore, after the reduction the resistivity of the material was found to decrease from 66 k$\Omega \cdot$ cm to 0.2 $\Omega \cdot$ cm and the carbon to oxygen ratio increased from 0.57 to 1.22. All the characterization described here was done in a previous PhD work in our group and more information can be found in [13]. Figure 3.1c shows a schematic representation of the hydrothermal reduction process.

3.1.2 GO film transfer

In order to use the GO for the fabrication of electrodes, it is necessary to detached it from the filtration membrane and transfer it to a suitable substrate on which we can perform the rest of the photolitographic fabrication. In this thesis we use rigid borosilicate substrates, however, it is also possible to perform the same transfer to

flexible PI substrates, like those employed in section 2.3.2, to fabricate completely flexible devices. For the fabrication process used in this thesis, the GO films are transferred on top of a Ti/Au (20/200 nm) layer evaporated on top of a borosilicate substrate. To improve the adhesion we introduce a self-assembled monolayer (SAM) functionalization (Hydrazide-PEGx-Thiol MW:2000Da [4]) between the GO film and the gold substrate, a standard procedure to improve the attachment between surfaces in microfabrication [207, 208, 209]. The SAM used in this thesis have a thiol group in one end, that covalently bonds to the gold substrate, and a hydrazide in the other, that creates covalent bonds with the hydroxyl groups from the GO [210, 211, 212, 213]. In order to maximize the electrical conductivity between the gold substrate and the GO film, the molecular chain that connects the thiol to the hydrazide in the SAM was chosen as short as possible [214].

During this thesis we used two different transfer methods: dry and wet transfer. The dry transfer of the GO film was the first approach we explored; however, as our technology progressed and with the goal to improve reproducibility and electrode yield, we developed a wet transfer method. Both methods share the same SAM functionalization strategy detailed above.

3.1.2.1 Dry transfer

The first method we used was a dry transfer method that relied on a conventional roll-to-roll technique [215], where pressure is used to attach the membrane to the target substrate. For this method, as stated before, a nitrocellulose filtering membrane was used.

To do so, the membrane was placed with he GO film facing to the target substrate and a tissue damp with DI water was applied to the back of the membrane. Once the membrane was uniformly damp, the tissue was removed and the membrane was blown dry with nitrogen. When blowing dry, the water trapped between the membrane and the first layer of GO pushes the GO film, detaching it from the membrane. Then the membrane is pressed along different directions with a roller press in order to homogenize and flatten the GO film. Finally, the filtration membrane is carefully peeled away, leaving the GO film attached to the gold substrate. The whole dry transfer process is depicted in Figure 3.2.

The main problem with this transfer method is that it has a poor reproducibility and is difficult to optimize, since the wetting, drying and pressing of the membrane are completely manual steps. Despite efforts being made to

[4] AWK1T1,Interchim Uptima

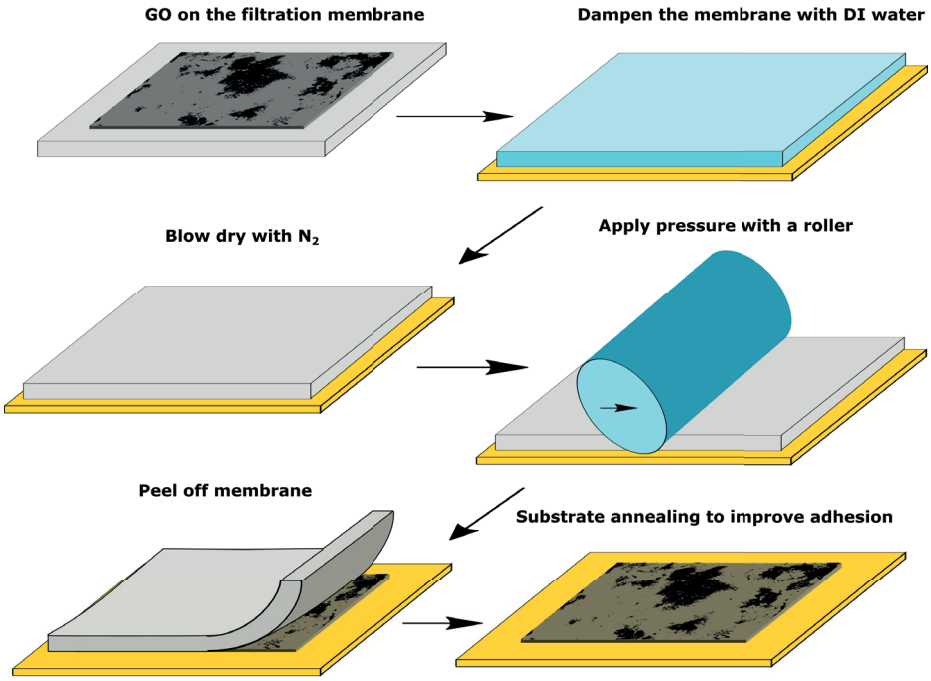

Figure 3.2: Dry Transfer method of GO films - Schematic representation of the steps involved in the dry transfer of GO films used in this thesis.

automatize and standardize the dry transfer, we finally decided to develop a completely different transfer method.

3.1.2.2 Wet transfer

For the wet transfer method, we used aluminum oxide based membranes[5]. When the filtration was complete and the GO film completely dry, it was possible to directly detach the GO film from the membrane. Once the GO film was peeled-off and carefully floated on a beaker with DI water, it was scooped from the beaker using the SAM-functionalized target substrate, paying attention not to form any wrinkles during the process. After that the substrate was placed on a hotplate at 60 ºC for 5 minutes, the temperature was ramped to 100 ºC at a rate of approximately 8 ºC/min and held at 100 ºC for another 5 minutes. The wet transfer process is depicted in Figure 3.3.

3.1.3 Wafer scale fabrication of rGO devices

To fabricate the rGO MEA used in this thesis, the GO film needs to be transferred to an appropriated substrate, cut in the shape of the electrodes, metal tracks need

[5]Anodisc 47, Whatman

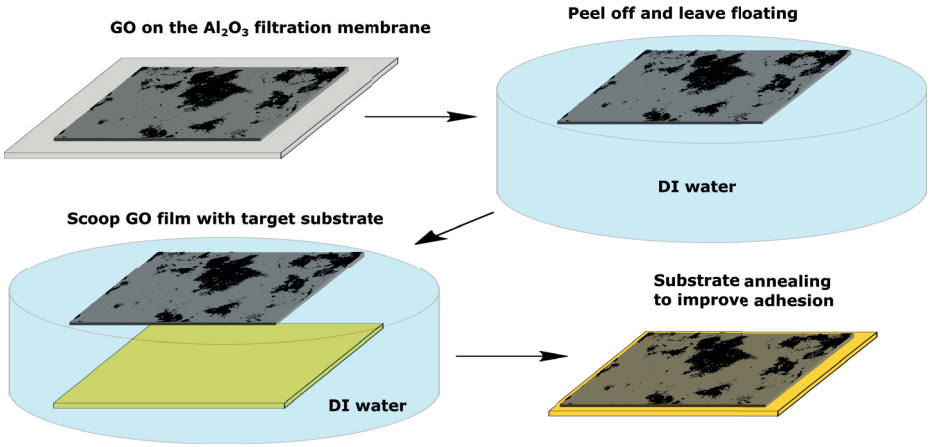

Figure 3.3: GO Wet Transfer - Schematic representation of the steps involved in the GO wet transfer method used in this thesis.

to be patterned and the MEA needs to be passivated, to ensure that only the rGO electrode active area is in contact with the electrolyte. Since the electrodes dimensions are in the order of the tens of micrometers, this whole process is made by using optical photolitography.

All the individual steps are depicted in Figure 3.4 and described below. A detailed description of the fabrication parameters used in each step can be found in Appendix C.2.

1. **Substrate metalization.** The metalization of the substrates serves two purposes. On the one hand, it acts as the substrate layer on which the thiol groups of the SAM are attached, improving the adhesion of the GO film. On the other hand, after being properly defined, it serves as the conductor between the electrode and the pad used to connect to the recording and stimulation setup. For this process we evaporate a layer of Ti/Au (20/200 nm) using and electron beam evaporator[6]. Shown in Figure 3.4b

2. **SAM functionalization.** To attach the SAM to the Au substrate, we first clean the Au using a ICP-RIE[7] process (150 W ICP, 150 W HF, 15 mTorr, 40 sccm O_2 and 1 minute duration). After that, we submerge the wafer in a solution containing 4 mg of SAM and 12 mL of ethanol for 12 hours, sealing the beaker with parafilm to prevent evaporation. Finally, we rinse the wafer with ethanol and blown dry with nitrogen.

3. **GO film transfer and partial reduction.** After we functionalize the substrate with the SAM, we transfer the GO film using one of the two

[6] ATC-8E Orion, AJA International
[7] PlasmaPro 100 Cobra, Oxford Instruments

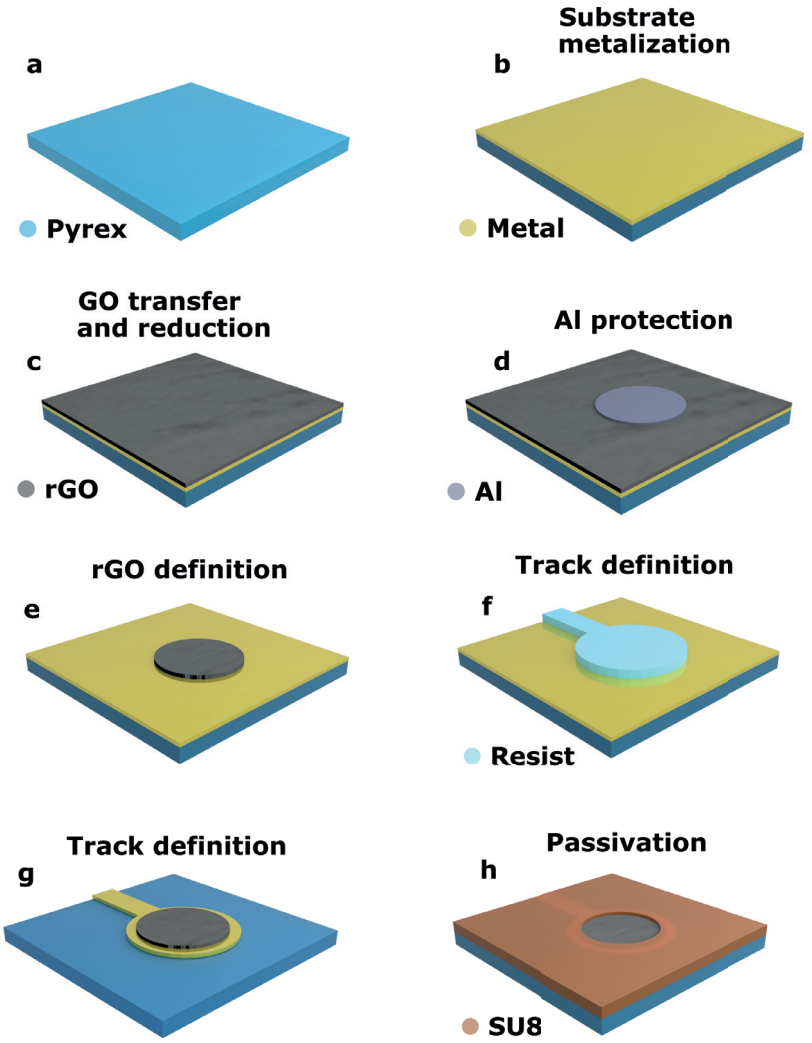

Figure 3.4: rGO Wafer scale fabrication - Main steps performed during the standard microfabrication of rGO MEAs: a) Bare pyrex substrate. b) Substrate metalization Ti/Au (20/200 nm). c) GO film transfer and partial reduction. d) Al protection. e) rGO definition. f) and g) Track definition. h) Passivation.

procedures described in 3.1.2. Then we partially reduce the GO film by introducing it in a commercial autoclave[8] at 134 ºC during 1 hour. This partial hydrothermal reduction ensures that the rGO is strong enough to withstand the photoligraphic processes while allowing us to define it using an ICP-RIE process. Shown in Figure 3.4c

4. **Al protection.** To create the mask to define the shape of the rGO electrodes, we use a thick negative resist[9] that covers the whole wafer but the electrode area. We then evaporate 60 nm of Al and perform a lift-off by immersing the wafer in a stripper[10] for at least 1 hour at 60 ºC. When the lift off is finished we are left with 60 nm Al discs that protect what will be the electrodes active area. Shown in Figure 3.4d

5. **rGO definition.** To etch the excess of rGO material, we perform an ICP-RIE etching step (15 W HF, 500 W ICP, 15 mTorr of pressure, 40 sccm of O_2 lasting 20 to 25 minutes). During this process the film is continuously monitored using a digital camera installed in the system. Once we have defined the rGO film, we remove the Al covering the electrodes by immersing the wafer in an aluminum etchant solution (74 ml H_3PO_4 + 2.5 ml HNO_3 + 23.5 ml DI water) at 60 ºC for 2 minutes. Finally, we introduce the wafer again in the autoclave at 134 ºC for 2 hours to complete the hydrothermal reduction. Shown in Figure 3.4e

6. **Track definition.** To define the metal tracks that connect the rGO electrodes to the recording and stimulation setup, we wet etch the Au/Ti metal layer. To do so, we protect the rGO and the areas of the metal we want to keep with a positive photoresist[11] and immerse the wafer in a Au etchant solution[12] for 50 seconds. After the Au has been etching, we rinse the wafer with DI water and submerge it into 10 % HF for 10 seconds to etch the Ti. Finally, the photoresist is removed with an acetone bath. Shown in Figures 3.4f and g

7. **Passivation.** In order to insulate the metal tracks and avoid that the electrolyte shortcuts the electrodes, we apply a 2.5 μm thick passivation layer using a permanent SU8 photoresist[13] covering all the device but the electrode´s active area. Shown in Figure 3.4h

[8] AH-21 N2, Raypa
[9] nLof 2070, Microchemicals GmbH
[10] TechniStrip NI555, Microchemicals GmbH
[11] HiPR 6512, Fujifilm
[12] Gold etchant 651818, Sigma-Aldrich
[13] SU8 2005, MicroChemicals GmbH

3.2 rGO MEA designs

For the *in vitro* neuron recordings with rGO MEAs, 2 different designs were used in this thesis.

The first design is the 60 electrode-hexagonal layout used for the rigid SLG recordings in section 2.2 and depicted in Figure 2.6. The only modification to that design is the ring contact between the metal and the SLG, which in the case of rGO electrodes is replaced by a complete back contact, to ensure better adhesion between the rGO and the metals.

The second design is depicted in Figure 3.5. It contains 60 electrodes distributed in 12 colums with 100 μm pitch and 6 rows with 200 μm pitch. The electrodes are grouped in structures of 5, such as the one showed on the top left part of Figure 3.5. The structures contain 3 circular electrodes of 25 μm diameter and 2 rectangular electrodes of 5 x 33 μm^2. They are arranged so they can fit the yJunction design of the PDMS structures used to guide neuronal growth, depicted in Figure 4.7 and that we will discuss in detail in section 4.4. Since these devices were to be used for simultaneous electrical recording, electrical stimulation and high resolution oil inverted microscopy, the MEA were fabricated on a 170 μm thick, 49 x 49 mm^2 borosilicate substrate[14]. In order to create the well for the cell culture, we glued a 24.5 mm inner diameter and 10 mm height metacrylate ring using a biocompatible epoxy[15]. Finally, and to improve the handling and the strength of the finished MEA, it was glued to a 49 x 49 mm^2 fiberglass holder with a 25 x 25 mm^2 square opening in the centre.

3.3 rGO electrochemical activation and characterization

After the fabrication, all rGO MEA devices are electrochemically activated and thoroughly characterized in terms of interfacial capacitance, voltage noise and charge injection, as discussed below.

3.3.1 rGO electrochemical activation and interfacial impedance

In order to achieve high charge injection capabilities and low interfacial impedance, it is common to perform a electrochemical activation in porous electrodes [216, 217]. This process is normally done by sweeping the electrode potential while

[14] W9QA0490490170 NNNNX1, Microchemicals GmbH
[15] 302-3M, Epo-Tek

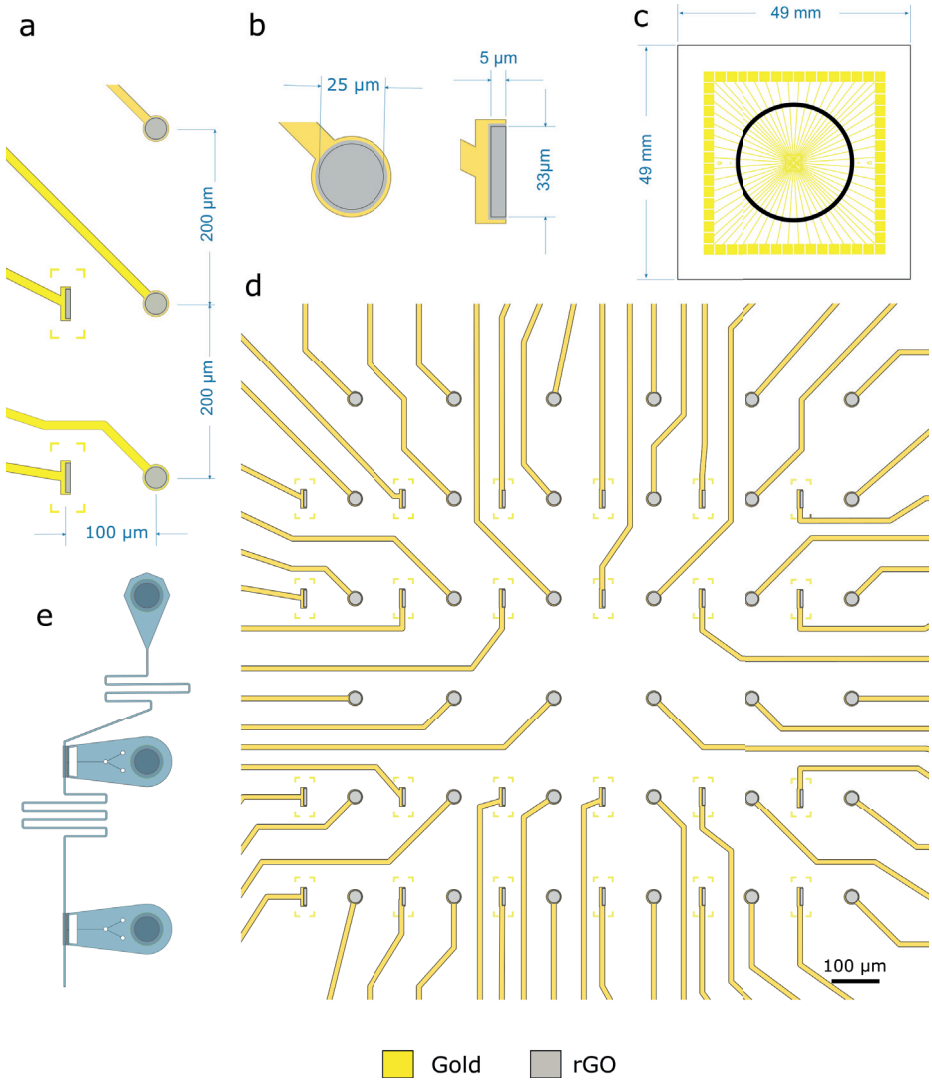

Figure 3.5: yJunction rGO MEA - Design specifications of the rGO MEA used in this thesis. The MEA is composed of 5 the electrode pattern shown in a, that repeats 12 times, designed to align with the PDMS wells shown in e. The pattern contains 2 different electrode geometries, shown in b: a circular electrode with 25 μm diameter and a rectangular electrode of 5 x 33 μm^2. The MEA dimensions are 49 x 49 mm; the pyrex substrate is only 170 μm thick. A 24.5 mm diameter methacrylate ring is glued to the surface of the MEA to act as culture well, shown as a black circle in c.

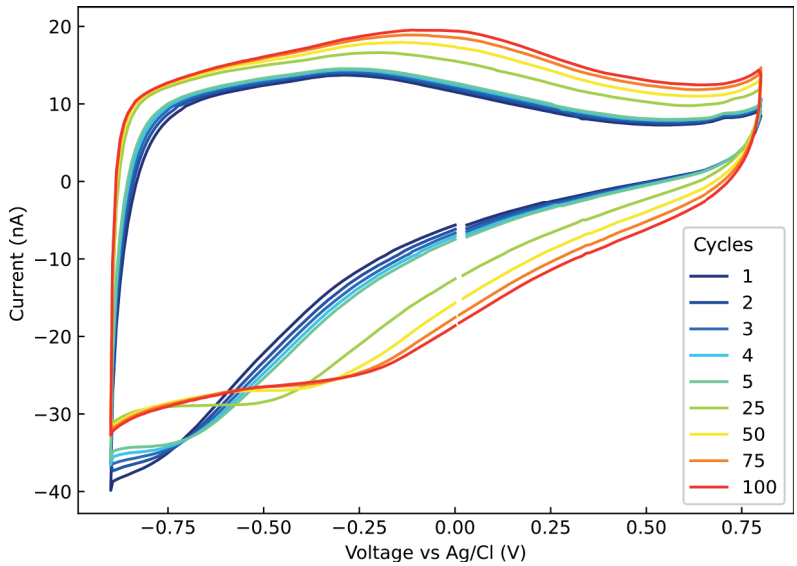

Figure 3.6: Activation of rGO microelectrodes - Evolution of the CV during the activation of a 25 μm diameter rGO electrode.

in solution. The main effect of these potential sweeps is to drive charged ions inside the pores of the material, leading to an increment of the double layer capacitance [218]. It has been reported in the literature that water permeation in hydrophobic pores can be modulated by applying electrical potentials [219, 220, 221, 222]. This phenomena is of special relevance to our material, since the minimum distance between carbon planes that water can fill naturally is 6 Å[223, 224, 225] and the interplanar distance of our rGO is 4 Å[13]; applying an electric field can force water into the bulk of the GO film. In addition, it has also been shown that, when ions are forced into pores smaller than 5 Åthey loose their solvation layers, further increasing the capacitance of the porous material [226, 227, 228, 229].

In our particular case, we activated the electrodes by performing 100 cycles of cyclic voltametry (CV) between 0.8 and -0.8 V, at a rate of 50 mV/s and by delivering 1000 current pulses of 1 ms duration at different currents, ranging from 5 to 25 μA. Figure 3.6 shows the evolution of the CV of a 25 μm diameter electrode during the activation using the parameters described above, where we can observe how the injected current in general increases with each cycle.

Figure 3.7 shows the EIS Bode plot of rGO electrodes with different sizes, using 1X PBS[16] as an electrolyte. We use the 1X PBS for this characterization because it mimics the conditions of the extracellular media used for cell cultures,

[16] PBS tablets, Sigma-Aldrich

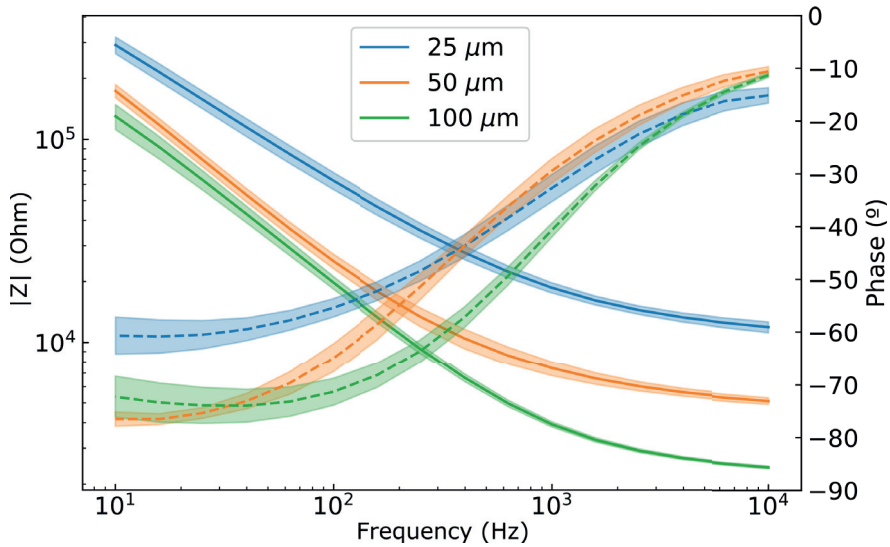

Figure 3.7: Impedance spectroscopy of rGO electrode with different sizes - Average EIS Bode plot of the 3 different sizes of rGO electrodes present in the hexagonal MEA design. The solid line represents the module of the impedance (|Z|), the dashed line the phase (ϕ) and the shadowed area the standard deviation of the average. n = 5, 6 and 18 for the 100, 50 and 25 μm diameter electrodes, respectively.

thus giving us a better understanding of the device performance in its real operation conditions. Figure 3.7 shows that the electrodes have a capacitive behaviour, with the impedance inversely proportional to the frequency and the phase close to -90 º, up to the few hundreds of Hz range, were the resistance of the solutions starts to appear, making the impedance independent of the frequency and the phase close to to 0 º. At low frequencies, where the impedance is dominated by the capacitance of the electrode, we should observe how the impedance decreases with the square of the electrode radius, however, this is not the case in Figure 3.7. The reason is that the maximum current of pulses delivered in the electrochemical activation is limited to 25 μA, in order not to damage the small electrodes. While currents up to 25 μA can induce a voltage drop of almost 1 V for the 25 μm diameter electrodes, the voltage drop for the 100 μm electrodes is way smaller, and thus this the activation is not as effective for the bigger electrode sizes. However, since the impedance of the 100 μm diameter electrodes is already quite low, reaching only a few kOhms at 1 kKz, it is not a major concern for us.

Another interesting behaviour we observed with the rGO MEA is the impedance evolution when they are used for cell cultures (see Figure 3.8). In this figure we can see the impedance at 1 kHz for the three different sizes of

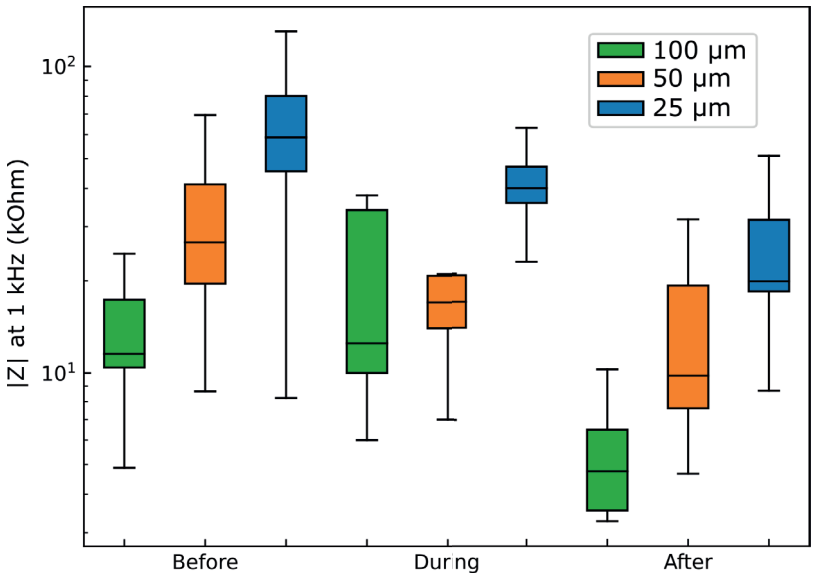

Figure 3.8: Impedance evolution of the rGO electrodes upon cell culture - Average impedance of the three rGO electrode sizes present in the hexagonal MEA design at 1 kHz. The impedances are shown before the start of the cell culture experiments, in between the first and the second cell cultures, marked as "During" and after the end of all the cell cultures.

electrodes present in the hexagonal MEA design before the MEA were used for cell cultures, in between the first and second cultures and after all the 3 cultures were done. The plot was done using the "boxplot" function from the matplotlib library, which creates a box that extends from the lower to the upper quartiles, with a line marking the average, while the whiskers show the 5 and 95 percentiles ranges. The before and after characterization were done using a potentiostat[17] and for the "During" characterization, the impedance was recorded using an impedance tester[18] because of time constrains. Figure 3.8 reveals that the impedance at 1 kHz progressively decreases with subsequent cultures. By the end of the experiments, the impedance had decreased to 40%, 52 % and 45 % of the initial impedance for the 100 μm, 50 μm and 25 μm diameter electrodes, respectively. We ruled out the possibility that these impedance decrease could be caused by passivation delamination by optically inspecting the electrodes under a microscope. Therefore, we hypothesize that the mechanisms responsible for this impedance decrease are the passive filling of the nanopores with water and the active filling induced by applying stimulating pulses with the electrodes during the cell culture experiments.

[17] Autolab PGSTAT128N, Metrohm
[18] nanoZ, Plexon

3.3.2 Noise performance of rGO electrodes

To asses the noise levels of our rGO MEA, we calculated the PSD *in vitro* voltage recordings acquired as described in section 3.4. To obtain the PSD, we calculated the FFT between 5 Hz and 4 kHZ using a custom Python 3.6 code. This calculation yields the PSD at each frequency, which is represented in Figure 3.9a for electrodes of the three different sizes present in the hexagonal MEA design. For reference, we also added the PSD of a particular *in vitro* recording with neural activity, such as that shown in the bottom part of Figure 3.13. Figure 3.9b shows the two raw voltage traces, used to calculate the PSD of the 100 μm diameter electrode and the PSD of the recording. Figure 3.9a shows that the noise PSD of the electrodes used for these experiments is, at least, 10 times lower than that of the recording with neural activity. We can also integrate the PSDs shown in Figure 3.9 between 5 Hz and 4 kHz to obtain the V_{RMS} noise of these electrodes. This calculation yields 1.7 μV, 3.6 μV and 2.9 μV for the 100 μm, 50 μm and 25 μm diameter electrodes, respectively. These low V_{RMS} demonstrate the good recording performance of the rGO electrodes.

3.3.3 Charge injection

In order to safely stimulate neural tissue, the voltage drop that occurs at the interface between the electrode and the electrolyte should be within the potential window of the electrode/electrolyte system. Within this potential window, only non-faradaic charge transfer occurs, avoiding the faradaic processes that were discussed in section 1.3. When delivering voltage pulses, this is easily controllable; the problem arises when we stimulate using current pulses. In this case, it is important to know the maximally safe charge injection capacity (CIC_{max}) [230] of the electrodes; CIC_{max} is defined as the amount of charge that the electrode can inject without producing faradaic reactions or crossing the water window [30].

To determine the CIC_{max} of our electrodes, first we need to determine their water window by performing cyclic voltammetry; this was measured to be (0.9, -0.9) V. Once the water window is known, different current pulses with increasing amplitude are applied and the voltage drop of the electrode is monitored. Typical voltage-time traces obtained with these experiments are shown in Figure 3.10a, where we can distinguish two different regimes: the ohmic drop regime, in which the current-potential relationship is linear, and the capacitive drop regime, where the current-potential relationship is exponential. The ohmic drop is produced by the access resistance of the system, i.e. the resistance of the electrolyte and the electrode tracks, while the charging of the double layer is responsible for the

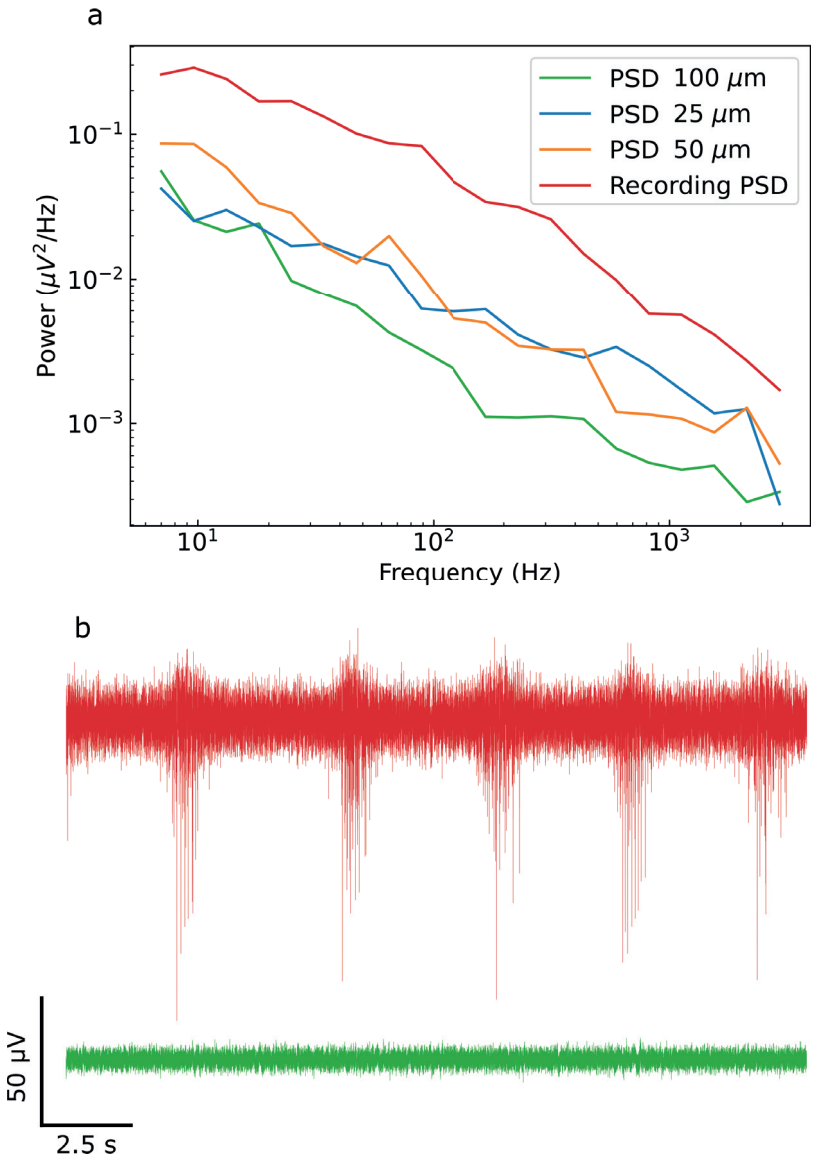

Figure 3.9: PSD of rGO electrodes - a) Noise PSD of the three different sizes of rGO present in the hexagonal MEA design. For reference, the PSD of an *in vitro* recording with neural activity is also shown, recorded with a 25 μm diameter electrode. b) Raw data used to calculate the PSD of the 100 μm electrode and the "Recording PSD".

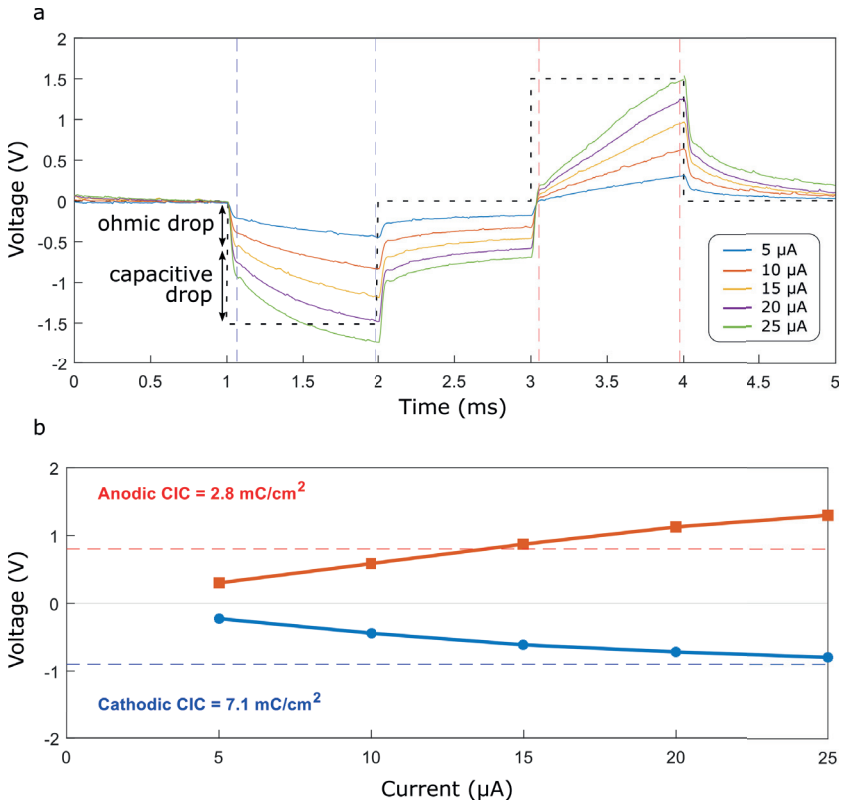

Figure 3.10: CIC$_{max}$ for the rGO electrodes - a) Voltage drop of a 25 μm diameter GO electrode created by applying current pulses of increasing amplitude. The blue dashed lines mark the beginning and the end of the capacitive drop. b) CIC$_{max}$ calculation for the anodic and cathodic pulse phase of the electrode shown in a).

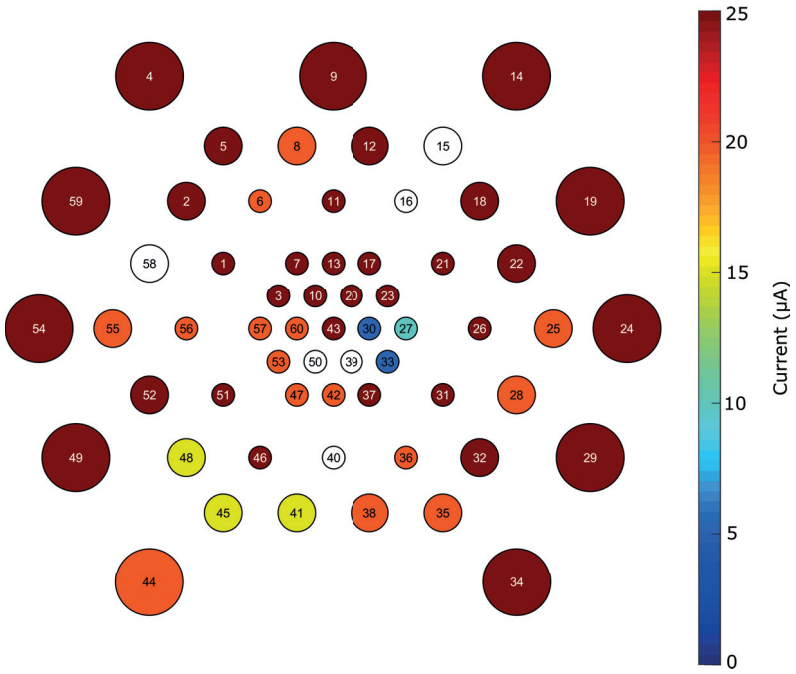

Figure 3.11: Current map of a rGO MEA - Maximum current that can be delivered by a 1 ms duration byphasic pulse at each electrode before the capacitive drop exceeds the water window. The white electrodes marked are deemed to be broken.

capacitive drop, the part of the voltage that drops in the electrode-electrolyte boundary. By increasing the amplitude of the current pulses and monitoring the capacitive drop, we can determine when it will cross the water window, thus determining the CIC_{max}. This process is shown in Figure 3.10b for the cathodic and anodic phases of the the pulses applied in Figure 3.10a.

If we repeat this process for all the electrodes in an MEA, we can obtain CIC_{max} maps, as the one depicted in Figure 3.11. This figure shows the highest current that can be delivered by a 1 ms duration byphasic pulse before the capacitive drop at the electrode interphase exceeds the water window. For this particular protocol, the current pulses were increased up to 25 μA, in order to avoid damage to the small electrodes. That is the reason why the maximum current does not reflect the true charge injection capabilities of the 100 μm diameter electrodes. Electrodes in which none of the stimulation amplitudes results in an electrode polarization that is inside the water window are deemed as broken, such as the white electrodes in Figure 3.11.

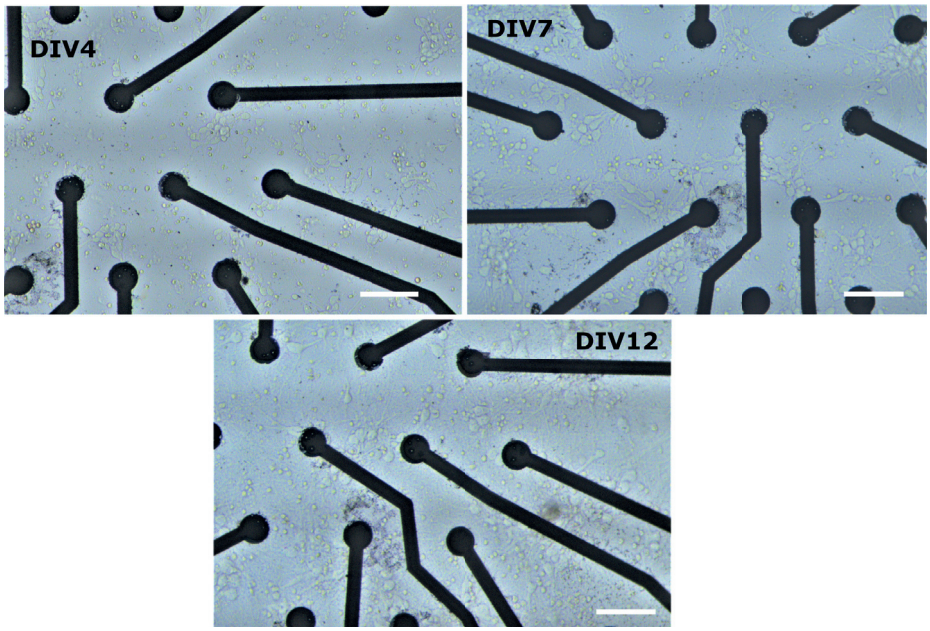

Figure 3.12: Hippocampal neuron culture - Culture of hippocampal neurons plated on top of a rGO MEA with the hexagonal design at DIV 4, 7 and 12. The scale bar is 100 μm.

All the calculations performed in this section to determine the CIC_{max} and produce the current maps are done by a Matlab code developed by Steven Walston, a member of our group.

3.4 *In vitro* recordings of cell activity with rGO MEA in neural cultures

All the *in vitro* recordings discussed in this section were performed during a research stay at the Laboratory of Biosensors and Bioelectronics (LBB-ETH) in the group of Prof. Janos Vöros.

Hippocampal neuron were cultured accordingly to the protocol described in Appendix D.2. For the hexagonal MEA design the neurons were directly seed on the PDL coated MEA; for the yJunction design, PDMS structures designed to guide the neuronal attachment and growth were assembled on the surface of the MEA prior to neuron seeding (see section 4.4 and Figures 4.7 and 4.8). The attachment of these structures was done as described in section 4.4; briefly: the surface of the MEA was cleaned and activated with an oxygen plasma process, then coated with PDL and the PDMS microstructure aligned manually. Then the wells of the microstructure were filled with PBS and then culture media, making

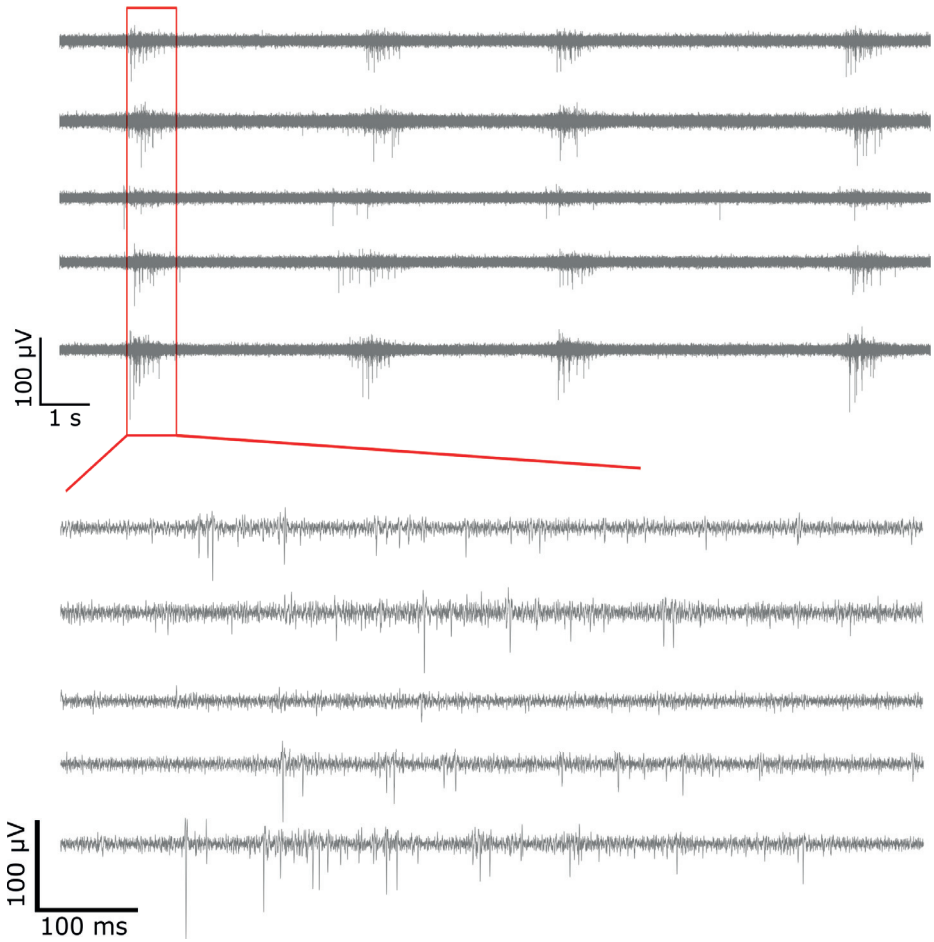

Figure 3.13: Spontaneous activity measured with an rGO MEA - Bursting activity of cultured hippocampal neurons recorded by 5 microelectrodes of the hexagonal rGO MEA design at DIV12. Data bandpass filtered between 200 and 1000 Hz.

sure no air bubbles were trapped in the wells. Figure 3.12 shows bright field images of hippocampal neurons cultured on a hexagonal rGO MEA at different growth stages.

When fluorescence measurements were needed, we added between 10^4 and 10^5 viral particles per cell of the adeno-associated virus mRuby3[19] and jGCaMP8m[20] [231] at DIV 2, to mark the structure and the calcium dynamics of the network, respectively.

[19] scAAV-DJ/2-hSyn1-chI-mRuby3-SV40p(A), created by the Viral Vector Facility at University of Zurich

[20] ssAAV-DJ/2-hSyn1-jGCaMP8m-WPRE-SV40p(A), Janelia

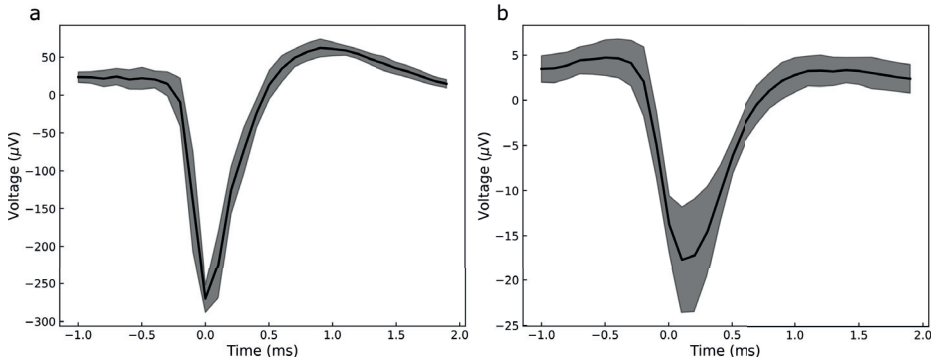

Figure 3.14: Difference in spikes size measured with the rGO MEAs - a) Axonal spikes measured in a PDMS structure using the yJunction MEA design, with an average peak to peak amplitude of 350 μV. b) Spikes measured from a random culture using the hexagonal MEA design, with an average peak to peak amplitude of 25 μV. The black line represents the averaged signal and the shadowed area the standard deviation of the population.

For the electrical recordings, the MEA were connected to a recording system[21] using an external platinum wire acting as a reference electrode. The recording system integrates a heating plate that was used to keep the temperature constant at 37 ºC; the CO_2 content was kept at 5% using a climate chamber[22]. The data was acquired using the Multi Channel Experimenter software and analysed and proccessed using a custom Python 3.6 script with the Neo [144] and PhyREC modules. Figure 3.13 shows typical spontaneous activity recorded with the hexagonal rGO MEA design and a random culture. Here we can see 5 different electrodes that record periodic bursting activity and a close up of one of the bursts, showing spikes with amplitudes up to 100 μV.

A particularly interesting phenomena we observe when recording action potentials from cells that are confined inside PDMS microwells is the large amplitude of said spikes. This peculiarity has been reported previously when recording action potentials produced by miocardiocites using nanocavity electrodes with high coupling resistance [232], reaching spike amplitudes up to 1.5 mV peak-to-peak. Furthermore, the use of PDMS microwells has enabled researchers to measure high amplitude axonal action potentials [233, 234, 235], signals that in random cultures would be impossible to measure due to the much higher amplitude of the spikes coming for the soma of the neurons [236]. This high amplitude recordings can be explained as follows: as the width of the PDMS wells and tunnels decrease, the resistance of the electrolytic solution in the channel increases, which translates in a larger voltage drop and, consequently, higher

[21] MEA2100-System, Multichannel Systems GmbH
[22] MEA2100-CO2-C, Multichannel Systems GmbH

spike amplitudes [237], as explained in section 1.4.3. This behaviour can also be observed when comparing Figure 3.14a and b. Both graphs were obtained using a custom Python 3.6 code that detected spikes using a threshold set at 5 times the standard deviation of the signal, taking a time window 1 ms before and 2 ms after the threshold was crossed and, then, averaging the spikes. Figure 3.14a shows an average of the axonal spikes recorded inside a microtunnel with one of the rectangular rGO electrodes in the yJunction MEA design. We can observe a high signal amplitude, reaching 350 μV peak-to-peak. Figure 3.14b, on the other hand, depicts an average of the spikes, detected and processed using the same script described before, in a random culture with a rGO hexagonal MEA. In this case the average peak-to-peak amplitude of the spikes barely reaches 25 μV and we can see a higher variability in the spike sizes, as represented by a higher standard deviation compared to that of Figure 3.14a.

3.4.1 Synchronization of spike timing

The aim of this set of experiments was to study the different characteristics of the spikes produced by electrical stimulation in random neuron cultures and in cultures guided with PDMS microstructures. To that regard, the culture and recording condition followed the guidelines described at the beginning of section 3.4. For the stimulation, we chose biphasic, charge balanced voltage pulses of varying duration and intensity. The pulses were separated by a resting period of 10 seconds and were repeated at least 15 times. The spikes were detected as explained before, with a custom Python 3.6 script that detected spikes using a threshold set at 5 times the standard deviation of the signal.

Figure 3.15 shows two examples of different voltage signals acquired during these experiments, in both cases stimulation and recording was done with the same electrode. In Figure 3.15a we can see 4 voltages traces recorded with the electrode shown in Figure 3.15b, after applying voltage pulses of 650 mV amplitude and 260 μs duration at the time marked by the red dashed line. Likewise, Figure 3.15c shows the voltage traces measured with the electrode marked with a red asterisc in Figure 3.15d, after delivering voltage pulses of 900 mV amplitude and 900 μs duration. In order to get rid of the voltage artefact produced by the stimulation, a bandpass filter between 200 and 1000 Hz was applied.

The first difference we notice is the already discussed effect of the increased well resistance in the spike amplitude. Further, in the PDMS guided cultures, only a few neurons are in close proximity with the recording, reducing the interference overlapping action potentials might have on the recorded signal [236]. As a result,

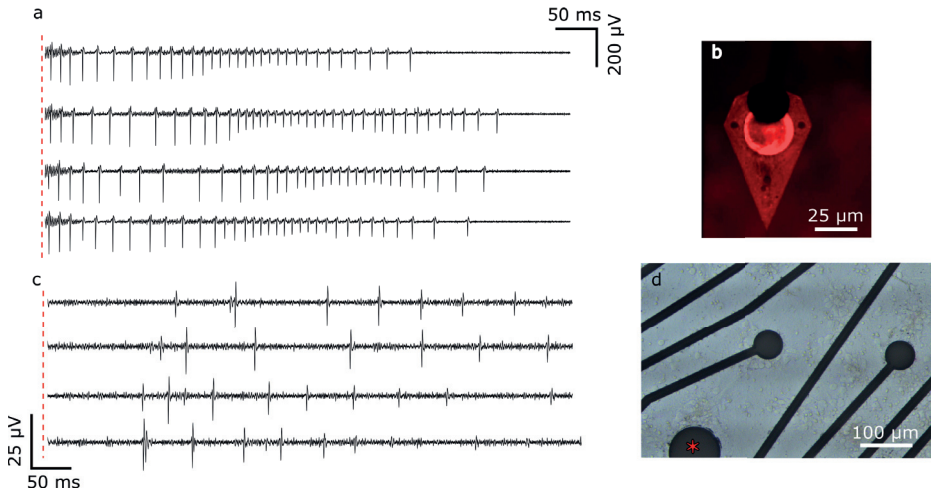

Figure 3.15: Voltage signals generated by rGO MEA electrical stimulation - a) Stimulation response of the neurons cultured in the PDMS well shown in b) after delivering 650 mV amplitude and 260 μs duration pulses at the time marked with the red dashed line. c) Stimulation response from a random neural culture shown in d). The electrode marked with the red asterisc deliverd pulses of 900 mV amplitude and 900 μs duration at the time marked by the red dashed line.

spikes in Figure 3.15a show a tenfold increase amplitude compared to those in Figure 3.15c.

Another difference we appreciate between this two groups of voltage traces is the number of spikes elicited. Although the voltage pulse delivered in the random culture have more amplitude and longer duration (900 mV/900 μs vs 650 mV/260 μs), we evoke more spikes in the PDMS guided culture. This can be explained by taking into consideration the higher resistance of the electrolyte inside the microwells. When we apply a potential pulse between our stimulating electrode, in close proximity to the neurons, and our reference electrode, place in the bulk of the solution, the higher resistance around the stimulating electrode means that there will be a larger voltage drop inside the microwell, meaning that the neurons inside are easier to depolarize, even with lower amplitude and duration pulses. Although we have presented here a direct comparison between the two cultures, we must keep in mind that the neuron number and distribution around the stimulating electrode, as well as the maturity of the culture play an important role in the excitability of neuron cultures. This means that even if both neural cultures were random or guided, there will be differences in the excitability, a fact that we will explore further in section 3.4.2

The final difference we can observe between the two experiments presented in Figure 3.15 is the spike timing. To study it in more detail, we have represented

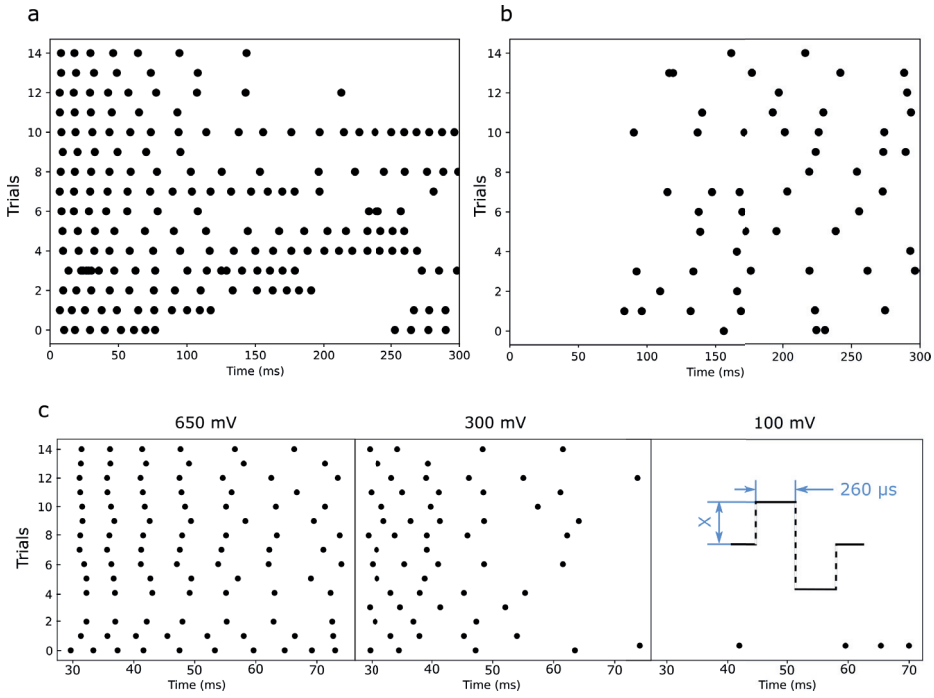

Figure 3.16: Spike timing scatter plot - a) Scatter plot of the spike times produced in different trials by delivering a 650 mV amplitude and 260 μs duration pulse in the electrode show in Figure 3.15b. b) Scatter plot of the spike times across 15 different trials produced by delivering a 900 mV amplitude and 900 μs duration pulse with a hexagonal rGO MEA in a random neural culture without any PDMS structure. c) Evolution of the spike timing with diminishing stimulation potential in a culture guided with a PDMS structure.

the timing of the spikes across different stimulation trial as scatter plots, shown in Figure 3.16. Figures 3.16a and b show the first 300 ms of 15 stimulation trials performed with the electrodes shown in Figure 3.15b and d respectively. We can readily see that the neuron response is not as immediate in the random culture when compared to the PDMS guided one, most likely due to the smaller voltage drop that happens in the random culture when compared to the guided one and the fact that the excited neurons might be further away from the recording electrode, thus the spikes take longer to arrive. In Figure 3.16c, we show scatter plots for the spike timing at different stimulation amplitudes. The shown time window starts 30 ms after the stimulation and has a duration of 50 ms. We can see how the spikes are highly synchronized between trials for a stimulation amplitude of 650 mV. Then, as the amplitude of the stimulating pulses decreases, so do the probability to elicit an action potential in the neurons, and we see how that lower probability translates into a less synchronized activity for pulses of 300 mV amplitude and how the neurons become almost completely non responsive for stimulation amplitudes of 100 mV.

3.4.2 Stimulus Effectiveness

Beside choosing an appropriated electrode material and MEA design, there is a wealth of stimulation parameters that need to be optimized when designing stimulating protocols. The first one is to choose the stimulation magnitude to control, either current or voltage, each of them with the advantages and disadvantages we already discussed in Chapter 1. Another aspect that needs to be optimized is the duration and amplitude of the pulse, for what we can use the strengh-duration relationship (see equation 1.20). In general, the pulse chosen is the shortest one that delivers enough charge to induce the desire electrical response in the tissue; normally, due to the voltage artefact that the stimulation causes, it is not possible to record during the pulse duration [238]. However, shorter pulses delivering high currents cause large voltage drops at the electrode/electrolyte interface, potentially damaging the electrode and the surrounding tissue [13].

In this section, we study the effectiveness of different pulses to evoke electrical activity in dissociated hippocampal neuron cultures, using our rGO MEA. The neuron culture and the recording/stimulating setup are the same as those already discussed in sections 3.4 and 3.4.1. The stimulating pulses were repeated 10 times, leaving 10 seconds between repetitions. Between each set of stimulus, a control stimulating pulse with the maximum amplitude and duration defined for each culture was applied. The objective of this control pulse was to monitor the

responsiveness of the culture: if the control pulse showed that the responsiveness of the neurons were decaying over time, that set of experiments was eliminated from this analysis. Also, in order to account for the spontaneous activity of the culture, 10 1 second time slots were chosen in a time window between 5 and 10 seconds after the each stimulation. The average number of spikes detected in this slots was used as an activity baseline for each experiment.

We studied negative and positive monophasic voltage pulses, biphasic voltage pulses, negative monophasic current pulses and biphasic negative-first current pulses. We left out of the study the positive current pulses because of time and culture constrains and the fact that they have been reported to be the less efficient to elicit neural responses [238]. We varied the amplitude and duration of the pulses in order to get the most complete data set possible. The script to process the data was writen in Python 3.6, using the Neo [144] and PhyREC modules; it detected the spikes that occurred within 1 second after the stimulus using a threshold set a 5 times the standard deviation of the voltage signal. It counted the spikes and calculated the average number of spikes over the 10 stimulations. Then, after a whole set of experiments was done, we took all the average spike numbers for a given pulse design (i.e. monophasic, negative voltage) and normalized it by the strength and duration parameters that gave us the highest number of spikes (see Figure 3.20). In this way, we can obtain the so-called relative efficacy [92], a parameter that allowed us to compare the stimulation efficacy across different neural cultures, regardless of the different number of cells or cell disposition around the electrode.

Figures 3.17 and 3.18 show examples of the experiments we just described, where we explore biphasic, positive-first voltage pulses. In Figure 3.17 we investigate the effect of the pulse duration on the stimulation by keeping the pulse amplitude fixed at 900 mV and decreasing progressively the pulse duration from 900 μs to 200 μs. Figure 3.17a shows 8 voltage traces of 1 second duration obtained by delivering a biphasic positive-first voltage pulse of 900 mV and 900 μs duration; Figure 3.17b shows the histogram of the spikes detected in Figure 3.17a. We repeated the same experiment every 100 μs for pulse lengths down to 200 μs. In Figure 3.17c we show the voltage traces of the last experiment, in which we delivered a biphasic positive-first voltage pulse on 900 mV amplitude and 200 μs; its histogram is represented in Figure 3.17d. By comparing Figure 3.17a and c we can clearly see how the number of detected spikes decreases with decreasing pulse duration, meaning lower efficacy of the delivered stimulus.

In Figure 3.18 we perform a similar experiment than the one described above, but it this case we keep the duration of the pulse fixed and vary its amplitude. Comparing 3.18a and c, we can see that the effect of decreasing the

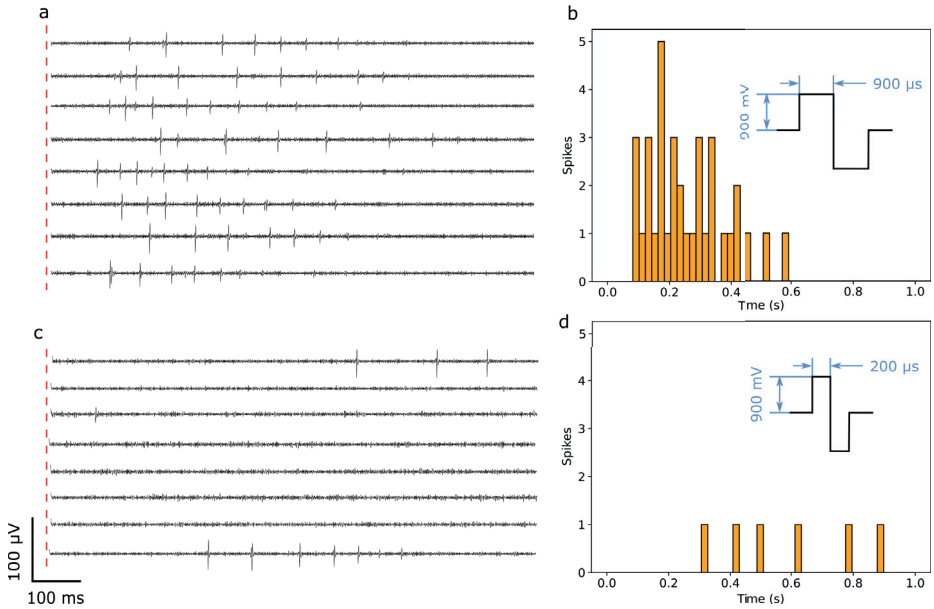

Figure 3.17: Stimulation Efficacy of biphasic, positive-first voltage pulses at a fixed pulse amplitude - a) Example of the voltage traces recorded after stimulating a hippocampal neuron culture with a 9000 mV, 900 μs, biphasic positive-first voltage pulse. b) Histogram of the spikes detected in a). c) Example of the voltage traces recorded after stimulating a hippocampal neuron culture with a 900 mV, 200 μs, biphasic positive-first voltage pulse. d) Histogram of the spikes detected in c).

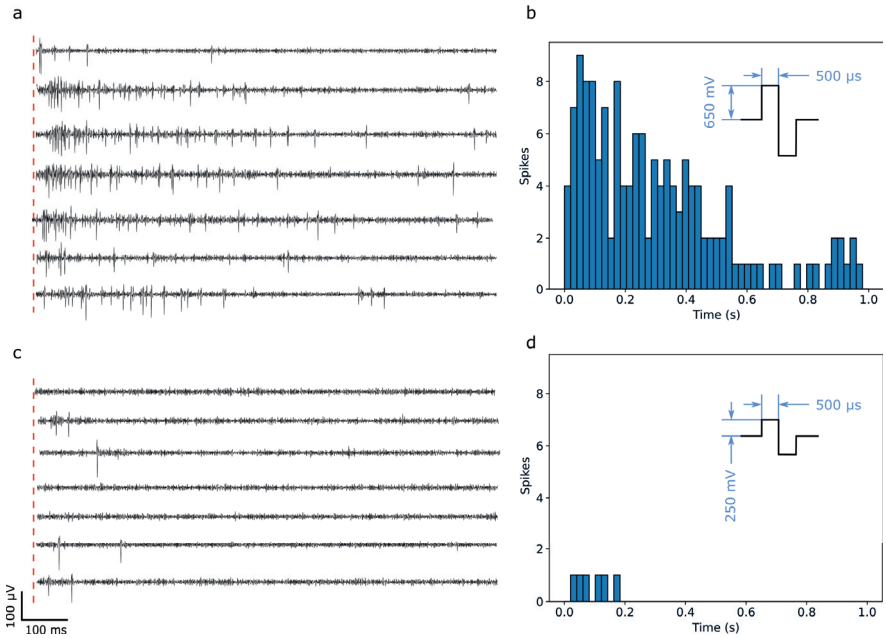

Figure 3.18: Stimulation Efficacy of biphasic, positive-first voltage pulses at a fixed pulse duration - a) Example of the voltage traces recorded after stimulating a hippocampal neuron culture with a 650 mV, 500 μs, biphasic positive-first voltage pulse. b) Histogram of the spikes detected in a). c) Example of the voltage traces recorded after stimulating a hippocampal neuron culture with a 250 mV, 500 μs, biphasic positive-first voltage pulse. d) Histogram of the spikes detected in c)

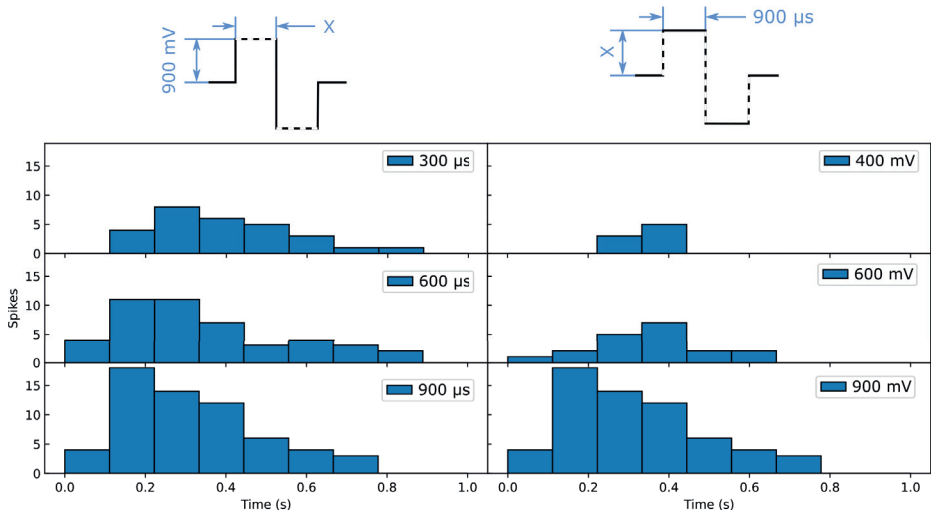

Figure 3.19: Sum up histograms of the stimulation efficacy - Number of spikes elicit at each time with biphasic, positive first voltage pulses of 900 mV amplitude and increasing duration (left) and 900 μs duration and increasing amplitudes (right).

pulse amplitude also decreases the efficacy of the stimulus; in this case the change is faster, with almost complete absence of elicited spikes after decreasing the amplitude just 400 mV.

Figure 3.19 shows a condensed view of two series of experiments. In the series of the left we apply biphasic positive-first voltage pulses, keeping the amplitude constant and varying the duration. In the panel of the right we keep the duration constant and change the pulse amplitude. We can see, again, that the number of spikes elicited with the two different stimulus decreases at different rates, being faster for the amplitude decreasing experiment set.

Comparing Figures 3.17 and 3.18 we can directly see that the total number of spikes elicited is very different in both series of experiments; this is due to culture conditions and number of neurons available near the electrode, among others. Despite this, the use of the relative stimulus efficacy let us compare them directly, allowing us to combine data from different cultures and represent it them as Figure 3.20.

Figure 3.20 shows a condensed view of all the stimulation efficacy experiments done in this thesis, where we have studied monophasic and biphasic rectangular pulses of various polarities and delivering either current or voltage stimulation. Figure 3.20 confirms that the electrical response of the tissue decreases when either the amplitude or the duration of the stimulus decreases. Increasing pulse duration does not always monotonically increase the efficacy of the stimulation,

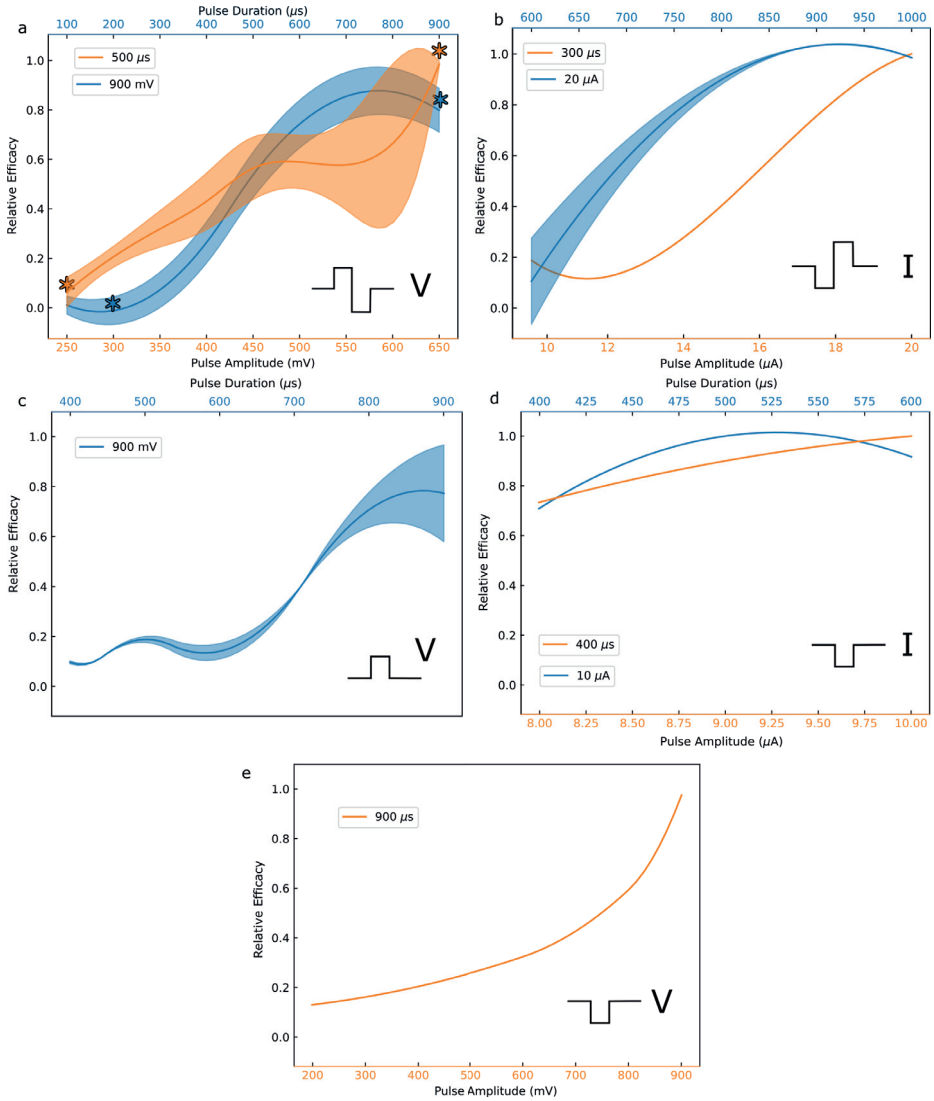

Figure 3.20: Summary of relative stimulation efficacy experiments - a) Biphasic positive-first voltage stimulation, where the asterisc mark the postion of the voltage traces shown in Figure 3.18 and 3.17. b) Biphasic negative-first current stimulation. c) Monophasic positive voltage stimulation. d) Monophasic negative current stimulation. e) Monophasic negative voltage stimulation. The solid line represent the average value and the shaded region the standard deviation.

since we can see how it rec hes its maximum before the longest pulse duration (seen in Figure 3.20a, b and d). Another common trend we observe in Figure 3.20 is that there is a steep decrease in efficacy when decreasing the voltage from 900 mV down to approximately 400 mV (shown in Figure 3.19 and Figure 3.20 e).

Although in this section we have studied how different pulses achieve different stimulation results, it is worth mentioning that to extract definitive conclusions about some of the finer aspect discussed in the section, more experiments are needed. Additionally, using different types of neural cultures other than hippocampal could broaden the applicability of the results presented in this section.

3.4.3 Spike sorting

In order to further explore the capabilities of the rGO MEAs to record spontaneous activity, we performed an analysis of the recorded spikes, following the same procedure and using the same scripts as for the one performed in section 2.10. The algorithm works in the following manner. It detected spikes by setting a threshold at 5 times the standard deviation of the voltage trace, as shown in Figure 3.21a, and stored a time window 1 millisecond prior to the threshold and 2 milliseconds after it. An example of this is shown in Figure 3.21b, where we analyse the spontaneous spiking activity from a hippocampal neural culture grown on top of a rGO MEA. Then, the algorithm calculated the spike amplitude as the difference between the maximum and the minimum potential of the spike and the duration as the time at which the minimum is reached, minus the time at which the maximum is achieved. That means that spikes were the minimum happens before the maximum will be represented as having negative duration. After this two parameters were extracted, a K-Means clustering algorithm was performed in order to find groups in the data and color code them accordingly, as shown in Figure 3.21c. Figure 3.21d show the spike average for each cluster, with the standard deviation represented as the shadowed area.

From Figure 3.21 we are able to identify six clearly differentiated clusters, three of positive duration (green, orange and purple) and three of negative duration (blue, brown and red). The purple and orange spikes are the highest in amplitude, suggesting that the neurons responsible for these spikes are the closest to the recording electrode. From these six clusters, we can identify two, red and brown, with the same signal shape and different amplitude, thus suggesting that are produced by the same type of neuron but at different locations. The neuron producing the red spikes would be closer to the electrode, allowing us to record spikes with higher amplitude than the neuron producing the brown spikes. The

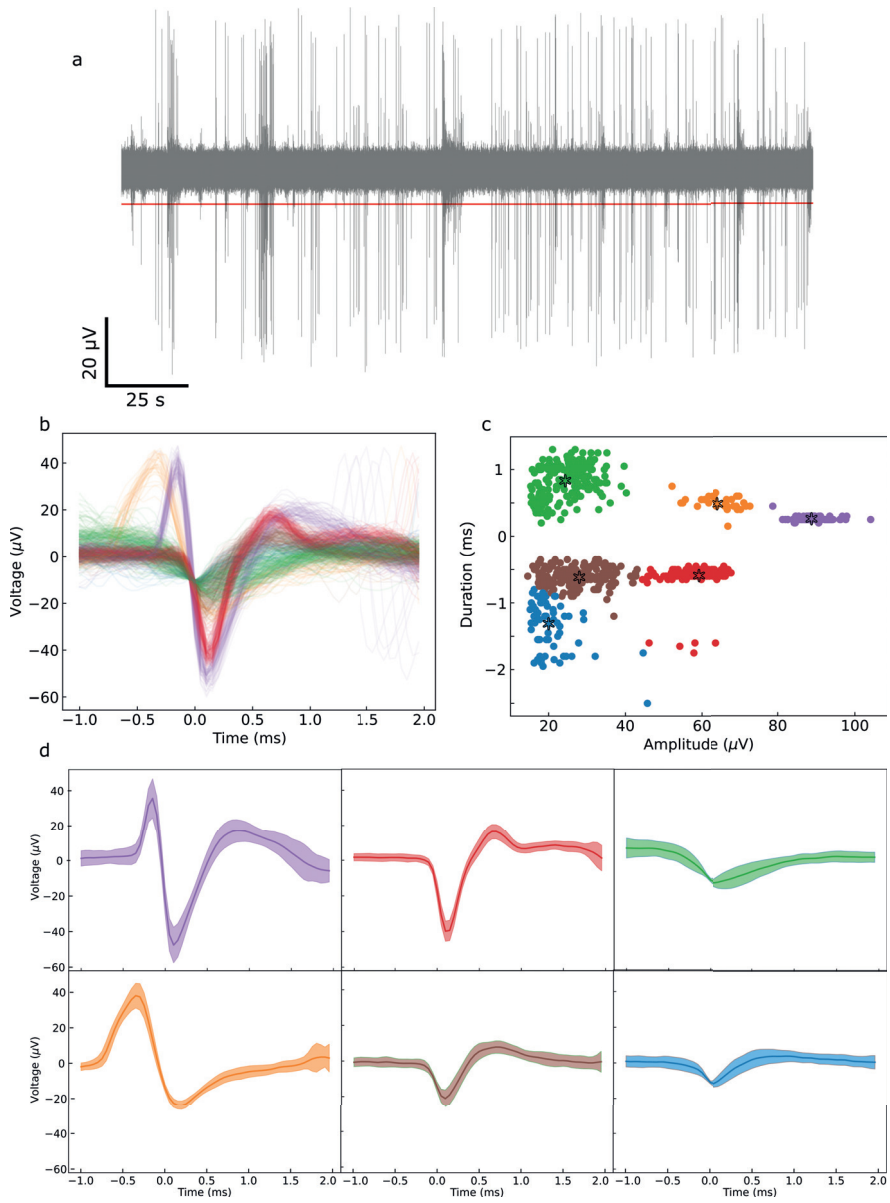

Figure 3.21: Spike sorting of recordings acquired using rGO electrodes - a) Raw voltage trace used for this analysis. The red line marks the 10 μV thershold. b) Spontaneous spiking activity detected using the rGO electrodes on a hexagonal MEA design in random hippocampal cultures, color coded accordingly to the K-Means clustering algorithm, whose results are shown in c). The center of each cluster is marked by an asterisc. d) Averages of the 6 distinctive spikes shapes found by the clustering algorithm. The solid line represents the average and the shadowed region the standard deviation.

last two spike shapes, green and blue, have the lowest amplitude suggesting that are produced by neurons far away from the recording electrode.

This section proves the capability of the rGO electrodes to measure different spike shapes coming, presumably, from different neurons at different positions, all while maintaining a good signal quality that allow us to perform some signal analysis.

3.4.4 Area activation study

In previous sections we have focused on discussing the electrical activity elicited only at a particular spot. In contrast, in this section we will study how the stimulation pulses elicit electrical activity across the area of the device, and how different stimulation parameters manage to activate different areas of the culture. To this end. we use confocal laser scanning microscopy (CLSM).

To do so, we labelled a hippocampal neuron culture grown on top of a hexagonal rGO MEA with Ca^{2+} indicators to monitor cell activity and cell structure indicators. Briefly, between 10^4 and 10^5 adeno-asociated virus (AAV) particles were added to each culture at DIV 2. The used AAV were mRuby318[23] and jGCaMP8m19[24] [231], to label the neuron superstructure and the calcium dynamics respectively. The cultures were left to mature and at DIV 16 were taken to a CLSM microscope[25] with an incorporated incubator and a MEA recording system[26]. There we monitored the area of the culture surrounding the stimulating electrode using bright field microscopy and two different laser wavelengths, one for each AVV protein. The pictures in Figure 3.22 show examples of the images obtained for each of the fluorescence channels. While optically recording this area, we applied different stimulation protocols at the electrode in the centre, repeating each stimulus between 5 and 10 times to get enough statistics. After that, the collected data was analyzed using ImageJ 1.52a and further processed using a custom code written in Python 3.6 with the Neo [144] and PhyREC libraries.

The data analysis pipeline began by manually defining regions of interest (ROI) at the areas were neurons were positioned in the bright field image shown in Figure 3.22a. The brightness and contrast of the Ca^{2+} imagining videos was adjusted and the average fluorescence intensity at each time point and on each ROI was detected using the "Measure" function in ImageJ´s ROI Manager. That data, together with the size and position of the ROIs was imported into Python,

[23] scAAV-DJ/2-hSyn1-chI-mRuby3-SV40p(A), created by the Viral Vector Facility at University of Zurich

[24] ssAAV-DJ/2-hSyn1-jGCaMP8m-WPRE-SV40p(A), Janelia

[25] FluoView3000 CLSM, Olympus

[26] MEA2100-Mini-System, Multichannel Systems GmbH

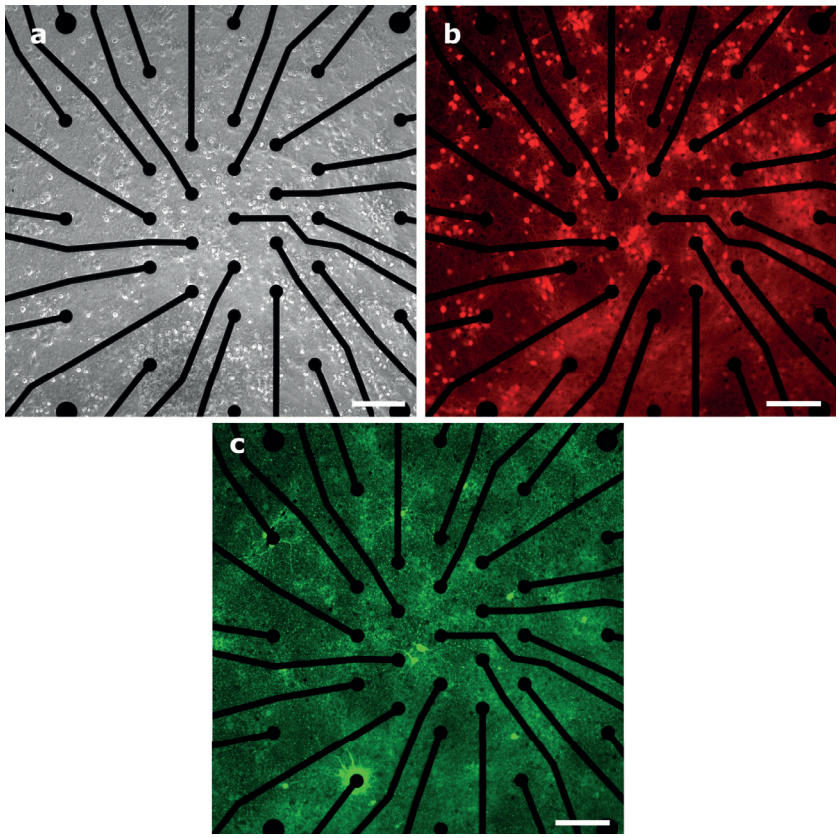

Figure 3.22: Bright field and fluorescence images of the hippocampal cultures used for the volume activation study - a) Bright field image of the hippocampal culture on a hexagonal rGO MEA. b) Fluorescence image of the same area in a) showing the neuron superstructure labelled by an mRuby3 adeno-asociated virus. c) Fluorescence image of the same area as in a) and b) showing the calcium concentration labelled by the ssAVV described in section 3.4. The images were taken at DIV 16 and the scale bar size is 300 μm.

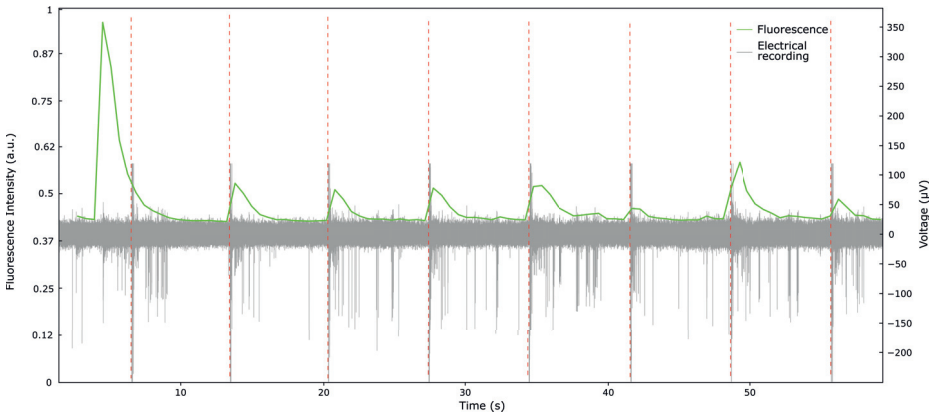

Figure 3.23: Raw data of a simultaneous electrical and fluorescence experiment - Simultaneous recordings of Ca^{2+} activity and electrical activity using the rGO MEA while 650 mV amplitude and 500 μs voltage pulses were delivered, marked by the dashed red lines. The Ca^{2+} intensity corresponds to an integration over the whole field of view shown in Figure 3.22.

where we removed any photobleaching of the fluorescence using a polynomial fit. Spikes were detected if, at any time, the fluorescence of the ROI was, at least, 2.75 times larger than the baseline intensity. Then, we imported the data from the stimulator and synchronized both recordings. The relative stimulation efficacy was calculated as the number of stimulus that induced a spike divided by the total number of stimulus delivered for each measurement, and it was represented as a grid plot, where each pixel in the grid denoted one of the ROIs. The videos recorded during these experiments can be found on the repository [239].

Figure 3.23 shows the voltage and calcium traces of one of these experiments. The depicted calcium intensity shown corresponds to the integration over the whole field of view of the CLSM, as shown in Figure 3.22. In Figure 3.23 we can see how all but the first Ca^{2+} spikes match the stimulation pulses (650 mV amplitude and 500 μs duration). The first Ca^{2+} is correlated with spontaneous activity previous to the delivery of the stimulation pulse, as we can see in the initial burst around second 4. In addition, we can see small fluorescence intensity increments between stimulus, like the one that happens around second 35, that are also correlated with spontaneous spiking activity, as revealed in the electrical recording. As a consequence to this burst of spontaneous activity, the stimulus delivered at second 42 elicits less activity, as seen in both the fluorescence and the electrical recording.

In order to explore the temporal resolution capabilities of the Ca^{2+} recording method, we tried to visualize the propagation of the electrical activity through the network. To that regard, we divided the CLSM field of view in three different

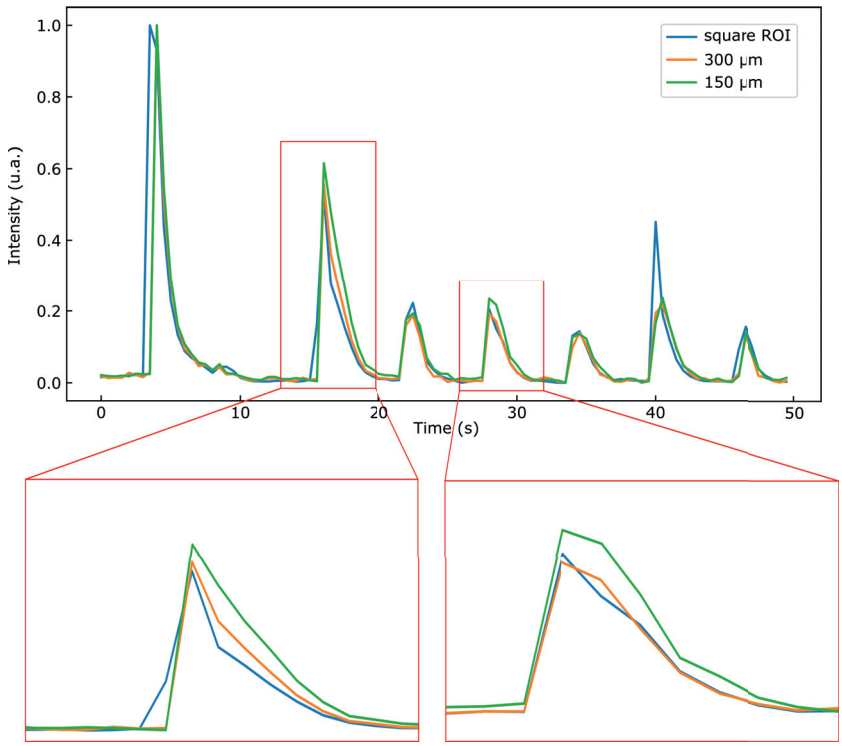

Figure 3.24: Analysis of the neural activity propagation using Ca^{2+} fluorescence - Intensity of the Ca^{2+} fluorescence in three different ROIs: a 150 μm circle centered in the stimulating electrode, a ring with 150 μ inner and 300 μm outer diameter centered in the stimulating electrode and the whole field of view minus a 300 μm circle centered in the stimulating electrode.

ROIs: the first one was a 150 μm diameter circle centered in the stimulating electrode, the one situated in the center of the MEA (see Figure 3.22); the second one was a ring, centered in the stimulating electrode, with an inner diameter of 150 μm and an outer diameter of 300 μm; the last one was the whole field of view of the CLSM (see Figure 3.22) minus a 300 μm diameter centered in the stimulating electrode. Figure 3.24 shows the intensity of the Ca^{2+} of these 3 ROIs. There we can see that the Ca^{2+} spikes begin at the same time for all 3 traces, while if we had enough temporal resolution to see the signal propagation, we would see the 150 μm precede the other two and the 300 μm precede the square ROI. Interestingly, in some spikes, like the first and the second, we see the signal from the square ROI begin before the other two. This happens because the CLSM is a scanning microscope that beggins scanning on the top left pixel of the field of view; if a Ca^{2+} spike occurs while the microscope is scanning the bottom part of the field of view, the increment in fluorescence will be first recorded in the square ROI than in the other two.

Figure 3.25 show the results of the data analysis explained above applied to a hippocampal culture performed as explained at the beginning of this section. Figure 3.25a shows three different grid plots corresponding to biphasic, negative-first pulses of 5 μA amplitude and durations of 120 μs, 320 μs and 520 μs, respectively. In the first grid plot we have also represented the layout of the rGO MEA and marked the stimulating electrode in red. In Figure 3.25a we can see how we barely elicit any spikes for the 120 μs and 320 μs pulse durations, while for the 520 μs pulse duration we already get activity in the whole field of view, with higher stimulus efficacy in the upper right quadrant of the grid plot. Figure 3.25b shows the same type of plot, but this time for biphasic, positive-first voltage pulses of 500 μs duration and 250 mV, 350 mV and 500 mV, respectively. There we can see how the lowest stimulation amplitude already creates a very faint response in the right half of the field of view, response that extends to the whole field of view for 350 mV amplitude and reaches almost total stimulation efficacy for 500 mV amplitude. The experiments described in this section allow us to visualize how different stimulating pulses activate different areas of the culture.

3.5 Conclusion

In this chapter we have shown the fabrication of a novel rGO material that has a wide electrochemical potential window, low electrochemical impedance and high charge injection capability. We have also shown two different procedures to transfer this material to target substrates that are compatible with photolitographic

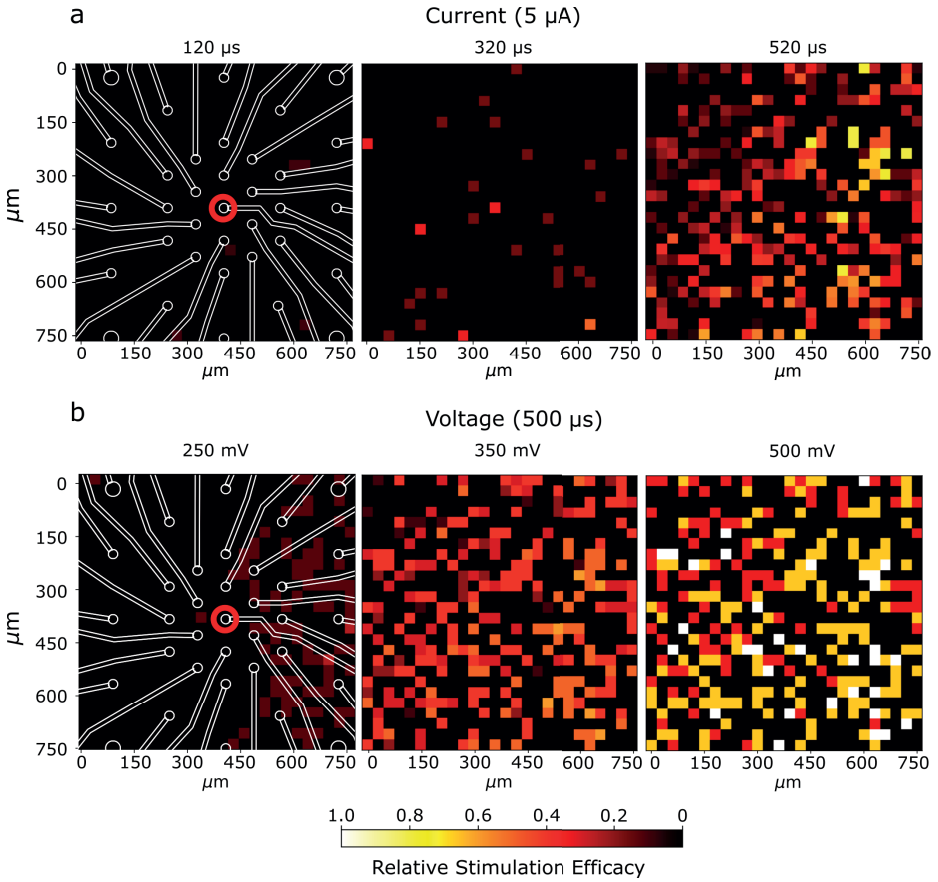

Figure 3.25: Area activation study with Ca^{2+} - a) Area of the culture activated by stimulating with the electrode marked in red, using biphasic, negative-first current pulse of 5 μA amplitude and different duration. b) Same experiment as a) but delivering a voltage pulse of 500 μs duration and different amplitudes.

fabrication techniques and developed a reproducible microfabrication protocol that allows us to obtain rGO MEA with electrode sizes in the range of tens of micrometers, suitable to interact with the nervous system. We have also thoroughly discussed the electrochemical characterization of such rGO MEA, studying the effect of the electrochemical activation process on the interfacial capacitance of the electrodes and monitoring how that impedance changes with time when we use the MEA to perform cell cultures. Additionally, we have discussed the noise spectra of different rGO sizes and shown a method to determine the CIC_{max} of the electrodes, a crucial parameter to safely stimulate neural tissue.

In order to test the capabilities of the fabricated devices to bidirectionally interface neural tissue we have used them to culture hippocampal neurons, recording their electrical activity. The MEA allowed for the development of healthy neural networks, giving us the possibility to observe a wealth of spike shapes and amplitudes using two different neuron culture approaches: random cultures and guided cultures using PDMS structures. Furthermore, we have used a spike sorting algorithm that allowed us to differentiate spikes coming from different neurons. Our spike sorting algorithm relies on a relatively primitive feature extraction method, such as the amplitude and duration of the spikes, that only yields good result with high SNR recordings [173], proving once again the excellent recording capabilities of our devices. When testing the stimulating capabilities of the rGO MEA, we were able to elicit electrical activity in both random and guided hippocampal cultures, studying the differences in spike timing between them. We also study various pulse shapes, delivering both controlled current and voltage. We obtained common trends in the efficacy of the stimulating pulses, such as a steep decrease in relative stimulation efficacy when decreasing the voltage amplitude of the pulses while keeping the duration constant. Finally, we studied how different stimulation pulses produce different spatial responses on cultured networks.

Altogether, the results presented in this chapter show that rGO is able to sustain neural cultures and it is compatible with most microfabrication techniques, making it an extraordinary material to fabricate MEA aimed to bidirectionally interact with the nervous system.

4

Neuronal Guidance

"It's a little experiment that might win me the Nobel Prize"
"In what field?"
"I don't care; they all pay the same"

Leela and Prof. Farnsworth
Futurama

4.1 Introduction

Over the last few decades our understanding of the human brain has developed considerably. However, the basic mechanisms of neural computation remain widely unknown. A promising way to expand our knowledge in this direction is to take a bottom-up approach to neuroscience [240]. As opposed to the top-down approach, that studies the nervous system as a whole, the bottom-up approach involves culturing controlled neural networks, in which the geometry and connectivity of the neurons are engineered in order to fabricate neural circuits [240, 241] designed to address specific questions. When the neural networks reach the desired maturity, it is possible to interact with them to infer their computational properties, that can be extrapolated to explain the computational characteristics of higher level systems.

Each approach has its weakness and its advantages. The most notorious advantage of the top-down approach is that it provides the opportunity to study

the nervous systems in its native conditions. The obvious drawback is that the huge complexity of the nervous systems, even in the most simple animals, can make this task daunting, difficulting the extraction of unambiguous conclusions. The bottom-down approach suffers the opposite problems; the relative simplicity of the artificially built networks makes easier to study concrete circuits, but at the cost of oversimplifying the study subject.

Nevertheless, the bottom-up approach allows for an accuracy and reliability that cannot be achieved when using top-down neuroscience. The possibility to reproducibly build the same neural network repeatedly, together with the ability to study the system response when individual neurons are added or removed, is the necessary base to extract conclusive and reproducible results when studying a system. Furthermore, studies have shown that artificial neural networks, in which the geometry has been controlled so the neurons grown on top of the electrodes on an MEA, retain properties present in brain scale activity patterns [242]. Finally, the ability to study the development of the neural networks and the possibility to integrate this approach with precise MEA or fluorescence recordings makes the bottom-up approach a valuable tool in pharmacological and toxicological studies [36].

In this section we explore three different techniques to fabricate controlled neural networks: a double passivation technique that exploits the different hydrophobicity of the passivation materials used, micro contact printing and the use of microstructures to constrain neural growth. Finally, we analyse the advantages and the disadvantages of each approach as well as the compatibility with different recording techniques and their ability to create finely defined custom neural networks.

4.2 Double Passivation

When a non-biological surface is exposed to biological media, it becomes coated with the proteins present in the media [243]. The properties of the material dictate the amount and the type of proteins adsorbed onto the surface and, through these proteins, the extend to which cells will attach to that surface. Once attached, the physical and chemical cues from the surface and the protein coating guide the cells down to a specific differentiation path, or even to apoptosis. [244, 245, 246, 247].

A variety of factors, such as the complex nature of the macro-molecular adsorption, the low adsorption selectivity of the substrate, the complexity of the biological media composition and the specificity of cell-protein interaction, makes the attachment of cells to a specific non-biological surface difficult to predict [248].

However, for more than 3 decades, a relationship between the surface energy of the substrate and the cell adhesion has been established [249]. This relationship has enabled some groups to propose models that predict some aspects of cell adhesion based on the surface energy of the substrate. In [250], they calculate the surface energy as function of the substrate roughness and the Water Contact Angle (WCA) [251] and relate it with the cell spread length, an indicator of cell attachment. For a fixed roughness, the lower the WCA, the higher the surface energy and the greater the attachment is [250].

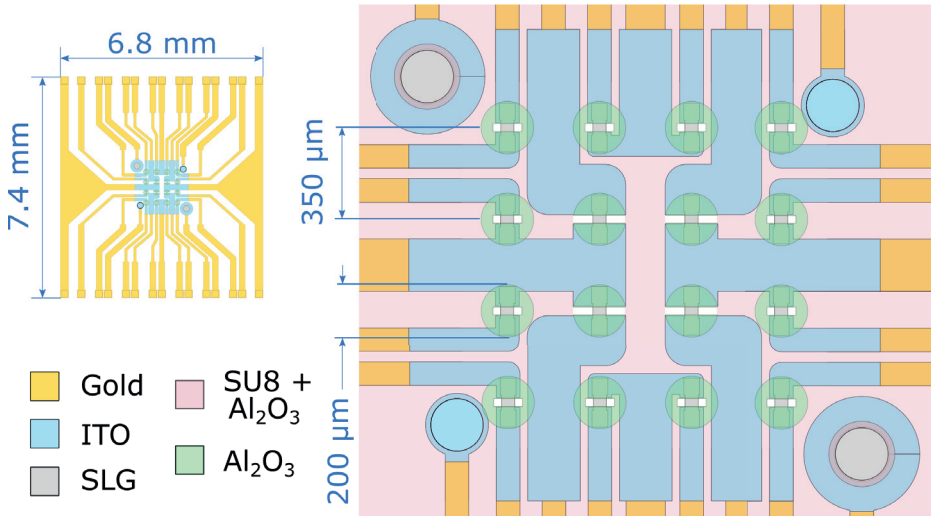

Figure 4.1: Design of the devices used for the double passivation strategy to guide neural growth. It consists of an array of 4 x 4 g-SGFETs with 2 SLG electrodes and 2 ITO electrodes at the corners. The tracks of the device are made of ITO in the central part of the device, in order to keep it transparent and facilitate microscopy experiments.

SU8 is a epoxy based, negative resist developed by IBM to be used in Micro-Electro-Mechanical-Systems (MEMS) [252]. Despite being the go-to material for many electromechanical applications, SU8 has limited biological application [253] because of its low surface energy [254] and the high content of surface epoxy rings, that create a low wettability surface [255]. SU8's WCA is normally reported to be around 105 º [256, 254] but can be lowered down to the 15º - 20º range by using oxygen plasma treatments, which enhances cell proliferation [256].

Al_2O_3 has been proven to be a biocompatible metal oxide with a relatively low WCA (55º) [257] and thus, higher hydrophilicity than SU8. Work from other groups has shown the ability of metal oxides, and Al_2O_3 in particular, to support neuronal cultures and even guide neurites along predefine paths [258]. In [258], Torimitsu *et al.*, showed that neurite growth cones spread further and grow more

vigorously on Al_2O_3, among other metal oxides, than on bare silica glass, which is and indicative of better neuron adhesion to the substrate [259]. Torimitsu *et al.* also showed that neurites prefer to adhere to Al_2O_3 over silica glass and the ability to guide dendrite development by patterning stripes of metal oxides on glass. All these results made us choose Al_2O_3 and SU8 as the two passivation materials to attract and repel, respectively, neuronal growth.

For our experiments we decided to use the difference in the hydrophilic properties of the Al_2O_3 and SU8 as passivation materials for an array of 4 by 4 graphene Solution Gated Field Effect Transistors (g-SGFET). A g-SGFET is a transistor in which the resistance of the graphene channel is modulated by an electrolyte gate. As a consequence, the current flowing between the drain and source is sensitive to potential and ion concentration changes in the electrolyte, making them useful biosensing tools [260]. Our group has optimized the fabrication of g-SGFET over many years [261] and successfully used them to detect relevant neural biomarkers [66, 32, 262].

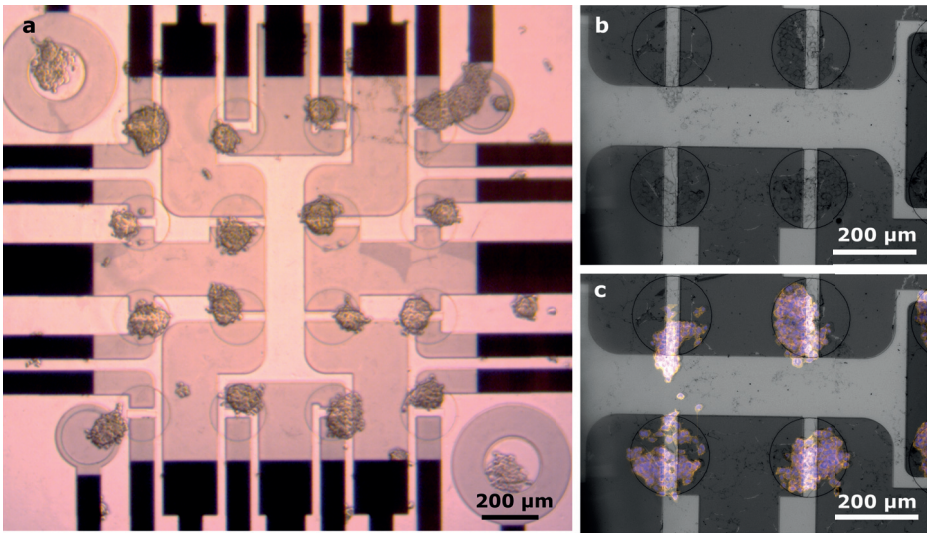

Figure 4.2: Neuro 2A cell culture on top of the g-SGFET devices - a) Bright field image of the active area of the 4x4 transistor array showing the preferential adhesion of the Neuro 2A cells to the Al_2O_3 regions. b) Bright field image of the center of the array and c) fluorescence image superposed on top of b) showing the cytoskeleton (Rhodamine Phalloidin in orange) and the nucleus (DAPI in blue) of the cells attached to the Al_2O_3 areas. Additional images can be found on the repository [263].

For the controlled neural growth experiments, we passivated the whole device but the transistor channel and the electrodes openings with a layer of 50 nm thick Al_2O_3. We then applied a second layer of SU8 passivation over the whole device leaving exposed a circular area of 200 nm diameter centered around each of the 16

transistors in the array and the 4 electrodes in the corners, as shown in Figure 4.1. To test the ability of this device to attract cells to the recording sites, we cultured Neuro 2A cancer cells[1] in collaboration with the group of Prof. Kostas Kostarelos, The University of Manchester. We tried two different types of experiments; in the first one, we coated the devices with a layer of Poly-D-Lysine (PDL) before seeding the cells; in the second one we left the devices uncoated. The protein coated devices showed uniform cell adhesion across the whole device, while the uncoated devices showed that the cells were repelled by the SU8 passivation and exibited a preferential adhesion on top of the exposed Al_2O_3 regions. Figure 4.2a shows an example of this behaviour; the bright field image of the whole device active area shows that the cells tend to agglutinate on top of the exposed Al_2O_3 regions. Figures 4.2 b and c show a close up of the central area of the array in bright field and fluorescence imaging superposed on top of the bright field image, respectively. The fluorescence imaging was done by labeling the cells with Rhodamine Phalloidin (orange) and DAPI (blue) that mark the cytoskeleton and the nucleus respectively. Figure 4.2 b and c confirm that the Neuro 2A cells cultured on top of these devices preferentially grow on top of the more hydrophilic Al_2O_3 regions.

Altogether the experiments shown in this section prove that combining different passivation materials, with different surface energies and WCA, it is possible to attract cell growth to specific target areas of an electrical biosensing device. Despite successful, this approach lacks the precise control needed to finely guide neuronal network growth, so we decided to look for a different control method.

4.3 Microcontact Printing of Proteins

Protein icrocontact printing (μCP) is a technique in which a protein ink is applied to a stamp and pressed into a surface in order to transfer the proteins with a predefined pattern [264]. In our particular case, we use protein μCP to print cell attracting proteins in a cell non-attractive substrate to be able to control neural growth.

Protein μCP was first developed by Whitesides *et al.* in 1994 [265]. This technique consists in pouring an elastomer, normally PDMS, on an inverted master mold, curing it to obtain a stamp, apply a protein ink to coat the surface of the stamp and press it against the target substrate in order to transfer proteins with a desired pattern. The whole process is depicted in Figure 4.3. PDMS stamps are hydrophobic, with WCA between 115º and 95º [264], and promote

[1] ATCC, CCL-131

the spontaneous and non-specific adsorption of the proteins in the ink. The adhesion of proteins to the PDMS stamp in also self-limiting, which ensures that only a protein monolayer covers the PDMS surface and the excess of proteins in the ink can be simply rinsed away [266]. The protein concentration in the ink and the duration of the coating process are crucial parameters to ensure a complete protein coverage of the stamp [267]. Regarding the protein transfer to the substrate, the chemical composition of the substrate does not play a role in the attachment;, the only relevant parameter is the difference in wettability between the stamp and the target substrate. Proteins transfer if the substrate has a higher work of adhesion than the stamp or is more wettable [264]. In naturally hydrophobic substrates, a common strategy is to use O_2 plasma to increase the wettability of the substrate and facilitate the transfer of proteins. However, in our case, it is not always possible to use O_2 plasma since it will destroy the SLG electrodes. Regarding the resolution of the μCP technique, the high molecular weight and the large interaction area allow to print arrays of individual proteins [267] when a sufficiently stiff PDMS is used and the master is created with electron-beam photolitography [268]. The flexibility of the μCP stamps allows to print in non-planar substrates and it is also possible to print two or more types of proteins in a single substrate. The easiest way to achieve this is to stamp one protein and add a solution containing the second protein to the substrate, so the second protein type can be adsorbed from the solution [266]. By sampling multiple patterns, designs with up to 16 different proteins have been created [269, 270] and, since a protein layer is in general more hydrophilic that the PDMS substrate, it is possible to stack proteins on top of each other.

To fabricate the SU8 master mold for our μCP experiments we use a 4" Si wafer on which we deposit a 2.5 μm thick SU8[2] seed layer. Following this step, we perform a plasma activation of the SU8 layer with an oxygen plasma process (300 W, 1 minute, 50 sccm O_2) in order to improve the adhesion of the second layer. After that we proceed to create the features of the master using a 40 μm thick layer of SU8[3]; finally, we anneal the wafer at 300 ^{o}C for 2 hours in vacuum. The detailed parameters of the photolitography steps can be found in Appendix C.3. When the master mold is ready, we coat the surface with HMDS to facilitate the release of the PDMS, pour a degassed PDMS[4] and cure it in an oven at 90^{o} C for 2 hours. We then release the PDMS layer and cut the individual stamps using a hole puncher.

[2]SU8 2005, MicroChemicals GmbH
[3]SU8 2025, MicroChemicals GmbH
[4]Sylgard 184 Silicone Elastomer Base with Sylgard 184 Silicone Elastomer Curing Agent, 10:1 ratio

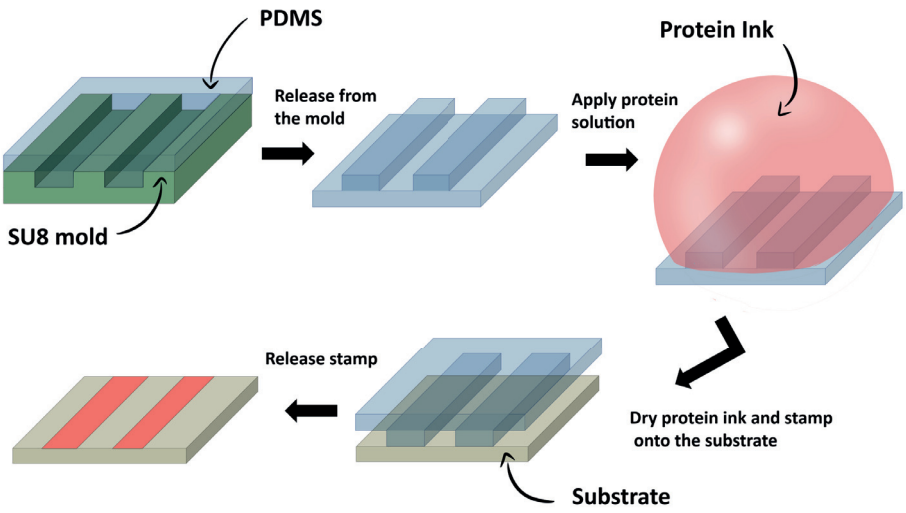

Figure 4.3: Microcontact printing (μCP) process - An SU8 master mold is covered with PDMS and then cured to create the stamp. The mold is released and submerged in a protein ink so the molecules are adsorbed at the stamp surface and the protein excess is rinsed away. The PDMS stamp is pressed against the target substrate in order to transfer the proteins and finally peeled off.

For these experiments we used four different designs. The first design has a hexagonal layout in which the nodes designed to house the neurons' soma match the position of the electrodes in the rigid SLG MEA design (Figure 2.6). The nodes have a diameter of 30 μm and they are connected to all neighbour nodes by 10 μm wide tracks meant to guide the neurites (Figure 4.4 a). The other three designs share the same basic layout; an external hexagon that has nodes placed in the position where the 100 μm diameter electrodes are in the rigid SLG MEA design (Figure 2.6) and a triangular mesh inside that hexagon composed of equilateral triangles with 75 μm long sides. At each vertex of the triangles there is a node meant to hold the soma of a neuron (Figure 4.4 b). The differences between the three designs are the sizes of the nodes and the tracks: 4 μm wide tracks and 12 μm diameter nodes for the first one, 8 μm wide tracks and 20 μm diameter nodes for the second one and 6 μm wide tracks and 16 μm diameter nodes for the third design.

Since our intention for these experiments was to pattern neurons, our protein ink was made of PDL[5] diluted in 0.1 M PBS to a concentration of 10 μg/mL. In order to maintain sterile conditions, all the inking protocol described below was done inside a class 2 biosafety cabinet[6] and the PDMS stamps and the substrates

[5]Sigma-Aldrich, P6407
[6]HERA Safe, Heraeus

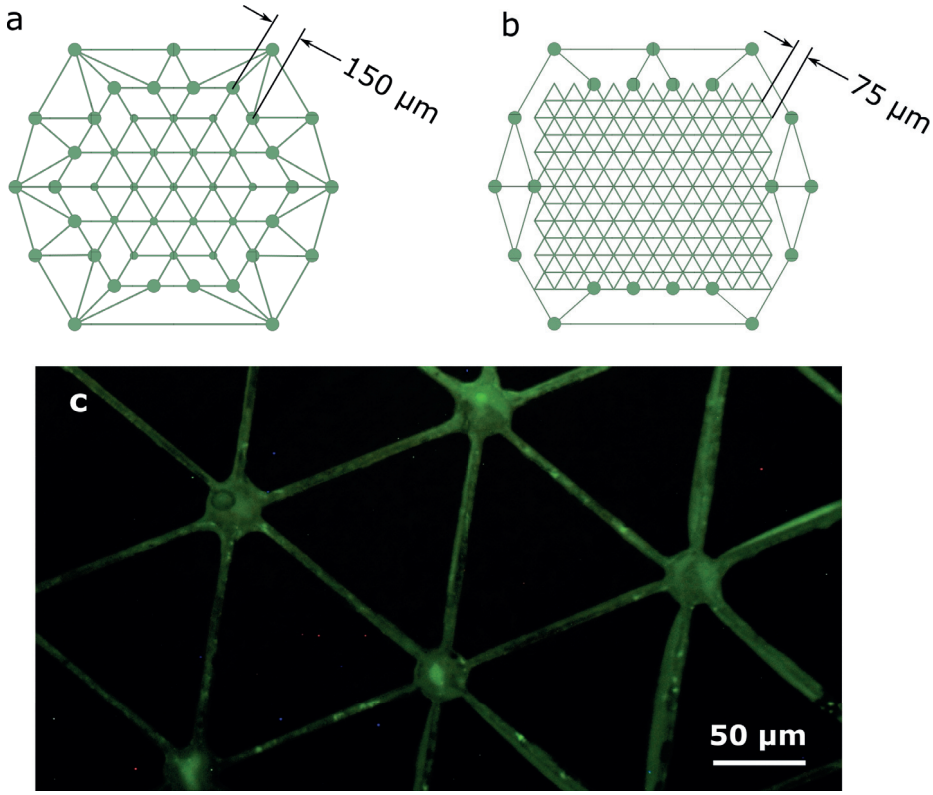

Figure 4.4: μCP stamp designs - a) Low density design with 30 μm diameter nodes and 10 μm wide tracks. b) High density design used in three different variants: 4 μm wide tracks and 12 μm nodes, 8 μm wide tracks and 20 μm nodes and 6 μm wide tracks and 16 μm nodes. c) Fluorescence image of a μCP process done with FITC label PLL and the low density stamp design.

were sterilized by immersion in 70 % ethanol during 15 minutes, left to dry and thoroughly rinsed with PBS 3 times. The inking protocol was adapted from [271] and [272] and it has the following steps:

1. Cover the top of the stamp with the PDL ink for 15 minutes
2. Blow dry with nitrogen
3. Place on top of the substrate for 15 minutes under 50 grams of weight
4. Rinse the substrate once with PBS and once with sterile DIW water

To test the suitability of the inking protocol and the different PDMS stamp design, we tested the protocol using FITC labelled PLL[7] printed on top of glass samples covered with a layer of photodefineable polyimide[8] and acquiring fluorescence images, like the one in Figure 4.4c. Using this method, we detected problems with the stamps that have 4 and 6 μm wide tracks. Due to the high aspect ratio of the features, the PDMS stamp could not replicate faithfully the master mold, and the tracks of the stamps were shorter and thinner than those in the SU8 mold. A potential fix to that problem could be to reduce the depth of the SU8 features in the master mold; however, in order to avoid the PDMS stamp collapsing during the inking process, we ruled out that idea. The other 2 designs, the one shown in Figure 4.4a and the 8 μm wide tracks with 20 μm diameter nodes, worked perfectly, yielding sharply defined protein patterns.

Following the optimization of the inking protocol and the selection of the 2 stamp designs that worked best, we proceed to culture rat E17 cortex neurons dissociated and cultured with the protocol described in Appendix D.1, with the exception that the substrates were not coated with PDL, but printed using PDL and the μCP printing protocol described in this section. Figure 4.5 shows the evolution of a primary cortical neuron culture, from DIV 5 to DIV 23, on top of a photodefineable PI substrate to which a μCP inking process was applied using the stamp of Figure 4.4b with 8 μm wide tracks and 20 μm diameter nodes. We can see how the neural network progressively develops from an incomplete network at DIV 5, where there are few connected nodes, to DIV 8, where there most of the nodes have bridged, to DIV 10, where all the pattern is finally covered by the neurons. At DIV 15 we see that the connections through the tracks strengthens, with thicker bundles of neurites growing over them. However, we can start to appreciate that the culture overcomes the pattern in some places, spreading neurites outside of it. We can also start to appreciate some instances of cellular death. The situation remains mostly unchanged at DIV18, with the

[7] Sigma-Aldrich, P3543
[8] HD8820, HD Microsystems

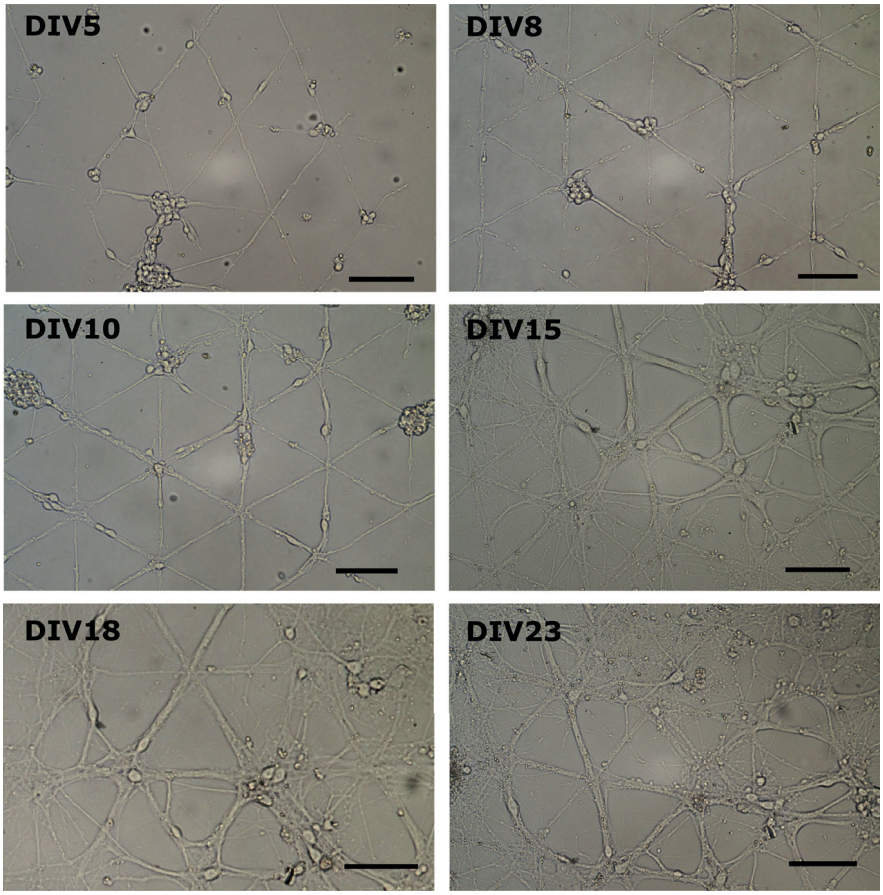

Figure 4.5: Cortex neurons grown on μCP patterned substrates - Evolution of a cortical neural culture from DIV5 to DIV 23. The images show how the neural networks develops following the PDL printed in the substrate and how from DIV10 on the growth starts to overcome the patterning. The stamp used is that of Figure 4.4b with 8 μm wide tracks and 20 μm diameter nodes. The scale bar is 100 μm. Additional images can be found on the repository [273].

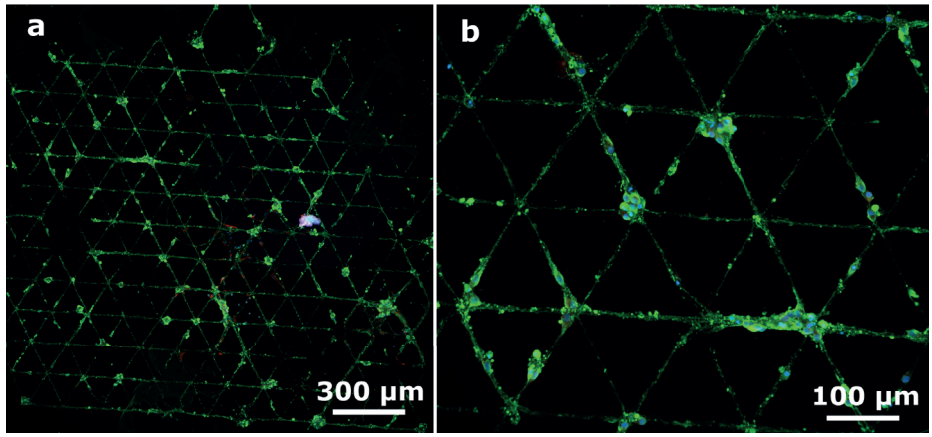

Figure 4.6: Inmunofluorescence image of a μCP grown neural network - In green is the neuron marker with the Beta-Tubluin antibody, blue marks the nuclei with DAPI and red marks the glia with GFAP antibody. Taken at DIV 14 and printed with the 8 μm tracks and 20 μm diameter nodes stamp design.

neurites growing outside the protein pattern and some cellular death. Finally, at DIV 23 we can appreciate how the patterned neural network has lost most of its initial structure, and many neurites and somas are now attached to regions where initially there was no protein. Also, we can observe a higher degree of cellular death.

We also performed inmunofluorescence imaging to asses the networks at DIV 14 (see Figure 4.6). To do so, we first immobilized the primary antibodies PE anti-tubulin β 3 (TUBB3)[9] and GFAP antibody[10] that stain the neuron structures and glia cells, respectively. After an overnight incubation, we added the secondary antibodies Alexa Fluor 488 Donkey x Mouse[11] and Alexa Fluor 594 Donkey x Mouse[12] to couple to the primary beta-tubulin and GFAP antibodies respectively. Finally, we added DAPI[13] to mark the DNA rich zones, i.e. the nuclei. These inmunofluorescence measurements were done in collaboration with the group of Prof. Xavier Navarro, at the Neuroscience Institute of the UAB.

After testing that we could grow patterned neural networks on top of photodefineable PI, we went ahead and try to adapt the μCP protocol to be able to print a protein pattern aligned with the electrodes in our rigid SLG MEA. To do so, we adapted a 3-axis micromanipulator to be clamped to the stage of an upright microscope and build a methacrylate arm that allowed us to hold the PDMS stamp during the alignment procedure. The alignment method was

[9] MMS-435P/801202, BioLegend
[10] AB5804, Millipore
[11] A21202, Invitrogen
[12] A21207, Invitrogen
[13] D9564-10MG, Sigma-Aldrich

working but the problem with these experiments was to control the pressure applied to the stamp during the protein transfer process. When performing μCP on regular substrates, we ensured that there was enough pressure to transfer the proteins without collapsing the features by placing a 50 grams weight on top of the stamp. However, this was more difficult to control when using the micromanipulator, we were not able to find the right balance between making proper contact and collapsing the stamp features.

Another problem that is apparent from Figure 4.5 is that, even with the 8 μm wide tracks, there are some somas that can grow on them; this indicates that our ideal initial scenario of somas attaching only to the nodes and neurites connecting them through the tracks is not realistic. The inability to control the cell body placement limits the design possibilities available to our protocol. For example, it prevents to control the directionality of the network. A common strategy to achieve this is to make long tracks that separate the node that transmits the information from the one who receives it [274]. Since the neural communication follows the dendrite-soma-axon direction and dendrites do not grow longer than 500 μm [67], separating the nodes long distances ensures that only axons reach from one node to the other, making the communication unidirectional. With our technique a soma can attach to the track so close to the target node that dendrites can reach it; thus, our approach does not ensure the unidirectional connectivity of the network.

As a short summary of this section, we successfully printed PDL on glass and photodefineable PI using μCP. Furthermore, we were able to successfully grow primary cortex neurons that followed the patterned PDL and monitor their development form DIV 5 up to DIV 23. However, μCP is not without limitations. Of special relevance for us were the impossibility to restrict the somas attachment to the nodes, our inability to use this technique to pattern the surface of MEA and the loss of network definition from DIV 15 on. Because of these reasons, we looked for a more precise, permanent and MEA compatible method to guide the development of neural networks.

4.4 PDMS microstructuring for patterned neural growth

Microstructuring is an alternative approach to the chemical attraction/repulsion methods we have described in sections 4.3 and 4.2 that relies in physically constraining the space available for neurons to attach and grow [240]. In its most simplest form, engineering a neural network with microstructures consists in

patterning the culture substrate with wells that have a diameter in the range of the few tens of micrometers and walls sufficiently tall to prevent cells to escape. Then, by adding connecting conducts between the wells, we can allow neurons from different wells to communicate. By carefully engineering the dimensions and length of those interconnecting conducts, it is possible to allow only certain types of neurites to grow across [274]. By adapting the shape and dimensions of the well it is also possible to control the directionality of the communication between neurons in different wells [275]. To place the neurons inside the wells they are normally seed in excess, so a fraction of the neurons get trapped in the micro-structured wells and the excess of cells that lay outside the microstructures can be washed away [276, 277]. Another alternative to place the neurons is by manually depositing them in the selected well by using micropipettes or hollow AFM tips [278]. Although this technique is much slower and has a lower throughput it allows a great degree of control, making possible, for example, to combine different types of cells in a single culture. Despite its novelty, there are already some companies offering commercial equipment to perform such tasks [279].

The use of microstructures to control neural growth can be divided in two main strategies, depending on the way the microstructure is built. The features can be patterned directly in the culture substrate or they can be made independently and then attached to the substrate. The first approach consists in directly etching the surface of the substrate we want to use for the culture. This is normally done by patterning the microstructures on the substrate with a permanent photoresist [280] or by directly etching the features in the substrate using plasma or dry reactive ion etching [281]. The second fabrication strategy uses lithography or micromachining to fabricate a master mold over which PDMS is poured. From this process we can obtain PDMS sheets that contain the features needed to immobilize neurons and guide their connectivity [282, 283]. Then the PDMS layer is immobilized on top of the culture substrate by plasma bonding or just held together by hydrophilic interaction [284]. This second strategy offers important advantages. If the bonding to the substrate is reversible, the PDMS structure can be reused. It can also be taken away from the culture at any point, allowing the cells a higher degree of freedom to continue their development [285]. In addition, this technique is compatible with MEA technology and allows for the reusability of the MEA at the end of the culture. These advantages, together with the availability of companies that offer custom made PDMS structures made us choose this last fabrication strategy.

The PDMS structures used in this section were designed by Sean Weaver from the Laboratory of Biosensors and Bioelectronics (LBB - ETH) in the group

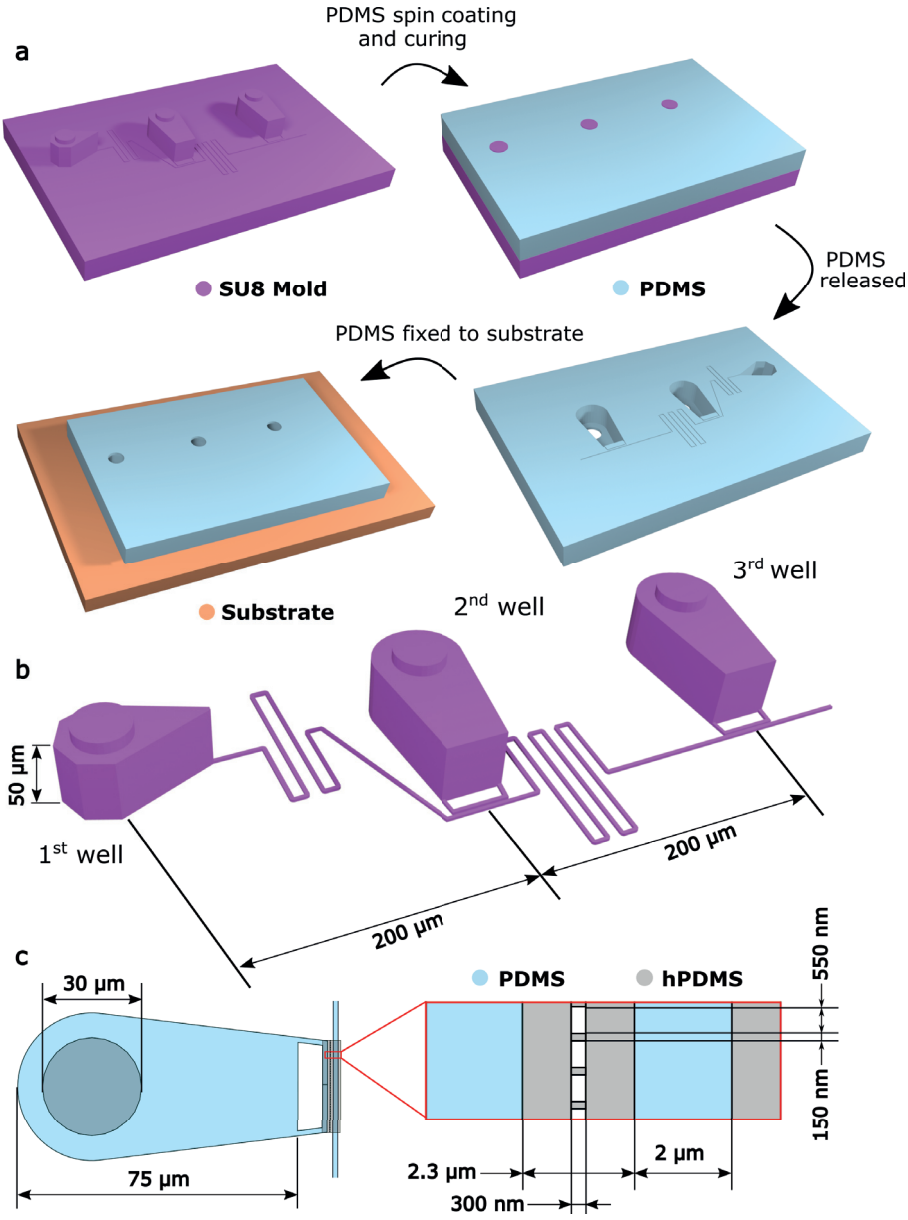

Figure 4.7: PDMS microstructures for neural guidance - a) Steps involved in the fabrication of the PDMS microstructures. The PDMS is spin coated and cured on top of the SU8 master mold, then peeled away and attached to the culture substrate. b) Detailed view of the SU8 master mold used for these experiments. c) Design specifications of the PDMS structure well, showing which parts are cast with PDMS and with hPDMS.

of Prof. Janos Vöros. All the experiments described were carried out during a research stay at the LBB-ETH.

The PDMS structures were fabricated by casting a stiffer PDMS version developed by IBM, known as hPDMS [268], on a master mold in which the sub micrometer features were etched in the silicon and the rest were molded in SU8. The fabrication of the master mold and the PDMS structures was done by Wunderlichips [286], a spin-off company of the LBB-ETH group, following the steps depicted in Figure 4.7a. A step by step description of the fabrication process can be found in [287].

The idea behind the design of the PDMS structures used in this section is to study how the signals elicited by electric stimulation in a well transfer to the two neighbouring wells at a localized synaptic region. The PDMS structure consisted of 3 oval-like wells 50 μm tall, 60 μm wide and 75 μm long separated 200 μm from each other. The wells have a 30 μm diameter opening in the top to allow the neurons to get in during the seeding. The 3 wells are communicated through a 2 x 2 μm^2 tunnel sprouting from the first well, designed to be long enough than only axons can reach the other two wells (Figure 4.7b). At the connecting point between wells, there is a 300 nm gap communicated by an array of 150 x 300 nm nanochannels separated 550 nm; the nanochannels are designed so only the dendritic spines can go through (see Figure 4.7c).

Before attaching the structures to the culture substrate we first cleaned it with oxygen plasma (2 minutes at 15 W) and then coated it with a PDL solution. If the substrate was a MEA and alignment between the structures and the electrodes was needed, we put a drop of DIW on the active area of the MEA and place the PDMS structure inside the drop. As the drop was drying, the PDMS structure was moved manually with a set of tweezers until it was properly aligned over the electrodes. Then, the MEA culture chamber was filled with PBS and the whole device was put inside a desiccator in order to remove the air bubbles trapped in the structure. Once we made sure that no air was left inside by inspecting it with a microscope, we replaced half of liquid in the culture chamber with the neural culture media five times. This was done to avoid exposing the wells of PDMS to air and minimize the formation of new bubbles in the structure. Finally, hippocampal neurons, obtained following the protocol described in Appendix D.2, were seeded on the devices at a density of 250 000 - 300 000 cells/cm^2 and at DIV 2 we added between 10^4 and 10^5 viral particles per cell of the adeno-associated virus mRuby3[14] and jGCaMP8m[15] [231] to label the neuron structure and calcium dynamics, respectively.

[14] scAAV-DJ/2-hSyn1-chI-mRuby3-SV40p(A), created by the Viral Vector Facility at University of Zurich

[15] ssAAV-DJ/2-hSyn1-jGCaMP8m-WPRE-SV40p(A), Janelia

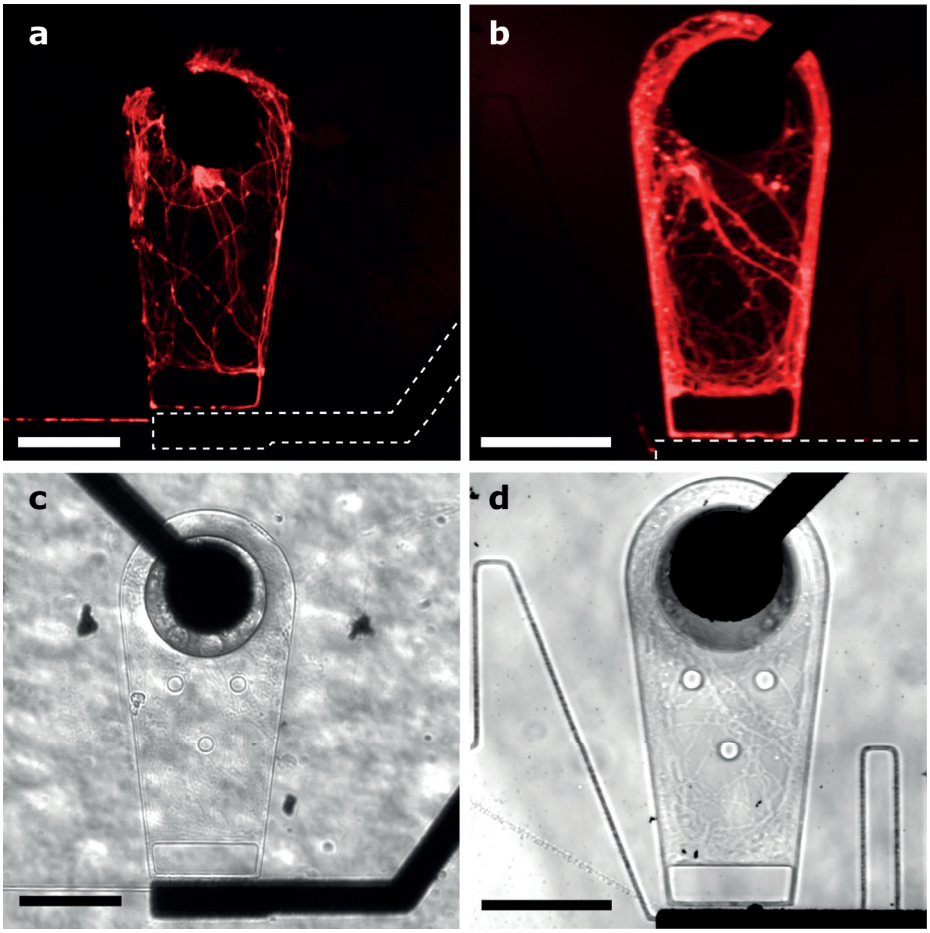

Figure 4.8: CSLM images of the cells grown in the PDMS wells - a) and b) images from a third and a second well, respectively, in a hippocampal culture at DIV 14. We can see the neurites from the neurons inside the wells being guided to meet with the axons coming from the first well. The dashed white line marks the position of the square microelectrodes. c) and d) show the bright field images of a) and b) respectively. All scale bars are 40 μm.

Figure 4.8 and 4.9 show images taken using a CLSM[16] of hippocampal neuron cultures (DIV 14) grown inside the PDMS structures attached to a rGO ultrathin MEA (see Chapter 3). Figures 4.8a and b show the third and the second well of a microstructure, respectively. We can see the neurites spreading from the soma, going around the perimeter of the well and growing into the channel that guides them towards the nanochannels; these nanochannels are occluded by the opaque MEA electrodes, as shown in the bright field images (Figure 4.8c and d). In Figure 4.9a we can see two complete neural networks. Because the MEA and the PDMS structures are slightly misaligned, the nanochannel area is visible. The structure at the top shows how the axon grows from the soma and into the channel of the first well, reaching the second. In the second well we can see how the neurites extend to the nanochannel region, where we can observe signs of the axons and the dendrites crossing over. However, the discontinuities in fluorescence along the axon could suggest that this axon died previously to this measurement, an observation that is supported by the fact that it never reached the third well. In the bottom network from Figure 4.9a, no soma can be observed in the first well, it is either hidden above the electrode or possibly outside the well projecting the axons down. In this structure we can see that the axon looks healthier and that has reached the second and third wells. The crossing of neurites in the nanochannel area of the second well it is easy to spot in the zoomed Figure 4.9b; meanwhile, it seems like there is no crossing in the third well.

Figure 4.9 illustrates quite well the strengths of our PDMS microstructuring technique as well as some key features that we need to improve in order to extract the full potential of this technique. Since dendritic spines typical sizes range in the few hundred of nanometers [288], we are not able to resolve it using this low magnification. The fact that in Figure 4.9b confirms that we are able to see structures crossing from the axon to the dendrite channel, strongly suggesting that not only the dendritic spines but whole neurites cross the nanochannels. This behaviour is caused by the difficulty to properly cast the nanochannels in the PDMS, since they are only 100 nm wide. That, together with the fact that when the DIW used to align the PDMS structures evaporates can make the nanochannels collapse, makes that often the whole communicating nanochannel structure is not properly defined and leads to neurites crossing over. Another consideration to take into account is the fact that the small opening at the top of the wells (only 30 μm in diameter) does not allow for enough medium circulation and elimination of the cells waste products, which is detrimental for the health of the culture.

[16] FluoView3000 CLSM, Olympus

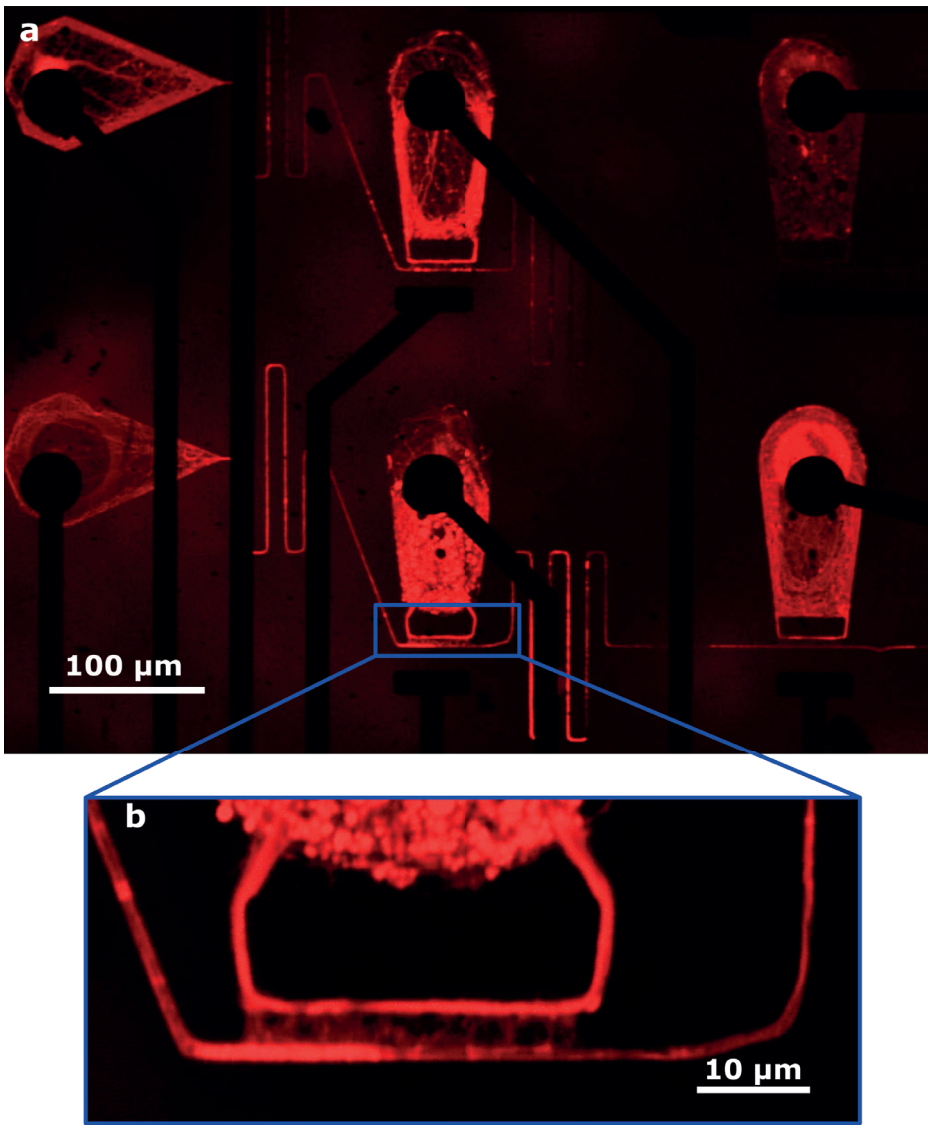

Figure 4.9: CSLM images of the cells grown in the PDMS structures - a) Two complete PDMS structures with neurons growing inside them. We can see the axons extending from the first wells down to the second (top) and third (bottom) wells. c) Zoom in of the second well in the bottom structure, showing the detail of the neurites growing through the nanochannels. Additional images can be found on the repository [239].

These problems have been taken into account in the design of the next version of these PDMS structures, with bigger openings to allow for better media exchange, marginally bigger nanochannels spaced further apart to avoid them collapsing and distributed along a longer perimeter. Additionally, it would be interesting to label axons, dendrites and dendritic spines separately, in order to get a clearer view of the interaction of the neurons in the different wells.

4.5 Conclusion

Controlled geometry neural networks offer the possibility to study the properties of the neural signals and its propagation without the noise and interference from the rest of the culture that is present when using random networks, yielding higher throughput that alternative methods, such as patch clamp. Altogether, custom geometry neural networks are a valuable tool to reliably study brain circuit and it is necessary to further develop them in order to harvest their full potential. This chapter describes three different strategies that were explored to control and guide neural growth.

The first strategy exploited the different wettability characteristics of the two types of passivation used in the fabrication of g-SGFET devices. The main advantage of this method is its durability; once the low and high adhesion materials are photolithographically patterned in the substrate, they can be cleaned and reutilized as many times as needed. On the down side, it is the strategy that allows for the lesser degree of control over the neurons, both in the control of the initial adhesion and the control in the development of the network.

The second strategy involved creating patterns of adhesive proteins using μCP techniques. We tried four different stamps designs and optimized the size of the nodes and the connecting track in order to successfully get reliable patterns. We followed the development of the network up to DIV 23; we saw how after DIV 15, the control we had over the development of the networks was gradually lost. That, together with the difficulties we had integrating this technique in our MEA were the reasons for which we looked into other control strategies.

The final method we tested was the use of microstructures to constrain neural development. During a research stay at the LBB-ETH group of Prof. Janos Vorös, we developed a strategy to implement PDMS microstructuring together with our rGO MEA and achieve reliable and long lasting custom neural networks. However, this approach is not without problems, and we were unable to achieve precise control of the synaptic spines due to complications in the casting process. This issue has been addressed in the new generation of PDMS microstructures, where increased space for neuron growth and the addition of nanochannels around

the whole perimeter of the well have managed to successfully control synaptic connectivity [287].

5

Conclusion and Outlook

Me gusta cuando tú hablas
y se calla Neruda

Ecuador
Benjamín Prado

5.1 Conclusions

Advancements in neuroscience have been made possible thanks to the progressive development of new tools and techniques that allow us to image and record more and more aspects of the nervous system. From the primitive lesion studies [18, 19] to the development of neural imaging [22, 23, 24, 25] and electrical recording techniques [26, 27, 29], technological developments have aided researchers with the necessary means to unravel the way our brains work. With this in mind, the main objective of this doctoral thesis was to explore the capabilities of single layer graphene (SLG) and reduced graphene oxide (rGO) to fabricate electrodes and microelectrode arrays (MEA) that expand the capabilities of current neuroscientific techniques to study the nervous system.

In Chapter 2 we discussed the fabrication and characterization of low noise rigid SLG MEAs and used them to record electrical activity in cortical primary cultures. The electrodes present on these MEA have a relatively high impedance, with the impedance modulus in the range of few MOhms at 1 kHz. These

electrodes behave almost as ideal polarizable electrodes, with a phase close to -90 º, in the frequency range between 1 and 10^5 kHz. This capacitive behaviour translates into a low V_{RMS} noise for these electrodes, yielding values of 2 μV integrated in the 5 Hz to 5 kHz frequency range. Using these SLG electrodes, we demonstrated high SNR recordings of individual neurons in cortical cultures. In addition to the rigid MEA, we have fabricated flexible and transparent electrodes and MEA to record electroretinograms (ERG). Since ERG are signals whose frequencies lie in the range of few hertz to few hundreds hertz, the study of the impedance and noise of these flexible SLG electrodes was centered in that frequency range. The Bode plot of these electrodes also showed an almost purely capacitive behaviour, with the phase lying close to -90 º, and the module of the impedance measured at 100 Hz ranges from the few MOhm for the 200 μm diameter electrodes to the tens of kOhm for the 0.8 mm diameter electrodes. Likewise, the V_{RMS} noise values, when the PSD is integrated between 0.5 and 300 Hz, yield around 5 and 2 μV for the two different electrode diameters. We have systematically benchmarked the SLG macroelectrodes against the current state of the art for animal recordings, in a commercially available clinical set up. Our results concluded that the SLG electrodes are able to follow the photoreceptor degeneration on a retinitis pigmentosa animal model, recording signals that are not significantly different to that from the commercial electrodes along the degeneration process. Additionally, and taking advantage of graphene's transparency, we have used the transparent MEA probes to record ERG. These multi-electrode probes allow us to obtain spatial information of the corneal potential; further, the flexible MEA are capable of capturing all ERG features at different points of the corneal surface. We used the MEA ERG to try to detect induced lesion on the retina, however our attempts were not successful. Further improvements to the MEA ERG will be discussed in section 5.2.

In Chapter 3 we present the fabrication of novel rGO films and describe the microfabrication techniques that allow us to obtain micrometer sized electrodes with high yields. The characterization of these MEA demonstrate their high charge injection capabilities, with CIC_{max} up to 7 mC/cm^2; low interfacial capacitance, down to the few kOhm at 1 kHz for 100 μm diameter electrodes; and low V_{RMS} noise levels, in the range of 3 μV when the PSD is integrated between 5 Hz and 4 kHz. We have also proved the capability of these MEA to sustain healthy hippocampal primary cultures, up to DIV 23, and record from them a wide variety of spike shapes and sizes. We were also able to perform spike sorting techniques using the duration and amplitude of the spike as extracted features, methods that are only useful in recordings with high SNR [173]. Additionally, we have used the rGO MEA to deliver electrical stimulation in hippocampal

cultures, eliciting action potentials using a wide variety of current and voltage pulses in both random and guided cultures and studying spike timing, relative stimulus efficacy and the spatial response of the stimulus.

In Chapter 4 we have studied three different methods to guide neural growth and build neural networks with controlled geometry. In the first approach, we exploit the different wetting characteristics of the materials used to passivate the devices to attract the neurons close to the SLG sensors. Despite being the most permanent method, this the approach that has the lowest degree of control of all three methods, attracting a high number of cells onto a relatively small area. In order to improve on this method, we developed a μCP approach, stamping substrates cell adhesive proteins in specific patterns and culturing primary cortex neurons on top of them. Despite initial success, at approximately DIV 15 we start to loose the pattern definition, as the cells begin to spread the proteins and grow into areas that initially were non-adhesive. In addition, we were unable to properly align the μCP patterns on top of our graphene-based MEA, which led us to pursue a different approach. The third method described in this thesis consisted in using PDMS structures aligned on top of MEA to guide neuronal growth. Despite achieving reliable and long lasting neural networks, we were unable to precisely control the formation of spikes due to problems with the PDMS molds. An optimization strategy will be further discussed in section 5.2.

5.2 Outlook

In this thesis we have present different graphene-based electrode technologies as promising tools to perform *in vitro* and *in vivo* neuroscience studies. Additionally, we have presented three different approaches to guide neural growth and build neural networks with predefined geometry, that could be used to study *in vitro* specific brain circuits. In the following paragraphs we will discuss approaches that can be taken to further improve different aspects of these techniques.

Regarding the graphene electrodes for ERG recordings, a key aspect to improve is the handling and manipulation of the electrodes, specially of the ERG MEA, that need precise and reproducible placement in order to obtain reproducible measurements in the same patient or to compare measurements across patients. An interesting approach to improve this aspect would be to substitute the PI passivation for viscoelastic isolating hydrogels [174]. These passivation materials have been shown to conform to intricate biological tissue, such as brain or heart tissue. Additionally, after being removed from the tissue, they retain the adapted form for up to an hour, what would greatly help when transferring the probe from animal to animal.

Concerning the rGO electrodes, it would be interesting to further their electrochemical properties. In particular, it would be important to understand the origin of the asymmetry of the positive and negative voltage regimes in the cyclic voltammetry curves, shown in Figure 3.6. The shape of the CV could be a hint that the processes by which the rGO electrodes inject charge in the electrolyte is governed by an intercalation pseudocapacity behaviour, such those discussed in [289] and [290]. Furthermore, the difference in the anodic and cathodic pulse shapes (see Figure 3.10) might indicate that the electrode/electrolyte interfase has a different behaviour for positive that for negative voltages. The exponential shape of the capacitive drop in the cathodic pulse contrast with the linear capacitive drop exhibited by the anodic phase, pointing out that the first one could be dominated by a CPE and the second one by a pure capacitor [291]. Exploring the electrode/electrolyte interfase of the rGO electrodes by performing EIS at different voltages could help us understand this issue.

Regarding the rGO electrode arrays, a bigger statistical population would be needed to obtain more robust conclusions in the stimulation efficacy studies. Ideally, primary neuron cultures other than hippocampal should be used to broaden the conclusion drawn from those experiments. Another promising field for the rGO MEA to expand is that of *in vivo* neuroscience. The combination of high charge injection capacity, low interfacial impedance, stability in biological conditions and its ability to be integrated in microfabricated probes with high yield, makes rGO electrodes and excellent candidate to build neural devices for bidirectionally interacting with the nervous system [13]. It is worth mentioning that the rGO technology discussed in this thesis has been transferred to the spin-off INBRAIN Neuroelectronics to develop implantable neural interfaces for neuromodulation therapies [292].

With regard to the μCP patterning, a way to align the stamp with the electrodes of the MEA must be devised. An approach to this could be to use a micromanipulator with an adaptor to hold the PDMS stamp perfectly parallel to the surface of the MEA, in order to ensure that all the features in the stamp make uniform contact. Additionally, a spring loaded mechanism could be added to the micromanipulator, ensuring that not too much pressure is put on the PDMS stamp, avoiding the collapse of the features. Concerning the PDMS microstructures to control the formation of synapses, a new structure has already been designed, with bigger wells that allow for a better exchange of culture culture media and overall improved culture health. Increasing the spacing the nanochannels reduce the chance of collapse and distributing them all along the perimeter of the wealth allows for a higher chance of dendritic spines crossing over the postsynaptic region. These structures have already proven the formation

of localized synapses [287]. However, their integration with MEA is still to be demonstrated.

To conclude, we can compare SLG and rGO and briefly discuss for which application each material is better suited. Due to its transparency, SLG should be the material of choice for applications in which light transmission is important, as we have already proven with the ERG experiments shown in section 2.3. SLG transparency also plays an important role when performing inverted microscopy in neural cultures or when electrical recording are combined with optogenetic stimulation, since completely transparent MEAs that allow for seamless imaging of the studied tissue can be fabricated. On the other hand, when the application requires the electrical stimulation of nervous tissue, rGO should be the material of choice since SLG's low capacitance is unable to inject enough current to elicit electrical activity. When comparing the V_{RMS} noise of the electrodes fabricated with these two materials, we can see that both are really similar, in the range of 2 to 3 μV. However it is worth noting that the recordings from where the PSD data for the rGO electrodes was obtained were not performed inside a Faraday cage, as the SLG recordings were. If both recording were done under the same conditions, the lower impedance of the rGO electrodes would translate into lower pickup noise. Additionally, in the case of rGO electrodes we would most likely observe an increased amplitude of the recorded signal and lower frequency dependant attenuation and phase shifts due to a lower voltage drop in the electrode/amplifier voltage divider, compared to the case of SLG electrodes [293]. A promising approach to find a way around this dichotomy could be to combine SLG and rGO electrodes in the same device, using SLG in areas where transparency and flexibility is requiered and rGO electrodes in zones where it is necessary to deliver electrical stimulation and opacity is not a concern.

A

Appendix A

A.1 Graphene Characterization Methods

The unique properties exhibited by graphene are only manifested on films that contain only one or few layers of graphene and that have a low enough defect density such that it does not significantly perturb the crystalline structure of the material. For this reason, the characterization of graphene plays a crucial role on the device fabrication process.

Fast, non-destructive methods that provide high resolution, give electronic and structural information and can be applied both at laboratory and mass production production scale are the preferred tools for the characterization of SLG and other graphene derivatives. The most commonly used methods are microscopy methods such as optical microscopy, Scanning Electron Microscopy (SEM), Atomic Force Microscopy (AFM) and Raman spectroscopy.

A.1.1 Optical Microscopy

Due to the ease of use and the wide availability of optical microscopes, optical microscopy is the easiest way to inspect graphene. Exfoliated graphene flakes can be directly imaged on Si substrates with a thin layer of SiO_2 because of light's destructive interference at specific wavelengths [294]. The same principle can be extrapolated to CVD graphene, where areas with multiple nucleation or wrinkles

produced during the graphene transfer can be optically identified as lighter areas (Figure A.1).

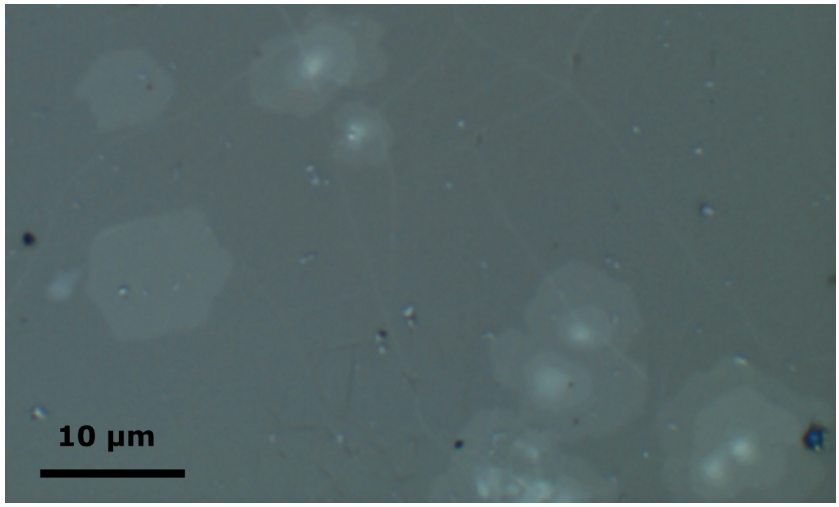

Figure A.1: Optical microscopy images of graphene films - Optical microscopy image of a CVD graphene film transferred on a Pyrex substrate. Areas with multiple nucleations are visible as lighter spots on the micrograph.

Another useful approach, specially to quickly assess CVD graphene growth, is the Cu oxidation method. Exploiting graphene's impermeability to gases, the copper film on which the CVD graphene has been grown is heated in the presence of oxygen, oxidizing the areas that are left uncovered by graphene. This oxidation increases the color contrast between Cu and Cu oxide and highlights areas in which the growth is incomplete as well as grain shapes and grain boundaries [295].

A.1.2 AFM

AFM is a scanning probe microscopy technique in which a cantilever with a sharp tip, in the order of few to tens of nanometers, is used to obtain topological information from a sample. It works by scanning across a surface in the X and Y directions while the tip of the cantilever contacts the surface of the sample, either continuously (contact mode) or by tapping (tapping mode). An electronic feedback loop on the Z axis continuously adjust the height of the probe to maintain a constant deflection (in contact mode) or vibration frequency (in tapping mode). From the adjustments done by the Z feedback loop to the height of the cantilever it is possible to obtain a 3D image of the sample.

When it comes to AFM use for graphene characterization, its main limitation is the inaccuracy and unreliability determining the number of layers. The reported

values in the literature can vary up to 1 nm due to differences on the cantilever oscillation parameters or the adsorbed water and impurities on the graphene surface [296]. Despite that limitation, clever measurement methods have been develop to, for example, visualize grain boundaries in closed layers of CVD graphene using conductive AFM [297].

One aspect in which AFM can be particularly useful, specially in connection with the work developed in this thesis, is in the assessment of surface contamination coming from photolitography fabrication techniques (Figure A.2). The root-mean-square (rms) value of the topographical AFM maps can be related to the amount of residual contamination after photolitographic fabrication and, furthermore, the progressive cleaning of the surface can be monitored by AFM imaging [298].

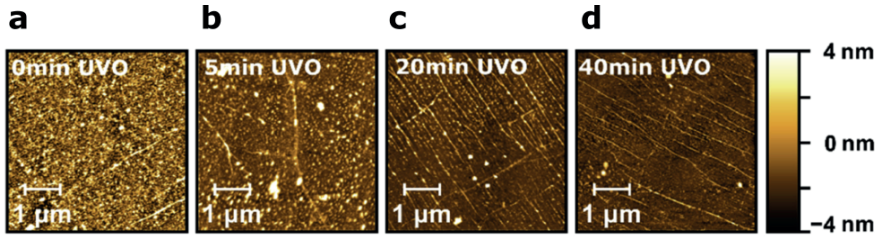

Figure A.2: Graphene surface roughness measured by AFM - The root-mean-square value of the AFM measurement decreases with the length of the UVO treatment showing the progressive cleaning of the residues. [a) 2.1 nm for 0 min, b) 1.3 nm for 5 min, c) 1.1 nm for 20 min and d) 0.8 nm for 40 min] indicates the continuous cleaning of surface residues. Source [298]

A.1.3 SEM

SEM uses a focused beam of high-energy electrons to generate secondary electrons at the surface of solid samples. These secondary provide useful information about morphology, chemical composition and crystalilinity of the sample. Another distinctive feature of the SEM images is their large depth of field, which provides a 3D appearance of the specimens.

SEM capabilities make them an ideal method to image CVD graphene grown samples on metal substrates and to characterise the coalescence of the film as well as the amount of second nucleation with little sample preparation and high throughput. One of its main setback is the possibility to introduce hydrocarbon contamination on the graphene film due to the decomposition of contaminants present on the SEM chamber, if the energy and the exposure time of the beam exposure are set to high values.

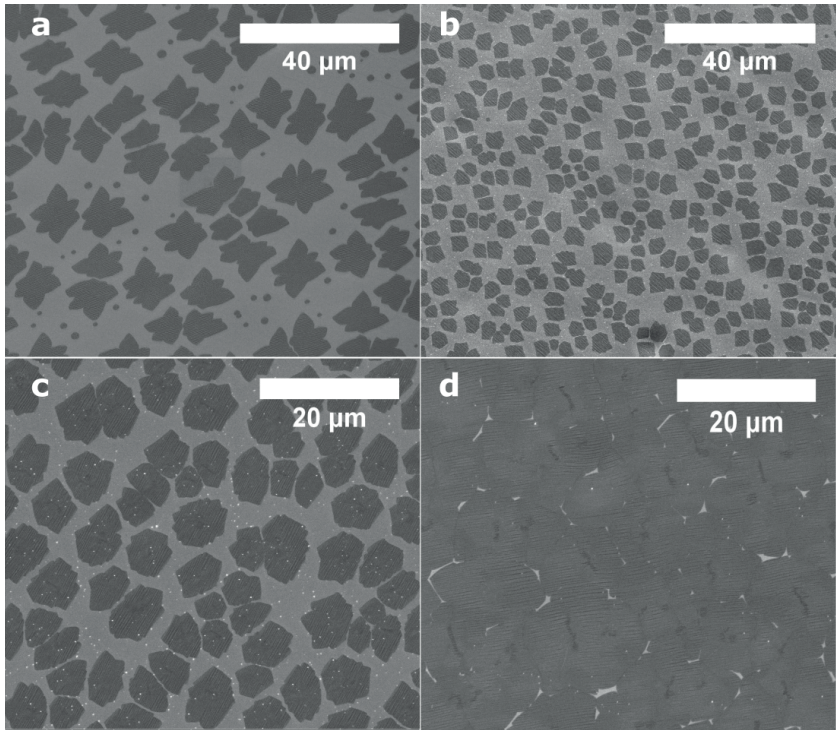

Figure A.3: SEM images of graphene on Cu - Examples of different CVD graphene grown on copper. a) Incomplete graphene growth showing a dendritic graphene growth. b) Incomplete hexagonal growth. c) Same dendritic growth as in b) but longer growth time, with some spots of second nucleation already present. d) Hexagonal growth such that in a) but almost completely coalescent.

Figure A.3 shows examples of different CVD graphene grown specimens. It illustrates the versatility of this characterization method and the amount of information it can be extracted from it.

A.1.4 Raman Spectroscopy

Since the first Raman spectrum of graphite was measured in 1970 [299], Raman spectroscopy has become a fundament technique in the characterization of amorphous carbon, fullerenes, nantubes and other carbon based materials [300].

Raman spectroscopy is based on measuring the energy of the photons emitted as an electron undergoes light scattering. There are two photon-electron scattering processes: elastic and inelastic. Elastic scattering, also known as Rayleigh scattering, takes place when a photon excites an electron to a higher energy level after which the electron falls back to the starting energy level, emitting a photon with the same frequency as the initial photon. Rayleigh scattering is the most common scattering process. Inelastic, or Raman, scattering occurs when

the energy of the incoming and outgoing photons are different. There are two different types of Raman scattering, Stokes and Anti-Stokes. Stokes scattering occurs when initially the electron is in the ground state of the system and after the absorption and emission of the photon, it ends up on a higher energy state. In this case, the energy of the emitted photon is smaller than the absorbed one, since the electron has gained energy. The Anti-Stokes scattering, on the other hand, occurs when an already excited electron absorbs a photon and then falls back to the ground state, emitting a photon whose energy is larger that that of the absorbed one. In this case, the electron losses energy. The Anti-Stokes scattering is less probable to occur, since it requires the electron to be in an excited state [300]. Figure A.4 a shows a schematic representation of the different photon-electron scattering processes.

Electron-photon scattering processes can also be differentiated into resonant or non-resonant, depending on the intermediate state of the electron. If that intermediate state is a real state, either electronic or vibrational, the scattering is resonant. If the intermediate state is a virtual state, the processes is non-resonant. Due to the absence of a band gap in the graphene electronic structure, as already discussed in section 1.2, graphene can have resonant Raman scattering with any incoming wavelength.

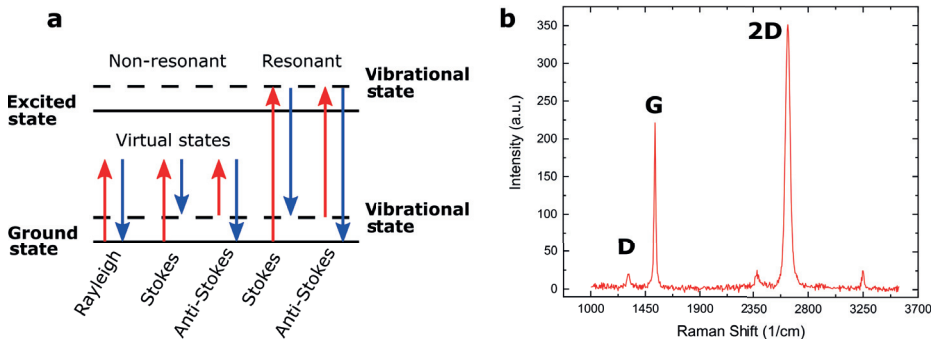

Figure A.4: Raman Processes in SLG - a) Schematic representation of the different electron-photon scattering processes. b) Raman spectrum taken from a sheet of CVD grown SLG after being transferred to a Pyrex substrate for device fabrication. Labels show the most important Raman bands in graphene.

As already shown in Figure A.4 b, the Raman spectrum of graphene consists of different bands, each of them associated to different scattering processes and from which different information can be extracted. The two main bands present in pristine graphene are the G band, a first order process, and the 2D band, a

second order process. When defects are present in the graphene structure, we can also observe the D band.

During this thesis, we have mainly used Raman spectroscopy for three purposes: evaluate the bilayer content of a sample, the amount of defects and the possible contamination created during the fabrication steps. To evaluate the bilayer content of a sample, we pay attention to the ratio of the 2D area to the G area and the full width at half maximum (FWHM) of the 2D band. Values bigger than 2 for the ratio of the areas and in the vicinity of 20 1/cm for the FWHM are characteristic of single layer graphene. To assess the defect defect level of a sample, we evaluate the D band. Finally, to check if rests of resist are left after the photolitography steps, we look for background signals.The absence of such signals indicates that the graphene is free of residues.

A.2 Cu foil electropolishing

To prepare the commercial Cu foils for the CVD graphene growth, we electropolish them by immersing them in the solution described in Table A.1 and applying a current density of approximately 90 mA/cm^2.

Compound	**ml**
DI water	480
Phosporic Acid (85 % wt)	275
Ethanol	205
Isopropanol	40
Urea (gr.)	4

Table A.1: Electropolishing solution - Recipe of the electropolishing solution used in this thesis in order to prepare the copper films for the graphene growth

B

Appendix B

B.1 Dry Transfer

The dry transfer method used in this thesis follows the procedure depicted by Yoong Yang *et al.* in [132].

For this process, the CVD grown graphene is immersed in a 10 g/L PVA[1] solution at 50 ºC during 18 hours. This step serves a double purpose: on the one hand it allows PVA to be adsorbed onto the hydrophobic graphene [132] and on the other hand, the water present in the solution oxidizes the copper substrate, decreasing its binding energy to the graphene layer and decoupling the graphene from the copper [301]. After that, the Cu/Graphene is taken out of the PVA, washed in water and blown dry with nitrogen. Once it is dry, a new PVA (10 g/L) layer is spin coated on top and dried at 80 ºC for 1 minute. Then a carrier layer of PDMS [2] is stamped on the graphene and retracted with high speed in order to detach the graphene from the copper foil. After that, the graphene is applied to the previously plasma cleaned target substrate, the PDMS/Graphene/substrate stack is placed on a hotplate at 130ºC during 1 minute and then the PDMS is peeled-off carefully, leaving the graphene attached to the target substrate. Finally, the PVA residues are cleaned by inmersion in DIW at 35ºC during 3 hours. The whole process is depicted in Figure B.1.

[1] Mw 9000–10000, 80% hydrolyzed, Aldrich
[2] Gel-Box

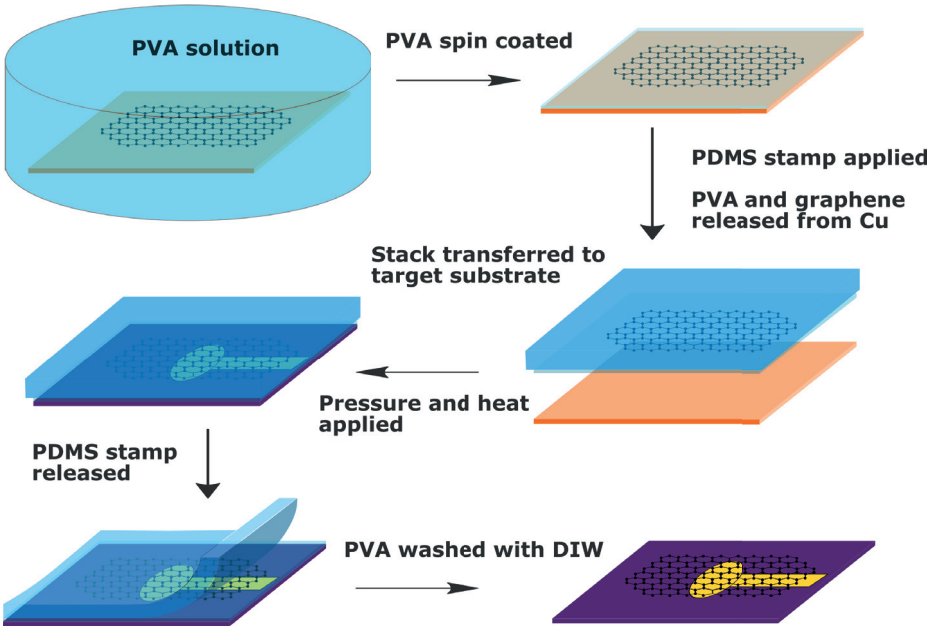

Figure B.1: Graphene Dry Transfer - Schematic representation of the steps involved in the graphene dry transfer process.

A variation of this process is used when fabricating on a wafer scale. There, instead of placing the PDMS/Gaphene/substrate stack on top of a hotplate, the stamp is pressed to the substrate using a hot press [3] at 130 ºC during 10 minutes under a 1 MPa pressure, as reported in [132].

As advantages of the dry transfer method, we can highlight that the stamp is easy to place precisely on the desired target area. This added precision means that smaller pieces of graphene can be used and that the more devices can be fabricated with the graphene produced during a single growth.

The main disadvantages of this method are that the wrinkles present of the copper foil are transferred to the SLG, creating differently doped areas throughout the graphene sheet, and the possibility to break the target substrate, specially when using 4" wafers and the hot press. This problem becomes even more severe when using cured polyimide on top of the carrier wafer for the fabrication of flexible devices, since there we have also to take into account the probability for the polyimide to be stripped off from the substrate. Antoher disadvantage is that the process is mainly manual, so the yield greatly depends on the ability of the operator to retrieve the PDMS/Graphene stack from the copper and to peel the PDMS after transferring the graphene to the target substrate. However, the AEMD group is devoting a significant amount of work in order to improve this

[3] Carver, Inc. with a custom made heating plate

transfer method and to use it to transfer, for example, graphene grown on top of evaporated copper [302].

Appendix C

C.1 Fabrication Protocols for SLG MEA

C.1.1 PI 2611 Protocol

7.5 μm thick

- Dehydrate Si wafer at 200 ºC for 30 minutes
- Plasma clean Si wafer at 500W, 600 sccm O_2 during 5 minutes
- Spin coating:
  - 50 seconds at 750 rpm
  - 70 seconds at 1500 rpm
  - 3 seconds at 0 rpm
- Relaxation for 15 minutes at room temperature
- Softbake: Ramp to 120 ºC during 30 min and cool down to room temperature again
- Hardbake:
  - Ramp to 200 ºC at 5 ºC/min
  - Hold 200 ºC for 60 minutes

  - Ramp to 350 ºC at 2.5 ºC/min
  - Hold 350 ºC for 60 minutes
  - Cool down to room temperature

C.1.2 AZ 5214 E Protocol

1.6 μm thick

- Dehydrate at 90 ºC for 10 minutes
- Spin coating:
  - 8 seconds at 1500 rpm
  - 23 seconds at 4500 rpm
  - 20 seconds at 600 rpm
  - 10 seconds at 1000 rpm
  - 10 seconds at 4500 rpm
- Softbake: 60 seconds at 90 ºC
- Exposure: 45 mJ/cm^2
- Hardbake: 2 minutes at 120 ºC
- Flooded exposure: 400 mJ/cm^2
- Develop:
  - AZ 726 MIF for 40 seconds
  - DIW for 1 minute

C.1.3 HIPR 6512 Protocol

2 μm thick

- Dehydrate at 90 ºC for 10 minutes
- Spin coating:
  - 4 seconds at 880 rpm
  - 40 seconds at 1550 rpm
  - 10 seconds at 880 rpm
  - 20 seconds at 4000 rpm

- Softbake: 150 seconds at 80 ºC
- Exposure: 220 mJ/cm^2
- Hardbake: 2 minutes at 80 ºC
- Develop:
  - OPD for 50 seconds
  - DIW for 1 minute

C.1.4 AZ 9260 Protocol

16 μm thick

- Dehydrate at 90 ºC for 10 minutes
- Spin coating:
  - 60 seconds at 2400 rpm
  - 10 seconds at 500 rpm
  - 10 seconds at 1000 rpm
- Softbake: 7 minutes and 30 seconds at 110 ºC
- Exposure: 900 mJ/cm^2 divided in 3 exposures with 40 seconds rest between them
- Develop:
  - AZ400K:DIW (1:3) for 6 minutes and 30 seconds
  - DIW for 1 minute

C.1.5 HD 8820 Protocol

5 μm thick

- Dehydrate at 90 ºC for 10 minutes
- Spin coating:
  - 5 seconds at 500 rpm
  - 30 seconds at 3000 rpm
  - 10 seconds at 600 rpm
- Softbake: 3 minutes at 120 ºC

- Exposure: 660 mJ/cm^2
- Develop:
  - OPD for 50 seconds
  - DIW for 1 minute
- Hardbake:
  - Ramp to 200 ºC at 5 ºC/min
  - Hold 200 ºC for 60 minutes
  - Ramp to 350 ºC at 2.5 ºC/min
  - Hold 350 ºC for 60 minutes
  - Cool down to room temperature

C.1.6 SU8 2005 Protocol

2.5 μm thick

- Dehydrate at 90 ºC for 10 minutes
- Spin coating:
  - 15 seconds at 400 rpm
  - 30 seconds at 3000 rpm
- Softbake:
  - 3 minutes at 65 ºC
  - Ramp to 95 ºC at 5ºC/min
  - 8 minutes at 95 ºC
  - Let cool down to room temperature
- Exposure: 150 mJ/cm^2
- Relaxation for 15 minutes at room temperature
- Postexpousure bake:
  - 2 minutes at 65 ºC
  - Ramp to 95 ºC at 5ºC/min
  - 3 minutes at 95 ºC
  - Cool down to room temperature

- Develop:
  - mrDev 600 for 50 seconds
  - Isopropanol for 1 minute
- Hardbake: 2 hours at 300 ºC in UHV

C.2 Fabrication Protocols for rGO MEA

The protocol used to passivate with the SU8 2005 resist is identical to that in section C.1

C.2.1 nLof 2070 Protocol

7 μm thick

- Dehydrate at 100 ºC for 10 minutes
- Spin coating:
  - 5 seconds at 500 rpm
  - 60 seconds at 2000 rpm
- Softbake: 90 seconds at 100 ºC
- Exposure: 220 mJ/cm^2
- Post-exposure bake: 90 seconds at 100 ºC
- Develop:
  - AZ 726 MIF for 50 seconds
  - DIW for 1 minute

C.2.2 HIPR 6512 Protocol

4 μm thick

- Dehydrate at 90 ºC for 10 minutes
- Spin coating:
  - 5 seconds at 550 rpm
  - 40 seconds at 600 rpm

- Softbake: 150 seconds at 80 ºC
- Exposure: 490 mJ/cm^2 divided in 2 exposures with 40 seconds rest between them
- Hardbake: 2 minutes at 80 ºC
- Develop:
  - OPD for 80 seconds
  - DIW for 1 minute

C.3 Fabrication protocols for the microcontact printing master mold

The protocol followed to deposit the SU8 seed layer with the SU8 2005 resist is identical to that in section C.1

C.3.1 SU8 2025 Protocol

40 μm thick

- Dehydrate at 90 ºC for 10 minutes
- Spin coating:
  - 15 seconds at 400 rpm
  - 30 seconds at 1500 rpm
- Lay flat for 10 minutes
- Softbake:
  - 3 minutes at 65 ºC
  - Ramp to 95 ºC at 5ºC/min
  - 8 minutes at 95 ºC
  - Cool down to room temperature
- Exposure: 180 mJ/cm^2
- Relaxation for 15 minutes at room temperature
- Postexposure bake:

  - 2 minutes at 65 ºC
  - Ramp to 95 ºC at 5ºC/min
  - 3 minutes at 95 ºC
  - Cool down to room temperature
- Develop:
  - mrDev 600 for 6 minutes
  - Isopropanol for 2 minute
- Hardbake: 2 hours at 300 ºC in UHV

D

Appendix D

D.1 Cortical Neuron culture protocol

The pregnant rats (E17) cortex were obtained from the UAB stabulary. The animals were sacrificed and the embryos cortex isolated by authorized personnel from the Neuroscience Institute.

- **Solution 1:**
  - 50 mL 1X Krebs-Ringer Bicarbonate Buffer[1]
  - 0.15 gr BSA[2]
  - 0.4 mL of a 3.8% $MgSO_4$ solution
- **Solution 2:**
  - 10 mL Solution 1
  - 2.5 mg Trypsin [3]
- **Solution 3:**
  - 10 mL Solution 1
  - 0.8 mg DNasa I[4]

[1]Sigma-Aldrich, K4002
[2]Sigma-Aldrich, BSAV-RO
[3]Sigma-Aldrich, T1426
[4]Sigma-Aldrich, 10104159001

  - 5.2 mg Trypsin inhibitor[5]
  - 0.1 ml of a 3.8% $MgSO_4$ solution

- **Solution 4:**
  - 8.4 mL Solution 1
  - 1.6 mL Solution 3

- **Solution 5:**
  - 5 mL Solution 1
  - 40 μL of a 3.8% $MgSO_4$ solution
  - 6 μL of a 1.2% $CaCl_2$ solution

- **Seeding Media:**

Compound	Provider	Amount	Percentage
DMEM	Life Technologies	445 mL	89%
Pen/strep	Life Technologies	5 mL	1%
FBS	Sigma	50 mL	10%

Table D.1: Seeding Media for cortical cultures

- **Maintenance Media:**

Compound	Provider	Amount	Percentage
Neurobasal	Life Technologies	482.5 mL	96.5%
B27	Life Technologies	10 mL	2%
Glutamax	Life Technologies	5 mL	1%
Pen/Strep	Life Technologies	2.5 mL	0.5%

Table D.2: Maintenance Media for cortical cultures

The disaggregation procedure begins with the cortex already triturated in a centrifuge tube containing 50 mL of Solution 1.

- Centrifuge the tube containing the cortex for 30 seconds at 750 G
- Remove supernatant and add 10 mL of Solution 2
- Incubate 10 minutes at 37ºC shaking every 2-3 minutes
- Add Solution 4 to stop the Trypsin digestion
- Centrifuge 30 seconds at 750 G

[5]Sigma-Aldrich, 10109886001

- Remove supernatant
- Add 3 mL of Solution 3 and disaggregate the cells pipetting in and out 10 times. Pass the cells through the grid another 10 times and add them to a centrifuge tube containing 5 mL of Solution 5.
- Add 7 mL of Solution 3 and repeat the former step
- Centrifuge 5 minutes at 350 G
- Remove supernatant and resuspend in 10 mL of Seeding Media
- Count the cells in a Neubauer chamber and dilute to the target concentration
- Seed the cells in the MEAs previously coated with PDL[6] for, at least, 2 hours.
- Keep the cells in an incubator at 37 ºC and 5 % CO_2
- After 3 hours, do a complete media change with the Maintenance Media
- Exchange half of the media every 3 - 4 days.

D.2 Hippocampal Neuron culture protocol

All experiments were approved by the Cantonal Veterinary Office Zurich.

Primary embryonic rat hippocampal or cortical neurons were isolated from Sprague Dawley embryo rats (E18). Tissues were enzymatically digested in 0.5 mg/ml papain[7] and 0.01 mg/mL Deoxyribonuclease[8] in PBS supplemented with 0.5 mg/mL Bovine Serum Albumin[9] and 10 mM D-(+)-glucose[10] for 30 min at 37 °C.

Subsequently, tissue fragments were washed once with 10% (v/v) heat-inactivated fetal bovine serum[11] in Neurobasal Plus medium [12] and twice with Neurobasal Plus medium. Tissue fragments were then mechanically dissociated with a 5 ml serological pipette and filtered with a 40 µm strainer[13]. Viable cells were counted using the trypan blue exclusion assay.

The cells were seeded at a concentration of 250 000 - 300 000 cells/cm^2 and kept in an incubator at 37ºC and 5 % CO_2 with the culture media described in Table D.1. Half of the media was exchanged every 3 to 4 days.

[6] Sigma-Aldrich, P6407
[7] P4762, Sigma-Aldrich
[8] D5025-15KU, Sigma-Aldrich
[9] BSA, 11020021, Gibco, Thermo Fisher Scientific
[10] G5400, Sigma-Aldrich
[11] FBS, F2442 Sigma Aldrich
[12] A3582901, Thermo Fisher Scientific
[13] CSS013040, Biofil

E

Appendix E

E.1 Animal handling for the ERG experiments

All procedures regarding animal housing and handling were carried out in accordance to the guidelines of the European community council directive (86/609/EEC) and approved by the Charles Darwin No5 Ethics Committee in Animal Experimentation (agreement #15219).

The animals used for the retinis pigmentosa study were generated by cross breeding homozygous transgenic P23H rats[1] with wild-type Sprague Dawley rat[2]. The animals were housed in a controlled environment with a 12 hour dark/light cycle and nutrition *ad libitum*. Prior to the experiments, the animals were kept in the dark for at least 8 hours and when handling was necessary it was done under red light conditions to maintain the dark adaptation.

Before the experiments, the animals were anesthetized using a mix of 60 mg/kg ketamine[3] and 0.4 mg/kg medetomidine[4] diluted in a NaCl solution[5] and administered via an intraperitoneal injection. We administrated Tropicamide 0.5 % drops[6] to dilate the pupils and oxybuprocaine chlorhydrate 0.4 % drops[7] to provide local corneal anaesthesia.

[1] Matthew LaVail Laboratory, USCF School of Medicine
[2] Janvier Labs, France
[3] Imalgene1000, Merial
[4] Domitor, Pfizer Sante
[5] B. Braum Medical
[6] Laboratoires Théa
[7] Bausch and Lomb

For the ERG recordings, the anesthetized animal was placed in a faraday cage and the ground and reference electrodes were inserted in the back and the forehead, respectively [162]. The ERG recording electrode was placed in the cornea and covered with ocular gel[8]. A heating plate was placed under the animal in order to maintain body temperature throughout the whole experiment, which lasted around 45 minutes.

[8] Dechra Pharmaceuticals

F

Appendix F

F.1 Resources available online

All the Python 3.6 scripts used to analyse and process the data used for this doctoral thesis can be found in the "Thesis Scripts" repository on my personal Github account: https://github.com/jmdelacruzsanchez/ThesisScripts

Additional microscopy images of the double passivation strategy to guide neural growth, μCP techniques, and CLSM images of the PDMS microstructures and videos used for in section 3.4.4 can be found in Zenodo's repositories [263, 273, 239].

References

[1] Monica DiLuca and Jes Olesen. "The cost of brain diseases: a burden or a challenge?" In: *Neuron* 82.6 (June 2014), pp. 1205–1208. ISSN: 1097-4199. DOI: 10.1016/J.NEURON.2014.05.044. URL: https://pubmed.ncbi.nlm.nih.gov/24945765/.

[2] Anders Gustavsson et al. "Cost of disorders of the brain in Europe 2010". In: *European Neuropsychopharmacology* 21.10 (Oct. 2011), pp. 718–779. ISSN: 0924-977X. DOI: 10.1016/J.EURONEURO.2011.08.008.

[3] J. Olesen et al. "The economic cost of brain disorders in Europe". In: *European Journal of Neurology* 19.1 (Jan. 2012), pp. 155–162. ISSN: 1468-1331. DOI: 10.1111/J.1468-1331.2011.03590.X. URL: https://onlinelibrary.wiley.com/doi/full/10.1111/j.1468-1331.2011.03590.x%20https://onlinelibrary.wiley.com/doi/abs/10.1111/j.1468-1331.2011.03590.x%20https://onlinelibrary.wiley.com/doi/10.1111/j.1468-1331.2011.03590.x.

[4] R. G.M. Morris et al. "Consensus Statement on European Brain Research: the need to expand brain research in Europe - 2015". In: *The European journal of neuroscience* 44.3 (Aug. 2016), pp. 1919–1926. ISSN: 1460-9568. DOI: 10.1111/EJN.13236. URL: https://pubmed.ncbi.nlm.nih.gov/26990697/.

[5] Katrin Amunts et al. "The Human Brain Project: Creating a European Research Infrastructure to Decode the Human Brain". In: *Neuron* 92.3 (Nov. 2016), pp. 574–581. ISSN: 1097-4199. DOI: 10.1016/J.NEURON.2016.10.046. URL: https://pubmed.ncbi.nlm.nih.gov/27809997/.

[6] Henry Markram. "The Human Brain Project". In: *Scientific American* 306.6 (Dec. 2012), pp. 50–55. ISSN: 00368733, 19467087. URL: http://www.jstor.org/stable/26014516.

[7] Lyric A. Jorgenson et al. "The BRAIN Initiative: developing technology to catalyse neuroscience discovery". In: *Philosophical Transactions of the Royal Society B: Biological Sciences* 370.1668 (May 2015). ISSN: 14712970. DOI: 10.1098/RSTB.2014.0164. URL: https://royalsocietypublishing.org/doi/abs/10.1098/rstb.2014.0164.

[8] Aravi Samuel, Herbert Levine, and Krastan B. Blagoev. "Scientific priorities for the BRAIN Initiative". In: *Nature Methods 2013 10:8* 10.8 (July 2013), pp. 713–714. ISSN: 1548-7105. DOI: 10.1038/nmeth.2565. URL: https://www.nature.com/articles/nmeth.2565.

[9] Meghan C. Mott, Joshua A. Gordon, and Walter J. Koroshetz. "The NIH BRAIN Initiative: Advancing neurotechnologies, integrating disciplines". In: *PLOS Biology* 16.11 (Nov. 2018), e3000066. ISSN: 1545-7885. DOI: 10.1371/JOURNAL.PBIO.3000066. URL: https://journals.plos.org/plosbiology/article?id=10.1371/journal.pbio.3000066.

[10] Allan R. Jones, Caroline C. Overly, and Susan M. Sunkin. "The Allen Brain Atlas: 5 years and beyond". In: *Nature Reviews Neuroscience 2009 10:11* 10.11 (Oct. 2009), pp. 821–828. ISSN: 1471-0048. DOI: 10.1038/nrn2722. URL: https://www.nature.com/articles/nrn2722.

[11] Robert T. Gerlai. *Molecular-genetic and statistical techniques for behavioral and neural research*. Elsevier, Jan. 2018, pp. 1–677. ISBN: 9780128040782. DOI: 10.1016/C2015-0-00036-3.

[12] Eric Van Reeth et al. "Super-resolution in magnetic resonance imaging: A review". In: *Concepts in Magnetic Resonance Part A* 40 A.6 (Nov. 2012), pp. 306–325. ISSN: 15466086. DOI: 10.1002/CMR.A.21249.

[13] Damià Viana. "EGNITE: Engineered Graphene for Neural Interface". PhD thesis. Universidad Autónoma de Barcelona, 2021.

[14] Gary H. Glover. "Overview of Functional Magnetic Resonance Imaging". In: *Neurosurgery clinics of North America* 22.2 (Apr. 2011), p. 133. ISSN: 10423680. DOI: 10.1016/J.NEC.2010.11.001. URL: /pmc/articles/PMC3073717/%20/pmc/articles/PMC3073717/?report=abstract%20https://www.ncbi.nlm.nih.gov/pmc/articles/PMC3073717/.

[15] William W. Moses. "Fundamental Limits of Spatial Resolution in PET". In: *Nuclear instruments & methods in physics research* 648 Supple.SUPPL. 1 (Aug. 2011), S236. ISSN: 01689002. DOI: 10.1016/J.NIMA.2010.11.092. URL: /pmc/articles/PMC3144741/%20/pmc/articles/PMC3144741/?report=abstract%20https://www.ncbi.nlm.nih.gov/pmc/articles/PMC3144741/.

[16] Guobao Wang. “High Temporal-Resolution Dynamic PET Image Reconstruction Using a New Spatiotemporal Kernel Method”. In: *IEEE transactions on medical imaging* 38.3 (Mar. 2019), pp. 664–674. ISSN: 1558-254X. DOI: 10.1109/TMI.2018.2869868. URL: https://pubmed.ncbi.nlm.nih.gov/30222553/.

[17] Nicole M Gage and Bernard J Baars. “Chapter 3 - Observing the Brain”. In: *Fundamentals of Cognitive Neuroscience*. Ed. by Nicole M Gage and Bernard J Baars. Second Edi. Academic Press, 2018, pp. 53–97. ISBN: 978-0-12-803813-0. URL: https://www.sciencedirect.com/science/article/pii/B9780128038130000039.

[18] Malcolm Macmillan. *An odd kind of fame : stories of Phineas Gage*. MIT Press, 2000, p. 562. ISBN: 9780262133630.

[19] S. Finger. “Paul Broca (1824–1880)”. In: *Journal of Neurology 2004 251:6* 251.6 (2004), pp. 769–770. ISSN: 1432-1459. DOI: 10.1007/S00415-004-0456-6. URL: https://link.springer.com/article/10.1007/s00415-004-0456-6.

[20] Dharmila Himanshu and Deepa Sarkar. “A Review of Behavioral Tests to Evaluate Different Types of Anxiety and Anti-anxiety Effects”. In: *Clinical psychopharmacology and neuroscience : the official scientific journal of the Korean College of Neuropsychopharmacology* 18.3 (May 2020), pp. 341–351. ISSN: 1738-1088. DOI: 10.9758/CPN.2020.18.3.341. URL: https://pubmed.ncbi.nlm.nih.gov/32702213/.

[21] Hua-Cheng Yan et al. “Behavioral animal models of depression”. In: *Neurosci Bull* 26.4 (2010), pp. 327–337. DOI: 10.1007/s12264-010-0323-7. URL: http://www.neurosci.cn.

[22] Mike P. Wattjes. “Structural MRI”. In: *International psychogeriatrics* 23 Suppl 2.S2 (2011), S13–S24. ISSN: 1741-203X. DOI: 10.1017/S1041610211000913. URL: https://pubmed.ncbi.nlm.nih.gov/21729419/.

[23] Chandrasekharan Kesavadas and Bejoy Thomas. “Clinical applications of functional MRI in epilepsy”. In: *The Indian Journal of Radiology & Imaging* 18.3 (Aug. 2008), p. 210. ISSN: 09713026. DOI: 10.4103/0971-3026.41829. URL: /pmc/articles/PMC2747426/%20/pmc/articles/PMC2747426/?report=abstract%20https://www.ncbi.nlm.nih.gov/pmc/articles/PMC2747426/.

[24] Thomas Deffieux et al. “Functional ultrasound neuroimaging: a review of the preclinical and clinical state of the art”. In: *Current Opinion in Neurobiology* 50 (June 2018), pp. 128–135. ISSN: 0959-4388. DOI: 10.1016/J.CONB.2018.02.001.

[25] Juan José Vaquero and Paul Kinahan. “Positron Emission Tomography: Current Challenges and Opportunities for Technological Advances in Clinical and Preclinical Imaging Systems”. In: *Annual review of biomedical engineering* 17 (Dec. 2015), pp. 385–414. ISSN: 1545-4274. DOI: 10.1146/ANNUREV-BIOENG-071114-040723. URL: https://pubmed.ncbi.nlm.nih.gov/26643024/.

[26] Changkyun Im and Jong Mo Seo. “A review of electrodes for the electrical brain signal recording”. In: *Biomedical Engineering Letters* 6.3 (Sept. 2017), pp. 104–112. ISSN: 2093-985X. DOI: 10.1007/S13534-016-0235-1. URL: https://link.springer.com/article/10.1007/s13534-016-0235-1.

[27] Sylvain Baillet. “Magnetoencephalography for brain electrophysiology and imaging”. In: *Nature Neuroscience* 20.3 (Feb. 2017), pp. 327–339. ISSN: 1546-1726. DOI: 10.1038/nn.4504. URL: https://www.nature.com/articles/nn.4504.

[28] Andrea Bonaccini Calia et al. “Full bandwidth electrophysiology of seizures and epileptiform activity enabled by flexible graphene micro-transistor depth neural probes”. In: (). DOI: 10.1101/2021.09.17.460765. URL: https://doi.org/10.1101/2021.09.17.460765.

[29] Ahuva Weltman, James Yoo, and Ellis Meng. “Flexible, Penetrating Brain Probes Enabled by Advances in Polymer Microfabrication”. In: *Micromachines* 7.180 (2016). DOI: 10.3390/mi7100180. URL: www.mdpi.com/journal/micromachines.

[30] Kenneth W. Horch and Daryl Kipke. “Neuroprosthetics : theory and practice”. In: (). URL: https://books.google.com/books/about/Neuroprosthetics_Theory_And_Practice_Sec.html?id=P_GtDgAAQBAJ.

[31] Merve Alaylioğlu et al. “A Bridge Between in vitro and in vivo Studies in Neuroscience: Organotypic Brain Slice Cultures”. In: *Archives of Neuropsychiatry* (2020). DOI: 10.29399/npa.26139. URL: https://doi.org/10.29399/npa.26139.

[32] AB Calia et al. “Full bandwidth electrophysiology of seizures and epileptiform activity enabled by flexible graphene micro-transistor depth neural probes”. In: *Nature Nanotechnology* (Sept. 2021). DOI: 10.1101/

2021.09.17.460765. URL: https://europepmc.org/article/ppr/ppr397365.

[33] Jerome Pine. "Recording action potentials from cultured neurons with extracellular microcircuit electrodes". In: *Journal of Neuroscience Methods* 2.1 (Feb. 1980), pp. 19–31. ISSN: 0165-0270. DOI: 10.1016/0165-0270(80)90042-4.

[34] D Jans et al. "Action potential-based MEA platform for in vitro screening of drug-induced cardiotoxicity using human iPSCs and rat neonatal myocytes". In: *Journal of pharmacological and toxicological methods* 87 (Sept. 2017), pp. 48–52. ISSN: 1873-488X. DOI: 10.1016/J.VASCN.2017.05.003. URL: https://pubmed.ncbi.nlm.nih.gov/28549786/.

[35] JK Law et al. "The use of microelectrode array (MEA) to study the protective effects of potassium channel openers on metabolically compromised HL-1 cardiomyocytes". In: *Physiological measurement* 30.2 (2009), pp. 155–167. ISSN: 0967-3334. DOI: 10.1088/0967-3334/30/2/004. URL: https://pubmed.ncbi.nlm.nih.gov/19136734/.

[36] Andrew F.M. Johnstone et al. "Microelectrode arrays: A physiologically based neurotoxicity testing platform for the 21st century". In: *NeuroToxicology* 31.4 (Aug. 2010), pp. 331–350. ISSN: 0161-813X. DOI: 10.1016/J.NEURO.2010.04.001.

[37] Jyh-Jang Sun, Werner Kilb, and Heiko J. Luhmann. "Self-organization of repetitive spike patterns in developing neuronal networks in vitro". In: *European Journal of Neuroscience* 32.8 (Oct. 2010), pp. 1289–1299. ISSN: 1460-9568. DOI: 10.1111/J.1460-9568.2010.07383.X. URL: https://onlinelibrary.wiley.com/doi/full/10.1111/j.1460-9568.2010.07383.x%20https://onlinelibrary.wiley.com/doi/abs/10.1111/j.1460-9568.2010.07383.x%20https://onlinelibrary.wiley.com/doi/10.1111/j.1460-9568.2010.07383.x.

[38] M. Abeles and G. L. Gerstein. "Detecting spatiotemporal firing patterns among simultaneously recorded single neurons". In: *https://doi.org/10.1152/jn.1988.60.3.909* 60.3 (1988), pp. 909–924. DOI: 10.1152/JN.1988.60.3.909. URL: https://journals.physiology.org/doi/abs/10.1152/jn.1988.60.3.909.

[39] Douglas J. Bakkum et al. "Tracking axonal action potential propagation on a high-density microelectrode array across hundreds of sites". In: *Nature Communications 2013 4:1* 4.1 (July 2013), pp. 1–12. ISSN: 2041-1723. DOI: 10.1038/ncomms3181. URL: https://www.nature.com/articles/ncomms3181.

[40] Alessandro Maccione et al. “Multiscale functional connectivity estimation on low-density neuronal cultures recorded by high-density CMOS Micro Electrode Arrays”. In: *Journal of Neuroscience Methods* 207.2 (June 2012), pp. 161–171. ISSN: 0165-0270. DOI: 10.1016/J.JNEUMETH.2012.04.002.

[41] Raeyoung Kim et al. “Recent trends in microelectrode array technology for in vitro neural interface platform”. In: *Biomedical Engineering Letters* 4.2 (2014), pp. 129–141. DOI: 10.1007/S13534-014-0130-6.

[42] Yoonkey Nam and Bruce C. Wheeler. “In vitro microelectrode array technology and neural recordings”. In: *Critical Reviews in Biomedical Engineering* 39.1 (2011), pp. 45–61. DOI: 10.1615/CRITREVBIOMEDENG.V39.I1.40.

[43] *Microelectrode Arrays | MultiChannel Systems*. URL: https://www.multichannelsystems.com/products/microelectrode-arrays.

[44] *MaxOne MEA Wells - MaxWell Biosystems*. URL: https://www.mxwbio.com/products/maxone-mea-system-microelectrode-array/maxone-mea-wells/.

[45] *cortiQ ECoG Electrodes | g.tec medical engineering GmbH*. URL: https://www.gtec.at/product/cortiq-ecog-electrodes/.

[46] *BioCAM DupleX*. URL: https://www.3brain.com/products/single-well/biocam-duplex.

[47] Benno M. Blaschke et al. “Mapping brain activity with flexible graphene micro-transistors”. In: *arXiv* (2016). ISSN: 2053-1583. DOI: 10.1088/2053-1583/aa5eff. URL: http://arxiv.org/abs/1611.05693.

[48] Clement Hébert et al. “Flexible Graphene Solution-Gated Field-Effect Transistors: Efficient Transducers for Micro-Electrocorticography”. In: *Advanced Functional Materials* 28.12 (2018), pp. 1–15. ISSN: 16163028. DOI: 10.1002/adfm.201703976.

[49] P. R. Wallace. “The Band Theory of Graphite”. In: *Physical Review* 71.9 (May 1947), p. 622. ISSN: 0031899X. DOI: 10.1103/PhysRev.71.622. URL: https://journals.aps.org/pr/abstract/10.1103/PhysRev.71.622.

[50] K. S. Novoselov et al. “Electric Field Effect in Atomically Thin Carbon Films”. In: *Science* 306.5696 (Oct. 2004), pp. 666–669. ISSN: 0036-8075. DOI: 10.1126/SCIENCE.1102896. URL: https://science.sciencemag.org/content/306/5696/666%20https://science.sciencemag.org/content/306/5696/666.abstract.

[51] *The Nobel Prize in Physics 2010*. URL: https://www.nobelprize.org/prizes/physics/2010/summary/.

[52] Changgu Lee et al. “Measurement of the elastic properties and intrinsic strength of monolayer graphene”. In: *Science* 321.5887 (July 2008), pp. 385–388. ISSN: 00368075. DOI: 10.1126/SCIENCE.1157996.

[53] Peter Blake et al. “Graphene-based liquid crystal device”. In: *Nano Letters* 8.6 (June 2008), pp. 1704–1708. ISSN: 15306984. DOI: 10.1021/NL080649I.

[54] R. R. Nair et al. “Fine structure constant defines visual transparency of graphene”. In: *Science* 320.5881 (June 2008), p. 1308. ISSN: 00368075. DOI: 10.1126/SCIENCE.1156965/SUPPL{_}FILE/PAP.PDF. URL: https://www.science.org/doi/abs/10.1126/science.1156965.

[55] R. Ansari, S. Ajori, and B. Motevalli. “Mechanical properties of defective single-layered graphene sheets via molecular dynamics simulation”. In: *Superlattices and Microstructures* 51.2 (Feb. 2012), pp. 274–289. ISSN: 0749-6036. DOI: 10.1016/J.SPMI.2011.11.019.

[56] Ardavan Zandiatashbar et al. “Effect of defects on the intrinsic strength and stiffness of graphene”. In: *Nature Communications* 5.1 (Jan. 2014), pp. 1–9. ISSN: 2041-1723. DOI: 10.1038/ncomms4186. URL: https://www.nature.com/articles/ncomms4186.

[57] Florian Banhart, Jani Kotakoski, and Arkady V. Krasheninnikov. “Structural Defects in Graphene”. In: *ACS Nano* 5.1 (Jan. 2010), pp. 26–41. ISSN: 19360851. DOI: 10.1021/NN102598M. URL: https://pubs.acs.org/doi/full/10.1021/nn102598m.

[58] *Electronic band structure of graphene.svg - Wikipedia*. URL: https://en.wikipedia.org/wiki/File:Electronic_band_structure_of_graphene.svg.

[59] *Graphene - sigma and pi bonds.svg - Wikipedia*. URL: https://en.wikipedia.org/wiki/File:Graphene_-_sigma_and_pi_bonds.svg.

[60] A. H. Castro Neto et al. “The electronic properties of graphene”. In: *Reviews of Modern Physics* 81.1 (Jan. 2009), pp. 109–162. ISSN: 00346861. DOI: 10.1103/REVMODPHYS.81.109/FIGURES/38/MEDIUM. URL: https://journals.aps.org/rmp/abstract/10.1103/RevModPhys.81.109.

[61] P A M Dirac. “The Quantum Theory of the Electron”. In: *Royal Society Procedures A* 43 (1927), p. 227.

[62] A. K. Geim and K. S. Novoselov. “The rise of graphene”. In: *Nature Materials* 6.3 (Mar. 2007), pp. 183–191. ISSN: 1476-4660. DOI: 10.1038/nmat1849. URL: https://www.nature.com/articles/nmat1849.

[63] Allen J. Bard and Larry R. Faulkner. *Electrochemical Methods: Fundamentals and Applications*. 2nd Editio. John Wiley and Sons, INC, 2001. ISBN: 0-471-04372-9.

[64] Elliot Krames, P Hunter Peckham, and Ali R Rezai. *Neuromodulation: Comprehensive Textbook of Principles, Technologias and Therapies*. Academic Press, 2009. ISBN: 978-0-12-374248-3.

[65] Stuart F Cogan. "Neural Stimulation and Recording Electrodes". In: (). DOI: 10.1146/annurev.bioeng.10.061807.160518. URL: www.annualreviews.org.

[66] E. Masvidal-Codina et al. "High-resolution mapping of infraslow cortical brain activity enabled by graphene microtransistors". In: *Nature Materials* 18.3 (2019). ISSN: 14764660. DOI: 10.1038/s41563-018-0249-4.

[67] Dale Purves et al. *Neuroscience*. 3rd Editio. Sinauer Associated, Inc., 2004. ISBN: 0-87893-742-0.

[68] H. Helmholtz. "Ueber einige Gesetze der Vertheilung elektrischer Ströme in körperlichen Leitern, mit Anwendung auf die thierisch-elektrischen Versuche (Schluss.)" In: *Annalen der Physik* 165.7 (1853), pp. 353–377. DOI: 10.1002/ANDP.18531650702.

[69] L. H. Hess et al. "High-transconductance graphene solution-gated field effect transistors". In: *Applied Physics Letters* 99.3 (July 2011), p. 033503. ISSN: 0003-6951. DOI: 10.1063/1.3614445. URL: https://aip.scitation.org/doi/abs/10.1063/1.3614445.

[70] Charles MacKin et al. "A current-voltage model for graphene electrolyte-gated field-effect transistors". In: *IEEE Transactions on Electron Devices* 61.12 (Dec. 2014), pp. 3971–3977. DOI: 10.1109/TED.2014.2360660.

[71] Mark E. Orazem and Bernard Tribollet. *Electrochemical Impedance Spectroscopy*. John Wiley & Sons, Inc. ISBN: 9780470381588.

[72] R. Kubo. "The fluctuation-dissipation theorem". In: *Reports on Progress in Physics* 29.1 (1966), pp. 255–284. DOI: 10.1088/0034-4885/29/1/306.

[73] J. B. Johnson. "Thermal Agitation of Electricity in Conductors". In: *Physical Review* 541.1918 (1927).

[74] Arjang Hassibi et al. "Comprehensive Study of Noise Processes in Electrode Electrolyte Interfaces". In: *Journal of Applied Physics* 96 (2004), p. 69903. DOI: 10.1063/1.1755429. URL: https://doi.org/10.1063/1.2040708.

[75] Virginia Pickel and Menahem Segal. *The Synapse: Structure and Function*. 1. Elsevier, 2014. ISBN: 978-0-12-418675-0.

[76] Claire Wood, Christine Williams, and Gareth J. Waldron. "Patch clamping by numbers". In: *Drug Discovery Today* 9.10 (May 2004), pp. 434–441. ISSN: 1359-6446. DOI: 10.1016/S1359-6446(04)03064-8.

[77] Etay Hay et al. "Models of Neocortical Layer 5b Pyramidal Cells Capturing a Wide Range of Dendritic and Perisomatic Active Properties". In: *PLOS Computational Biology* 7.7 (July 2011), e1002107. ISSN: 1553-7358. DOI: 10.1371/JOURNAL.PCBI.1002107. URL: https://journals.plos.org/ploscompbiol/article?id=10.1371/journal.pcbi.1002107.

[78] *NEURON | empirically-based simulations of neurons and networks of neurons*. URL: https://neuron.yale.edu/neuron/.

[79] Michael L. Hines, Andrew P. Davison, and Eilif Muller. "NEURON and Python". In: *Frontiers in Neuroinformatics* 3.JAN (Jan. 2009), p. 1. ISSN: 16625196. DOI: 10.3389/NEURO.11.001.2009/BIBTEX.

[80] Henrik Lindén et al. "LFPy: A tool for biophysical simulation of extracellular potentials generated by detailed model neurons". In: *Frontiers in Neuroinformatics* 7.JAN (Jan. 2014). ISSN: 16625196. DOI: 10.3389/FNINF.2013.00041/ABSTRACT.

[81] Vijay Viswam et al. "Optimal electrode size for multi-scale extracellular-potential recording from neuronal assemblies". In: *Frontiers in Neuroscience* 13.APR (2019). ISSN: 1662453X. DOI: 10.3389/FNINS.2019.00385/FULL.

[82] Marie Engelene J. Obien et al. "Revealing neuronal function through microelectrode array recordings". In: *Frontiers in Neuroscience* 9.JAN (2015), p. 423. ISSN: 1662453X. DOI: 10.3389/fnins.2014.00423.

[83] Michael M Halassa et al. "Local Field Potentials: Myths and Misunderstandings". In: *Frontiers in Neural Circuits* 10 (2016), p. 101. DOI: 10.3389/fncir.2016.00101. URL: www.frontiersin.org.

[84] Henrik Lindén et al. "Modeling the Spatial Reach of the LFP". In: *Neuron* 72.5 (Dec. 2011), pp. 859–872. ISSN: 0896-6273. DOI: 10.1016/J.NEURON.2011.11.006.

[85] David Tsai et al. "A very large-scale microelectrode array for cellular-resolution electrophysiology". In: (). DOI: 10.1038/s41467-017-02009-x. URL: www.nature.com/naturecommunications.

[86] Marco Ballini et al. "A 1024-channel CMOS microelectrode array with 26,400 electrodes for recording and stimulation of electrogenic cells in vitro". In: *IEEE Journal of Solid-State Circuits* 49.11 (2014), pp. 2705–2719. ISSN: 00189200. DOI: 10.1109/JSSC.2014.2359219.

[87] Andreas Kuhn et al. “The influence of electrode size on selectivity and comfort in transcutaneous electrical stimulation of the forearm”. In: *IEEE Transactions on Neural Systems and Rehabilitation Engineering* 18.3 (June 2010), pp. 255–262. ISSN: 15344320. DOI: 10.1109/TNSRE.2009.2039807.

[88] Andrea Corna, Thoralf Herrmann, and Günther Zeck. “Electrode-size dependent thresholds in subretinal neuroprosthetic stimulation”. In: *Journal of Neural Engineering* 15.4 (June 2018), p. 045003. ISSN: 1741-2552. DOI: 10.1088/1741-2552/AAC1C8. URL: https://iopscience.iop.org/article/10.1088/1741-2552/aac1c8%20https://iopscience.iop.org/article/10.1088/1741-2552/aac1c8/meta.

[89] Jan Reinoud Buitenweg, Wim L.C. Rutten, and Enrico Marani. “Extracellular stimulation window explained by a geometry-based model of the neuron-electrode contact”. In: *IEEE Transactions on Biomedical Engineering* 49.12 I (Dec. 2002), pp. 1591–1599. ISSN: 00189294. DOI: 10.1109/TBME.2002.804504.

[90] Makoto Taketani and Michel Baudry. “Advances in network electrophysiology: Using multi-electrode arrays”. In: *Advances in Network Electrophysiology: Using Multi-Electrode Arrays* (2006), pp. 1–478. DOI: 10.1007/B136263.

[91] Daniel R. Merrill, Marom Bikson, and John G.R. Jefferys. “Electrical stimulation of excitable tissue: Design of efficacious and safe protocols”. In: *Journal of Neuroscience Methods* 141.2 (2005), pp. 171–198. ISSN: 01650270. DOI: 10.1016/j.jneumeth.2004.10.020.

[92] Robert Plonsey and Roger C. Barr. “Bioelectricity: A quantitative approach”. In: *Bioelectricity: A Quantitative Approach* (2007), pp. 1–528. DOI: 10.1007/978-0-387-48865-3.

[93] D. C. West and J. H. Wolstencroft. “Strength-duration characteristics of myelinated and non-myelinated bulbospinal axons in the cat spinal cord”. In: *The Journal of physiology* 337.1 (Apr. 1983), pp. 37–50. ISSN: 0022-3751. DOI: 10.1113/JPHYSIOL.1983.SP014610. URL: https://pubmed.ncbi.nlm.nih.gov/6875936/.

[94] H. Bostock. “The strength-duration relationship for excitation of myelinated nerve: computed dependence on membrane parameters.” In: *The Journal of Physiology* 341.1 (Aug. 1983), p. 59. ISSN: 14697793. DOI: 10.1113/JPHYSIOL.1983.SP014792. URL: /pmc/articles/PMC1195322/?report=abstract%20https://www.ncbi.nlm.nih.gov/pmc/articles/PMC1195322/.

[95] Ilona Mogyoros, Matthew C. Kiernan, and David Burke. "Strength-duration properties of human peripheral nerve". In: *Brain : a journal of neurology* 119 (Pt 2.2 (1996), pp. 439–447. ISSN: 0006-8950. DOI: 10.1093/BRAIN/119.2.439. URL: https://pubmed.ncbi.nlm.nih.gov/8800939/.

[96] Eduardo N. Warman, Warren M. Grill, and Dominique Durand. "Modeling the effects of electric fields on nerve fibers: determination of excitation thresholds". In: *IEEE transactions on bio-medical engineering* 39.12 (1992), pp. 1244–1254. ISSN: 0018-9294. DOI: 10.1109/10.184700. URL: https://pubmed.ncbi.nlm.nih.gov/1487287/.

[97] A. L. Hodgkin and A. F. Huxley. "A quantitative description of membrane current and its application to conduction and excitation in nerve". In: *The Journal of Physiology* 117.4 (Aug. 1952), p. 500. ISSN: 14697793. DOI: 10.1113/JPHYSIOL.1952.SP004764. URL: https://www.ncbi.nlm.nih.gov/pmc/articles/PMC1392413/.

[98] Robert V. Shannon. "A model of safe levels for electrical stimulation". In: *IEEE transactions on bio-medical engineering* 39.4 (1992), pp. 424–426. ISSN: 0018-9294. DOI: 10.1109/10.126616. URL: https://pubmed.ncbi.nlm.nih.gov/1592409/.

[99] Ingmar Schoen and Peter Fromherz. "The mechanism of extracellular stimulation of nerve cells on an electrolyte-oxide-semiconductor capacitor." In: *Biophysical journal* 92.3 (2007), pp. 1096–1111. ISSN: 00063495. DOI: 10.1529/biophysj.106.094763. URL: http://dx.doi.org/10.1529/biophysj.106.094763.

[100] Rebecca S. Edwards and Karl S. Coleman. "Graphene synthesis: Relationship to applications". In: *Nanoscale* 5.1 (2013), pp. 38–51. ISSN: 20403364. DOI: 10.1039/c2nr32629a.

[101] Enlai Gao et al. "Journal of the Mechanics and Physics of Solids Mechanical exfoliation of two-dimensional materials". In: *Journal of the Mechanics and Physics of Solids* 115 (2018), pp. 248–262. ISSN: 0022-5096. URL: https://doi.org/10.1016/j.jmps.2018.03.014.

[102] Guoxiu Wang et al. "Highly efficient and large-scale synthesis of graphene by electrolytic exfoliation". In: *Carbon* 47.14 (2009), pp. 3242–3246. ISSN: 00086223. DOI: 10.1016/j.carbon.2009.07.040. URL: http://dx.doi.org/10.1016/j.carbon.2009.07.040.

[103] Ching Yuan Su et al. “High-quality thin graphene films from fast electrochemical exfoliation”. In: *ACS Nano* 5.3 (2011), pp. 2332–2339. ISSN: 19360851. DOI: 10.1021/nn200025p.

[104] Peter Blake et al. “Graphene-based liquid crystal device”. In: *Nano Letters* 8.6 (2008), pp. 1704–1708. ISSN: 15306984. DOI: 10.1021/nl080649i.

[105] Yenny Hernandez et al. “High-yield production of graphene by liquid-phase exfoliation of graphite”. In: *Nature Nanotechnology* 3.9 (2008), pp. 563–568. ISSN: 17483387. DOI: 10.1038/nnano.2008.215.

[106] Yani Chen et al. “Mass-production of highly-crystalline few-layer graphene sheets by arc discharge in various H2–inert gas mixtures”. In: *Chemical Physics Letters* 538 (June 2012), pp. 72–76. ISSN: 0009-2614. DOI: 10.1016/J.CPLETT.2012.04.020.

[107] K. S. Subrahmanyam et al. “Simple Method of Preparing Graphene Flakes by an Arc-Discharge Method”. In: *Journal of Physical Chemistry C* 113.11 (Mar. 2009), pp. 4257–4259. DOI: 10.1021/JP900791Y. URL: https://pubs.acs.org/doi/abs/10.1021/jp900791y.

[108] Prashant Kumar, L. S. Panchakarla, and C. N. R. Rao. “Laser-induced unzipping of carbon nanotubes to yield graphene nanoribbons”. In: *Nanoscale* 3.5 (May 2011), pp. 2127–2129. DOI: 10.1039/C1NR10137D. URL: https://pubs.rsc.org/en/content/articlehtml/2011/nr/c1nr10137d%20https://pubs.rsc.org/en/content/articlelanding/2011/nr/c1nr10137d.

[109] Dmitry V. Kosynkin et al. “Longitudinal unzipping of carbon nanotubes to form graphene nanoribbons”. In: *Nature 2009 458:7240* 458.7240 (Apr. 2009), pp. 872–876. ISSN: 1476-4687. DOI: 10.1038/nature07872. URL: https://www.nature.com/articles/nature07872.

[110] Claire Berger et al. “Electronic Confinement and Coherence in Patterned Epitaxial Graphene”. In: (). URL: http://science.sciencemag.org/.

[111] Peter Sutter. “How silicon leaves the scene”. In: *Nature Materials 2009 8:3* 8.3 (2009), pp. 171–172. ISSN: 1476-4660. DOI: 10.1038/nmat2392. URL: https://www.nature.com/articles/nmat2392.

[112] Xuesong Li et al. “Large-Area Synthesis of High-Quality and Uniform Graphene Films on Copper Foils”. In: *Science* 324.5932 (June 2009), pp. 1312–1314. ISSN: 0036-8075. DOI: 10.1126/SCIENCE.1171245. URL: https://science.sciencemag.org/content/324/5932/1312%20https://science.sciencemag.org/content/324/5932/1312.abstract.

[113] Konstantin V. Emtsev et al. “Towards wafer-size graphene layers by atmospheric pressure graphitization of silicon carbide”. In: *Nature Materials 2009 8:3* 8.3 (Feb. 2009), pp. 203–207. ISSN: 1476-4660. DOI: 10.1038/nmat2382. URL: https://www.nature.com/articles/nmat2382.

[114] L. H. Hess et al. “High-transconductance graphene solution-gated field effect transistors”. In: *Applied Physics Letters* 99.3 (2011). ISSN: 00036951. DOI: 10.1063/1.3614445.

[115] In Hyuk Son et al. “CO2 enhanced chemical vapor deposition growth of few-layer graphene over NiOx”. In: *ACS Nano* 8.9 (Sept. 2014), pp. 9224–9232. ISSN: 1936086X. DOI: 10.1021/NN504342E/SUPPL{_}FILE/NN504342E{_}SI{_}001.PDF. URL: https://pubs.acs.org/doi/abs/10.1021/nn504342e.

[116] Sukang Bae et al. “Roll-to-roll production of 30-inch graphene films for transparent electrodes”. In: *Nature Nanotechnology 2010 5:8* 5.8 (June 2010), pp. 574–578. ISSN: 1748-3395. DOI: 10.1038/nnano.2010.132. URL: https://www.nature.com/articles/nnano.2010.132.

[117] Bingyan Chen et al. “How good can CVD-grown monolayer graphene be?” In: *Nanoscale* 6.24 (Nov. 2014), pp. 15255–15261. ISSN: 2040-3372. DOI: 10.1039/C4NR05664G. URL: https://pubs.rsc.org/en/content/articlehtml/2014/nr/c4nr05664g%20https://pubs.rsc.org/en/content/articlelanding/2014/nr/c4nr05664g.

[118] Sami Ullah et al. “Graphene transfer methods: A review”. In: *Nano Research 2021 14:11* 14.11 (Feb. 2021), pp. 3756–3772. ISSN: 1998-0000. DOI: 10.1007/S12274-021-3345-8. URL: https://link.springer.com/article/10.1007/s12274-021-3345-8.

[119] H. S. Song et al. “Origin of the relatively low transport mobility of graphene grown through chemical vapor deposition”. In: *Scientific Reports 2012 2:1* 2.1 (Mar. 2012), pp. 1–6. ISSN: 2045-2322. DOI: 10.1038/srep00337. URL: https://www.nature.com/articles/srep00337.

[120] Wei Guo et al. “Governing Rule for Dynamic Formation of Grain Boundaries in Grown Graphene”. In: *ACS Nano* 9.6 (June 2015), pp. 5792–5798. DOI: 10.1021/ACSNANO.5B01827. URL: https://pubs.acs.org/doi/abs/10.1021/acsnano.5b01827.

[121] Bin Zhang et al. “Low-Temperature Chemical Vapor Deposition Growth of Graphene from Toluene on Electropolished Copper Foils”. In: *ACS Nano* 6.3 (Mar. 2012), pp. 2471–2476. DOI: 10.1021/NN204827H. URL: https://pubs.acs.org/doi/abs/10.1021/nn204827h.

[122] Hong Wang et al. “Controllable Synthesis of Submillimeter Single-Crystal Monolayer Graphene Domains on Copper Foils by Suppressing Nucleation”. In: (2012). DOI: 10.1021/ja2105976. URL: https://pubs.acs.org/sharingguidelines.

[123] Zheng Yan et al. “Toward the Synthesis of Wafer-Scale Single-Crystal Graphene on Copper Foils”. In: *ACS Nano* 6.10 (Oct. 2012), pp. 9110–9117. DOI: 10.1021/NN303352K. URL: https://pubs.acs.org/doi/abs/10.1021/nn303352k.

[124] Yufeng Hao et al. “The Role of Surface Oxygen in the Growth of Large Single-Crystal Graphene on Copper”. In: *Science* 342.6159 (Nov. 2013), pp. 720–723. ISSN: 0036-8075. DOI: 10.1126/SCIENCE.1243879. URL: https://science.sciencemag.org/content/342/6159/720%20https://science.sciencemag.org/content/342/6159/720.abstract.

[125] Philipp Braeuninger-Weimer et al. “Understanding and Controlling Cu-Catalyzed Graphene Nucleation: The Role of Impurities, Roughness, and Oxygen Scavenging”. In: *Chemistry of Materials* 28.24 (Dec. 2016), pp. 8905–8915. DOI: 10.1021/ACS.CHEMMATER.6B03241. URL: https://pubs.acs.org/doi/abs/10.1021/acs.chemmater.6b03241.

[126] Elena Loginova et al. “Evidence for graphene growth by C cluster attachment”. In: *New Journal of Physics* 10.9 (Sept. 2008), p. 093026. ISSN: 1367-2630. DOI: 10.1088/1367-2630/10/9/093026. URL: https://iopscience.iop.org/article/10.1088/1367-2630/10/9/093026%20https://iopscience.iop.org/article/10.1088/1367-2630/10/9/093026/meta.

[127] E Loginova et al. “Factors influencing graphene growth on metal surfaces”. In: *New Journal of Physics* 11.6 (June 2009), p. 063046. ISSN: 1367-2630. DOI: 10.1088/1367-2630/11/6/063046. URL: https://iopscience.iop.org/article/10.1088/1367-2630/11/6/063046%20https://iopscience.iop.org/article/10.1088/1367-2630/11/6/063046/meta.

[128] HoKwon Kim et al. “Activation Energy Paths for Graphene Nucleation and Growth on Cu”. In: *ACS Nano* 6.4 (Apr. 2012), pp. 3614–3623. DOI: 10.1021/NN3008965. URL: https://pubs.acs.org/doi/abs/10.1021/nn3008965.

[129] Ivan Vlassiouk et al. “Role of Hydrogen in Chemical Vapor Deposition Growth of Large Single-Crystal Graphene”. In: *ACS Nano* 5.7 (July 2011), pp. 6069–6076. DOI: 10.1021/NN201978Y. URL: https://pubs.acs.org/doi/abs/10.1021/nn201978y.

[130] Aaesha Alnuaimi et al. “Toward fast growth of large area high quality graphene using a cold-wall CVD reactor”. In: (2017). DOI: 10.1039/c7ra10336k.

[131] Ji Won Suk et al. “Transfer of CVD-Grown Monolayer Graphene onto Arbitrary Substrates”. In: *ACS Nano* 5.9 (Sept. 2011), pp. 6916–6924. DOI: 10.1021/NN201207C. URL: https://pubs.acs.org/doi/pdf/10.1021/nn201207c.

[132] Sang Yoon Yang et al. “Metal-Etching-Free Direct Delamination and Transfer of Single-Layer Graphene with a High Degree of Freedom”. In: *Small* 11.2 (Jan. 2015), pp. 175–181. ISSN: 1613-6829. DOI: 10.1002/SMLL.201401196. URL: https://onlinelibrary.wiley.com/doi/full/10.1002/smll.201401196%20https://onlinelibrary.wiley.com/doi/abs/10.1002/smll.201401196%20https://onlinelibrary.wiley.com/doi/10.1002/smll.201401196.

[133] Alberto Boscá et al. “Automatic graphene transfer system for improved material quality and efficiency”. In: *Scientific Reports 2016 6:1* 6.1 (Feb. 2016), pp. 1–8. ISSN: 2045-2322. DOI: 10.1038/srep21676. URL: https://www.nature.com/articles/srep21676.

[134] Niccolò Paolo Pampaloni et al. “Advances in Nano Neuroscience: From Nanomaterials to Nanotools”. In: *Frontiers in Neuroscience* 0.JAN (2019), p. 953. ISSN: 1662-453X. DOI: 10.3389/FNINS.2018.00953.

[135] Alessandra Fabbro et al. “Graphene-Based Interfaces Do Not Alter Target Nerve Cells”. In: *ACS Nano* 10.1 (Jan. 2016), pp. 615–623. DOI: 10.1021/ACSNANO.5B05647. URL: https://pubs.acs.org/doi/abs/10.1021/acsnano.5b05647.

[136] Amel Bendali et al. “Purified Neurons can Survive on Peptide-Free Graphene Layers”. In: *Advanced Healthcare Materials* 2.7 (July 2013), pp. 929–933. ISSN: 2192-2659. DOI: 10.1002/ADHM.201200347. URL: https://onlinelibrary.wiley.com/doi/full/10.1002/adhm.201200347%20https://onlinelibrary.wiley.com/doi/abs/10.1002/adhm.201200347%20https://onlinelibrary.wiley.com/doi/10.1002/adhm.201200347.

[137] Viviana Lovat et al. “Carbon Nanotube Substrates Boost Neuronal Electrical Signaling”. In: *Nano Letters* 5.6 (June 2005), pp. 1107–1110. DOI: 10.1021/NL050637M. URL: https://pubs.acs.org/doi/abs/10.1021/nl050637m.

[138] Fabbro A et al. “Spinal cord explants use carbon nanotube interfaces to enhance neurite outgrowth and to fortify synaptic inputs”. In: *ACS nano* 6.3 (Mar. 2012), pp. 2041–2055. ISSN: 1936-086X. DOI: 10.1021/NN203519R. URL: https://pubmed.ncbi.nlm.nih.gov/22339712/.

[139] Greg D. Field et al. “Functional connectivity in the retina at the resolution of photoreceptors”. In: *Nature* 467.7316 (2010), pp. 673–677. ISSN: 00280836. DOI: 10.1038/nature09424.

[140] Ramon Garcia-Cortadella et al. “Distortion-Free Sensing of Neural Activity Using Graphene Transistors”. In: *Small* 16.16 (2020), pp. 1–10. ISSN: 16136829. DOI: 10.1002/smll.201906640.

[141] Duygu Kuzum et al. “Transparent and flexible low noise graphene electrodes for simultaneous electrophysiology and neuroimaging”. In: *Nature Communications* (2014). DOI: 10.1038/ncomms6259. URL: www.nature.com/naturecommunications.

[142] Gytis Baranauskas et al. “Carbon nanotube composite coating of neural microelectrodes preferentially improves the multiunit signal-to-noise ratio”. In: *J. Neural Eng* 8 (2011), pp. 66013–66025. DOI: 10.1088/1741-2560/8/6/066013.

[143] Scott F Lempka et al. “Theoretical analysis of intracortical microelectrode recordings”. In: *Journal of Neural Engineering* 8.4 (July 2011), p. 045006. ISSN: 1741-2552. DOI: 10.1088/1741-2560/8/4/045006. URL: https://iopscience.iop.org/article/10.1088/1741-2560/8/4/045006%20https://iopscience.iop.org/article/10.1088/1741-2560/8/4/045006/meta.

[144] Samuel Garcia et al. “Neo: an object model for handling electrophysiology data in multiple formats”. In: *Frontiers in Neuroinformatics* 0.FEB (Feb. 2014), p. 10. ISSN: 1662-5196. DOI: 10.3389/FNINF.2014.00010.

[145] Hiroyuki Kamioka et al. “Spontaneous periodic synchronized bursting during formation of mature patterns of connections in cortical cultures”. In: *Neuroscience Letters* 206.2-3 (Mar. 1996), pp. 109–112. ISSN: 0304-3940. DOI: 10.1016/S0304-3940(96)12448-4.

[146] Fabian Pedregosa et al. “Scikit-learn: Machine Learning in Python”. In: *Journal of Machine Learning Research* 12.85 (2011), pp. 2825–2830. ISSN: 1533-7928. URL: http://jmlr.org/papers/v12/pedregosa11a.html.

[147] Rishi Chandra and Lance M. Optican. "Detection, classification, and superposition resolution of action potentials in multiunit single-channel recordings by an on-line real-time neural network". In: *IEEE Transactions on Biomedical Engineering* 44.5 (1997), pp. 403–412. DOI: 10.1109/10.568916.

[148] J de la Cruz et al. "Single and Multisite Graphene-Based Electroretinography Recording Electrodes: A Benchmarking Study". In: *Advanced Materials Technologies* (2021). DOI: 10.1002/admt.202101181.

[149] Li Xu et al. "Pharmacological analysis of the rat cone electroretinogram". In: *Visual Neuroscience* 20.3 (2003), pp. 297–306. ISSN: 09525238. DOI: 10.1017/S0952523803203084.

[150] Kenneth Brown and Motohiko Murakami. "A New Receptor Potential of the Monkey Retina with no etectable Latency". In: *Nature* 201 (1964), pp. 626–628.

[151] K. T. Brown and T. N. Wiesel. "Localization of origins of electroretinogram components by intraretinal recording in the intact cat eye". In: *The Journal of Physiology* 158.2 (1961), pp. 257–280. ISSN: 14697793. DOI: 10.1113/jphysiol.1961.sp006768.

[152] Perry Speros and James Price. "Oscillatory potentials. History, techniques and potential use in the evaluation of disturbances of retinal circulation". In: *Survey of Ophthalmology* 25.4 (1981), pp. 237–252. ISSN: 00396257. DOI: 10.1016/0039-6257(81)90093-X.

[153] Daizo Yonemura and Kazuo Kawasaki. "New approaches to ophthalmic electrodiagnosis by retinal oscillatory potential, drug-induced responses from retinal pigment epithelium and cone potential". In: *Documenta Ophthalmologica* 48.1 (1979), pp. 163–222. ISSN: 00124486. DOI: 10.1007/BF00207350.

[154] A. E. Weymouth and A. J. Vingrys. "Rodent electroretinography: Methods for extraction and interpretation of rod and cone responses". In: *Progress in Retinal and Eye Research* 27.1 (2008), pp. 1–44. ISSN: 13509462. DOI: 10.1016/j.preteyeres.2007.09.003.

[155] E. Tan et al. "The relationship between opsin overexpression and photoreceptor degeneration". In: *Investigative Ophthalmology and Visual Science* 42.3 (2001), pp. 589–600. ISSN: 01460404.

[156] Nicolás Cuenca et al. “Early changes in synaptic connectivity following progressive photoreceptor degeneration in RCS rats”. In: *European Journal of Neuroscience* 22.5 (2005), pp. 1057–1072. ISSN: 0953816X. DOI: 10.1111/j.1460-9568.2005.04300.x.

[157] Rongkang Yin et al. “Soft transparent graphene contact lens electrodes for conformal full-cornea recording of electroretinogram”. In: *Nature Communications* 9.1 (2018). ISSN: 2041-1723. DOI: 10.1038/s41467-018-04781-w. URL: http://dx.doi.org/10.1038/s41467-018-04781-w.

[158] F. Carpi and F. Tomei. “Non-invasive electroretinography”. In: *Biomedicine and Pharmacotherapy* (2006). ISSN: 07533322. DOI: 10.1016/j.biopha.2006.07.002.

[159] L Esakowitz, A Kriss, and F Shawkat. “A Comparison of Flash Electroretinograms Recorded From Burian-Allen, Jet, C-Glide, Gold Foil, DTL and Skin Electrodes”. In: *Documenta Ophthalmologica* (1993), pp. 169–171.

[160] Magnus Gjötterberg. “Electrodes for Electroretinography”. In: *Archives of Ophthalmology* 104.4 (1986), p. 569. ISSN: 0003-9950. DOI: 10.1001/archopht.1986.01050160125027.

[161] Yelena Krakova et al. “Spatial differences in corneal electroretinogram potentials measured in rat with a contact lens electrode array”. In: *Documenta Ophthalmologica* 129.3 (2014), pp. 151–166. ISSN: 15732622. DOI: 10.1007/s10633-014-9459-5.

[162] Zahra Derafshi et al. “Corneal potential maps measured with multi-electrode electroretinography in rat eyes with experimental lesions”. In: *Investigative Ophthalmology and Visual Science* 58.7 (2017), pp. 2863–2873. ISSN: 15525783. DOI: 10.1167/iovs.16-20726.

[163] R Heywood. “SOME CLINICAL OBSERVATIONS ON THE EYES OF SPRAGUE-DAWLEY RATS”. In: *Laboratory Animals* 7 (1973), pp. 19–27.

[164] *Retinitis Pigmentosa*. URL: https://www.nei.nih.gov/learn-about-eye-health/eye-conditions-and-diseases/retinitis-pigmentosa.

[165] Laura Fernández-Sánchez et al. “Proinsulin slows retinal degeneration and vision loss in the P23H rat model of retinitis pigmentosa”. In: *Human Gene Therapy* 23.12 (2012), pp. 1290–1300. ISSN: 10430342. DOI: 10.1089/hum.2012.067.

[166] Laura Fernández-Sánchez et al. “Retinal Vascular Degeneration in the Transgenic P23H Rat Model of Retinitis Pigmentosa”. In: *Frontiers in Neuroanatomy* 12.June (2018), pp. 1–14. ISSN: 16625129. DOI: 10.3389/fnana.2018.00055.

[167] Dao Yi Yu et al. “Photoreceptor death, trophic factor expression, retinal oxygen status, and photoreceptor function in the P23H rat”. In: *Investigative Ophthalmology and Visual Science* 45.6 (2004), pp. 2013–2019. ISSN: 01460404. DOI: 10.1167/iovs.03-0845.

[168] Elise Orhan et al. “Genotypic and phenotypic characterization of P23H line 1 rat model”. In: *PLoS ONE* 10.5 (2015), pp. 1–21. ISSN: 19326203. DOI: 10.1371/journal.pone.0127319.

[169] G. B. J. Keiner. “The Electroretinogram (ERG)”. In: *Webvision: The Organization of the Retina and Visual System*. 2001, pp. 76–80. DOI: 10.1007/978-94-017-6770-5{_}5.

[170] Daphne L. McCulloch et al. “ISCEV Standard for full-field clinical electroretinography (2015 update)”. In: *Documenta Ophthalmologica* 130.1 (2015), pp. 1–12. ISSN: 15732622. DOI: 10.1007/s10633-014-9473-7.

[171] Raj K. Maturi and Lori Bleau. *Multifocal ERG in Practice*. 2004. URL: https://www.reviewofophthalmology.com/article/multifocal-erg-in-practice.

[172] Ashley N. Selner et al. “Three-Dimensional Model of Electroretinogram Field Potentials in the Rat Eye”. In: *IEEE Transactions on Biomedical Engineering* 65.12 (2018), pp. 2781–2789. ISSN: 15582531. DOI: 10.1109/TBME.2018.2816591.

[173] Sarah Gibson, Jack W. Judy, and Dejan Marković. “Spike sorting: The first step in decoding the brain: The first step in decoding the brain”. In: *IEEE Signal Processing Magazine* 29.1 (2012), pp. 124–143. DOI: 10.1109/MSP.2011.941880.

[174] Christina M. Tringides et al. “Viscoelastic surface electrode arrays to interface with viscoelastic tissues”. In: *Nature Nanotechnology* (2021). ISSN: 17483395. DOI: 10.1038/s41565-021-00926-z.

[175] S. Chehreh Chelgani et al. “A Review of Graphite Beneficiation Techniques”. In: *http://dx.doi.org/10.1080/08827508.2015.1115992* 37.1 (Jan. 2016), pp. 58–68. ISSN: 15477401. DOI: 10.1080/08827508.2015.1115992. URL: https://www.tandfonline.com/doi/abs/10.1080/08827508.2015.1115992.

[176] Mathis Wissler. “Graphite and carbon powders for electrochemical applications”. In: *Journal of Power Sources* 156.2 (June 2006), pp. 142–150. ISSN: 0378-7753. DOI: 10.1016/J.JPOWSOUR.2006.02.064.

[177] Yanwu Zhu et al. “Graphene and graphene oxide: Synthesis, properties, and applications”. In: *Advanced Materials* 22.35 (Sept. 2010), pp. 3906–3924. ISSN: 09359648. DOI: 10.1002/ADMA.201001068.

[178] Daniel R. Dreyer et al. “The chemistry of graphene oxide”. In: *Chemical Society Reviews* 39.1 (Jan. 2010), pp. 228–240. ISSN: 03060012. DOI: 10.1039/B917103G.

[179] J. I. Paredes et al. “Graphene Oxide Dispersions in Organic Solvents”. In: *Langmuir* 24.19 (Oct. 2008), pp. 10560–10564. ISSN: 07437463. DOI: 10.1021/LA801744A. URL: https://pubs.acs.org/doi/abs/10.1021/la801744a.

[180] Alan P. Kauling et al. “The Worldwide Graphene Flake Production”. In: *Advanced Materials* 30.44 (Nov. 2018), p. 1803784. ISSN: 1521-4095. DOI: 10.1002/ADMA.201803784. URL: https://onlinelibrary.wiley.com/doi/full/10.1002/adma.201803784%20https://onlinelibrary.wiley.com/doi/abs/10.1002/adma.201803784%20https://onlinelibrary.wiley.com/doi/10.1002/adma.201803784.

[181] Amaia Zurutuza and Claudio Marinelli. “Challenges and opportunities in graphene commercialization”. In: *Nature Nanotechnology 2014 9:10* 9.10 (Oct. 2014), pp. 730–734. ISSN: 1748-3395. DOI: 10.1038/nnano.2014.225. URL: https://www.nature.com/articles/nnano.2014.225.

[182] Li Peng et al. “An iron-based green approach to 1-h production of single-layer graphene oxide”. In: *Nature Communications* 6 (Jan. 2015). ISSN: 20411723. DOI: 10.1038/NCOMMS6716. URL: /pmc/articles/PMC4354147/%20/pmc/articles/PMC4354147/?report=abstract%20https://www.ncbi.nlm.nih.gov/pmc/articles/PMC4354147/.

[183] Yuan Tian et al. “Micro-Spherical Sulfur/Graphene Oxide Composite via Spray Drying for High Performance Lithium Sulfur Batteries”. In: *Nanomaterials 2018, Vol. 8, Page 50* 8.1 (Jan. 2018), p. 50. ISSN: 20794991. DOI: 10.3390/NANO8010050. URL: https://www.mdpi.com/2079-4991/8/1/50/htm%20https://www.mdpi.com/2079-4991/8/1/50.

[184] Luis Baptista-Pires et al. “Water activated graphene oxide transfer using wax printed membranes for fast patterning of a touch sensitive device”. In: *ACS Nano* 10.1 (Jan. 2016), pp. 853–860. ISSN: 1936086X. DOI: 10.1021/ACSNANO.5B05963/SUPPL{_}FILE/NN5B05963{_}SI{_}002.AVI. URL: https://pubs.acs.org/doi/pdf/10.1021/acsnano.5b05963.

[185] Xuewen Wang et al. “Exfoliation at the Liquid/Air Interface to Assemble Reduced Graphene Oxide Ultrathin Films for a Flexible Noncontact Sensing Device”. In: *Advanced Materials* 27.8 (Feb. 2015), pp. 1370–1375. ISSN: 1521-4095. DOI: 10.1002/ADMA.201404069. URL: https://onlinelibrary.wiley.com/doi/full/10.1002/adma.201404069%20https://onlinelibrary.wiley.com/doi/abs/10.1002/adma.201404069%20https://onlinelibrary.wiley.com/doi/10.1002/adma.201404069.

[186] Yagang Yao et al. “Large-scale production of two-dimensional nanosheets”. In: *Journal of Materials Chemistry* 22.27 (June 2012), pp. 13494–13499. ISSN: 09599428. DOI: 10.1039/C2JM30587A. URL: https://pubs.rsc.org/en/content/articlehtml/2012/jm/c2jm30587a%20https://pubs.rsc.org/en/content/articlelanding/2012/jm/c2jm30587a.

[187] Ayrat M. Dimiev and Siegfried Eigler. *Graphene oxide : fundamentals and applications*. Wiley, 2016, p. 439. ISBN: 978-1-119-06940-9. URL: https://www.wiley.com/en-us/Graphene+Oxide%3A+Fundamentals+and+Applications-p-9781119069409.

[188] Yan Li et al. “In Situ Exfoliation of Graphene in Epoxy Resins: A Facile Strategy to Efficient and Large Scale Graphene Nanocomposites”. In: *ACS Applied Materials and Interfaces* 8.36 (Sept. 2016), pp. 24112–24122. ISSN: 19448252. DOI: 10.1021/ACSAMI.6B07492/SUPPL{_}FILE/AM6B07492{_}SI{_}001.PDF. URL: https://pubs.acs.org/doi/abs/10.1021/acsami.6b07492.

[189] Cheng Zhan et al. “Computational insight into the capacitive performance of graphene edge planes”. In: *Carbon* 116 (May 2017), pp. 278–285. ISSN: 0008-6223. DOI: 10.1016/J.CARBON.2017.01.104.

[190] Wenjing Yuan et al. “The edge- and basal-plane-specific electrochemistry of a single-layer graphene sheet”. In: *Scientific Reports* 3 (2013). ISSN: 20452322. DOI: 10.1038/SREP02248.

[191] Jung Joon Yoo et al. “Ultrathin planar graphene supercapacitors”. In: *Nano Letters* 11.4 (Apr. 2011), pp. 1423–1427. ISSN: 15306984. DOI: 10.1021/NL200225J/SUPPL{_}FILE/NL200225J{_}SI{_}001.PDF. URL: https://pubs.acs.org/doi/abs/10.1021/nl200225j.

[192] Iman Khosravi et al. “The application of graphene oxide as corrosion barrier”. In: *Corrosion Protection at the Nanoscale* (2020), pp. 127–140. DOI: 10.1016/B978-0-12-819359-4.00008-8.

[193] Communication Siegfried Eigler et al. “Wet Chemical Synthesis of Graphene”. In: *Advanced Materials* 25.26 (July 2013), pp. 3583–3587. ISSN: 1521-4095. DOI: 10.1002/ADMA.201300155. URL: https://onlinelibrary.wiley.com/doi/full/10.1002/adma.201300155%20https://onlinelibrary.wiley.com/doi/abs/10.1002/adma.201300155%20https://onlinelibrary.wiley.com/doi/10.1002/adma.201300155.

[194] By Kris Erickson et al. “Determination of the Local Chemical Structure of Graphene Oxide and Reduced Graphene Oxide”. In: *Advanced Materials* 22.40 (Oct. 2010), pp. 4467–4472. ISSN: 1521-4095. DOI: 10.1002/ADMA.201000732. URL: https://onlinelibrary.wiley.com/doi/full/10.1002/adma.201000732%20https://onlinelibrary.wiley.com/doi/abs/10.1002/adma.201000732%20https://onlinelibrary.wiley.com/doi/10.1002/adma.201000732.

[195] Sasha Stankovich et al. “Synthesis of graphene-based nanosheets via chemical reduction of exfoliated graphite oxide”. In: *Carbon* 45.7 (June 2007), pp. 1558–1565. ISSN: 0008-6223. DOI: 10.1016/J.CARBON.2007.02.034.

[196] Dan Li et al. “Processable aqueous dispersions of graphene nanosheets”. In: *Nature Nanotechnology 2008 3:2* 3.2 (Jan. 2008), pp. 101–105. ISSN: 1748-3395. DOI: 10.1038/nnano.2007.451. URL: https://www.nature.com/articles/nnano.2007.451.

[197] Sungjin Park et al. “Colloidal suspensions of highly reduced graphene oxide in a wide variety of organic solvents”. In: *Nano Letters* 9.4 (Apr. 2009), pp. 1593–1597. ISSN: 15306984. DOI: 10.1021/NL803798Y/SUPPL{_}FILE/NL803798Y{_}SI{_}001.PDF. URL: https://pubs.acs.org/doi/abs/10.1021/nl803798y.

[198] Alexander Sinitskii et al. “Graphene Nanoribbon Devices Produced by Oxidative Unzipping of Carbon Nanotubes”. In: *ACS Nano* 4.9 (Sept. 2010), pp. 5405–5413. ISSN: 19360851. DOI: 10.1021/NN101019H. URL: https://pubs.acs.org/doi/abs/10.1021/nn101019h.

[199] Ming Zhou et al. “Controlled Synthesis of Large-Area and Patterned Electrochemically Reduced Graphene Oxide Films”. In: *Chemistry – A European Journal* 15.25 (June 2009), pp. 6116–6120. ISSN: 1521-3765. DOI: 10.1002/CHEM.200900596. URL: https://onlinelibrary.wiley.com/doi/full/10.1002/chem.200900596%20https://onlinelibrary.wiley.com/doi/abs/10.1002/chem.200900596%20https://

chemistry-europe.onlinelibrary.wiley.com/doi/full/10.1002/chem.200900596.

[200] Yuyan Shao et al. "Graphene based electrochemical sensors and biosensors: A review". In: *Electroanalysis* 22.10 (2010), pp. 1027–1036. ISSN: 10400397. DOI: 10.1002/elan.200900571.

[201] Adriano Ambrosi and Martin Pumera. "Precise Tuning of Surface Composition and Electron-Transfer Properties of Graphene Oxide Films through Electroreduction". In: *Chemistry – A European Journal* 19.15 (Apr. 2013), pp. 4748–4753. ISSN: 1521-3765. DOI: 10.1002/CHEM.201204226. URL: https://onlinelibrary.wiley.com/doi/full/10.1002/chem.201204226%20https://onlinelibrary.wiley.com/doi/abs/10.1002/chem.201204226%20https://chemistry-europe.onlinelibrary.wiley.com/doi/full/10.1002/chem.201204226.

[202] Daoqing Liu, Qianwei Li, and Huazhang Zhao. "Electrolyte-assisted hydrothermal synthesis of holey graphene films for all-solid-state supercapacitors". In: *Journal of Materials Chemistry A* 6.24 (June 2018), pp. 11471–11478. ISSN: 20507496. DOI: 10.1039/C8TA02580K. URL: https://pubs.rsc.org/en/content/articlehtml/2018/ta/c8ta02580k%20https://pubs.rsc.org/en/content/articlelanding/2018/ta/c8ta02580k.

[203] Hsin Hui Huang et al. "Structural Evolution of Hydrothermally Derived Reduced Graphene Oxide". In: *Scientific Reports 2018 8:1* 8.1 (May 2018), pp. 1–9. ISSN: 2045-2322. DOI: 10.1038/s41598-018-25194-1. URL: https://www.nature.com/articles/s41598-018-25194-1.

[204] Hong Chen et al. "Reduction of free-standing graphene oxide papers by a hydrothermal process at the solid/gas interface". In: *RSC Advances* 3.9 (Feb. 2013), pp. 2971–2978. ISSN: 20462069. DOI: 10.1039/C2RA21576D. URL: https://pubs.rsc.org/en/content/articlehtml/2013/ra/c2ra21576d%20https://pubs.rsc.org/en/content/articlelanding/2013/ra/c2ra21576d.

[205] Harshal P. Mungse et al. "Hydrothermal deoxygenation of graphene oxide in sub- and supercritical water". In: *RSC Advances* 4.43 (May 2014), pp. 22589–22595. ISSN: 20462069. DOI: 10.1039/C4RA01085J. URL: https://pubs.rsc.org/en/content/articlehtml/2014/ra/c4ra01085j%20https://pubs.rsc.org/en/content/articlelanding/2014/ra/c4ra01085j.

[206] Tae Hee Han et al. “Steam etched porous graphene oxide network for chemical sensing”. In: *Journal of the American Chemical Society* 133.39 (Oct. 2011), pp. 15264–15267. ISSN: 00027863. DOI: 10.1021/JA205693T/SUPPL{_}FILE/JA205693T{_}SI{_}001.PDF. URL: https://pubs.acs.org/doi/abs/10.1021/ja205693t.

[207] James L. Wilbur et al. “Microcontact printing of self-assembled monolayers: applications in microfabrication”. In: *Nanotechnology* 7.4 (Dec. 1996), p. 452. ISSN: 0957-4484. DOI: 10.1088/0957-4484/7/4/028. URL: https://iopscience.iop.org/article/10.1088/0957-4484/7/4/028%20https://iopscience.iop.org/article/10.1088/0957-4484/7/4/028/meta.

[208] Jung Mu Kim et al. “Continuous anti-stiction coatings using self-assembled monolayers for gold microstructures”. In: *Journal of Micromechanics and Microengineering* 12.5 (Aug. 2002), p. 688. ISSN: 0960-1317. DOI: 10.1088/0960-1317/12/5/327. URL: https://iopscience.iop.org/article/10.1088/0960-1317/12/5/327%20https://iopscience.iop.org/article/10.1088/0960-1317/12/5/327/meta.

[209] Chuanzhen Zhou, Gabriella Nagy, and Amy V. Walker. “Toward molecular electronic circuitry: Selective deposition of metals on patterned self-assembled monolayer surfaces”. In: *Journal of the American Chemical Society* 127.35 (Sept. 2005), pp. 12160–12161. ISSN: 00027863. DOI: 10.1021/JA052614F/SUPPL{_}FILE/JA052614FSI20050803{_}101229.PDF. URL: https://pubs.acs.org/doi/abs/10.1021/ja052614f.

[210] Francisco Palazon et al. “Carbodiimide/NHS derivatization of COOH-terminated SAMs: Activation or byproduct formation?” In: *Langmuir* 30.16 (Apr. 2014), pp. 4545–4550. ISSN: 15205827. DOI: 10.1021/LA5004269/SUPPL{_}FILE/LA5004269{_}SI{_}001.PDF. URL: https://pubs.acs.org/doi/abs/10.1021/la5004269.

[211] Elisabet Prats-Alfonso et al. “Facile solid-phase synthesis of biotinylated alkyl thiols”. In: *Tetrahedron* 62.29 (July 2006), pp. 6876–6881. ISSN: 0040-4020. DOI: 10.1016/J.TET.2006.04.090.

[212] Colin D. Bain and George M. Whitesides. “Molecular-Level Control over Surface Order in Self-Assembled Monolayer Films of Thiols on Gold”. In: *Science* 240.4848 (Apr. 1988), pp. 62–63. ISSN: 00368075. DOI: 10.1126/SCIENCE.240.4848.62. URL: https://www.science.org/doi/abs/10.1126/science.240.4848.62.

[213] Lauren Newton et al. “Self assembled monolayers (SAMs) on metallic surfaces (gold and graphene) for electronic applications”. In: *Journal of Materials Chemistry C* 1.3 (Dec. 2012), pp. 376–393. ISSN: 2050-7534. DOI: 10.1039/C2TC00146B. URL: https://pubs.rsc.org/en/content/articlehtml/2013/tc/c2tc00146b%20https://pubs.rsc.org/en/content/articlelanding/2013/tc/c2tc00146b.

[214] C Zhou, M R Deshpande, and M A Reed. “Nanoscale metal/self-assembled monolayer/ metal heterostructures”. In: *Appl. Phys. Lett* 71 (1997), p. 611. DOI: 10.1063/1.120195. URL: https://doi.org/10.1063/1.120195.

[215] Hyun Woo Jang and Woo Soo Kim. “Shear-induced dry transfer of reduced graphene oxide thin film via roll-to-roll printing”. In: *Applied Physics Letters* 108.9 (Feb. 2016). ISSN: 00036951. DOI: 10.1063/1.4943083.

[216] Tsutomu Nagaoka and Takashi Yoshino. “Surface properties of electrochemically pretreated glassy carbon”. In: *Analytical Chemistry* 58.6 (2002), pp. 1037–1042. ISSN: 15206882. DOI: 10.1021/AC00297A012. URL: https://pubs.acs.org/doi/abs/10.1021/ac00297a012.

[217] Tsutomu Nagaoka et al. “Uptake of Ions into Electrochemically Treated Glassy Carbon”. In: *Analytical Chemistry* 60 (1988), pp. 2766–2769. URL: https://pubs.acs.org/sharingguidelines.

[218] Tung Yu Ying et al. “Electrosorption of Ions from Aqueous Solutions by Nanostructured Carbon Aerogel”. In: *Journal of Colloid and Interface Science* 250.1 (June 2002), pp. 18–27. ISSN: 0021-9797. DOI: 10.1006/JCIS.2002.8314.

[219] Steven A. Spronk, Donald E. Elmore, and Dennis A. Dougherty. “Voltage-dependent hydration and conduction properties of the hydrophobic pore of the mechanosensitive channel of small conductance”. In: *Biophysical journal* 90.10 (2006), pp. 3555–3569. ISSN: 0006-3495. DOI: 10.1529/BIOPHYSJ.105.080432. URL: https://pubmed.ncbi.nlm.nih.gov/16500980/.

[220] Zhongjin He et al. “Electric-Field Effects on Ionic Hydration: A Molecular Dynamics Study”. In: *Journal of Physical Chemistry B* 122.22 (June 2018), pp. 5991–5998. ISSN: 15205207. DOI: 10.1021/ACS.JPCB.8B02773/SUPPL{_}FILE/JP8B02773{_}SI{_}001.PDF. URL: https://pubs.acs.org/doi/abs/10.1021/acs.jpcb.8b02773.

[221] Xiaojing Gong et al. “Molecular switch for tuning ions across nanopores by an external electric field”. In: *Nanotechnology* 24.2 (Dec. 2012), p. 025502. ISSN: 0957-4484. DOI: 10.1088/0957-4484/24/2/025502. URL: https:

//iopscience.iop.org/article/10.1088/0957-4484/24/2/025502%20https://iopscience.iop.org/article/10.1088/0957-4484/24/2/025502/meta.

[222] J. Dzubiella, R. J. Allen, and J. P. Hansen. "Electric field-controlled water permeation coupled to ion transport through a nanopore". In: *The Journal of chemical physics* 120.11 (Mar. 2004), pp. 5001–5004. ISSN: 0021-9606. DOI: 10.1063/1.1665656. URL: https://pubmed.ncbi.nlm.nih.gov/15267365/.

[223] E. P. Schulz, L. M. Alarcón, and G. A. Appignanesi. "Behavior of water in contact with model hydrophobic cavities and tunnels and carbon nanotubes". In: *The European Physical Journal E* 34.10 (Oct. 2011), pp. 1–6. ISSN: 1292-895X. DOI: 10.1140/EPJE/I2011-11114-8. URL: https://link.springer.com/article/10.1140/epje/i2011-11114-8.

[224] Sebastián R. Accordino et al. "Hydrophilic behavior of graphene and graphene-based materials". In: *The Journal of chemical physics* 143.15 (Oct. 2015). ISSN: 1089-7690. DOI: 10.1063/1.4933011. URL: https://pubmed.ncbi.nlm.nih.gov/26493919/.

[225] G. Hummer, J. C. Rasaiah, and J. P. Noworyta. "Water conduction through the hydrophobic channel of a carbon nanotube". In: *Nature* 414.6860 (Nov. 2001), pp. 188–190. ISSN: 1476-4687. DOI: 10.1038/35102535. URL: https://www.nature.com/articles/35102535.

[226] Xu Zhang et al. "Insights into the effect of the interlayer spacings of bilayer graphene on the desolvation of H+, Li+, Na+, and K+ ions with water as a solvent: a first-principles study". In: *Physical Chemistry Chemical Physics* 21.42 (Oct. 2019), pp. 23697–23704. ISSN: 1463-9084. DOI: 10.1039/C9CP02922B. URL: https://pubs.rsc.org/en/content/articlehtml/2019/cp/c9cp02922b%20https://pubs.rsc.org/en/content/articlelanding/2019/cp/c9cp02922b.

[227] Qing Shao et al. "Anomalous hydration shell order of Na + and K + inside carbon nanotubes". In: *Nano Letters* 9.3 (Mar. 2009), pp. 989–994. ISSN: 15306984. DOI: 10.1021/NL803044K/SUPPL{_}FILE/NL803044K{_}SI{_}001.PDF. URL: https://pubs.acs.org/doi/abs/10.1021/nl803044k.

[228] J. Chmiola et al. "Anomalous increase in carbon at pore sizes less than 1 nanometer". In: *Science* 313.5794 (Sept. 2006), pp. 1760–1763. ISSN: 00368075. DOI: 10.1126/SCIENCE.1132195/SUPPL{_}FILE/PAP.PDF. URL: https://www.science.org/doi/abs/10.1126/science.1132195.

[229] J. Marañón Di Leo and J. Marañón. "Hydration and diffusion of cations in nanopores". In: *Journal of Molecular Structure: THEOCHEM* 729.1-2 (Sept. 2005), pp. 53–57. ISSN: 0166-1280. DOI: 10.1016/J.THEOCHEM.2005.02.070.

[230] Christian Boehler et al. "Tutorial: guidelines for standardized performance tests for electrodes intended for neural interfaces and bioelectronics". In: *Nature Protocols* 15.11 (2020), pp. 3557–3578. ISSN: 17502799. DOI: 10.1038/s41596-020-0389-2. URL: http://dx.doi.org/10.1038/s41596-020-0389-2.

[231] Y Zhang et al. *jGCaMP8 Fast Genetically Encoded Calcium Indicators*. 2020. DOI: 10.25378/janelia.13148243. URL: https://www.janelia.org/jgcamp8-calcium-indicators.

[232] Boris Hofmann et al. "Nanocavity electrode array for recording from electrogenic cells". In: *Lab on a Chip* 11.6 (Feb. 2011), pp. 1054–1058. DOI: 10.1039/C0LC00582G. URL: https://pubs.rsc.org/en/content/articlehtml/2011/lc/c0lc00582g%20https://pubs.rsc.org/en/content/articlelanding/2011/lc/c0lc00582g.

[233] Marta K Lewandowska et al. "Recording Large Extracellular Spikes in Microchannels along Many Axonal Sites from Individual Neurons". In: (2015). DOI: 10.1371/journal.pone.0118514.

[234] Bradley J. Dworak and Bruce C. Wheeler. "Novel MEA platform with PDMS microtunnels enables the detection of action potential propagation from isolated axons in culture". In: *Lab on a Chip* 9.3 (Feb. 2009), pp. 404–410. ISSN: 1473-0189. DOI: 10.1039/B806689B. URL: https://pubs.rsc.org/en/content/articlehtml/2009/lc/b806689b%20https://pubs.rsc.org/en/content/articlelanding/2009/lc/b806689b.

[235] Liangbin Pan et al. "Propagation of action potential activity in a predefined microtunnel neural network". In: *Journal of Neural Engineering* 8.4 (July 2011), p. 046031. ISSN: 1741-2552. DOI: 10.1088/1741-2560/8/4/046031. URL: https://iopscience.iop.org/article/10.1088/1741-2560/8/4/046031%20https://iopscience.iop.org/article/10.1088/1741-2560/8/4/046031/meta.

[236] Udit Narula et al. "Narrow microtunnel technology for the isolation and precise identification of axonal communication among distinct hippocampal subregion networks". In: *PLoS ONE* (2017). DOI: 10.1371/journal.pone.0176868. URL: https://doi.org/10.1371/journal.pone.0176868.g001.

[237] Ling Wang et al. “Biophysics of microchannel-enabled neuron–electrode interfaces”. In: *Journal of Neural Engineering* 9.2 (Feb. 2012), p. 026010. DOI: 10.1088/1741-2560/9/2/026010. URL: https://iopscience.iop.org/article/10.1088/1741-2560/9/2/026010%20https://iopscience.iop.org/article/10.1088/1741-2560/9/2/026010/meta.

[238] Daniel A. Wagenaar, Jerome Pine, and Steve M. Potter. “Effective parameters for stimulation of dissociated cultures using multi-electrode arrays”. In: *Journal of Neuroscience Methods* 138.1-2 (2004), pp. 27–37. ISSN: 01650270. DOI: 10.1016/j.jneumeth.2004.03.005.

[239] *PDMS microstructures and rGO MEA primary hippocampal cultures | Zenodo*. URL: https://zenodo.org/record/5801777.

[240] Mathias J. Aebersold et al. “"Brains on a chip": Towards engineered neural networks”. In: *TrAC - Trends in Analytical Chemistry* 78 (2016), pp. 60–69. ISSN: 18793142. DOI: 10.1016/j.trac.2016.01.025. URL: http://dx.doi.org/10.1016/j.trac.2016.01.025.

[241] Mark Shein-Idelson, Eshel Ben-Jacob, and Yael Hanein. “Engineered Neuronal Circuits: A New Platform for Studying the Role of Modular Topology”. In: *Frontiers in Neuroengineering* 4.September (2011), pp. 1–8. DOI: 10.3389/fneng.2011.00010.

[242] Emanuele Marconi et al. “Emergent functional properties of neuronal networks with controlled topology”. In: *PLoS ONE* 7.4 (Apr. 2012). ISSN: 19326203. DOI: 10.1371/JOURNAL.PONE.0034648.

[243] R. E. BAIER and L. WEISS. “Demonstration of the Involvement of Adsorbed Proteins in Cell Adhesion and Cell Growth on Solid Surfaces”. In: *Applied Chemistry at Protein Interfaces*. AMERICAN CHEMICAL SOCIETY, June 1975. Chap. 14, pp. 300–307. ISBN: 9780841202153. DOI: 10.1021/BA-1975-0145.CH014. URL: https://pubs.acs.org/doi/pdf/10.1021/ba-1975-0145.ch014.

[244] Mohiuddin Mohammed, Tsung Sheng Lai, and Hsin Chieh Lin. “Substrate stiffness and sequence dependent bioactive peptide hydrogels influence the chondrogenic differentiation of human mesenchymal stem cells”. In: *Journal of Materials Chemistry B* 9.6 (Feb. 2021), pp. 1676–1685. ISSN: 2050-7518. DOI: 10.1039/D0TB02008G. URL: https://pubs.rsc.org/en/content/articlehtml/2021/tb/d0tb02008g%20https://pubs.rsc.org/en/content/articlelanding/2021/tb/d0tb02008g.

[245] Heloísa Gerardo et al. “Soft culture substrates favor stem-like cellular phenotype and facilitate reprogramming of human mesenchymal stem/stromal cells (hMSCs) through mechanotransduction”. In: *Scientific Reports 2019 9:1* 9.1 (June 2019), pp. 1–18. ISSN: 2045-2322. DOI: 10.1038/s41598-019-45352-3. URL: https://www.nature.com/articles/s41598-019-45352-3.

[246] Nicholas D. Evans et al. “Substrate stiffness affects early differentiation events in embryonic stem cells”. In: *European Cells and Materials* 18 (2009), pp. 1–13. ISSN: 14732262. DOI: 10.22203/ECM.V018A01.

[247] Wen Tai Chiu et al. “Soft substrate induces apoptosis by the disturbance of Ca2+ homeostasis in renal epithelial LLC-PK1 cells”. In: *Journal of Cellular Physiology* 212.2 (Aug. 2007), pp. 401–410. ISSN: 1097-4652. DOI: 10.1002/JCP.21037. URL: https://onlinelibrary.wiley.com/doi/full/10.1002/jcp.21037%20https://onlinelibrary.wiley.com/doi/abs/10.1002/jcp.21037%20https://onlinelibrary.wiley.com/doi/10.1002/jcp.21037.

[248] J. Vitte et al. “Is there a predictable relationship between surface physical-chemical properties and cell behaviour at the interface?” In: *European Cells and Materials* 7 (2004), pp. 52–63. ISSN: 14732262. DOI: 10.22203/ECM.V007A06.

[249] Donald F. Gerson et al. “Adhesion, phagocytosis and cell surface energy. The binding of fixed human erythrocytes to rat macrophages and polymethylpentene”. In: *Biochimica et Biophysica Acta (BBA) - Biomembranes* 692.1 (Oct. 1982), pp. 147–156. ISSN: 0005-2736. DOI: 10.1016/0005-2736(82)90512-0.

[250] B Majhy, P Priyadarshini, and A K Sen. “Effect of surface energy and roughness on cell adhesion and growth-facile surface modification for enhanced cell culture †”. In: *RSC Advances* (2021), pp. 15467–15476. DOI: 10.1039/d1ra02402g.

[251] B. Majhy, V. P. Singh, and A. K. Sen. “Understanding wetting dynamics and stability of aqueous droplet over superhydrophilic spot surrounded by superhydrophobic surface”. In: *Journal of Colloid and Interface Science* 565 (Apr. 2020), pp. 582–591. ISSN: 0021-9797. DOI: 10.1016/J.JCIS.2020.01.056.

[252] J. M. Shaw et al. “Negative photoresists for optical lithography”. In: *IBM Journal of Research and Development* 41.1-2 (1997), pp. 81–94. ISSN: 00188646. DOI: 10.1147/RD.411.0081.

[253] Peng Xue et al. “Protein covalently conjugated SU-8 surface for the enhancement of mesenchymal stem cell adhesion and proliferation”. In: *Langmuir* 30.11 (Mar. 2014), pp. 3110–3117. ISSN: 15205827. DOI: 10.1021/LA500048Z.

[254] Ferdinand Walther et al. “Stability of the hydrophilic behavior of oxygen plasma activated SU-8”. In: *Journal of Micromechanics and Microengineering* 17.3 (Mar. 2007), pp. 524–531. ISSN: 09601317. DOI: 10.1088/0960-1317/17/3/015.

[255] Maria Nordström et al. “Rendering SU-8 hydrophilic to facilitate use in micro channel fabrication”. In: *Journal of Micromechanics and Microengineering* (2004), 1614–1617 JOURNAL. DOI: 10.1088/0960-1317/14/12/003. URL: stacks.iop.org/JMM/14/1614.

[256] Qudus Hamid et al. “Surface modification of SU-8 for enhanced cell attachment and proliferation within microfluidic chips”. In: *Journal of Biomedical Materials Research - Part B Applied Biomaterials* 103.2 (Feb. 2015), pp. 473–484. ISSN: 15524981. DOI: 10.1002/JBM.B.33223.

[257] Dudley S. Finch et al. “Biocompatibility of atomic layer-deposited alumina thin films”. In: *Journal of Biomedical Materials Research - Part A* 87.1 (Oct. 2008), pp. 100–106. ISSN: 15493296. DOI: 10.1002/JBM.A.31732.

[258] K Torimitsu and A Kawana. “Selective growth of sensory nerve fibers on metal oxide patterns in culture”. In: *Dev. Brain Res.* 51 (1990), pp. 128–131.

[259] Paul C. Letourneau. “Cell-substratum adhesion of neurite growth cones, and its role in neurite elongation”. In: *Experimental Cell Research* 124.1 (1979), pp. 127–138. ISSN: 00144827. DOI: 10.1016/0014-4827(79)90263-5.

[260] Peter Fromherz et al. “A Neuron-Silicon Junction: A Retzius Cell of the Leech on an Insulated-Gate Field-Effect Transistor”. In: *Science* 252.5010 (1991), pp. 1290–1293. ISSN: 00368075. DOI: 10.1126/SCIENCE.1925540. URL: https://www.science.org/doi/abs/10.1126/science.1925540.

[261] Markus Dankerl et al. “Graphene solution-gated field-effect transistor array for sensing applications”. In: *Advanced Functional Materials* 20.18 (2010), pp. 3117–3124. ISSN: 1616301X. DOI: 10.1002/adfm.201000724.

[262] Lucas H. Hess et al. “Graphene transistor arrays for recording action potentials from electrogenic cells”. In: *Advanced Materials* 23.43 (2011), pp. 5045–5049. ISSN: 09359648. DOI: 10.1002/adma.201102990.

[263] *Dobule Passivation | Zenodo*. URL: https://zenodo.org/record/5801677.

[264] Christof Niemeyer and Chad Mirkin. *Nanobiotechnology: Concepts, Applications and Perspectives*. Wiley, 2004. ISBN: 978-3-527-30658-9. URL: https://www.wiley.com/en-us/Nanobiotechnology%3A+Concepts%2C+Applications+and+Perspectives-p-9783527306589.

[265] Amit Kumar, Hans A. Biebuyck, and George M. Whitesides. "Patterning Self-Assembled Monolayers: Applications in Materials Science". In: *Langmuir* 10.5 (May 1994), pp. 1498–1511. ISSN: 15205827. DOI: 10.1021/LA00017A030. URL: https://pubs.acs.org/doi/abs/10.1021/la00017a030.

[266] Andre Bernard et al. "Printing Patterns of Proteins". In: *Langmuir* 14.9 (Jan. 1998), pp. 2225–2229. ISSN: 07437463. DOI: 10.1021/LA980037L. URL: https://pubs.acs.org/doi/abs/10.1021/la980037l.

[267] J. P. Renault et al. "Fabricating Arrays of Single Protein Molecules on Glass Using Microcontact Printing". In: *Journal of Physical Chemistry B* 107.3 (Jan. 2002), pp. 703–711. ISSN: 10895647. DOI: 10.1021/JP0263424. URL: https://pubs.acs.org/doi/abs/10.1021/jp0263424.

[268] H. Schmid and B. Michel. "Siloxane Polymers for High-Resolution, High-Accuracy Soft Lithography". In: *Macromolecules* 33.8 (Apr. 2000), pp. 3042–3049. ISSN: 00249297. DOI: 10.1021/MA982034L. URL: https://pubs.acs.org/doi/full/10.1021/ma982034l.

[269] A Bernard et al. "Microcontact Printing of Proteins". In: *Advanced Materials* 12.14 (2000), pp. 1067–1070. URL: https://sci-hubtw.hkvisa.net/https://onlinelibrary.wiley.com/doi/abs/10.1002/1521-4095(200007)12:14%3C1067::AID-ADMA1067%3E3.0.CO;2-M?casa_token=gT3LoHIO8a8AAAAA:-je39XWRmYc0_LojQ8hvwGdZkbCwI6fApQkTK76BYcZOAOYDBBHgbXxbQxf_hZ16ecdguonAcdxM4ZE.

[270] H. D. Inerowicz et al. "Multiprotein Immunoassay Arrays Fabricated by Microcontact Printing". In: *Langmuir* 18.13 (June 2002), pp. 5263–5268. ISSN: 07437463. DOI: 10.1021/LA0157216. URL: https://pubs.acs.org/doi/abs/10.1021/la0157216.

[271] C. D. James et al. "Patterned Protein Layers on Solid Substrates by Thin Stamp Microcontact Printing". In: *Langmuir* 14.4 (Feb. 1998), pp. 741–744. ISSN: 07437463. DOI: 10.1021/LA9710482. URL: https://pubs.acs.org/doi/pdf/10.1021/la9710482.

[272] Sébastien G. Ricoult et al. "Generation of microisland cultures using microcontact printing to pattern protein substrates". In: *Journal of neuroscience methods* 208.1 (June 2012), pp. 10–17. ISSN: 1872-678X. DOI: 10.1016/J.JNEUMETH.2012.04.016. URL: https://pubmed.ncbi.nlm.nih.gov/22561087/.

[273] *Microcontact Printing | Zenodo*. URL: https://zenodo.org/record/5801701.

[274] Arseniy Gladkov et al. "Design of Cultured Neuron Networks in vitro with Predefined Connectivity Using Asymmetric Microfluidic Channels". In: *Scientific Reports* 7.1 (2017), pp. 1–14. ISSN: 20452322. DOI: 10.1038/s41598-017-15506-2. URL: http://dx.doi.org/10.1038/s41598-017-15506-2.

[275] Csaba Forró et al. "Modular microstructure design to build neuronal networks of defined functional connectivity". In: *Biosensors & bioelectronics* 122 (Dec. 2018), pp. 75–87. ISSN: 1873-4235. DOI: 10.1016/J.BIOS.2018.08.075. URL: https://pubmed.ncbi.nlm.nih.gov/30243047/.

[276] Matthias Merz and Peter Fromherz. "Silicon chip interfaced with a geometrically defined net of snail neurons". In: *Advanced Functional Materials* 15.5 (May 2005), pp. 739–744. ISSN: 1616301X. DOI: 10.1002/ADFM.200400316.

[277] Matthias Merz and Peter Fromherz. "Polyester Microstructures for Topographical Control of Outgrowth and Synapse Formation of Snail Neurons". In: *Advanced Materials* 14.2 (2002), pp. 142–144. URL: https://sci-hubtw.hkvisa.net/https://onlinelibrary.wiley.com/doi/abs/10.1002/1521-4095(20020116)14:2%3C141::AID-ADMA141%3E3.0.CO;2-R?casa_token=y_1TLGyvCjYAAAAA%3A82pC9ENZzA5WLRGk74I8T-1IyiwqlyS6eL6GuyDyGhj1cdMhpR_2IcHp4DVZ3vWypzSId28TJtD1te0.

[278] Vincent Martinez et al. "Controlled single-cell deposition and patterning by highly flexible hollow cantilevers". In: *Lab on a Chip* 16.9 (2016), pp. 1663–1674. ISSN: 14730189. DOI: 10.1039/c5lc01466b.

[279] *Cytosurge*. URL: https://www.cytosurge.com/.

[280] Agnes Szabó et al. "SU-8 microstructures alter the attachment and growth of glial cells in vitro". In: *Materials Today Communications* 27 (2021), pp. 2352–4928. DOI: 10.1016/j.mtcomm.2021.102336. URL: https://doi.org/10.1016/j.mtcomm.2021.102336.

[281] Seog Woo Rhee et al. “Patterned cell culture inside microfluidic devices”. In: *Lab on a Chip* 5.1 (Dec. 2005), pp. 102–107. ISSN: 14730197. DOI: 10.1039/B403091E. URL: https://pubs.rsc.org/en/content/articlehtml/2005/lc/b403091e%20https://pubs.rsc.org/en/content/articlelanding/2005/lc/b403091e.

[282] Yufei Ren et al. “A Simple and Reliable PDMS and SU-8 Irreversible Bonding Method and Its Application on a Microfluidic-MEA Device for Neuroscience Research”. In: *Micromachines* 6.12 (2015), pp. 1923–1934. ISSN: 2072666X. DOI: 10.3390/mi6121465.

[283] Wei Li et al. “NeuroArray: A Universal Interface for Patterning and Interrogating Neural Circuitry with Single Cell Resolution”. In: *Scientific Reports 2014 4:1* 4.1 (Apr. 2014), pp. 1–7. ISSN: 2045-2322. DOI: 10.1038/srep04784. URL: https://www.nature.com/articles/srep04784.

[284] Shantanu Bhattacharya et al. “Studies on surface wettability of poly(dimethyl) siloxane (PDMS) and glass under oxygen-plasma treatment and correlation with bond strength”. In: *Journal of Microelectromechanical Systems* 14.3 (June 2005), pp. 590–597. ISSN: 10577157. DOI: 10.1109/JMEMS.2005.844746.

[285] Heike Hardelauf et al. “High fidelity neuronal networks formed by plasma masking with a bilayer membrane: analysis of neurodegenerative and neuroprotective processes.” In: *Lab on a chip* 11.16 (2011), pp. 2763–2771. ISSN: 1473-0197. DOI: 10.1039/c1lc20257j.

[286] *Wunderlichips*. URL: https://wunderlichips.ch/en/home.

[287] José C. Mateus et al. “Nanoscale patterning of in vitro neuronal circuits”. In: *bioRxiv* (Dec. 2021), p. 2021.12.16.472887. DOI: 10.1101/2021.12.16.472887. URL: https://www.biorxiv.org/content/10.1101/2021.12.16.472887v2%20https://www.biorxiv.org/content/10.1101/2021.12.16.472887v2.abstract.

[288] Ekaterina Pchitskaya and Ilya Bezprozvanny. “Dendritic Spines Shape Analysis—Classification or Clusterization? Perspective”. In: *Frontiers in Synaptic Neuroscience* 12 (Sept. 2020), p. 31. ISSN: 16633563. DOI: 10.3389/FNSYN.2020.00031/BIBTEX.

[289] Simon Fleischmann et al. “Pseudocapacitance: From Fundamental Understanding to High Power Energy Storage Materials”. In: *Chemical Reviews* 120.14 (2020), pp. 6738–6782. ISSN: 15206890. DOI: 10.1021/acs.chemrev.0c00170.

[290] Y. Liu, S. P. Jiang, and Z. Shao. "Intercalation pseudocapacitance in electrochemical energy storage: recent advances in fundamental understanding and materials development". In: *Materials Today Advances* 7 (Sept. 2020), p. 100072. ISSN: 2590-0498. DOI: 10.1016/J.MTADV.2020.100072.

[291] E. Hernández-Balaguera and J. L. Polo. "A generalized procedure for the coulostatic method using a constant phase element". In: *Electrochimica Acta* 233 (Apr. 2017), pp. 167–172. ISSN: 00134686. DOI: 10.1016/J.ELECTACTA.2017.03.026.

[292] *INBRAIN Neuroelectronics*. URL: https://www.inbrain-neuroelectronics.com/.

[293] Matthew J. Nelson et al. "Review of signal distortion through metal microelectrode recording circuits and filters". In: *Journal of Neuroscience Methods* 169.1 (Mar. 2008), pp. 141–157. ISSN: 0165-0270. DOI: 10.1016/J.JNEUMETH.2007.12.010.

[294] S. Roddaro et al. "The optical visibility of graphene: Interference colors of ultrathin graphite on SiO2". In: *Nano Letters* 7.9 (Sept. 2007), pp. 2707–2710. ISSN: 15306984. DOI: 10.1021/nl0711581.

[295] Chuancheng Jia et al. "Direct Optical Characterization of Graphene Growth and Domains on Growth Substrates". In: *Scientific Reports 2012 2:1* 2.1 (Oct. 2012), pp. 1–6. ISSN: 2045-2322. DOI: 10.1038/srep00707. URL: https://www.nature.com/articles/srep00707.

[296] P. Nemes-Incze et al. "Anomalies in thickness measurements of graphene and few layer graphite crystals by tapping mode atomic force microscopy". In: *Carbon* 46.11 (Sept. 2008), pp. 1435–1442. ISSN: 0008-6223. DOI: 10.1016/J.CARBON.2008.06.022.

[297] Hyungwoo Lee et al. "Nanoscale Direct Mapping of Noise Source Activities on Graphene Domains". In: *ACS Nano* 10.11 (Nov. 2016), pp. 10135–10142. DOI: 10.1021/ACSNANO.6B05288. URL: https://pubs.acs.org/doi/abs/10.1021/acsnano.6b05288.

[298] Nathan Schaefer et al. "Improved metal-graphene contacts for low-noise, high-density microtransistor arrays for neural sensing". In: *Carbon* 161 (2020), pp. 647–655. ISSN: 00086223. DOI: 10.1016/j.carbon.2020.01.066.

[299] F Tuinstra and J L Koenig. "Raman Spectrum of Graphite". In: *J. Chem. Phys* 53 (1970), p. 1126. DOI: 10.1063/1.1674108. URL: https://doi.org/10.1063/1.1674108.

[300] Andrea C. Ferrari and John Robertson. *Raman Spectroscopy in Carbons: From Nanotubes to Diamond : Papers of a Theme Issue*. Royal Society, 2004, p. 299.

[301] Da Luo et al. "Role of Graphene in Water-Assisted Oxidation of Copper in Relation to Dry Transfer of Graphene". In: *Chemistry of Materials* 29.10 (May 2017), pp. 4546–4556. DOI: 10.1021/ACS.CHEMMATER.7B01276. URL: https://pubs.acs.org/doi/abs/10.1021/acs.chemmater.7b01276.

[302] Li Tao et al. "Uniform Wafer-Scale Chemical Vapor Deposition of Graphene on Evaporated Cu (111) Film with Quality Comparable to Exfoliated Monolayer". In: (2012). DOI: 10.1021/jp3068848. URL: https://pubs.acs.org/sharingguidelines.